Charles University in Prague
Faculty of Mathematics and Physics

DOCTORAL THESIS

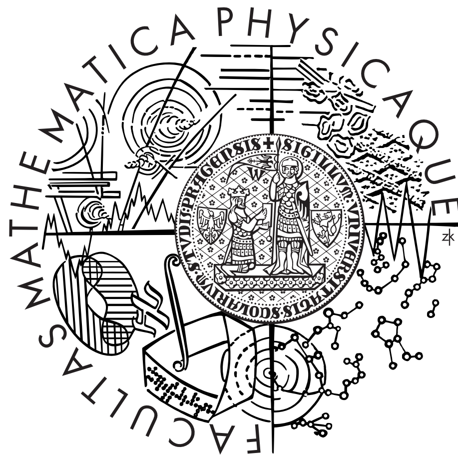

Lukáš Horák

Study of the structure of ferromagnetic semiconductors by x-ray scattering methods

Department of Condensed Matter Physics

Supervisor of the doctoral thesis:	prof. RNDr. Václav Holý, CSc.
Study programme:	Physics
Specialization:	Physics of Nanostructures

Prague 2014

motto:

Nullus est liber tam malus, ut non aliqua parte prosit

This work would be never finished without kind support of many people. In the first place, I would thank to my supervisor Václav Holý for his helpful advices and for sharing his extensive knowledge. At the most, I would appreciate his patience that, indeed, fulfilled the definition from the vocabulary: 'Content to wait if necessary; not losing one's temper while waiting.'

Also, I would express my gratitude to my colleague Zdeněk Matěj for everything he taught me and for his readiness to discuss anything any time. As well, I would like to thank other colleagues so willing to spent time with discussions, which were so fruitful for me: Stanislav Daniš, Václav Valeš, Jana Stránská, and Tereza Brunátová.

My thanks belong also to Vít Novák from Institute of Physics (ASCR) for the sample preparation and for some helpful consultations.

Last but not least, I express my thanks to my whole family for a moral and a financial support, which allowed me to finish this work.

dedicated to the memory of my beloved father

I declare that I carried out this doctoral thesis independently, and only with the cited sources, literature and other professional sources.

I understand that my work relates to the rights and obligations under the Act No. 121/2000 Coll., the Copyright Act, as amended, in particular the fact that the Charles University in Prague has the right to conclude a license agreement on the use of this work as a school work pursuant to Section 60 paragraph 1 of the Copyright Act.

In .... date .... signature of the author

Název práce: Studium struktury feromagnetických polovodičů metodami rtg rozptylu

Autor: Lukáš Horák

Katedra: Katedra fyziky kondenzovaných látek

Vedoucí disertační práce: prof. RNDr. Václav Holý, CSc., Katedra fyziky kondenzovaných látek

Abstrakt: Studovali jsme epitaxní vrstvy arsenidu gallia a manganu různými metodami RTG rozptylu. Protože polohy Mn dopantu v hostitelské mřížce arsenidu gallia jsou zcela zásadní pro magnetické vlastnosti tohoto materiálu, zaměřili jsme se hlavně na vývoj laboratorní difrakční metody schopné identifikovat mangan v konkrétních krystalografických polohách. Z naměřené difraktované intenzity rozložené podél useklic je možné dovodit hustotu Mn intersticiálů ve dvou neekvivalentních krystalografických polohách. Žíháním je možno snižit hustotu Mn intersticiálů. Demonstrovali jsme naši metodu na epitaxní vrstvě, která prošla několikerým žíháním. Po každém z nich byl určen hloubkový profil hustoty intersticiálů. Proces žíhání byl simulován řešením drift-difuzních rovnic. Z porovnání s experimentálně určenými koncentracemi intersticiálů jsme odhadli difusivitu Mn intersticiálů v mřížce arsendiu gallia.

Klíčová slova: (Ga,Mn)As, RTG difrakce ve vysokém rozlišení, intersticiály, difuze

Title: Study of the structure of ferromagnetic semiconductors by x-ray scattering methods

Author: Lukáš Horák

Department: Department of Condensed Matter Physics

Supervisor: prof. RNDr. Václav Holý, CSc., Department of Condensed Matter Physics

Abstract: We studied epitaxial layers of Gallium Manganese Arsenide by various x-ray scattering methods. Since the positions of the Mn dopant in the a host GaAs lattice are crucial for magnetic properties of this material, we focused mainly on a development of the laboratory diffraction method capable to identify Mn in particular crystallographic positions. From the measured diffracted intensity distributed along Crystal Truncation Rods, it is possible deduce the density of Mn interstitials in two non-equivalent crystallographic positions. It is possible to decrease the interstitial Mn density by annealing. We demonstrated our method on severally annealed epitaxial layer. The depth profile of interstitial density was determined after each annealing. The annealing process was simulated by the solving of the Drift-Diffusion equations. From the comparison with the experimentally determined interstitial densities, we estimated the diffusivity of Mn interstitials in the GaAs lattice.

Keywords: (Ga,Mn)As, High-Resolution x-Ray Diffraction, Interstitials, Diffusion

Contents

Preface 4

1 Overview of Gallium Manganese Arsenide research 7
- 1.1 Diluted magnetic semiconductor . . . 7
- 1.2 Gallium Manganese Arsenide . . . 8
- 1.3 Growth and preparation of (Ga,Mn)As . . . 10
- 1.4 Experimental techniques for sample characterization . . . 13
- Prospects . . . 15

2 Dynamical theory of diffraction 16
- 2.1 Wavefield in a material . . . 16
- 2.2 Boundary conditions . . . 20
- 2.3 Simulated diffraction on layered sample . . . 21
- Summary . . . 23

3 Influence of defect density on diffracted intensity 25
- 3.1 Structural model of (Ga,Mn)As . . . 25
  - 3.1.1 Assumption on lattice parameter . . . 27
- 3.2 Structure factor . . . 27
  - 3.2.1 Averaged structure factor . . . 28
  - 3.2.2 Diffraction maxima types . . . 29
  - 3.2.3 Same maxima types with different scattering vector length 32
  - 3.2.4 Local structural distortion . . . 33
  - 3.2.5 Atoms shifted from their regular positions . . . 33
  - 3.2.6 Structure factor corrected to local distortion . . . 35
  - 3.2.7 Neighbourhood of anti-site defect . . . 36
  - 3.2.8 Iso-intensity surfaces . . . 38
- Conclusion . . . 39

4 Description of HRXRD measurement 40
- 4.1 Experimental equipment . . . 40
  - 4.1.1 x-ray tube . . . 40
  - 4.1.2 Incident beam path . . . 41
  - 4.1.3 Diffracted beam path . . . 44
  - 4.1.4 Control of experiment . . . 45
  - 4.1.5 Available modes for line scans . . . 47
- 4.2 Measurement procedure . . . 49
  - 4.2.1 Sample adjustment . . . 49
  - 4.2.2 Relation between angular and reciprocal space . . . 52

4.2.3 Snakes in reciprocal space 59
Conclusion 66

5 Interstitial density determined by HRXD 67
5.1 Samples 67
5.2 Measurement 68
5.3 Data treatment and fitting procedure 72
5.4 Fitted experimental data 79
Conclusion 87

6 Surface Mn oxide evidenced by XAS 89
6.1 Samples 89
6.2 Experimental prove of Mn oxide forming 90
Conclusion 93

7 Mn densities determined using anomalous diffraction 94
7.1 Anomalous dispersion of atomic scattering factor 95
7.2 Anomalous diffraction experiment 98
Conclusion 101

8 Diffusion of interstitials 102
8.1 Drift-diffusion equations 102
8.1.1 Laterally homogeneous (Ga,Mn)As layer 103
8.1.2 Boundary conditions 104
8.1.3 Surface container 105
8.2 Numerical computation of D-D equations 107
8.2.1 Bounded D-D equations 107
8.2.2 Solving D-D equations for particles with incomparable diffusivities 109
8.2.3 Final remarks on calculation method 110
8.3 Diffusion only 111
Summary 112

9 Simulation of annealing procedure 113
9.1 Initial guess at D-D model parameters 113
9.2 Guess at D-D model parameters from D-D simulation 116
Conclusion 119

10 (Ga,Mn)As/AlGaAs multilayers studied by x-ray reflectivity 120
10.1 Experiment 120
10.2 Interpretation of relative electron densities 124
10.3 Estimation of substitutional-interstitial ratio 126
Conclusion 129

11 (Ga,Mn)As microbars 131
11.1 Samples 131
11.2 Strain field computations 132
11.3 Simulation of x-ray diffraction experiment on micro-bars 134
11.4 Experiment 138

Conclusion 142
Accompaniments 142

Summary **148**

Bibliography **164**

List of Tables **165**

List of Figures **168**

List of Abbreviations **169**

List of Publications **170**

List of Conference contributions **172**

Preface

Since the second half of a previous century, the semiconductor electronics has been enormously and continuously flourishing in the means of a performance and a usage diversity. Essentially, its success in both categories has been driven by the advancing miniaturization. Till now, the technology concept which uses a transistor as an active element persists from its very beginning. Obviously, current semiconductor devices cannot be shrunk neither to infinitesimally small, nor behind atomic dimensions.

It seems that a call for the performance improvement will not quiet, moreover, the need of a lower power consumption becomes more and more urgent. The spintronics, introducing the spin degree into the devices, is one of several tries to meet these demands. Completely new concepts of the information processing and storing require new materials which allow to handle with spin polarization as well as with classical charge currents. The ferromagnetic semiconductors, exhibiting the magnetic ordering and semiconductor behaviour, are very promising materials for such a purpose.

Obviously, the structural information on the ferromagnetic semiconductor materials is crucial for their further theoretical studies. In this thesis, we study a structure of the (Ga,Mn)As, which is an archetypal diluted ferromagnetic semiconductor, by means of the x-ray scattering. The magnetism is brought into this system by the magnetic impurities, manganese atoms, incorporated in the GaAs host lattice. The exact position of the impurities and a possible presence of other lattice defects affects both the magnetic and the charge-carriers transport properties. The aim of our work is to test capabilities and limitations of x-ray methods for the investigation of these impurities and defects in (Ga,Mn)As epitaxial layers.

There are two main objectives of this thesis. Firstly, being experimentally methodological, we want to develop a reliable approach using the High-resolution x-ray diffraction to determine the impurity occupancy of the non-equivalent lattice sites. In other words, to determine the degree of the sample perfectness relatively to the structure intended by technologists. These structural parameters are directly related to the functional properties of the material, therefore it is desired to develop a non-destructive and commonly available probing method for the routine samples characterization in order to feedback the technological process.

The second objective, being of a principal nature, is to experimentally answer the question which of the theoretically considered impurities positions in the host lattice are occupied. There are still doubts if the occupancies of two specific interstitial defects in different crystallographic positions are equal, or one of them is more favoured and/or the presence of the latter is completely suppressed. An-

other important aim is to answer the question how the annealing process, which is often the final technological step of the material preparation, affects the defects distribution in the lattice. It is just such density decrease of certain defects suspected from the magnetic improvement of the material after the annealing treatment.

We organize the text of the thesis as follows. Depicting the current state of the art, we start with the introductory chapter. There, we describe briefly the technological development of the (Ga,Mn)As material together with some theoretical predictions. The final properties are essentially susceptible to the condition of the sample preparation. And since this is connected with the investigated structural information, we include some related aspects of the growth technique into the text. Finally, we summarize the current experimental findings of various techniques capable to reveal the structurally related information on (Ga,Mn)As.

The measured diffraction patterns by the High resolution x-ray diffraction are interpreted by the comparison with the numerical simulation of the experiment. Since we use the dynamical theory of the diffraction for such simulations, we describe its basics in the next, theoretical, chapter. Here, we focus on the derivation of exact formulas used in our later calculations considering the most often system of the (Ga,Mn)As epitaxial layer on the GaAs (001) substrate.

In the third chapter, we describe the (Ga,Mn)As material from the structural point of view. Here, we discuss the relation between occupancies of the particular lattice positions and the scattering power of the material with respect to the scattered-wave direction relatively to the incident primary x-ray beam. From that, we derive the measurement strategy and expected sensitivity to the occupancies. The influence of the local structural distortion due to the presence of the non-native atoms in the GaAs lattice is discussed, as well.

Since the main experimentally method used in this work is the High resolution x-ray diffraction, we dedicate the forth chapter to the experiment description. The one of the thesis aims is the development of a routine laboratory characterization procedure. Therefore, we describe thoroughly the laboratory equipment and the diffraction measurement using the specific High resolution diffractometer. The advantages of various measurement approaches are discussed in order to suggest the most robust measurement strategy.

Further, we introduce the sample set dedicated for the experimental demonstration of the laboratory High-Resolution x-Ray Diffraction method described in previous chapters. Here, we present a laboratory measurements. We interpret these results by the fitting of experimental data with the theoretical simulation. The optimization procedure is introduced and discussed. The obtained most probable densities of the Mn atoms in different lattice positions are presented together with their uncertainties. We discuss some limitations of our interpretation, mainly the most controversial assumption of the theoretical occupancy-predeterminated lattice expansion.

In the sixth chapter, we verify the speculation on the surface degradation during the annealing. We performed this experimental proof with the x-Ray Absorption Spectroscopy measurement. We show that during natural ageing and annealing, the Mn oxide layers is formed on the surface. In the contrary, the rinsing in HCl successfully removes this oxide away.

The seventh chapter introduce the anomalous diffraction techniques, which

use the significant change of the scattering power of certain element within the small energetic range around its absorption edge. Here, we discuss how this phenomena is manifested in the diffraction contrast of the Mn atoms in various lattice positions. With no *apriori* assumptions on he samples studied in the previous chapter, we interpret the synchrotron measurement of them obtaining some parameters to be compared with previous results.

Focusing to the annealing process in the fourth chapter, we postulate a theoretical model of the mobilized-impurities migration. We formulate the drift-diffusion equations describing the local change of the impurities density when the material is exposed to the air-ambient heating. The solution of these equations represents the change on the structural level of the (Ga,Mn)As induced by the heating. Therefore, the resulted model is discussed with the intention to interpret, later, the experimentally determined occupancy changes after the annealing treatment.

In the next chapter, we drive our attention to the analysis of the our samples annealing. Using the theory introduced in the previous chapter, we seek for the drift-diffusion equations solution comparable with the previously obtained structural information on the samples in various annealing states. This allows to estimate very roughly the parameters controlling the atom migration within the annealing temperatures. We discuss the relevance of our annealing model consisting of a migration of mobile defects in the internal electric field.

Our focus turns from the diffraction to the x-ray reflectivity in the tenth chapter. Here, we present a short study of (Ga,Mn)As/AlGaAs multilayer samples. The specular x-ray reflectivity curves, measured on samples with different Al content, are fitted with the numerically simulated data. From the comparison, the depth profiles of the average electron density follows. Since the mean electron density in the AlGaAs is well predictable, we speculate on the determined depth profiles of the densities using AlGaAs constituent layer as a referential one. Although the unit cell in the (Ga,Mn)As constituent layer is undoubtedly larger with respect to GaAs, we show that the mean electron density in (Ga,Mn)As can be larger or smaller than that in GaAs. From the exact experimental values we are able to estimate the ratio of the Mn in substitutional and interstitial lattice positions.

In last chapter, we study the spatial distribution of the elastic strain in patterned uniform (Ga,Mn)As micro-bars epitaxially bounded with a GaAs substrate. The elastic strain field manifests in the diffracted intensity distribution in the reciprocal space. We compare the data for several samples measured at the synchrotron facility with the numerical simulation. These consists of a strain field calculation in the arbitrary shaped micro-bar and of a diffraction experiment simulation using the calculated strain field.

Finally, last pages of this thesis text summarize and synthesise all generated conclusions.

Chapter 1

Overview of Gallium Manganese Arsenide research

In this introductory chapter, we want to summarise the state of the art in Diluted Magnetic Semiconductor (DMS) research with emphasis on Gallium Manganese Arsenide ((Ga,Mn)As). We will introduce the basics of the theoretical background to make clear the motivation for the finding new DMS materials that are promising for the spintronics applications [1], for instance, non-volatile memory devices [2–4] or low-voltage transistors [5, 6]. Besides the introduction to last-decades findings on properties of the new materials, we will briefly describe the preparation of the (Ga,Mn)As material using Molecular Beam Epitaxy (MBE) technique. Together with that, we will mention the difficulties of such a growth and consequences for resulting samples. Since the main topic of this thesis is the structural analysis, we will make an overview of commonly used experimental methods for the structural investigation of (Ga,Mn)As. x

1.1 Diluted magnetic semiconductor

The standard semiconductor transistors, whose density on a chip still more or less obeys the predictive Moore's law [7], cannot keep going smaller forever as their size is physically limited. Moreover, a contemporary architecture of separated logic and memory elements limits the speed of devices because information has to be transferred between them via metal wires. Even if people were happy with the speed and the size of their computers and smart phones, such devices would spent a lot of electricity on calculating, on storing information and consequently on cooling of heated chips. Those are several reasons why the need of new concepts of electronic devices has arisen. There is a hope that such an answer can be given by the spin transport electronics (SPINTRONICS). Its development could lead to power saving high speed devices, moreover, devices whose functional and non-volatile storing capability could be integrated together.

The roots of the spintronics can be identified with the discovery of the Giant Magnetoresistance effect in 1988 [8, 9]. The concept including the spin degree of freedom into the electronics, which is based on the charge carriers current [10], induced the searching for the appropriate materials. Such materials that offer both a semiconductor behaviour and a ferromagnetic ordering are ferromagnetic semiconductors, e.g., certain metal oxides doped by Mn, Cr, Fe, Co or Ni [11, 12]. The

reasonable approach, apparently, is to build on basics of a conventional semiconductor electronics in order to keep the compatibility with the current technology. In other words, a new material is derived from the well known and widely used non-magnetic semiconductor material that is improved by the introducing some magnetic ions into its lattice. Such a material is known as DMS. The dilution is related just to those magnetic ions carrying the magnetic moments whose mutual interaction is indirect and it is mediated by the charge carriers.

The attention was firstly drawn to DMS based on II-VI type of semiconductors, e.g., (Cd,Mn)Se and (Hg,Mn)Te [13, 14], and on IV-VI type, e.g., PbSnMnTe [15]. Those materials are substitutional solid solutions, which form stable phases even for higher atomic concentration of a magnetic element. Studying of such compounds led to a better understanding of the magnetic ordering mechanisms in DMS, but their Curie temperature was very low.

The DMS based on III-V semiconductors would be for its compatibility optimal for the integration of the DMS into the at least experimental devices [16–18]. Those semiconductors, e.g., GaAs or InAs, are commonly used for optoelectronics and a high-speed electronics. In the contrary to the previously mentioned ternary alloys, the main problem is the low solubility of a magnetic element in the III-V compounds. The magnetic dopant atoms tend to segregate and to create incoherent binary-phase clusters in a semiconductor matrix [19, 20].

This evident obstacle was overcome using a non-equilibrium crystal growth technique, i.e., Low-Temperature Molecular Beam Epitaxial (LT-MBE) growth. The substrate is heated below the usual growth temperature and the meta-stable phase is obtained. Consequently, no segregation of dopant is observed and all magnetic ions are incorporated into the semiconductor lattice. Obviously, this technique produces additional crystal defects, such as vacancies and anti-sites (cations in anionic positions and vice versa).

The first adept for the LT-MBE growth of III-V DMS was the InAs as it seemed to be suitable choice for its relatively small bond energy. Being doped by the Mn atoms, the (In,Mn)As was prepared [21, 22]. The ferromagnetic ordering for Curie temperature below 7.5 K was observed in the p-type DMS [23]. These works were followed by the successful growth of p-type (Ga,Mn)As with Curie temperature (T_C) being 60 K. [24].

1.2 Gallium Manganese Arsenide

Since its first preparation, the DMS material research focused on the (Ga,Mn)As. It is sometimes denoted as $\mathrm{Ga}_{1-x}\mathrm{Mn}_x\mathrm{As}$, where x corresponds to the atomic fraction of Mn ions at the expense of Ga. After 12 years of intensive growth optimization, the Curie temperature has been risen to 180 K [25], but it is still far below room temperature. Last progress in this field indicates that this material will not be practicably usable for the future commercial spintronics devices because it is necessary to cool it strongly. Nevertheless, it became an archetypal, or model, DMS material for its compatibility with a contemporary semiconductor technology and for its relatively high Curie temperature. Such a temperature is sufficiently convenient for the experimental devices testing spintronics concepts.

The GaAs has a zinc-blend crystal structure. Each Ga atom is surrounded by four As neighbours forming a tetrahedron and vice versa. The Mn atoms,

incorporated into this structure during the growth, sit in the Ga (substitutional) positions bringing the local magnetic moment $5\mu_B$. In addition, these atoms act as acceptors due to the lack of $4p$ valence electron. The infrared spectroscopy experiments [26, 27] and the photoluminiscence experiments [28, 29] indicate that the substitutional Mn is the a moderately shallow acceptor. The details can be found in the review [30].

As we mentioned above, the non-equilibrium LT-MBE growth produces point defects in GaAs. It is assumed that the major defect in pure GaAs is an As anti-site due to the As overpressure during the growth. Some Ga sites are occupied by As atoms, and from the ideal crystal's point of view, they are located in 'wrong' places. They bring two extra electrons per defect, i.e, As antisites are double donors. In low-temperature GaAs (LT-GaAs), they cause n-type conductivity. In case of p-type (Ga,Mn)As, they compensate the holes partially. If the material is heated up to 450 °C, the As anti-sites diffuse close together and form As precipitates. Therefore, their density in the surrounding lattice decreases [31]. Unfortunately, the (Ga,Mn)As would be destroyed by the simultaneous segregation of substitutional Mn forming Mn precipitates [21, 32]. Still we can decrease the anti-site density already during the LT-MBE growth using As dimers instead of As tetramers in the MBE chamber [33].

In addition to the brief structure description, there are two non-equivalent interstitial spaces surrounded also by four Ga (or As) atoms forming tetrahedrons. It was shown that Mn atoms are incorporated also to these interstitial positions during the deposition [34]. From the theoretical calculations, it follows that each such interstitial Mn, being double donor, compensates two substitutional atoms [35]. Moreover, it orients its magnetic moment anti-parallelly to the moments of the substitutional atoms [36]. Since, the net magnetic moment is decreased [35].

The number of interstitials is very low for a low total Mn content [34]. For total Mn content of 2%, almost all Mn ions are expected in the substitutional positions[37].

Similarly to the anti-site, the Mn in the interstitial positions can be isolated by the annealing, as well. It results in the improvement of the (Ga,Mn)As in sense of a higher T_C. The annealing increases a net magnetic moment and also a charge carrier density. However sometimes, the latter increase is not considered as an improvement as it pushes the material close to a semi-metals. Firstly, the temperature can be comparable with the low-temperature growth for which the substitutional Mn atoms are stable[38] and the material does not degrade to GaAs with Mn clusters. Secondly, the Mn in interstitial positions diffuse towards the free surface of the material, where they are passivated by the oxygen creating Mn-rich oxidized layer. It is assumed that the mechanism is jumping of atom between the neighbouring interstitial positions [39]. The annealing procedure is necessary in particular for samples with higher total Mn content where the many of interstitial defects are created and nearly all substitutional Mn atoms are compensated.

On the other hand, if the annealing of (Ga,Mn)As is performed at higher temperatures compared with those of LT-MBE, Mn atoms tends to segregate forming Mn-rich clusters [32, 40–52]. Generally, it does not matter if the (Ga,Mn)As precursor is grown by LT-MBE [32, 40–42, 46, 47] or it is ion-implanted GaAs with Mn [43–45]. These cited works mostly agree on two types of clusters. Firstly, for

the annealing temperatures around 500 K, the abundant smaller (≈ 6 nm) tetragonal clusters having a zinc-blend structure are observed. In fact, it is not certain if it those are pure zinc-blend MnAs, or they are just Mn-rich nano-regions of (Ga,Mn)As with extremely low content of Ga. Their crystal lattice is fully coherent with the surrounding host lattice. These clusters exhibit weak ferromagnetic behaviour, i.e., small coercivity, but with T_C well above the room temperature (360–400 K) [43, 44, 49, 52]. Secondly, for the annealing temperatures around 600 K, the larger (≈ 20 nm) spherical clusters of a pure metallic MnAs are observed. These clusters corresponds to the hexagonal NiAs-type phase, often labelled as α-MnAs. These clusters coherently embedded in host GaAs lattice are ferromagnetic with T_C around 310–320 K [40, 45, 47]. However, the annealing temperature is not determinative on the type of the clusters, but the defect density and the placement of Mn atoms in the precursor lattice has its role, as well [41]. Nevertheless, the materials with segregated Mn although being magnetic are not DMS at all.

The ferromagnetism in zinc-blend DMS can be described by the Zener model ([53, 54]), which was originally proposed for transition metals. This description allows to explain and successfully predict the Curie temperature of acGaMnAs from the effective Mn density (c_{eff}) and the carrier (hole) density (p) [55]:

$$T_C \propto c_{\text{eff}} p^{1/3} . \tag{1.1}$$

Such a relation has been experimentally observed [56–58]. The effective Mn density is the density of magnetically uncompensated substitutional Mn atoms, i.e., the difference between those in substitutional and interstitial position. In addition, the interstitial Mn atoms together with other structural defect affect (decrease) the density of the holes p.

The DMS materials are interesting mainly due to their magnetotransport properties. Just these properties decide on a potential use of such a material. And just these properties, being measured and compared to theoretical predictions, can affirm or reject our picture, or model, of the (Ga,Mn)As. The description of such a phenomena as temperature-dependent resistivity, (anisotropic) magnetoresistance, (anomalous) Hall effects are beyond the intention of this work. The details can be found in reviews [30, 59].

1.3 Growth and preparation of (Ga,Mn)As

Of course, the making of the sample itself is crucial for the future properties of the sample. We are not going to describe details of this art, but we will briefly mention the basics of (Ga,Mn)As preparation as some of those facts are important and sometimes limiting in the structural characterization of (Ga,Mn)As layers, which is the topic of this work.

Molecular Beam Epitaxy is a usual method for the making of the new materials, especially for epitaxial, i.e., monocrystalline, layers on monocrystalline substrate. It allows to control many parameters, such as ratio of fluxes of the individual molecular beams, substrate temperature, deposition rate and many others. The optimal parameters are not exactly known when tailoring new material. This wide tunability allows to control precisely the final composition (doping level) and thickness. Another advantage is the possibility of monitoring the

growth by the reflection High-Energy Electron Diffraction during the operation. The MBE experimental setup is illustratively shown in Figure 1.1.

Figure 1.1: The MBE device Veeco in the MBE Laboratory in the Institute of Physics of the ASCR. The picture was taken from http://department.fzu.cz/surfaces/mbe/soubory/veeco/veeco.htm

For certain parameters controlling the deposition, the non-equilibrium growth can be enabled. Such a growth is necessary for the successful obtaining of the (Ga,Mn)As epitaxial layer. The main controlling parameter is the substrate temperature. Its influence on the resulted structure is schematically depicted in the Figure 1.2, which was adopted from Reference 17. To keep the stable temperature of the substrate can be tricky task. For instance, the temperature change of the substrate during LT-MBE deposition has been reported, and it was caused by the changing absorption/emission characteristics of the growing epitaxial layer (also called epilayer) [60].

Usually, the growth is operated with low ratio of arsenic to gallium to suppress the incorporation of the As antisite defects [33]. (Ga,Mn)As epilayers grown with As_2 dimers exhibit better structural, electrical, and magnetic properties than those grown with As_4 tetramers [33].

It was demonstrated that as-grown samples can be improved in term of Curie temperature by a post-growth annealing when exposed to ambient air [34, 39]. During such an annealing, the interstitials diffuse through the (Ga,Mn)As lattice towards the free surface. There, they are passivated and create a thin Mn-rich oxide layer [61–63].

Very similar results were obtained when annealing was performed with an amorphous arsenic capping layer [64, 65]. The difference is that the Mn interstitials form then MnAs with the arsenics in the capping layer. Since, the mechanism of the passivation is little bit different.

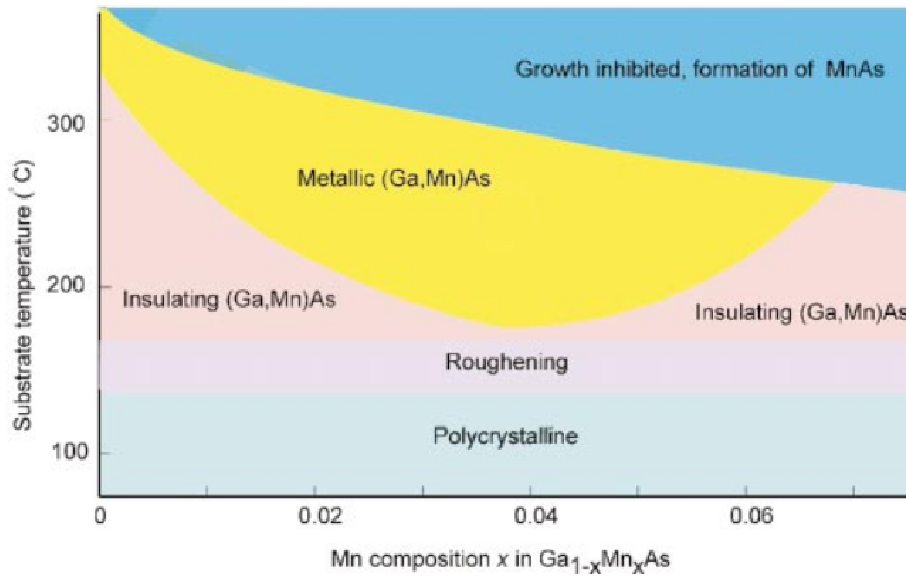

Figure 1.2: A schematic phasediagram of (Ga,Mn)As taken from Reference 17. It shows also the temperatures for that the material is 'destroyed' by the MnAs clusters formation. The insulating (Ga,Mn)As is probably (almost) fully compensated by the high defect density. The border between the metallic and the insulating growth depends on other parameters, as well, e.g., if the film is grown with As_2 or As_4 ([33]).

The surface of GaAs material naturally oxidise. The typical thickness of just such oxidized layer is 2–3 nm [66], further details can be found in [67]. The study of the (Ga,Mn)As layer using the x-ray standing wave fluorescence (XSWF) shows that there is 3 nm thick Mn-rich surface layer after four hours of annealing at 200 °C [62]. Moreover, the Mn is in random crystallographic positions, which probably indicates Mn oxide [62]. The thickness of this surface layer is noticeably comparable with the thickness of a naturally oxidized surface. Taking into account that the surface of the just deposited film oxidise immediately after the removal from the growing chamber, the surface is always more or less oxidized. The angular-dependent x-ray photoelectron spectroscopy study in Reference 25 indicates that the Mn interstitials are passivated below the thin native oxide. It means that interstitials do not migrate just above the surface, but the oxygen diffuse towards them into the film where they react together.

The annealing of as-grown samples is greatly improved by the removing of the surface oxide from the (Ga,Mn)As film by the HCl etching. This leads to higher T_C. Moreover, the T_C indicating the quality of the film, reaches its maximum value in shorter annealing time, if the long-term annealing procedure is replaced by the multiple short-time annealing combined with subsequent surface etching [25]. This etch-assisted annealing procedure has led to the highest achieved T_C for (Ga,Mn)As. It seems to be reasonable that the surface with access to an oxygen is capable to passive the nearby diffusing Mn ion, and after a certain time the barrier slowing and finally stopping this process is created. The rinsing in HCl refresh again this oxidizing capability.

1.4 Experimental techniques for sample characterization

The magnetic properties of resulted material are strongly affected by the real positions of the magnetic ions in the lattice [34]. Therefore, it is crucible task to determine their position and quantify their concentration since it gives the useful feedback between the theory and the technology. On the other hand, the presence of the magnetic ions is manifested rather weakly in the structure analysis as their concentration is usually low. Here, besides the brief remark on measurement of magnetic properties, we summarise the experimental techniques used for the structural investigation of (Ga,Mn)As thin films.

For most of the methods, it is impossible to discriminate the different Mn positions in the lattice [68] as they are only element sensitive, and thus, unable to resolve chemical bonds or the neighbourhood of the measured atoms. For instance, this is the case for x-Ray Fluorescence (XRF), Electron Probe Microanalysis (EPMA) or Secondary Ion Mass Spectrometry (SIMS).

In contrast, it is possible to determine the decrease of the Mn content in interstitial positions from the transport Hall measurement of the charge carrier density before and after the annealing [37, 39]. These measurements gives directly information on the T_C, as well [37]. Let us remind that the substitutional Mn ions act as acceptors while the interstitial Mn ions act as double donors. Since, the decrease of the carrier density due to the annealing is equal to the half of the removed interstitials. Moreover, the concentration of the Mn in interstitial and substitutional positions can be estimated for the as-grown sample if the total Mn concentration is measured by complementary measurements such as SIMS. To do this estimation it is necessary to assume that all interstitial Mn ions diffused out during the annealing, but this is valid or certain only for thin or very low doped epilayers.

Similarly, the distributions of Mn ions in different lattice sites can be studied by x-Ray Absorption Spectroscopy (XAS) methods at the MnK-edge [69]. The x-Ray Near-Edge Structure (XANES) technique confirms that the majority of Mn atoms are in the substitutional positions [69], but experiments fail to quantify exactly the interstitial density from the XANES data. On the other hand, the interstitial and substitutional Mn atoms can be discriminated by the Extended x-Ray Absorption Fine Structure (EXAFS) method. The particular concentrations can be estimated taking into account the known total Mn content. It can be determined by other methods, for instance again, SIMS. The EXAFS data also proved the expansion of the lattice due to the presence of the substitutional and interstitial Mn ions. However, to distinguish the different types of interstitial atoms, it is behind the limit of XAS because of the very similar scattering amplitudes and phases of Ga and As.

The concentration of Mn in particular lattice positions can be determined by diffraction techniques using Transmission Electron Microscopy (TEM) together with TEM Energy Dispersive x-Ray (EDX) microanalysis [70]. In this TEM diffraction method [70], the intensities of weak diffraction maxima are measured, for instance, (002) maxima, which allows to obtain the difference of those two interstitial occupancies. The absolute values of the concentrations can be estimated using values of the total content of Ga and Mn, being determined by EDX.

The concept of weak diffraction maxima measurement can be also used for x-ray diffraction, in particular in the High-Resolution x-Ray Diffraction (HRXRD) method. This is nondestructive and nonlocal, in contrast to TEM. This HRXRD approach was demonstrated on a set of (Ga,Mn)As samples with various total Mn concentrations in Reference 71. The authors show that the ratio of substitutional and interstitial Mn densities varies with the total Mn concentration. This ratio is determined from the change of the intensity diffracted from (Ga,Mn)As with respect to the calculated intensity of the diffraction for a pure GaAs. Such a change is caused by the contributions of substitutional and interstitial atoms to the (Ga,Mn)As structure factor. The effect of the local lattice distortion around the Mn atoms, the As interstitials, the Ga vacancies and the As anti-site defects are introduced in their model. However, it does not follow from the paper if the authors consider only one type of interstitial Mn atoms or both types with the same concentration. The theoretical estimations of the difference in the Mn densities in different lattice sites are not unambiguous. In the paper [72], the authors claim that the probability of the Mn occupying different types of interstitial positions is nearly the same, whereas other results indicate that the energetic difference between the Mn interstitials in As and Ga tetrahedra is large enough to suppress the presence of the latter [39].

A measurement of the diffracted-intensity dependence on the photon energy belongs to an x-ray methods. It is performed within the energies around the MnK absorption edge, anomalous diffraction. From this dependence, it is possible to determine the difference of the densities of Mn atoms placed in non-equivalent interstitial lattice positions [73].

Other x-ray based method for the investigation of the lattice positions of Mn atoms in (Ga,Mn)As is the x-Ray Standing-Wave (XRSW) method. It uses the effect of an x-ray standing wave produced by the diffraction process in the GaAs substrate. The standing wave excites a fluorescence of the Mn atoms. From the incident angle of the primary radiation, the particular lattice positions of the fluorescing Mn atoms can be deduced [62, 74]. From the XRSW data, it follows that the density of Mn interstitial atoms, indeed, decreases during annealing, however, a quantitative determination of the Mn density profile is practically impossible.

Using Scanning Tunneling Microscopy (STM), it is possible to map electronic states across the sample surface. In other words, it is possible to discriminate different impurities, and therefore, directly visualize the surface composition of (Ga,Mn)As samples[75]. Much more comprehensive information on the samples can be obtained from the sample cross-section, for which the cleaved surface is studied by STM, being denoted as Cross-Sectional Scanning Tunneling Microscopy (XSTM). For instance, this technique can be used for the imaging of the embedded MnAs nano-clusters in surrounding GaAs lattice [40] as well as for the direct visualization of the acceptors, i.e., substitutional Mn, distribution in the lattice [76–88]. It is possible to reveal the presence of defects up to several atomic layers [84]. The XSTM is capable to discriminate isolated substitutional atoms and anti-site defects [81] as well as substitutional-vacancy and substitutional-anti-site complexes [85]. Moreover, it is possible to detect isolated Mn atoms in all crystallographic positions [86, 87] or pairs of two substitutional and/or substitutional-interstitial Mn [88]. The direct imaging gives clear imagine

on the presence of various defects in the samples, however, this method is local and only semi-quantitative.

Finally, a crucial parameter of the (Ga,Mn)As samples is the T_C, often considered to be the synonym of the (Ga,Mn)As quality. Its being routinely determined by the Superconducting Quantum Interference Device magnetometry from the dependence of the measured magnetic moment with respect to temperature [24, 89]. The measured saturated magnetic moment allows to estimate the effective Mn density c_{eff} [37]. With the information on the total Mn content, it is possible to estimate both the substitutional and the interstitial densities.

More detailed information on the local magnetic moments is reachable by the x-Ray Magnetic Circular Dichroism (XMCD) method. In fact, XMCD spectrum is a differential XAS signal for the magnetization being parallel and antiparallel to the helicity of the primary circularly polarised x-ray radiation. It allows to separate the contributions of the spin and orbital origin to the magnetic moment. Such a measurement of Mn $L_{2,3}$ XMCD spectra determined a net magnetization of around $4.5\mu_B$ per Mn atom, and the antiferromagnetic coupling of the nearest neighbour interstitial-substitutional pairs at 22 K for the un-annealed sample was detected, as well [90].

Prospects

We emphasised the obstacles to overcome for a successful growth the (Ga,Mn)As epitaxial layers. The most significant parameter indicating the 'quality' of the film is the T_C, and this parameter is strictly related to the density of the impurities in the material. Therefore, the structural characterization in the mean of defect densities is very important for the technology feedback and the preparation of the material.

We summarized methods capable to determine or to indicate the presence of the impurities in the sample. Some of them are limited by their localness, e.g., STM or XSTM. Some of them are destructive, e.g., SIMS, XSTM, or TEM, and thus, they are not convenient for the post-growth characterization. Some powerful methods demand the availability of the not so accessible facilities, e.g., EXAFS, XANES, XMCD, XRSW, anomalous diffraction. These methods needs synchrotron radiation facility, because of a necessary tunability of a primary-radiation wavelength or a quality of a primary beam in means of an intensity or a divergence. Some of the well accessible methods are completely insensitive to crystallographic positions of the impurities, e.g., XRF, EPMA, SIMS.

On the other hand, there is a need of easily accessible, non-destructive, and non-local method for a routine laboratory characterization of the produced samples. The HRXRD fulfils all these requirements, therefore we are motivated in the development of such a characterization method using HRXRD. In the further chapters, we describe the measurement procedure of the (Ga,Mn)As samples and the basic well-established theory convenient for the simulation of the diffraction experiment. We derive the relations describing the influence of the impurities densities on the diffraction intensity, i.e., how the presence of the impurities in the different crystallographic positions is pronounced in the diffraction experiment. The experimental data treatment is described, and whole suggested characterization approach is demonstrated on a set of (Ga,Mn)As samples.

Chapter 2

Dynamical theory of diffraction

The main method of the investigation studied and used in this thesis is HRXRD. Although some information, such as the layer thickness or the lattice parameter, can be extracted almost directly from the measured data [91], majority of the structural parameters are pronounced indirectly in the distribution of the collected signal in the angular space. For the further analysis one has to be able to compute a numerical simulation of diffraction curves which should be compared with experimental data subsequently. From this comparison, some parameters connected to the atomic arrangement can be determined if the theoretical structural model is correct.

The thin epitaxial layers diffracts kinematically as their thickness is much smaller than the extinction length [92]. Usually, the substrate is a material with similar lattice parameters to the layer, and consequently, it diffracts within the similar diffraction conditions. However, the large substrate crystal diffracts dynamically. Due to the similar diffraction conditions, we measure the result of the interference of waves in the layer and in the substrate [91]. The substrate diffraction has to be treated dynamically. This processes and the interference of the waves from the layer/substrate can be easily described by the dynamical theory of diffraction. Its basics are reminded in this chapter and the final formulas for the diffraction curve simulation are derived step by step.

Firstly, we describe the electromagnetic wavefield in periodic medium, perfect crystal. Then we add boundary conditions for electromagnetic intensities at interfaces in the material. Finally, the exact formulas for the calculation of the diffracted intensity is derived.

2.1 Wavefield in a material

The spatial propagation of the electromagnetic wave field is described by the time independent Wave equation

$$(\Delta + K^2)\boldsymbol{E}(\boldsymbol{r}) = \hat{\mathrm{V}}(\boldsymbol{r})\,\boldsymbol{E}(\boldsymbol{r}) \tag{2.1}$$

following from the Maxwell's equations. The wave field is represented by the electric intensity $\boldsymbol{E}(\boldsymbol{r})$, the time dependent term $\mathrm{e}^{\mathrm{i}\omega t}$ is omitted. The monochromatic radiation of a wavelength λ is described as a sum of plane waves with the vacuum wave vector $K = 2\pi/\lambda$. The amplitudes of magnetic component of the wave field $\boldsymbol{H}$ and electric intensity $\boldsymbol{E}$ are connected via Maxwell equation, for

non-magnetic material we can write $\boldsymbol{H} = \sqrt{\epsilon_0/\mu_0}/K(\boldsymbol{k} \times \boldsymbol{E})$, where ϵ_0 and μ_0 are the permittivity and the permeability of the vacuum. The $\boldsymbol{k}$-vector is the wave vector giving the direction of the electromagnetic wave propagation.

The scattering potential $\hat{\mathbf{V}}(\boldsymbol{r})$ in case of a non-magnetic material can be written as

$$\hat{\mathbf{V}}(\boldsymbol{r}) = \text{grad div} - K^2\chi(\boldsymbol{r})\,, \tag{2.2}$$

where the $\chi(\boldsymbol{r})$ is the dielectric susceptibility and it is related to the local electron density.

If we insert the form of the scattering potential (2.2) into Equation 2.1 using the vector identity curl curl = grad div − Δ, we obtain

$$K^2\boldsymbol{E}(\boldsymbol{r}) - \nabla \times (\nabla \times \boldsymbol{E}(\boldsymbol{r})) = -K^2\chi(\boldsymbol{r})\,\boldsymbol{E}(\boldsymbol{r})\,. \tag{2.3}$$

The electron density in the crystal is a periodic function with the translation symmetry, which allows to rewrite the dielectric susceptibility as a Fourier series

$$\chi(\boldsymbol{r}) = \sum_{\boldsymbol{g}} \chi_{\boldsymbol{g}} \mathrm{e}^{\mathrm{i}\boldsymbol{g}\cdot\boldsymbol{r}}, \tag{2.4}$$

the summation goes over all reciprocal lattice points $\boldsymbol{g}$.

The wave field $\boldsymbol{E}(\boldsymbol{r})$, propagating through the crystal, has the same translation symmetry as the crystal. Therefore, we search for the solution in the form of Bloch waves

$$\boldsymbol{E}(\boldsymbol{r}) = \sum_{\boldsymbol{g}} \boldsymbol{E}_{\boldsymbol{g}} \mathrm{e}^{\mathrm{i}\boldsymbol{k}_{\boldsymbol{g}}\cdot\boldsymbol{r}}\,, \tag{2.5}$$

where $\boldsymbol{k}_{\boldsymbol{g}} = \boldsymbol{k}_0 + \boldsymbol{g}$. The $\boldsymbol{k}_0$ is the vector from the first Brillouin zone corresponding to the non-scattered wave. With the explicit form of the electric intensity (2.5) it is possible to simplify the term $\nabla \times (\nabla \times \boldsymbol{E}(\boldsymbol{r}))$:

$$\nabla \times (\nabla \times \sum_{\boldsymbol{g}} \boldsymbol{E}_{\boldsymbol{g}} \mathrm{e}^{\mathrm{i}\boldsymbol{k}_{\boldsymbol{g}}\cdot\boldsymbol{r}}) = \nabla \times (\mathrm{i}\sum_{\boldsymbol{g}} \boldsymbol{k}_{\boldsymbol{g}} \times \boldsymbol{E}_{\boldsymbol{g}} \mathrm{e}^{\mathrm{i}\boldsymbol{k}_{\boldsymbol{g}}\cdot\boldsymbol{r}}) = -\sum_{\boldsymbol{g}} \boldsymbol{k}_{\boldsymbol{g}} \times (\boldsymbol{k}_{\boldsymbol{g}} \times \boldsymbol{E}_{\boldsymbol{g}} \mathrm{e}^{\mathrm{i}\boldsymbol{k}_{\boldsymbol{g}}\cdot\boldsymbol{r}})\,. \tag{2.6}$$

Using Fourier series for the susceptibility in Equation 2.4 and the electric intensity (2.5), the wave equation (2.3) can be rewritten as

$$\begin{aligned} K^2\sum_{\boldsymbol{g}} \boldsymbol{E}_{\boldsymbol{g}} \mathrm{e}^{\mathrm{i}\boldsymbol{k}_{\boldsymbol{g}}\cdot\boldsymbol{r}} + \sum_{\boldsymbol{g}} \boldsymbol{k}_{\boldsymbol{g}} \times (\boldsymbol{k}_{\boldsymbol{g}} \times \boldsymbol{E}_{\boldsymbol{g}} \mathrm{e}^{\mathrm{i}\boldsymbol{k}_{\boldsymbol{g}}\cdot\boldsymbol{r}}) &= -K^2\sum_{\boldsymbol{g}'} \chi_{\boldsymbol{g}'} \mathrm{e}^{\mathrm{i}\boldsymbol{g}'\cdot\boldsymbol{r}} \sum_{\boldsymbol{g}} \boldsymbol{E}_{\boldsymbol{g}} \mathrm{e}^{\mathrm{i}\boldsymbol{k}_{\boldsymbol{g}}\cdot\boldsymbol{r}} \\ &= -K^2\sum_{\boldsymbol{g}}\sum_{\boldsymbol{g}''} \chi_{\boldsymbol{g}''-\boldsymbol{g}} \boldsymbol{E}_{\boldsymbol{g}} \mathrm{e}^{\mathrm{i}\boldsymbol{k}_{\boldsymbol{g}''}\cdot\boldsymbol{r}}\,. \end{aligned} \tag{2.7}$$

This leads to the homogeneous system of equations for unknown $\boldsymbol{E}_{\boldsymbol{g}}$ corresponding to all possible $\boldsymbol{g}$-vectors of the reciprocal lattice:

$$K^2\boldsymbol{E}_{\boldsymbol{g}} + \boldsymbol{k}_{\boldsymbol{g}} \times (\boldsymbol{k}_{\boldsymbol{g}} \times \boldsymbol{E}_{\boldsymbol{g}}) = -K^2\sum_{\boldsymbol{g}''} \chi_{\boldsymbol{g}''-\boldsymbol{g}} \boldsymbol{E}_{\boldsymbol{g}}\,. \tag{2.8}$$

We restrict ourselves to the case of the coplanar geometry which means that scattering process takes place only in the *diffraction* plane that is perpendicular to the surface of the crystal. In case of S-polarization geometry, the electric

intensity vector is parallel to the surface and perpendicular to the diffraction plane. There, it stays perpendicular to the wavevector and the double vector product $\boldsymbol{k_g} \times (\boldsymbol{k_g} \times \boldsymbol{E_g})$ can be simplified to $-k_{\boldsymbol{g}}^2 \boldsymbol{E_g}$. Generally, this simplification is not possible for the P-polarization geometry, in which the electric intensity vector is within the diffraction plane and the electric wave does not have to be strictly transverse. It is beyond this brief introduction how the double vector product is treated in P-polarization case, and it is derived in [91]. There is also shown that the exact formulas for S-polarization are sufficiently approximative also for the P-polarization case, if incidence and exit angles of the primary and the diffracted beams are much larger than the critical angle (*conventional diffraction*). The polarization factor C is introduced into the formulas in a way that the susceptibility $\chi_{\boldsymbol{g}}$ is substituted by $\chi_{\boldsymbol{g}} C$. Here, $C = 1$ for S-polarization and $C = |\cos(2\theta)|$ in P-polarization case. The scattering angle 2θ is the angle between wave vectors $\boldsymbol{k_0}$ and $\boldsymbol{k_g}$.

Usually we measure the diffracted signal in the vicinity of the certain Bragg position corresponding to the reciprocal lattice point $\boldsymbol{h}$. Therefore, only diffracted waves $\boldsymbol{E_h}$ and transmitted wave $\boldsymbol{E_0}$ are present in the crystal. Considering only these two non-zero terms in Equation 2.8, we obtain a system of two equations

$$\left(k_{\boldsymbol{0}}^2 - K^2(1+\chi_{\boldsymbol{0}})\right) E_{\boldsymbol{0}} = K^2 \chi_{-\boldsymbol{h}} C E_{\boldsymbol{h}} \,, \tag{2.9}$$

$$\left(k_{\boldsymbol{h}}^2 - K^2(1+\chi_{\boldsymbol{0}})\right) E_{\boldsymbol{h}} = K^2 \chi_{\boldsymbol{h}} C E_{\boldsymbol{0}} \,. \tag{2.10}$$

We define the length of the wave vector in material $k \equiv nK$ using the refractive index $n = \sqrt{1+\chi_{\boldsymbol{0}}}$.

The demand of the non-trivial solution of a homogeneous system is the zero determinant. This leads to the condition for the wave vectors $\boldsymbol{k_0}$ and $\boldsymbol{k_h} = \boldsymbol{k_0} + \boldsymbol{h}$, which is called dispersion equation:

$$(k_{\boldsymbol{0}}^2 - k^2)(k_{\boldsymbol{h}}^2 - k^2) = K^4 \chi_{-\boldsymbol{h}} \chi_{\boldsymbol{h}} C^2 \,. \tag{2.11}$$

The all waves are refracted or reflected at the interfaces, where the susceptibility changes. The in-plane component of the wave vectors stays constant in any depth of the sample. This is another condition for ($\boldsymbol{k_0}$)-vectors, which together with Equation 2.11 fully determines the permitted wave vectors. A geometrical interpretation is depicted in Figure 2.1. We search for the intersections of the sample surface normal and the dispersion surface, these points are origins of the vectors $\boldsymbol{k_0}$ and $\boldsymbol{k_h}$ pointing to the points $\mathbf{0}$ and $\mathbf{H}$, respectively.

Let us introduce a coordinate system defined in Figure 2.1. The wave vectors are

$$\boldsymbol{k_0} = (K \sin\theta_{\mathrm{B}} - q_1 \,,\, K \cos\theta_{\mathrm{B}} - q_2) \,, \tag{2.12}$$

$$\boldsymbol{k_h} = (-K \sin\theta_{\mathrm{B}} - q_1 \,,\, K \cos\theta_{\mathrm{B}} - q_2) \,, \tag{2.13}$$

where q_1 and q_2 are unknown coordinates of the origins of the wave vectors. They lie on the sample surface normal, which is described by the equation

$$q_2 = -q_1 \tan\phi + p \,. \tag{2.14}$$

The asymmetry parameter ϕ is the angle between the sample surface normal and the diffraction vector $\boldsymbol{h}$. It is defined as a positive number if the incidence

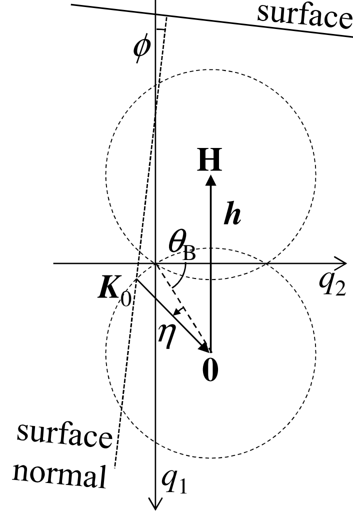

Figure 2.1: Coordinate system q_1q_2 in reciprocal space. The direction of the vacuum wave vector $\boldsymbol{K}_0$ is a known input parameter, the length of the vector is K. The deviation angle η from the Bragg position is negative for the situation in this picture. The asymmetry ϕ is a tilt of the sample-surface normal with respect to the axis q_1, i.e., coordinate system q_1q_2 is rotated for value relatively to the coordinate system of the sample having z-axis perpendicular to the surface.

angle of the primary beam is smaller than the exit angle of the diffracted beam. The asymmetry parameter is negative for the opposite case. The parameter p is connected with the known wave vector of the primary beam $\boldsymbol{K}_0$, whose origin is located at the sample surface normal, as well, and it ends in the **0**-point.

We define η as the angular deviation of the primary beam wave vector from the kinematic diffraction position. The vector $\boldsymbol{K}_0$ and coordinates of the **0**-point can be easily written in q_1q_2-coordinates:

$$\mathbf{0} = [K\sin(\theta_B)\,,\ K\cos(\theta_B)]\,, \tag{2.15}$$

$$\boldsymbol{K}_0 = (K\sin(\theta_B+\eta)\,,\ K\cos(\theta_B+\eta))\,. \tag{2.16}$$

If we combine the coordinates of the $\boldsymbol{K}_0$-vector origin $(\mathbf{0}-\boldsymbol{K}_0)$ with the surface normal equation (Equation 2.14). The parameter p can be expressed as

$$p = \frac{2K}{\cos\phi}\sin\frac{\eta}{2}\sin\left(\theta_B-\phi+\frac{\eta}{2}\right)\,. \tag{2.17}$$

The dispersion equation Equation 2.11 in new coordinates

$$K^2\chi_{-\boldsymbol{h}}\chi_{\boldsymbol{h}}C^2 = \left(q_1^2+q_2^2-2Kq_2\cos\theta_B-\chi_{\mathbf{0}}K^2\right)^2 - 4q_1^2K^2\sin^2\theta_B \tag{2.18}$$

can be rewritten as the quartic equation for the variable q_1 in the form

$$q_1^4A_1^2+q_1^3 2A_1A_2+q_1^2(2A_1A_3+A_2^2-A_4^2)+q_1 2A_2A_3 = K^2\chi_{-\boldsymbol{h}}\chi_{\boldsymbol{h}}C^2-A_3^2\,, \tag{2.19}$$

where parameters A_j are

$$A_1 = \frac{1}{\cos^2\phi}\,, \tag{2.20}$$

$$A_2 = -2p\tan\phi + 2K\cos\theta_{\mathrm{B}}\tan\phi\,, \tag{2.21}$$

$$A_3 = p^2 - 2Kp\cos\theta_{\mathrm{B}} - \chi_{\mathbf{0}}K^2 \tag{2.22}$$

$$A_4 = 2K\sin\theta_{\mathrm{B}}\,. \tag{2.23}$$

The quartic equation can be easily solved, for instance, by the non-iterative Ferrari method (e.g., described in Reference 93). The solution give us four possible couples of $\boldsymbol{k}_{\mathbf{0}j}$ and $\boldsymbol{k}_{\boldsymbol{h}j}$ vectors. That means eight allowed plane waves propagating through the crystal. The amplitudes $E_{\mathbf{0}j}$ and $E_{\boldsymbol{h}j}$ are bound together by Equation 2.9, from which we compute ratios $c_j = \frac{E_{\boldsymbol{h}j}}{E_{\mathbf{0}j}}$.

We focus on a conventional diffraction case, where the incidence and the exit angles are much larger than the critical angle, and therefore, the asymmetry parameter is rather small. In such a case, only two non-scattered and two diffracted waves are strong [91]. It is sufficient to take into account only four waves defined by two pairs of the wave-vectors $\boldsymbol{k}_{\mathbf{0}}$ and $\boldsymbol{k}_{\boldsymbol{h}}$. Those are just such $\boldsymbol{k}$-vectors that their origin is located near the origin of the coordinate system q_1q_2.

The wave field in two beam approximation propagating through the crystal taking into account only four possible strong waves is

$$\boldsymbol{E}(\boldsymbol{r}) = \sum_{j=1}^{2} \boldsymbol{E}_{\mathbf{0}j}\mathrm{e}^{\mathrm{i}\boldsymbol{k}_{\mathbf{0}j}\cdot\boldsymbol{r}} + \sum_{j=1}^{2} \boldsymbol{E}_{\boldsymbol{h}j}\mathrm{e}^{\mathrm{i}\boldsymbol{k}_{\boldsymbol{h}j}\cdot\boldsymbol{r}}\,, \tag{2.24}$$

which is sufficiently approximative also for P-polarization case.

2.2 Boundary conditions

An investigated sample is not an infinite medium, moreover, we assume that the sample consists of some homogeneous layers separated by flat interfaces parallel to the surface. The surface is, in fact, an interface between the top layer and the air surrounding the sample. The electromagnetic wave field in such a homogeneous medium is described in the previous section. The ratio of amplitudes of the non-scattered and the diffracted waves can be calculated in every layer. The amplitudes in neighbouring layers are connected via boundary conditions following from the Maxwell equations. And thus, the lateral components of electric and magnetic intensities are continuous within the interface.

Since the electric intensity for the S-polarization case is directly parallel to the surface, it is parallel to any interface from the definition. Using $\boldsymbol{H} = \sqrt{\epsilon_0/\mu_0}/K(\boldsymbol{k}\times\boldsymbol{E})$, we can express the lateral component of the vector $\boldsymbol{H}$ as $H_{\parallel} = \sqrt{\epsilon_0/\mu_0}k_z/KE$. From the continuity of the lateral components of electromagnetic intensities, it follows the condition for the amplitudes of the waves present at the interface between medium A and B

$$\sum_j E_j^{\mathrm{A}}\mathrm{e}^{\mathrm{i}\boldsymbol{k}_j^{\mathrm{A}}\cdot\boldsymbol{r}} = \sum_j E_j^{\mathrm{B}}\mathrm{e}^{\mathrm{i}\boldsymbol{k}_j^{\mathrm{B}}\cdot\boldsymbol{r}} \tag{2.25}$$

$$\sum_j k_{zj}^{\mathrm{A}}E_j^{\mathrm{A}}\mathrm{e}^{\mathrm{i}\boldsymbol{k}_j^{\mathrm{A}}\cdot\boldsymbol{r}} = \sum_j k_{zj}^{\mathrm{B}}E_j^{\mathrm{B}}\mathrm{e}^{\mathrm{i}\boldsymbol{k}_j^{\mathrm{B}}\cdot\boldsymbol{r}}\,, \tag{2.26}$$

while $\boldsymbol{r}$ is within the interface. These conditions can be also used for P-polarization case (see Figure 2.2), where just the vector $\boldsymbol{H} = \boldsymbol{H}_{\parallel}$ is parallel to the interface. It can be expressed as $H_{\parallel} = \sqrt{\epsilon_0/\mu_0}/KE$. Together with the lateral component $E_{\parallel} = k_z/KE$ it leads to the same equations (2.25 and 2.26).

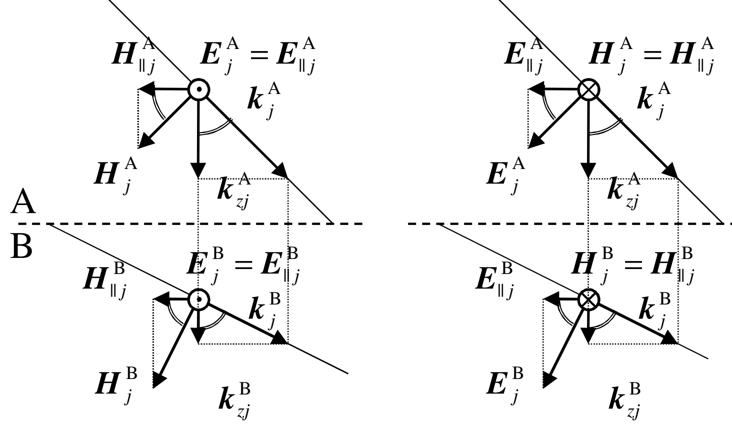

Figure 2.2: The Lateral components of the electromagnetic intensities for the S-polarization (left) and the P-polarization case (right) are relevant for the boundary conditions at the interface between material A and B. Lateral component of the wave vector is continuous at the interface, as well.

The amplitudes $E_j^{\mathrm{A,B}}$ are spatially constant within the interface. The lateral component of the wave vectors of non-scattered waves differs from that of diffracted ones. Therefore, there are just two different oscillatory terms in those sums. It allows us to reformulate conditions by separating prefactors of both oscillatory terms in Equation 2.25 and Equation 2.26:

$$\sum_j E^{\mathrm{A}}_{\mathbf{0}j} = \sum_j E^{\mathrm{B}}_{\mathbf{0}j} \qquad \sum_j c^{\mathrm{A}}_j E^{\mathrm{A}}_{\mathbf{0}j} = \sum_j c^{\mathrm{B}}_j E^{\mathrm{B}}_{\mathbf{0}j} \tag{2.27}$$

$$\sum_j k^{\mathrm{A}}_{\mathbf{0}jz} E^{\mathrm{A}}_{\mathbf{0}j} = \sum_j k^{\mathrm{B}}_{\mathbf{0}jz} E^{\mathrm{B}}_{\mathbf{0}j} \qquad \sum_j k^{\mathrm{A}}_{\boldsymbol{h}jz} c^{\mathrm{A}}_j E^{\mathrm{A}}_{\mathbf{0}j} = \sum_j k^{\mathrm{B}}_{\boldsymbol{h}jz} c^{\mathrm{B}}_j E^{\mathrm{B}}_{\mathbf{0}j}. \tag{2.28}$$

In case of the conventional diffraction, we can expect a very similar z-component of wave vectors $\boldsymbol{k}_{\mathbf{0}1}$ and $\boldsymbol{k}_{\mathbf{0}2}$ (consequently also $\boldsymbol{k}_{\boldsymbol{h}1}$ and $\boldsymbol{k}_{\boldsymbol{h}2}$). The difference is so small that Equation 2.28 is approximatively identical with Equation 2.27. Recalling the form of the wave field for the conventional diffraction and the two beam approximation in Equation 2.24), we can write

$$E^{\mathrm{A}}_{\mathbf{0}1} + E^{\mathrm{A}}_{\mathbf{0}2} = E^{\mathrm{B}}_{\mathbf{0}1} + E^{\mathrm{B}}_{\mathbf{0}2} \tag{2.29}$$

$$c^{\mathrm{A}}_1 E^{\mathrm{A}}_{\mathbf{0}1} + c^{\mathrm{A}}_2 E^{\mathrm{A}}_{\mathbf{0}2} = c^{\mathrm{B}}_1 E^{\mathrm{B}}_{\mathbf{0}1} + c^{\mathrm{B}}_2 E^{\mathrm{B}}_{\mathbf{0}2}. \tag{2.30}$$

2.3 Simulated diffraction on layered sample

Let us describe a sample under investigation as a system of N layers numbered from the bottom layer (1st) to the top layer (Nth) as it is depicted in Figure 2.3. There is a semi-infinite substrate (labeled as the 0th layer) below the most bottom

layer. The kth layer is characterised by the reciprocal lattice vector $\boldsymbol{h}^k$, the thickness of the layer T^k, and the susceptibility of a material, where only Fourier coefficients $\chi^k_{\mathbf{0}}$, $\chi^k_{\boldsymbol{h}}$, $\chi^k_{-\boldsymbol{h}}$ are relevant for the further computations. The wave vectors $\boldsymbol{k}^k_{\boldsymbol{g}j}$ of four waves ($\boldsymbol{g} = \mathbf{0}, \boldsymbol{h}$ and $j = 1, 2$) can be calculated separately for each kth layer by solving Equation 2.19.The amplitude ratios

$$c^k_j = \frac{E^k_{\boldsymbol{h}j}}{E^k_{\mathbf{0}j}} = \frac{k^2_0/K^2 - 1 - \chi_{\mathbf{0}}}{\chi_{-\boldsymbol{h}} C} \tag{2.31}$$

can be obtained from Equation 2.9.

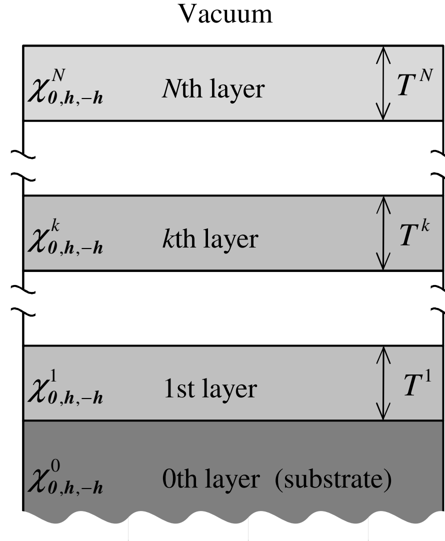

Figure 2.3: The sample is considered to be a stack of N homogeneous layers on semi-infinite substrate. Each layer in the stack is defined by its thickness and Fourier coefficients of dielectric susceptibility.

Let us define wave amplitudes $E^k_{\boldsymbol{g}j}$ just below the top boundary interface of the kth layer. Therefore, amplitudes at the bottom of this layer are $E^k_{\boldsymbol{g}j} \mathrm{e}^{\mathrm{i}k^k_{\boldsymbol{g}jz}(-T^k)}$. The absorption of the electromagnetic radiation is included via the imaginary part of the vertical component $k^k_{\boldsymbol{g}jz}$. This imaginary part is negative for the waves going from the surface towards to the substrate and it is positive for the waves going in the opposite direction. The amplitudes in the kth layer can be expressed by the amplitudes in the lower layer $(k-1)$ using Equation 2.29 and Equation 2.30:

$$E^k_{\mathbf{0}1} = \mathrm{e}^{\mathrm{i}k^k_{\mathbf{0}1z}} \frac{(c^{k-1}_1 - c^k_2)E^{k-1}_{\mathbf{0}1} + (c^{k-1}_2 - c^k_2)E^{k-1}_{\mathbf{0}2}}{c^k_1 - c^k_2} \tag{2.32}$$

$$E^k_{\mathbf{0}2} = \mathrm{e}^{\mathrm{i}k^k_{\mathbf{0}2z}} \frac{(-c^{k-1}_1 + c^k_1)E^{k-1}_{\mathbf{0}1} + (-c^{k-1}_2 + c^k_1)E^{k-1}_{\mathbf{0}2}}{c^k_1 - c^k_2}. \tag{2.33}$$

There are only two waves in the substrate, the transmitted wave going deeper to the substrate and the corresponding diffracted wave. Let us label such waves by index $j = 1$. The amplitude $E^0_{\mathbf{0}1}$ is only one unknown variable in the substrate because diffracted wave amplitude is $c^0_1 E^0_{\mathbf{0}1}$. All other amplitudes are zero as those

waves are not present in the substrate. For the numerical evaluation, the unknown amplitude $E^0_{\mathbf{01}}$ can be set to any arbitrary value that, in fact, acts as a scaling factor. From the 'known' amplitudes in the 0th layer, we can iteratively calculate the amplitudes in all layers up to the last Nth layer. After the application of the boundary conditions in Equation 2.29 and in Equation 2.30 to the surface interface, we obtain the amplitudes of the incident wave (E_i) and the diffracted wave (E_f) above the sample:

$$E_i = E^N_{\mathbf{01}} + E^N_{\mathbf{02}}\,, \qquad E_f = c^N_1 E^N_{\mathbf{01}} + c^N_2 E^N_{\mathbf{02}}. \tag{2.34}$$

Usually, we measure a total energy flux of an electromagnetic field in the direction of the diffracted beam. It is being normalized to the total energy flux of a radiation hitting the sample. Therefore, we calculate the total energy fluxes ratio of the diffracted and the incident beam through the irradiated sample area:

$$R = \left|\frac{E_\mathrm{f}^2 \sin\alpha_\mathrm{f}}{E_\mathrm{i}^2 \sin\alpha_\mathrm{i}}\right|. \tag{2.35}$$

The calculated dependence of the diffractivity R on the disorientation from the Bragg position is called simulated diffraction curve.

Finally, the polarization of the incident beam has to be taken into account. The measured diffractivity is averaged over both polarizations

$$R = \frac{R_S + R_P}{2}, \tag{2.36}$$

where the R_S and R_P are the diffractivies calculated for S and P polarizations, respectively. This is valid for not polarized radiation that is produced by laboratory x-ray tubes. Usually, there are some optic elements in the incident and the diffracted path of the beam, and they change the ratio of polarization components in the radiation. For instance, the incident beam can diffract four times on perfect crystals in Bartels monochromator [92], which is often used for High-Resolution experiments. In that case the polarization factor $\cos 2\theta_\mathrm{B,mono}$ for the monochromator crystal has to be included. Then, the calculated diffractivity is

$$R = \frac{R_S + R_P \cos^4 2\theta_\mathrm{B,mono}}{1 + \cos^4 2\theta_\mathrm{B,mono}}\,. \tag{2.37}$$

Summary

We followed the basics of the Dynamical theory of diffraction as it is introduced in Reference 91, and we rephrased the formulas to final form that gives, to our feeling, comprehending and clear prescription for the simulation of the diffraction experiment. Now, we can calculate the diffraction curve for the case of several layers on semi-infinite substrate.

Here, there is no definite presumption on a structural model. We just assume the stack of crystalline layers with similar structure. The structural model is introduced in chapter 3. The simulation has to be scaled to be comparable with the experimental data. It can be scaled to correspond the known primary beam intensity, or it can be scaled by the arbitrary value to fit the experimental data (see

chapter 5). Next step is to find somehow the parameters of proposed structural model to make the simulated curve matching the experimental curve (chapter 5). In chapter 3, there will be discussed the sensitivity and the ambiguity of such found parameters.

Chapter 3

Influence of defect density on diffracted intensity

It was shown in chapter 1 that not only the amount of Mn ions incorporated in GaAs lattice determinates the magnetic and electric properties of the (Ga,Mn)As material, but a donor/acceptor role of the Mn ions is crucial. We present the x-ray method for the determination of the Mn content in particular lattice sites in the crystal.

The intensity of the diffracted beam is given by the scattering power of the elements, from which the material is composed, and it is also given by the location of the atoms in the lattice. The detection of Mn ions and other point defects is complicated by the fact, that the presence of a relatively small amount of Mn ions in the lattice affects the scattering rather weakly. It is very advantageous to measure those diffraction maxima, which are weak for GaAs. Then, the presence of other ions or defects is more pronounced in the measured intensity [70, 71]. We showed in [94] that it is possible to determine the occupancy of donor Mn ions in two non-equivalent positions from the measurement of the optimal set of diffraction maxima. The method is explained and discussed in this chapter.

Initially, we introduce a structural model for (Ga,Mn)As and GaAs material. As a basic structural characteristic, we mention the prediction on the average lattice parameter of (Ga,Mn)As. We derive the structure factor for (Ga,Mn)As and we discuss how it is affected by the particular defect densities. Showing the influence of the structural local distortion due to the impurity presence, we correct the structure factor for this effect. Finally, we see which diffraction maxima has to be measured for the reliable determination of the defect densities.

3.1 Structural model of (Ga,Mn)As

The (Ga,Mn)As forms a zinc-blend structure, and it can be described as a GaAs lattice, where some of Ga atoms are substituted by Mn atom (see Figure 3.1). Let us the symbol c_{sub} denote the probability of finding a Mn atom in a randomly chosen Ga lattice position. We call those atoms in substitutional positions as the substitutional Mn atoms (or ions). In fact, that probability is just the occupancy of Mn atoms in the substitutional position. These Mn atoms act as acceptors in the GaAs material [30, 57].

The solubility of the Mn in GaAs lattice is very low, it is necessary to grow the

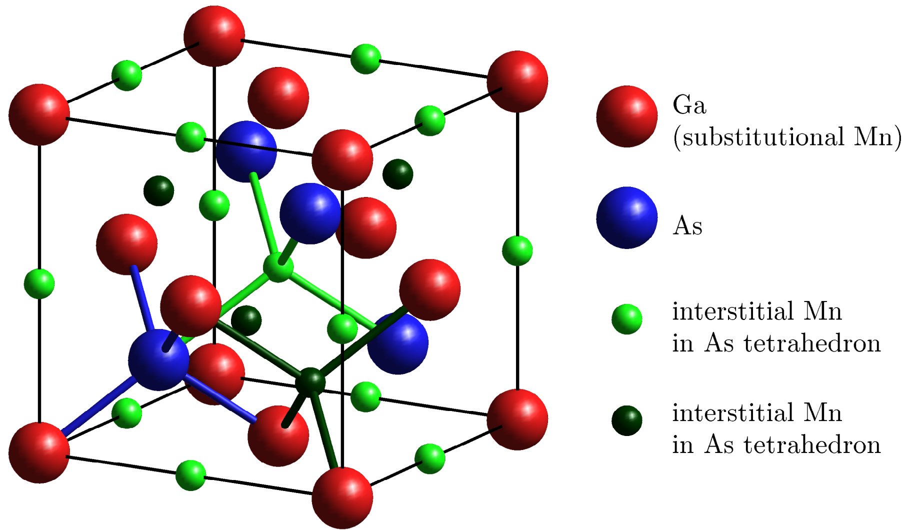

Figure 3.1: (Ga,Mn)As face-centred unit cell. The fractional coordinates of four lattice points in the unit cell are $(0,0,0)$, $(0,0,\frac{1}{2})$, $(\frac{1}{2},0,0)$ and $(0,\frac{1}{2},0)$. The basis is formed by Ga atom (or substitutive Mn, As) and As atom relatively shifted by $(\frac{1}{4},\frac{1}{4},\frac{1}{4})$. Each Ga atom (red) is surrounded by four neighbouring As atoms (blue) and vice versa. Smaller spheres in the picture indicate the interstitial positions where the Mn atoms can occur. The site in the centre of the As tetrahedron (light green) is shifted by $(\frac{1}{2},\frac{1}{2},\frac{1}{2})$ from the Ga lattice site, whereas the shift of interstitial position inside the Ga tetrahedron (dark green) is $(-\frac{1}{4},-\frac{1}{4},-\frac{1}{4})$.

material at low temperatures in order to incorporate more Mn atoms in substitutional positions. There are a lot of defects in the material as a consequence of the non-equilibrium growing conditions,LT-MBE [95]. The major defect known in LT-GaAs is so called anti-site defect [96, 97]. It is a situation when the Ga sites are occupied by As atoms, it is also present in (Ga,Mn)As [81], and we denote this occupancy by c_{anti}.

Besides the substitutional positions, the Mn atoms can be located also in interstitial positions of the GaAs lattice. There, they have the role of double donors [34]. The creation of these interstitial double-donor defects is probably due to the auto-compensation process during the growth [34]. In contrast to substitutional Mn, which is relatively stable, the amount of the metastable interstitial Mn atoms (interstitials) can be decreased by means of a post-growth annealing [38]. There are two non-equivalent interstitial positions in the GaAs lattice [35, 72]. They are located in the centre of hypothetical tetrahedrons formed by the Ga or the As atoms as it is depicted in Figure 3.1. The symbols for occupancies at those positions are $c_{\mathrm{int,Ga}}$ and $c_{\mathrm{int,As}}$, respectively. From the theoretical predictions, it follows that the positions inside the As tetrahedra is energetically little bit more preferable [72] (few meV).

The occupancy is usually called (*atomic*) *concentration* in the literature. Sometimes, the term ‘concentration’ can be misleading as it can evoke the ratio between the number of all Mn atoms and the number of the Ga lattice positions. But, this quantity we strictly call ‘total concentration’ denoted by c_{total}. The

multiplicity of the Ga lattice site and both interstitial sites in the unit cell is the same (four), therefore we can write

$$c_{\text{total}} = c_{\text{sub}} + c_{\text{int,As}} + c_{\text{int,Ga}} \,. \tag{3.1}$$

3.1.1 Assumption on lattice parameter

The next difference between latices of the GaAs and the (Ga,Mn)As is in the their relaxed lattice parameters. For a cubic material the only one lattice parameter is relevant. It is $a_{\text{GaAs}} = 5.65325$ Å for the GaAs [98]. Firstly, the lattice parameter changes due to the presence of low-temperature defects. Secondly, the lattice parameter value rises with the amount of the incorporated Mn into the lattice [24]. The approximative formula for the dependence of the (Ga,Mn)As lattice parameter a_{GaMnAs} on a composition follows from the theoretical calculations in Reference 99:

$$a_{\text{GaMnAs}} = a_{\text{GaAs}} + 0.02c_{\text{sub}} + 0.69c_{\text{anti}} + 1.05(c_{\text{int,As}} + c_{\text{int,Ga}}) \text{ (Å)} \,. \tag{3.2}$$

We should keep in mind that there is no free standing crystal of (Ga,Mn)As. In practice, the (Ga,Mn)As material is in the form of epitaxial layers fully strained on substrates or other strained layers. The cubic lattice is then elastically deformed and its symmetry is lower. The calculated a_{GaMnAs} is the lattice parameter of a relaxed (non-deformed) lattice. Usually, (Ga,Mn)As is grown on the top of the cubic GaAs(001), i.e., the lattice plane (001) of the GaAs is parallel to the surface [100]. For the whole work, we focus just to this case.

Then, the (Ga,Mn)As lattice is tetragonally distorted, and lattice parameters in the basal plane (001) are the same as in the substrate ($a = a_{\text{GaAs}}$). The second tetragonal lattice parameter (c) can be calculated using the theory of elasticity

$$c = \frac{-2C_{12}}{C_{11}}(a - a_{\text{GaMnAs}}) + a_{\text{GaMnAs}} \,. \tag{3.3}$$

We assume that the elastic constants of (Ga,Mn)As C_{jk} do not significantly differ from those of the GaAs: $C_{11} = 11.90 \cdot 10^{11}$ dyn/cm^2 and $C_{12} = 5.34 \cdot 10^{11}$ dyn/cm^2 [98].

3.2 Structure factor

The intensity of the x-ray diffraction maximum with Miller indices (hkl) is proportional to the absolute value of the square of the structure factor F_{hkl} defined as

$$F_{hkl} = \sum_j f_j(Q)\, \mathrm{e}^{-2\pi \mathrm{i}(x_j h + y_j k + z_j l)} \,, \tag{3.4}$$

where the summation goes over all atoms in the unit cell. Each atom at a position with fractional coordinates (x_j, y_j, z_j) is represented by the atomic scattering factor f_j, which depends on the length of the scattering vector Q [92]. The scattering vector is defined as a difference of the wave vectors of the incident ($\boldsymbol{K}_\text{i}$) and the diffracted ($\boldsymbol{K}_\text{f}$) radiation: $\boldsymbol{Q} = \boldsymbol{K}_\text{f} - \boldsymbol{K}_\text{i}$. [92].

From the Laue condition, it follows that the scattering vector coincidences with a reciprocal lattice vector in the diffraction maximum hkl [92]. This allows to express the length of the scattering vector by Miller indices and the lattice parameters. We assume that (Ga,Mn)As structure is tetragonally distorted, therefore we can explicitly write

$$Q = |\boldsymbol{h}| = 2\pi\sqrt{\frac{h^2+k^2}{a^2}+\frac{l^2}{c^2}}\,. \tag{3.5}$$

The structure factor for a pure and perfect GaAs can expressed using fractional coordinates introduced in Figure 3.1 as

$$F_{hkl}^{\mathrm{GaAS}} = 4(f_{\mathrm{Ga}} + f_{\mathrm{As}}\mathrm{e}^{-\mathrm{i}\pi/2(h+k+l)})\,. \tag{3.6}$$

The subscripts within the atomic scattering factors denote the corresponding elements. This expression for the structure factor is valid only when indices h, k and l are all odd or all even. Only such a diffraction maxima are allowed as a consequence of the cubic face-centring. Any other diffraction maxima are forbidden having the zero structure factor. Later, we compare the GaAs structure factor with that one modified by the presence of Mn in various positions.

The phase factor of As atoms in Equation 3.6 can have four possible values according to their hkl indices. We recognize three groups of the diffraction maxima. If the sum of hkl indices is divisible by 4, the phase factor is $+1$ and the Ga and As atomic factors are summed. In other words, there is a constructive interference of the waves scattered by Ga and As atoms and the diffraction maxima is called *strong*. If $h+k+l \equiv 2 \pmod 4$, then the phase factor is -1 and the scattering power is proportional to the difference of the atomic factors, but their values are very similar. In such a case, we talk about the *weak diffraction* maxima. Let us call the *intermediate* diffraction maxima those with odd Miller indices. Here. the phase factor is $\pm\mathrm{i}$, and for those, the scattering power is higher than for the weak and lower than for the strong diffractions.

3.2.1 Averaged structure factor

Individual cells in the (Ga,Mn)As crystal are not all the same. Since, we are not able to write simply the structure factor $F_{hkl}^{\mathrm{GaMnAs}}$ as it should be different for every cell. We work with a concept of randomly occupied sites by point defects or randomly substituted Ga atoms with the given probability (occupancy). It can be assumed that the diffracting volume is large enough to contain all possible configurations of such unit cells. Therefore, we measure the diffracted signal that is averaged for a statistical ensemble of all possible configurations. The measured intensity,

$$I \propto \langle|F_{hkl}^{\mathrm{GaMnAs}}|^2\rangle = |\langle F_{hkl}^{\mathrm{GaMnAs}}\rangle|^2 + \mathrm{Cov}(F_{hkl}^{\mathrm{GaMnAs}}, F_{hkl}^{\mathrm{GaMnAs}})\,, \tag{3.7}$$

can be expressed as a sum of two separated terms. First one, coherent, is given by the averaged structure factor, which can be computed from the occupancies. The second covariance term corresponds to a diffuse scattering that produces an intensity distributed between Bragg peaks. The diffusely scattered intensity changes very slowly in the scanned area in a reciprocal space in the vicinity of

the reciprocal lattice points. Therefore, the diffuse scattering intensity can be included in a constant background. This allows us to consider the measured intensity to be diffracted by averaged (Ga,Mn)As crystal.

In the first approximation, the fractional coordinates of the sites stay the same because there is assumed no local distortion of the unit cells. The atomic scattering factors are replaced by the averaged ones, i.e., by the sum of atomic factors for different elements weighted by their corresponding occupancies. In contrast to the GaAs, here we have partially occupied also interstitial positions. Therefore, two additional terms are included in the structure factor formula.

The averaged structure factor for (Ga,Mn)As can be written as a correction to the GaAs one:

$$\langle F_{hkl}^{\mathrm{GaMnAs}} \rangle = F_{hkl}^{\mathrm{GaAs}} + 4\big[c_{\mathrm{anti}}(f_{\mathrm{As}} - f_{\mathrm{Ga}}) + c_{\mathrm{sub}}(f_{\mathrm{Mn}} - f_{\mathrm{Ga}}) + \\ + c_{\mathrm{int,As}} f_{\mathrm{Mn}} \mathrm{e}^{-\mathrm{i}\pi(h+k+l)} + c_{\mathrm{int,Ga}} f_{\mathrm{Ga}} \mathrm{e}^{\mathrm{i}\pi/2(h+k+l)}\big] \,. \tag{3.8}$$

The first two correction terms express the presence of the anti-site defects and the substitutional Mn, respectively. The last two terms add the scattering contribution of the Mn interstitial atoms inside the As and the Ga tetrahedra, respectively. The measured intensity is apparently affected by the presence of the defects, and thus, their occupancies can be determined from the measurement of several diffraction maxima. The appropriate *hkl* indices have to be chosen for the measurement, for which the influence of the defects to the intensity is emphasized.

Considering temperature vibrations of atoms, B is an exponential prefactor equivalent to the $\frac{8\pi^2}{3} \times$ *mean squared displacement*. It defines the isotropic Debye-Waller (D-W) (in accordance with Reference 92) factor

$$DWF = \mathrm{e}^{-B\left(\frac{\sin\theta}{\lambda}\right)^2} \,, \tag{3.9}$$

which multiplies the calculated structure factor. The temperature vibrations cause the random shifts of atoms from their averaged positions, i.e., from the ideal-lattice positions. On the other hand, atoms are displaced also statically due to the non-uniformity of individual unit cells. For instance, the presence of Mn atoms changes the lattice parameter of averaged crystal lattice. However, the variation of individual unit-cells volume is pronounced in the whole crystal. Formally, the averaging in order to express the coherently scattered intensity is equivalent to that of D-W [101]. Therefore, the determined prefactor B from the experiment can be overestimated as it is affected by the static disorder, as well.

3.2.2 Diffraction maxima types

The phase terms in Equation 3.6 and Equation 3.8 can have only four possible values ($\pm 1, \pm \mathrm{i}$) for any allowed combination of *hkl* indices. The distinction of three diffraction maxima types (*strong, intermediate* and *weak*), introduced for the GaAs, stays also for the (Ga,Mn)As. The intensity of *hkl* maxima of one diffraction type decreases with the longer scattering vector in the same way as the atomic scattering factors. Let us discuss how the anti-site defects and Mn ions located in the lattice affect the structure factor. And consequently, how they affect the diffracted intensity with respect to the diffraction maxima type.

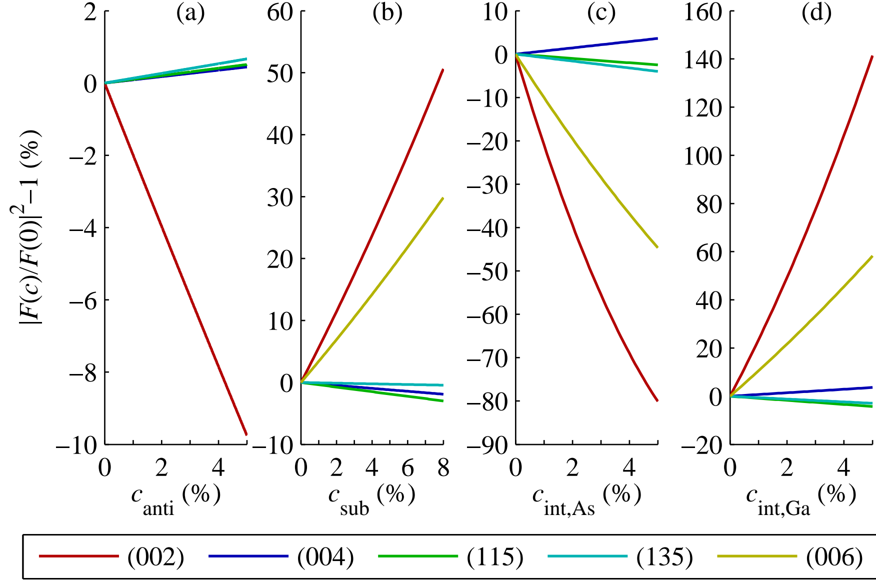

Figure 3.2: Dependence of the diffracted intensity on defect concentration c_{anti} (a), c_{sub} (b), $c_{\mathrm{int,As}}$ (c) and $c_{\mathrm{int,Ga}}$ (d). The diffracted intensity of (Ga,Mn)As is normalized to the intensity of non-defected GaAs crystal. It is assumed that there is only one type of defects for each plot (a)–(d). The concentration of the rest defects is zero. The different maxima types are represented by (002) and (006) for the *weak*, (004) the *strong*, (115) and (135) for the *intermediate* diffraction type. The curves for the maxima (002) and (006) coincide in the plot (a) as it follows from Equation 3.10.

The scattering factor of As atoms is approximately for 10–20 % larger than that of Ga atoms (see Figure 3.3). The presence of the As anti-site atoms increases the average scattering power located at Ga lattice points. Therefore, the intensity of the *strong* and the *intermediate* diffraction maxima increases. Nevertheless, if we take into account that only few percent (less than 5 %) of the Ga sites are occupied by the As atoms, the change of just such intensity is below one percent, and it is hardly measurable (see Figure 3.2).

On the other hand, the intensity of the *weak* diffraction maxima decreases due to the destructive interference. If we express the relative contribution due to the presence of anti-site defects to the structure factor, it can be simplified in case of *weak* diffraction to

$$\frac{4c_{\mathrm{anti}}(f_{\mathrm{As}} - f_{\mathrm{Ga}})}{F^{\mathrm{GaAs}}_{hkl}} = -c_{\mathrm{anti}}\,. \tag{3.10}$$

It depends only on the concentration of the anti-site defects and values of the atomic factors do not play any role. The relative decrease of the diffracted intensity will be for the small concentrations approximately $2c_{\mathrm{anti}}$, which practically means below 10 %.

The Mn atoms in substitutional positions affect the intensity similarly, but in opposite way because the Mn atomic factor is smaller than that of Ga atoms (for about 20–25 %). The intensities of the strong and the intermediate diffraction maxima are only slightly decreased whereas the weak diffraction intensity increases approximately for 10–30 % for the Mn atoms at 3–5 % of the Ga lattice

sites. This effect is stronger than for the As anti-sites because the atomic factor of the Mn substantially differs from that of the Ga. On the other hand, those of the Ga and the As are similar. The contribution of the Mn substitutional atoms to the structure factor is

$$\frac{4c_{\text{sub}}(f_{\text{Mn}} - f_{\text{Ga}})}{F_{hkl}^{\text{GaAs}}} = c_{\text{sub}} \frac{f_{\text{Mn}} - f_{\text{Ga}}}{f_{\text{Ga}} - f_{\text{As}}}, \tag{3.11}$$

where the nominator and the denominator are negative numbers. Since, the structure factor is increased. It strongly depends on atomic factors of all three elements.

The last considered defects are the interstitial Mn atoms in two non-equivalent positions. Those atoms do not substitute any atom, but they are added to original GaAs lattice. Therefore, their contribution to the structure factor does not depend directly on the atomic scattering factor difference. It is, roughly said, proportional to their concentration (occupancy). The phase terms in Equation 3.8 are equal to +1 in case of strong diffraction maxima. There, the waves scattered at both interstitial positions constructively interfere with the waves scattered by atoms at GaAs lattice sites. The structure factor is a simple sum of the atomic factors multiplied by the corresponding occupancies. And the change of the structure factor is proportional to the sum of concentrations of the Mn atoms in both interstitial positions $c_{\text{int,As}} + c_{\text{int,Ga}}$. Here, their individual contributions cannot be discriminated. In contrast to the substitutional atoms, the interstitial Mn atoms with the concentration assumed around 3 % increase the intensity of the strong diffraction maxima approximately for 10 %.

The intermediate diffraction maxima are also affected by the presence of the Mn interstitials. The phase shift of the waves scattered by the Mn atoms in the As and Ga tetrahedra is opposite to the phases of waves scattered by Ga and As, respectively. Their presence effectively decreases the scattering power of the Ga and the As lattice sites, and this decrease is again proportional to the $c_{\text{int,As}}$ (resp. $c_{\text{int,Ga}}$). The resulted intensity is smaller than in case of no interstitial atoms independently on which type of the interstitial position is occupied.

On the other hand, there is a subtraction of the interstitial concentration in case of the weak diffraction maxima. The relative contribution to the structure factor is proportional to the $c_{\text{int,As}} - c_{\text{int,Ga}}$:

$$\frac{4(c_{\text{int,As}} - c_{\text{int,Ga}})f_{\text{Mn}}}{F_{hkl}^{\text{GaAs}}} = (c_{\text{int,As}} - c_{\text{int,Ga}}) \frac{f_{\text{Mn}}}{f_{\text{Ga}} - f_{\text{As}}}. \tag{3.12}$$

The small difference of the atomic factors in the denominator makes the *weak* diffraction sensitive to the difference of the occupancies of Mn atoms in non-equivalent interstitial positions. If those occupancies are equal or similar, the weak diffraction maxima stays unaffected. As the interstitial position in As tetrahedron is more energetically favourable [72], we expect larger occupancy $c_{\text{int,As}}$ than $c_{\text{int,Ga}}$. This would lead to the decreased intensity because the denominator in Equation 3.12 is negative.

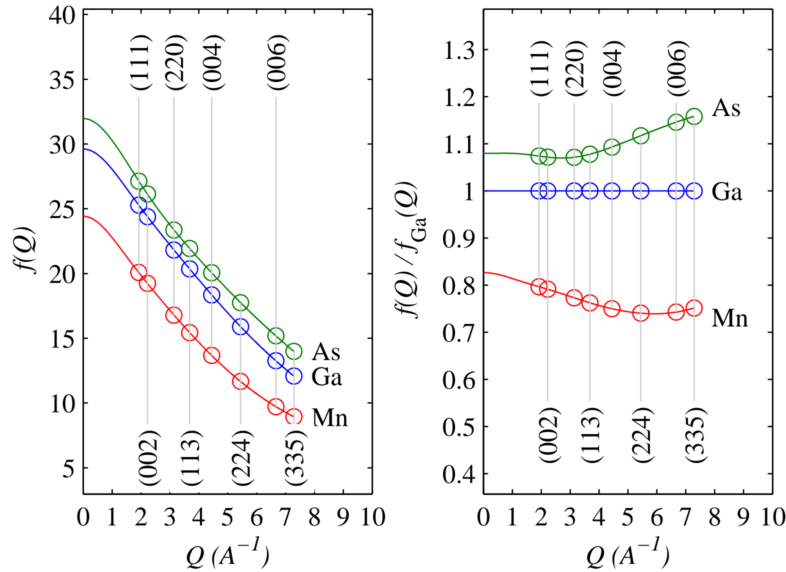

Figure 3.3: The dependencies of the atomic factors of Ga, As and Mn on the scattering vector length Q (left plot) is shown. The coefficient for the atomic scattering factors were taken from Reference 102. The Q-values for several diffraction *hkl* maxima for GaAs crystal are indicated by vertical lines. The shape of curves is similar for all elements. The right plot shows their relative values with respect to the Ga atomic factor, this depict how the relative scattering power changes with *hkl*.

3.2.3 Same maxima types with different scattering vector length

The dependencies of the individual atomic scattering factors on the scattering vector $\boldsymbol{Q}$ (shown in Equation 3.4) describe how the scattering power of considered elements differs for various *hkl* indices. Although the curves describing these dependencies look very similar, the relative scattering power of As and Mn related to the Ga atomic factor changes approximately for 10 % with the increasing scattering vector length. This makes Equation 3.8 for various *hkl* linearly independent with respect to the occupancies of the different elements. Theoretically, it allows to discriminate the contribution from the As and the Mn atoms located at the Ga sites. Nevertheless, it can be said for the case of the *strong* and the *intermediate* diffractions that this effect is very weak because quite small changes of the atomic factors are multiplied by the small defect concentrations. The change of the atomic factors ratio causes the intensity change below one percent compared with the hypothetical case of constant atomic ratio for any diffraction maxima.

This is not valid, apparently, for the *weak* diffractions as it can be seen in Figure 3.2. The denominator in Equation 3.11 and Equation 3.12 is the difference of the similar atomic scattering factors, i.e., a small number which is nearly the same for all *hkl* indices. To evidence this, see the left plot in Figure 3.3). The relative contribution of the Mn atoms in any positions to the *weak* diffraction maxima is scaled with the atomic scattering factor of the Mn. In other words, the normalized intensity for the weak diffractions follows the dependence of the

atomic scattering factors on the *hkl* indices.

3.2.4 Local structural distortion

The substitutional atoms (Mn and As) affect their neighbourhood differently in comparison with Ga atoms in the perfect GaAs structure. Also the atoms 'inserted' to the interstitial space bring new additional interactions with their closest atoms. The attractive and repulsive forces between the neighbouring atoms push some of them from their ideal lattice positions of the GaAs crystal. This local structural distortion results in the change of the volume of the neighbouring unit cells and in the change of the fractional coordinates of pushed atoms.

The lattice parameter of the (Ga,Mn)As described in the Sect. 3.1.1 are nothing but the averaged unit cell diameters. The random distribution of the foreign atoms, modifying the perfect GaAs lattice, enters into the scattering process via their different scattering power, which was described above. In addition, it makes the positions of the scattering centres (atoms) random, as well. This static disorder affects the diffracted intensity mainly of the *weak* diffractions as it is shown in detailed studies of InGaAs semiconductor alloys [103, 104]. Although these works calculate the scattering factors for the TEM diffraction, the local distortion of GaAs lattice due to the presence of the In atoms is similar to our case of anti-site atoms. For the detailed information on the static disorder, one can study the diffusively scattered intensity distributed between the Bragg positions, which can be found in [105].

3.2.5 Atoms shifted from their regular positions

We do not intend to determine the static disorder in crystals using diffraction techniques, which is thoroughly described somewhere else [106, 107]. We just want to quantify approximatively and to include simply the influence of the local structural distortion on the diffracted intensity. Similarly to the random distribution of atomic factors in Equation 3.7, we express how the displacement of atoms around randomly distributed defects affects the coherent scattering part.

It is expectable that positions of the neighbours in several closest coordination shells around the interstitial or the substitutional atom are the most influenced. The positions of more distant atoms stay practically unaffected. We will take into account only atoms in the first and the second coordination shells, and we will consider the change of the positions only radially with respect to the position of the defect. The local distortion of the GaAs lattice around inserted atom into the interstitial space is predicted and quantified by the theoretical *ab initio* simulations in Reference 72. The predicted atom distances are in agreement with the experimentally observed bond lengths for the interstitial site [108]. The interstitial Mn atom in the interstitial position inside of the As tetrahedron pushes radially away the four closest As atoms (the first coordination sphere) by 0.7% (denoted as $\xi^{\mathrm{int}}_{4\mathrm{As}}$) and the six closest Ga atoms (the second coordination sphere) by 1.5% ($\equiv \xi^{\mathrm{int}}_{6\mathrm{Ga}}$) of their original distance from that interstitial position. On the other hand, the distance of the four closest Ga and the six closest As atoms is increased by 2.74% ($\equiv \xi^{\mathrm{int}}_{4\mathrm{Ga}}$) and 0.5% ($\equiv \xi^{\mathrm{int}}_{6\mathrm{As}}$) from the occupied interstitial position inside of the Ga tetrahedron, respectively.

The theoretical *ab initio* predictions claim that there is no change in bond length if Ga is substituted by Mn [109]. Although, it was experimentally shown by XAS that the Mn-As bond is about 2–3 % longer than that of Ga-As [69, 108, 110, 111]. There is no agreement on the shift of the Ga atoms in the second coordination sphere. The radial shift of the second closest neighbours by approximately 0.5 % is reported in Reference 108 whereas no change of bond length with respect to bulk GaAs value was observed in Reference 110. We will take into account only shift of the atoms in the first coordination sphere using average value $\xi^{\mathrm{sub}}_{\mathrm{4As}} = 2\%$.

In the literature, there is no definite answer concerning the influence of the anti-site As atoms on the shift of the neighbouring atoms. Unfortunately, one can hardly measure this quantity with the XAS because it is not possible to separate the signal corresponding to As-As from the stronger signal corresponding to Ga-As bonds. Therefore, we have to rely only on *ab initio* calculations, which produce different results for the repulsion shift of atoms in the first coordination sphere: 4% ([112]), 8% ([97, 113]), 9% ([114]), and 13% ([115] where also the shift of the 12 Ga atoms in the second coordination sphere was calculated as 2%). The repulsion for anti-site atoms found in the literature is so dispersed that we can hardly fix it to certain value. Let us denote formally the radial repulsive shift of 4 As atom in the first coordination sphere due to the anti-site atoms as $\xi^{\mathrm{anti}}_{\mathrm{4As}}$ and the unambiguity of this parameter will be discussed later.

Let us write the fractional coordinates of the atoms in the first coordination spheres relatively to the atom, from which they are repulsed, i.e., directions of the repulsion

$$\boldsymbol{r}^{\mathrm{int}}_{\mathrm{4Ga}} = -\boldsymbol{r}^{\mathrm{int}}_{\mathrm{4As}} = \boldsymbol{r}^{\mathrm{sub}}_{\mathrm{4As}} = \boldsymbol{r}^{\mathrm{anti}}_{\mathrm{4As}} = \left\{ \begin{array}{cccc} (& \frac{1}{4}, & \frac{1}{4}, & \frac{1}{4} \ ) \\ (& -\frac{1}{4}, & -\frac{1}{4}, & \frac{1}{4} \ ) \\ (& \frac{1}{4}, & -\frac{1}{4}, & -\frac{1}{4} \ ) \\ (& -\frac{1}{4}, & \frac{1}{4}, & -\frac{1}{4} \ ) \end{array} \right. , \tag{3.13}$$

where $\boldsymbol{r}^{\mathrm{int}}_{\mathrm{4Ga}}$ and $\boldsymbol{r}^{\mathrm{int}}_{\mathrm{4As}}$ correspond to 4 atoms around the interstitial position in the Ga and the As tetrahedron, respectively. The minus sign indicates that local arrangement of the closest neighbours for two non-equivalent interstitial positions is spatially inverted (see Figure 3.1). The relative positions of the 4 As atoms around the Ga lattice site, being identical to Mn substitutional positions and As anti-site positions, are represented by $\boldsymbol{r}^{\mathrm{sub}}_{\mathrm{4As}}$ and $\boldsymbol{r}^{\mathrm{anti}}_{\mathrm{4As}}$, respectively.

The influence of the Ga substitution on the atoms behind the first coordination sphere is not known nor theoretically predicted, therefore the second closest neighbors with relative positions $\boldsymbol{r}^{\mathrm{int}}_{\mathrm{6Ga}}$ and $\boldsymbol{r}^{\mathrm{int}}_{\mathrm{6As}}$ are considered only for the interstitial positions in As and Ga tetrahedrons:

$$\boldsymbol{r}^{\mathrm{int}}_{\mathrm{6Ga}} = \boldsymbol{r}^{\mathrm{int}}_{\mathrm{6As}} = \left\{ \begin{array}{cccc} (& \frac{1}{2}, & 0, & 0 \ ) \\ (& -\frac{1}{2}, & 0, & 0 \ ) \\ (& 0, & \frac{1}{2}, & 0 \ ) \\ (& 0, & -\frac{1}{2}, & 0 \ ) \\ (& 0, & 0, & \frac{1}{2} \ ) \\ (& 0, & 0, & -\frac{1}{2} \ ) \end{array} \right. . \tag{3.14}$$

The spatial arrangement of the neighbours in the second coordination sphere around both interstitial positions is the same only the elements differ.

We defined $\boldsymbol{r}^{\text{int(sub,anti)}}_{4(6)\text{Ga(As)}}$ as a relative positions of all neighbouring atoms with respect to specific defect of GaAs perfect crystal lattice. All particular positions for each lattice position type (i.e., Ga and As lattice sites and interstitial positions in the centres of Ga and As tetrahedrons) are fully equivalent.

3.2.6 Structure factor corrected to local distortion

We include the effect of the atom repulsion on the structure factor only in the first order approximation. In order to estimate its influence very roughly, let us make two assumptions. Firstly, let us assume that the concentration of all defects is very low. Therefore, the probability of finding just one defect in the first and the second coordination shell of the Ga (or As) atom is much higher than the probability of finding more of them there. According to this, the displacement of the atoms caused by two or more defects located close to each other is neglected. Secondly, we assume no interaction between single Mn atoms during the growth, i.e., the relative positions of any two Mn atoms are completely random. Therefore the displacement of the distorted atoms does not correlate with the positions and with the types of the rest of the atoms included in the structure factor.

The Ga and As atoms far from the defects stay in undistorted lattice positions. Their contribution to the averaged structure factor is not changed. The affected atoms are pushed away in the direction relative to the defect. Their contribution to the structure factor is changed due to the change of their phase. The magnitude of the displacement of all atoms around the defect in the same coordination shell is the same. If we concentrate on one GaAs lattice site, we can conclude that the probability of the displacement in all assumed directions are equal due to the symmetry of the crystal. The averaged position of such atoms stays the same but the averaged phase changes. We can average the term containing the phase shift due to the displacement independently:

$$d^{\text{int(sub,anti)}}_{4(6)\text{Ga(As)}} = \langle \exp(-2\pi \mathrm{i}(h,k,l) \cdot \boldsymbol{r}^{\text{int(sub,anti)}}_{4(6)\text{Ga(As)}} \xi^{\text{int(sub,anti)}}_{4(6)\text{Ga(As)}})\rangle \,. \tag{3.15}$$

The averaging goes over all possible values of $\boldsymbol{r}^{\text{int(sub,anti)}}_{4(6)\text{Ga(As)}}$, which are allowed directions of the repulsion.

Then, the local distortion can be included directly in the undistorted model as a correction, using the probabilities given by the appropriate defect concentrations:

$$\begin{aligned}\langle F^{\text{GaMnAs}}_{hkl,\text{distorted}}\rangle =& \langle F^{\text{GaMnAs}}_{hkl}\rangle \\ & - 4f_{\text{Ga}}(1 - c_{\text{anti}} - c_{\text{sub}}) \\ & \quad \times \big(4c_{\text{int,Ga}}(1 - d^{\text{int}}_{4\text{Ga}}) + 6c_{\text{int,As}}(1 - d^{\text{int}}_{6\text{Ga}}) \\ & \qquad + 6c_{\text{sub}}(1 - d^{\text{sub}}_{6\text{Ga}}) + 6c_{\text{anti}}(1 - d^{\text{anti}}_{6\text{Ga}})\big) \\ & - 4f_{\text{As}}\mathrm{e}^{-\mathrm{i}\pi/2(h+k+l)} \\ & \quad \times \big(4c_{\text{int,As}}(1 - d^{\text{int}}_{4\text{As}}) + 6c_{\text{int,Ga}}(1 - d^{\text{int}}_{6\text{As}}) \\ & \qquad + 4c_{\text{sub}}(1 - d^{\text{sub}}_{4\text{As}}) + 4c_{\text{anti}}(1 - d^{\text{sub}}_{4\text{As}})\big) \,.\end{aligned} \tag{3.16}$$

The repulsion of Ga atoms due to the interstitial atoms are represented by the third line in Equation 3.16 where the first term can be ascribed to the interstitials

in Ga tetrahedrons (the first coordination sphere). The second term comes from the repulsive force of the interstitials in As tetrahedrons (the second coordination sphere). The sixth line of that equation is similar, but the roles of anti-sites are interchanged. The fourth and the seventh line represent the repulsion of the second and the first coordination sphere, respectively, around the substitutional atoms (and anti-sites).

The effect of the local distortion is simulated in Figure 3.4 where the change of the calculated intensity due to this first order correction is depicted. We can see that this effect is very small (around 1%). Anyway, the repulsion distances found in the literature seems quite reliable as they are in agreement with the experiments. Therefore, it is not a problem to include this correction into the simulation of the diffraction measurement with certain values of the repulsion.

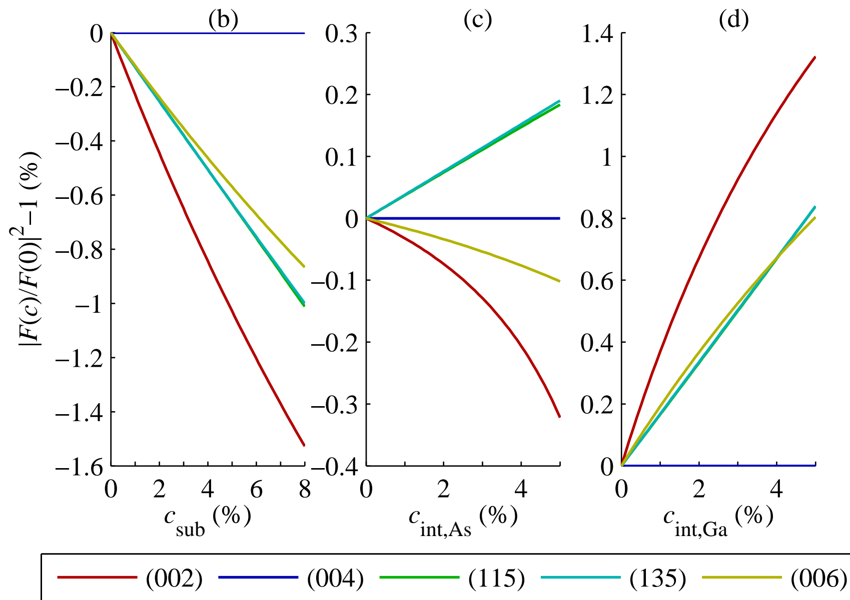

Figure 3.4: Influence of the distortion correction with respect to individual defect concentrations. Simulations are made for the presence of only one type of defect: the substitutional Mn atoms (left), the interstitial atom in As tetrahedral position (middle), and the interstitial atom in Ga tetrahedral position (right).

3.2.7 Neighbourhood of anti-site defect

Figure 3.5 shows that the influence of the local distortion due to the presence of the anti-site defects is quite important, and its change of the intensity is dramatical for the higher anti-site concentration. Moreover, we do not know exact values for the atoms shifts because there is not an agreement in the literature and all values come from theoretical predictions without any experimental proof. It is obvious that we cannot include this correction in this form. Luckily, we can estimate the limit of the anti-site defects concentration. The defect concentration was the long-ago important question also for pure GaAs when the LT-GaAs was being studied, as well. The major defect in LT-GaAs is the anti-site defect, whose concentration is around 10^{20} cm^{-3} ([96, 97]). There are $4.42 \cdot 10^{22}$ atoms in a cm^3 volume of GaAs [98], half of them is gallium atoms, i.e., possible lattice sites for

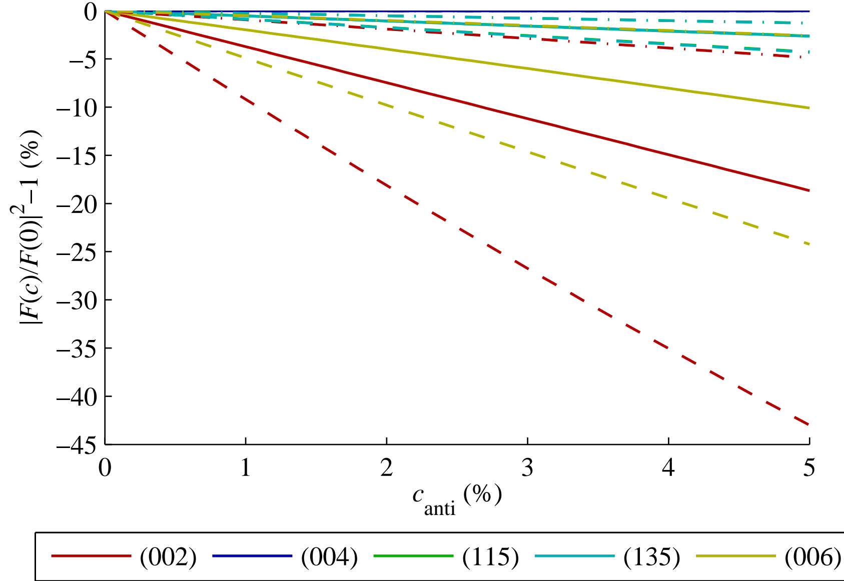

Figure 3.5: The influence of the distortion due to the anti-site concentration for several diffractions (different colours) and different repulsion factors taken from the literature (solid line ($\xi_{4\mathrm{As}}^{\mathrm{anti}} = 4\%$) and dashed line ($\xi_{4\mathrm{As}}^{\mathrm{anti}} = 13\%$)). The change of intensity is related to calculated values without a distortion correction.

As anti-site defects. Since, their typical occupancy is approximately 0.5%. There are the similar finding also in (Ga,Mn)As material where the anti-site occupancy are determined to be below 1% [74, 85, 116, 117].

During the (Ga,Mn)As growth, the system tends to reach the compensation of the substitutional Mn by introducing of donor-like defects. This is some kind of self-compensation effect [118]. The forming of anti-site double donors compensate the acceptors (substitutional Mn), this is enough to get full compensation for low Mn concentrations. Consequently, the low number of double donor interstitial defects are present [117]. On the other hand, for the higher Mn content incorporated into original GaAs matrix the self-compensation is driven by the forming of the more interstitials. This mechanism predominates the compensation due to the anti-sites and the concentration of the anti-sites stays below 1% and it is affected by the higher content of the Mn only very weakly [117].

Even for the most pessimistic case considering the strongest predicted repulsion around anti-site atom, we can see from Figure 3.5 that such concentrations below 1% does not change intensity very much. But, we have to admit that this change is comparable with the influence of the anti-sites on the structure factor without distortion represented by Equation 3.10. It seems that only one possibility how to deal with this problem is to abandon the effort of the determining of the anti-site density from the measured data. Then, if we are not interested in this value, we can proceed our data repeatedly using local distortion correction with different theoretical repulsion factors. This gives us some uncertainty in all determined parameters, i.e., in the concentrations. Briefly said, it will increase our error bar of our results.

3.2.8 Iso-intensity surfaces

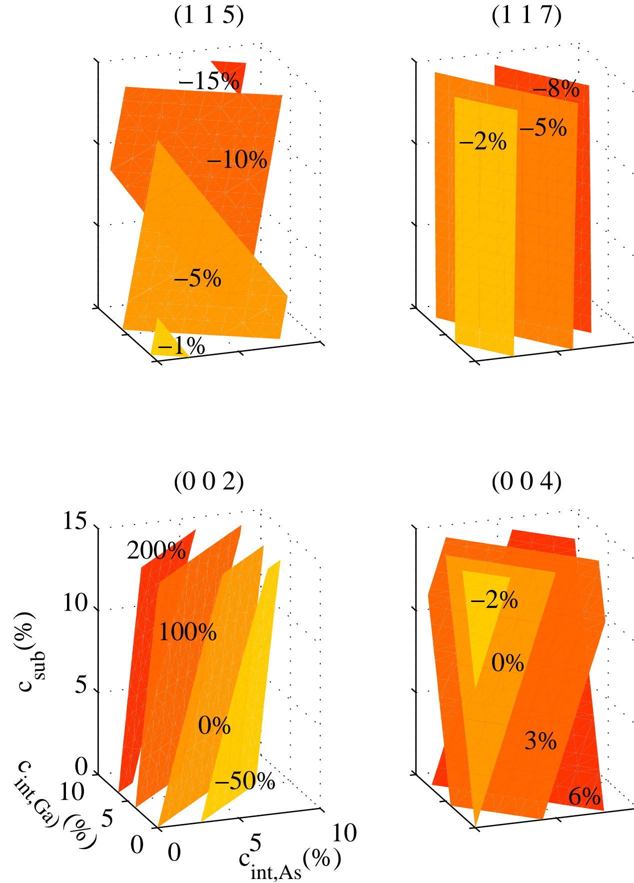

Figure 3.6: The distribution of the calculated intensity in the 3D space on Mn concentrations. Each point represents the intensity for the corresponding concentrations of Mn in all considered lattice positions. Only a few iso-intensity surfaces are plotted for clarity for each diffraction. The numbers within the planes indicate the intensity change with respect to the intensity of pure GaAs. The distributions of intensity are plotted for weak diffraction maximum (002), strong (004) and two intermediate diffraction maxima (115) and (117).

If we restrict ourselves to determine three free parameters: c_{sub}, $c_{\mathrm{int,As}}$ and $c_{\mathrm{int,Ga}}$ assuming that the concentration of anti-site atoms is below 1%, we can extract desired parameters from the measured intensity of several diffractions. Previously, we show the intensity change with respect to certain defect concentration where other two defect types were not present. It is obvious that there is some correlation between those free parameters. In other words, the certain intensity change can be achieved by several values of free parameters in the simulation. To visualize this correlation, let us imagine 3D space of parameters. Each dimension is represented by one of our free parameter. Now, we can calculate the intensity for all possible values of c_{sub}, $c_{\mathrm{int,As}}$ and $c_{\mathrm{int,Ga}}$ (it is a vector in our parameter space, in fact). In Figure 3.6, we can see that points with the same value of the calculated intensity form some iso-intensity surfaces, let us say, planes. If we measure the intensity in our experiment, we can identify the correct iso-intensity surface for the measured diffraction. This itself does not give us

the exact values of concentration. We need to measure more diffractions and to identify iso-intensity surface for each diffraction. The values of concentration, we are searching for our sample, is given by the intersection point of those identified surfaces. In practice, every measurement is done with an error, so the result is not the point in 3D parametric space, but it is rather a small object. The most probable value will be the centre of the object, the variance will be given by the size of the object.

The visualization of the iso-intensity surfaces for many diffractions gives us the hint which set of diffraction maxima to measure. We have to choose those diffractions for which the iso-intensity surfaces are mutually not parallel. Let us say that the set of diffractions maxima (002), (004), (115) and (117) is good choice for that. We should note that in practice we will not work with intensities of the peaks, but with whole diffraction curve that should be compared to the simulated profile. This calculation is described in chapter 2. The resulted structure factor introduced here enters there as an input dependant on the free parameters.

Conclusion

Here, the structural model of (Ga,Mn)As was introduced. We showed how the structure factor is affected by the different scattering power of impurities in GaAs lattice. As well, we derived the correction of the structure factor for the displacement of the atoms around these impurities.

In conclusion, we introduced a theoretical recipe for the determination of the concentration of Mn in three non-equivalent lattice positions. We got to know the limits of this approach, mainly that the as-grown samples are assumed to be self-compensated by the interstitial Mn. The experimental problems and the main interpretation of the real experimental data will be described in next chapters.

Chapter 4

Description of HRXRD measurement

We dedicate this chapter to the x-ray diffraction measurement and collected data processing. We start with the description of the used experimental equipment for the HRXRD. All x-ray laboratory measurements are carried out with the X'Pert Panalytical Multi Resolution Diffractometer in High-Resolution mode. We mention the parameters of the used instrument. With that, we thoroughly describe the optic elements of the diffractometer. Later, the measurement procedure is introduced and discussed. And, the treatment of raw collected data from which we obtain the final diffraction curves is depicted.

4.1 Experimental equipment

Generally, the experimental setup for the diffraction experiment consists of several distinguishable parts. The x-ray radiation is generated in the x-ray source that is the x-ray tube in case of laboratory experiments. The generated radiation goes through optical elements forming the *incident beam path*. Here, the radiation can be made partially monochromatic by the *monochromator* device. Usually, there are some optical elements in the incident beam path, which define a spatial and an angular distribution of the x-ray beam impacting the sample. The sample emits a diffracted radiation that is detected by the detector in a defined position. We are interested in the angular distribution of the intensity of the radiation diffracted by the sample. But, the beams coming from the finite sample, from the sample holder (and possibly other elements) approach the detector from the several directions. We use another optical elements inserted in *diffracted beam path* to define rays that can finally reach the active component of the detector.

We describe briefly all functional components of the instrument (*diffractometer*), and we mention the specifications of such components in the diffractometer used for our experiments.

4.1.1 x-ray tube

The x-ray tube is evacuated, and generally, it consists of an anode and a cathodic filament. The electrons thermally emitted, usually, from the tungsten filament are

accelerated by the anode-cathode voltage. At the same time, they are focussed to the target on the anode (*focus*).

Shortly said, the electrons impacting the anode can bounce out the anode electrons from the inner atomic shells of an atom. This results in an emission of the gamma quantum due to the intra-atomic transition filling back the free empty shell. It produces *characteristic* radiation, whose wavelengths correspond to the energetic difference of the electron states acting in these transitions. There are more allowed jumps between the higher and the lower energetic states, therefore, there are more possible wavelengths of the gamma quantum with higher or lower probability of being emitted. These discrete wavelengths are specific for different materials. The metals, such as Cu, Mo, Co, or W, are widely used in the x-ray tubes. Usually, the doublet $K_{\alpha1,2}$ is used for the highest emission probability.

This is not the only one way how the x-ray radiation is generated in the anode. Also, it is being emitted due to the deceleration of the impacted electrons in the material as the accelerated charge emits the electromagnetic wave. This radiation is called *Bremsstrahlung*, and it has a continuous emission spectrum with the smallest wavelength corresponding to the energy of impacted electrons.

The envelopes of x-ray tubes, usually made of glass or ceramic, have beryllium windows through which the generated radiation goes out with the minimal intensity loss.

We used PW333/00 Ceramic Tube Cu LFF that is a tube with the copper anode. The maximum operating power is 2.2 kW, the maximum voltage and the maximum current are 60 kV and 55 mA, respectively. The recommended maximum settings is 40 kV and 55 mA. We operate this tube with settings 40 kV and 35 mA. This enhances the lifetime of the tube at the expense of the smaller intensity of the primary beam.

The transmission of four different beryllium windows (14 mm in diameter and 300 μm thick) is 94 %. The line-like focus of the tube ($12\,\text{mm} \times 0.4\,\text{mm}$) can be viewed by two Be windows as a spot when operating in a point-focus mode. The other two windows allow to keep the focus being line when operating in line-focus mode, our configuration. The take-off angle of the x-ray radiation is 0°–12°.

The manufacturer announces the spectral purity being less than one percent. The spectral purity is ‘the relative intensity of characteristic foreign lines to $K\alpha$ line measured with a β-filter (attenuator suppressing the Cu K_β) at 40 kV’. This quantity increases for another less than percent per 1000 hours of tube life. In practise, it means that the tungsten from the filament contaminates the surface of the anode, and it starts to produce the W characteristic radiation, as well.

The tube is cooled by the water with flow of 3.5–5 l per minute with maximum pressure 0.8 MPa. The tube operates in surrounding temperature 5–40 °C.

4.1.2 Incident beam path

The radiation coming from the beryllium window is not collimated, only limited just by that window. The focus of the tube is oriented vertically. The x-ray beam is going through several optical elements in the incident beam path as it is depicted in Figure 4.1.

There is a component called Goebel mirror just behind the x-ray tube. It is parabolic multilayer that converts a divergent x-ray beam leaving the tube to a

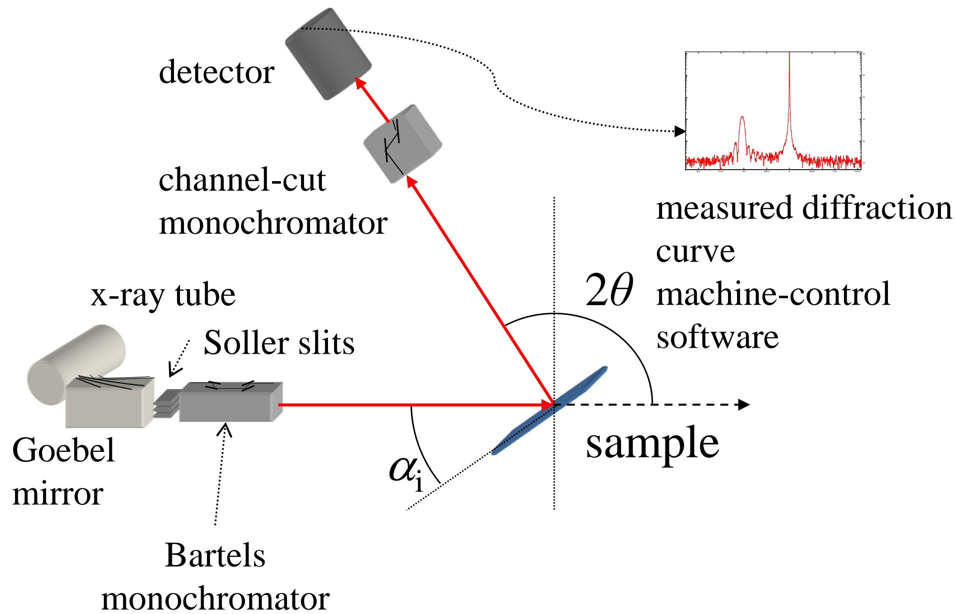

Figure 4.1: Sketch of the experimental setup. We measure the intensity distribution of the diffracted beam in angular space (α_i, 2θ). The x-ray radiation generated in the x-ray tube approaches through the incident beam path (Goebel mirror, Soller slits and Bartels monochromator) the sample. There is a channel-cut monochromator in the diffracted beam path increasing the resolution.

monochromatic quasi-parallel beam. This process is provided by the reflection of the x-ray beam on the multilayer. This multilayer is parabolically curved in horizontal direction. It collects the radiation from the line focus of the tube that is identical to the focus of the parabola. It is not curved vertically. The period of the curved multilayer is locally changing to keep the constructive interference of the reflected beam on individual sub-layers.

As a consequence of the parabolic curvature, the mirror significantly decreases the divergence in the horizontal direction, often called as *equatorial*. It is in the plane where our detector moves, i.e., the diffraction plane defined by the primary beam direction and the direction of the diffracted beam. The divergence in the vertical direction, perpendicular to the diffraction plane, is not controlled by the x-ray mirror. We call vertical divergence as *axial*.

The x-ray mirror increases the intensity per unit area of the x-ray beam above value produced by the x-ray tube itself. This is because of the collimating the divergent beam into a parallel beam. Our diffractometer has x-ray mirror designed to diffract K_α radiation. The manufacturer claims that intensity of the K_β radiation is reduced to a level below 0.5 % of its original value.

The mirror in our experimental setup accepts the divergent x-ray beam from the line focus in angular range approximately 0.8°. The divergence in the horizontal direction is significantly decreased by passing through the mirror whereas the vertical divergence remains unchanged.

The vertical divergence is limited by the Soller slits behind the Goebel mirror in the incident beam path. Those slits are multiple metal sheets equidistantly positioned and horizontally oriented. The divergent beam has to pass through

the gaps between those sheets. The beams being too declined from the right direction hit the sheets, and they are attenuated. Our configuration allowed to pass the beam with the smaller vertical divergence than 0.04 rad and 0.02 rad.

The last optical element is the high resolution monochromator (Bartels monochromator) that reduces the $K_{\alpha 1,2}$ doublet to the single $K_{\alpha 1}$ line with the well defined angular shape of the beam. This is very important for the high resolution measurement when we are interesting in the precise shape of the experimental diffraction curves.

The monochromator consists of the two U-shaped single nearly-perfect crystals. The both incident beams for $K_{\alpha 1,2}$ doublet is two times diffracted on the first crystal. However, the beam with $K_{\alpha 2}$ wavelength, fulfilling the Bragg condition on the first crystal, exits in the inappropriate direction. It is not able to fulfil the same condition on the second crystal. Only the beams with wavelength $K_{\alpha 1}$ with proper direction can survive the passing through. The angular profile of resulted beam is sharpened by the four-times diffraction.

The crystals are usually made of germanium using diffraction Ge (220) or Ge (440). The *symmetric* Ge monochromator is cut to have (110) surfaces accepting the incident beam. To increase the intensity of the monochromatic beam it is possible to cut these surfaces inclined relatively to the (110) planes. The beam coming from this *asymmetric* monochromator has a higher angular divergence. We can use both types in our setup. The manufacturer specify the angular divergence for the symmetric Ge(220) 4-crystal (12 mm wide) should be less than 0.0039° while the asymmetric variant has angular divergence less than 0.0053° with the 2.5 times higher intensity then the symmetric one.

Besides the optical elements described above, there is a system of additional slits, foils, and masks to define the incident beam (see Figure 4.2). The first slit, sometimes called anti-scatter slit, is located just behind the x-ray tube in the incident beam. This is the vertical slit limiting very roughly the divergence of the beam passing into the x-ray mirror. By the choice of this slit ($^1/_{16}{}^\circ$, $^1/_8{}^\circ$, $^1/_4{}^\circ$, $^1/_2{}^\circ$ and 1°), we can define the irradiated area of the parabolically shaped multilayer in the x-ray mirror. This results in a defined width of the parallel beam produced by the mirror.

The height of the beam, i.e., the size in the vertical direction, is controlled by the mask located between the anti-scatter slit and the x-ray mirror. We can use mask with the 2, 4, 10 or 20 mm window height. The horizontal size of the window is large enough not to affect the beam size. We have to keep in mind that the height of the window is not reproduced in the vertical size of the beam exactly because the beam is still divergent in the vertical direction.

Anywhere in the incident or diffracted beam path, there can be inserted attenuating foil to decrease the intensity of primary or diffracted beam. In our case, it is inserted between the Soller slits and the Bartels monochromator. This optional attenuation is present in order to decrease the intensity of the detected radiation to levels safe for the detector if the beam in the diffracted path is too intense, e.g., when the intense substrate peak is being measured.

Finally, we can set the beam size in both directions with tunable cross-slits mounted behind the Bartels monochromator. The gap between the movable metal stops is defined by the micro-metric screws.

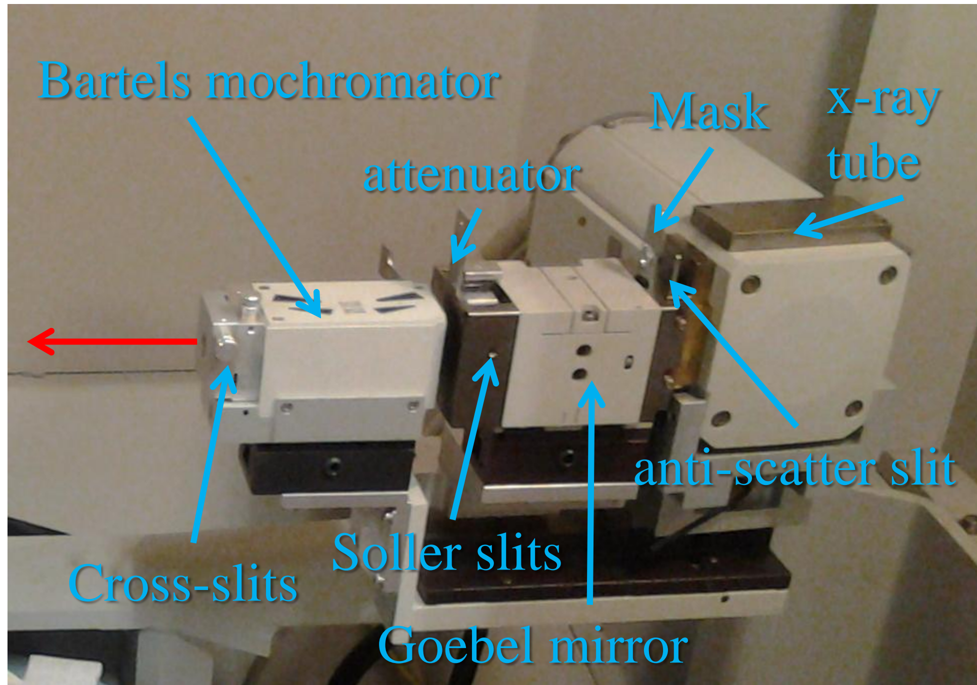

Figure 4.2: Optical elements in the incident beam path in detail. The x-ray radiation is generated in the tube on the very right. The beam is then passing through an anti-scatter slit and a mask to the x-ray parabolic mirror. Consequently, the parallel beam is going through Soller slits and optionally through an attenuating foil into the Bartels monochromator. It leaves the incident beam optics through a tunable cross-slits and approaches the sample on left out of the picture in the direction of the red arrow.

4.1.3 Diffracted beam path

There are not so many functional components in the diffracted beam path. The last component finalizing the journey of the x-ray beam is the detector. Generally, it counts the number of photons going through its the window to the active element of the detector.

There are several types of the detectors, e.g., sealed proportional detectors or scintillation detectors, based on the different detection technique of the passing gamma quantum. Basically, we distinguish between energy dispersive and non-dispersive detectors, that are (not) able to resolve the wavelength of the counted gamma quantum. Usually, we do not need this ability for the standard diffractometry in the limits of the Compton elastic scattering. Lastly, we can divide detectors according to the dimension in which they are able to resolve the position of the passing photon (position sensitive detectors), i.e., those simply counting photons passing through the window (0D), linear detectors (1D), or area detectors (2D).

There is a proportional detector in our x-ray instrument. It consists of a cylindrical chamber having its axis in the direction of the incoming beam. The active area is behind the beryllium rectangular window ($20\,\mathrm{mm} \times 24\,\mathrm{mm}$). The detection gas is a mixture of xenon and methane. The photon entering through the window into the chamber can ionize the inert detection gas along its path.

This results in an electric current between the metal wire (anode) located along the cylinder axis and the inner coating of the detector (cathode). From the electric current the number of photons in the chamber is deduced.

Our detector is possible to measure the fluxes of one photon per second, it safely works in the linear regime to the 1 million counts per second (cps). Above this flux level of detected x-ray beam, the detection starts to be very non-linear, i.e., there are less successfully detected photons than it is flowing through the chamber. Finally, for more higher fluxes, the detector is completely saturated giving non-representative results. We have to measure in the range of the linear regime which can be ensured by the insertion of the attenuating foil somewhere in the incident or in diffracted beam path.

We have a choice to have no other optical components before the detector. In such a case we collect all x-ray beams approaching the window of the detector, i.e., beams coming from the different parts of the sample with different directions as well as the radiation scattered by the sample holder and possibly other objects in the diffractometer. If we overlook this, we can use the fact that the detector window covers the angular range over one degree. It is advantageous for the aligning of the sample and searching for diffraction maxima in the angular space.

For the high-resolution in the angular space, we use the multiple diffraction on the *analyser* crystal in front of the detector. It cuts off the x-ray beams being deviated from the desired direction of the detection. The analyser crystal is a channel-cut germanium crystal, where the x-ray beam is three times diffracted (Ge (220) diffraction). The final beam passed through the analyser is declined for 6° (*offset* of the analyser) in the horizontal direction from the original path. The acceptance of our crystal is 12 arcseconds that is the angular resolution of the system in the diffracted beam path.

Practically, one needs to align sample with low angular resolution because there can be only rough knowledge of the diffracted beam directions, for instance, roughly estimated lattice parameters. In such a case, we use no analyser crystal to align sample properly. We use the advantage of detecting the intensity integrated over the relatively wide range of diffraction angle (1°). When the sample is aligned, one wants to switch to high resolution for the HRXRD measurement. Our instrument carries two detectors with and without analyser crystal. It is capable to switch between them, i.e., to choose if the diffracted beam path (b) or (c) is active as depicted in Figure 4.3.

4.1.4 Control of experiment

As we mentioned above, we are interested in the intensity distribution in the angular space $(\alpha_\mathrm{i}, 2\theta)$. The angles correspond to the incidence angle of the x-ray beam impacting the sample and the diffraction angle, respectively. We restrict ourselves to a coplanar diffraction where the diffraction plane is perpendicular to the surface. Then, the third important angle is the azimuth of the sample, which is the orientation of the intersection line of the surface and the diffraction planes on the sample.

We have several motors, we can control during the experiment. The desired three angles are derived from some of these motor positions. Some motors are only for the proper sample alignment having no direct influence on the angles α_i,

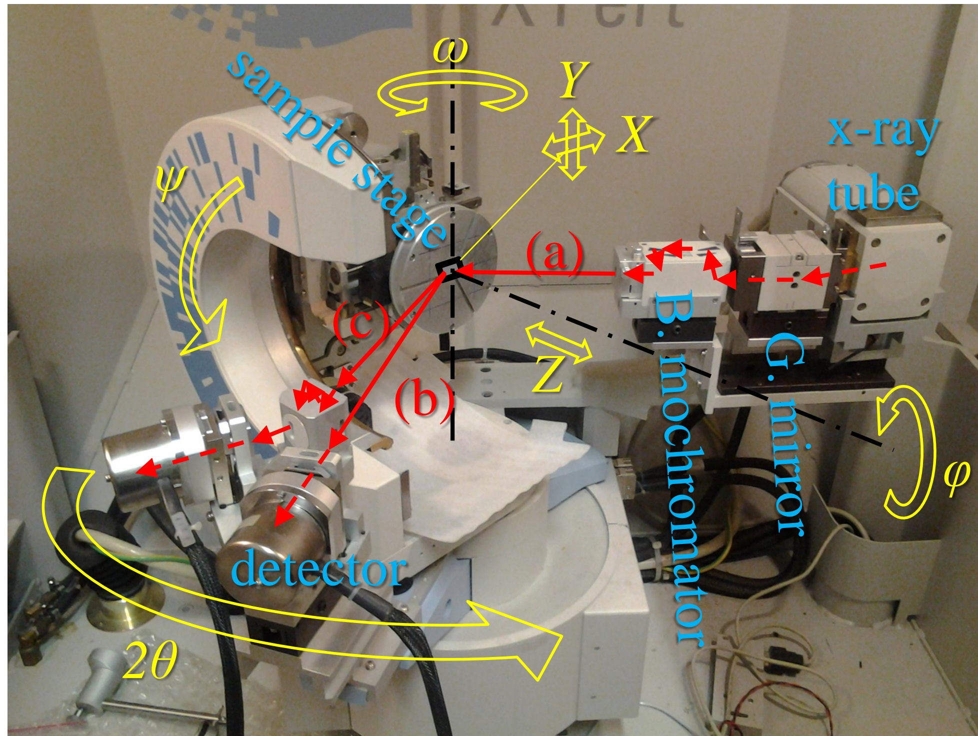

Figure 4.3: Real experimental HRXRD machine. The red lines schematically guides the beams in incident beam path (a) and in the diffracted beam paths (b, c). The blue labels describe the functional parts of the instrument. The motors that can be controlled by the user are indicated by the yellow signs, and their movement direction by yellow arrows. The sample is located roughly in the centre of the photo, being mounted on the sample stage.

2θ and the azimuth.

The sample is mounted vertically on the sample holder, ideally in such a way, that any rotation of the sample will keep the central point of the sample in the axis of the incident x-ray beam. The sample stage allows movement of the sample holder in all three spatial directions relatively to the intersection point of all rotation axis. These motors are labelled X, Y and Z as it is depicted in Figure 4.3. It is assumed that mentioned intersection point of sample-stage rotation axis is just in the centre of the incident beam. To align properly the sample, we have to set X, Y and Z motors to move the central point of the sample surface into this intersection point. For the clarity, see Figure 4.4.

The sample stage has three motors controlling the rotation of the sample holder and consequently the sample. The first one is the ω-motor which rotates whole sample stage along the vertical axis, i.e., perpendicular to the diffraction plane. If sample is properly aligned, this ω-motor corresponds to the α_{i} angle except of some offset.

The second rotation allowed by the sample stage is the rotation of the sample holder around the strictly horizontal axis, and it is performed by the ψ-motor. The whole sample stage is rotated by the ω-motor. Therefore, it defines the azimuthal orientation of the axis for the ψ-motor rotation, as well. This motor serves to adjust the sample surface perpendicular to the diffraction plane because, generally, the sample holder surface and sample surface do not need to be parallel.

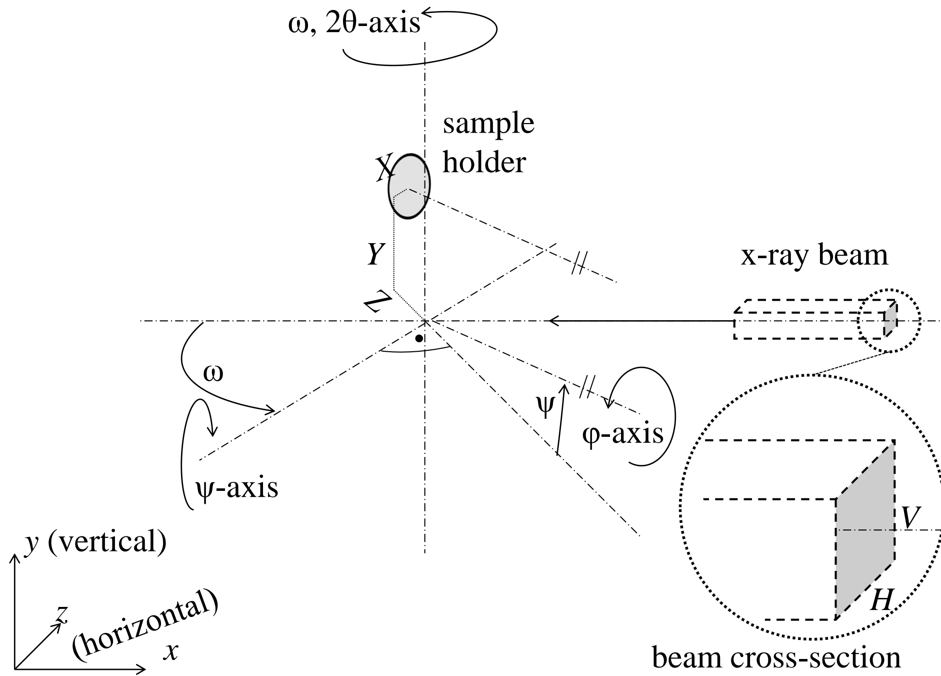

Figure 4.4: All rotation axes of the diffractometer are depicted. There is just one intersection point of all axes, the sample holder can be moved relatively to this point to adjust a sample properly.

It depends on the mounting of the sample and its shape.

The last motor defining the azimuthal orientation of the sample is the ϕ-motor. It is mounted on the arm controlled by the ψ-motor that inclines the ψ-axis. Therefore, the axis of the ϕ rotation is perpendicular to the ψ-axis. Concurrently, the angular deviation of the ϕ-axis with respect to the static ω-axis is $90 - \psi$.

The diffracted beam path is controlled by only one motor 2θ corresponding to the diffraction angle.

After the successful adjustment of the sample, we can set the inner offsets of the motors to identify the ω motor with the incident angle and the ϕ with the azimuthal deviation from the certain crystallographic direction.

4.1.5 Available modes for line scans

The control software allows to move the motors positions manually for the alignment or for the setting the starting position before the measurement program is executed. There are two basic possibilities how to measure a diffraction curve. We can collect the detected intensity during the simultaneous movement of some motor or pre-set motors combination (*continuous* mode). Or, we can measure the intensity without movement in some certain defined points (*step* mode), usually, equidistantly distributed along the angular path of some motor (or motors combination). We call both these measurements as *scans* (or line scans) revealing an intensity distribution along one dimensional path in the angular space of motors movement. The path in the angular space is for both modes the same, except of

a later mentioned q-scan available only in the step mode.

For the step mode, all motors are stopped during the count rate collection. In fact, they are automatically correcting and oscillating to keep the desired position. Although, there should be no vibrations due to the simultaneous movement of the motors, it is ensured also for the step mode as it is claimed by the manufacturer.

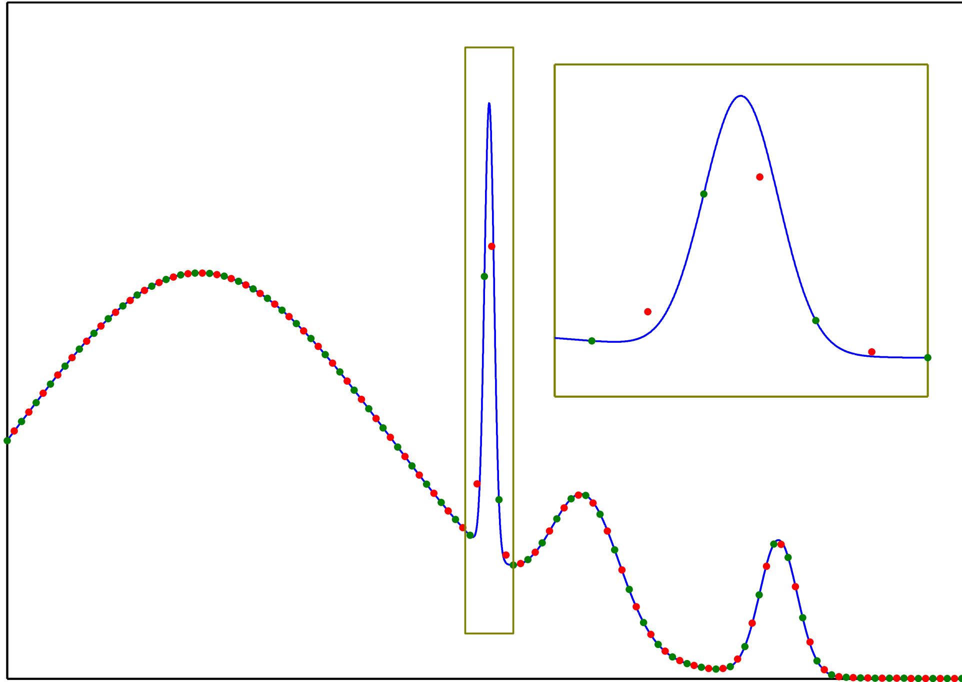

Figure 4.5: Comparison of the two basic measurement modes. The blue curve is an arbitrary chosen curve with gaussian-like peaks of different width. Assuming this curve to be real distribution of the intensity, we simulated the intensity obtained using the step mode (green points) and the continuous (red points) measurement with the same step. The resolution function is much smaller than the chosen step, being the same for both modes. The part of the curve with the thinner peak is enlarged in the inset.

There are two cases where it is not possible to use the continuous mode. Firstly, we can decide not to wait in each step for the same counting time, but to measure at each point as long as it is necessary for the collection of defined counts. However, this acquiring time is limited by the maximal time that is set by the user. It allows to increase the statistics of the low intense peaks and to measure relatively quickly high intense peaks. But usually, the time consumption due to the separation of the movement and intensity detecting is larger than for any continuous scan. Secondly, if we want to measure scan that cannot be achieved by the constant movement of two motors, e.g., due to the changing step of one or both motors, the step-mode measurement is necessary. This is the case of q-scan, i.e., the scan along the straight line in a reciprocal space.

On the other hand, the continuous mode is much faster because the motors are moving with constant speed while the count rate is being detected. There is no wasted time due to the static measurement or due to the aligning precisely just to the calculated position after each step. This aligning in step mode is an

iterative process controlled by the internal electronics of the instrument.

If there are no disturbing vibrations due to the movement and if the motors are well synchronized, the quality of the collected data does not significantly differ for both modes. We show the simulation of both types of measurement on the model curve in Figure 4.5. It is obvious that both modes describes the curve equally when the step is small enough compared with the width of the features present in the curve. If we assume that the resolution is smaller than step, the step mode describes the curve by the interpolated values at equidistantly distributed points. In contrary, the continuous mode integrates the curve between these points and places the normalized integrated value between the neighbouring points, i,.e., in the centre of the measured interval.

Unfortunately, if we use too large step with respect to the width of the peak, none of these modes is possible to describe the peak profile sufficiently. This happens very often when the very narrow peak of almost perfect crystal of the substrate is measured. If this peak is not measured with a finer step than the rest of the curve, one has to be very careful in the data interpretation because the peak seems to be less intense than it is, in fact.

The line scans can be also measured for the ϕ- and ψ-motors movement, but they are not relevant for our coplanar diffraction measurement taking into account how we defined our angular space. These scans are useful for the sample (re-)adjustment.

To measure the intensity distribution in some area of the angular space we have to perform a sequence of the line scans mutually shifted in the angular space. This measurement we call the *map* and it can be performed automatically by the software as so called two-axis measurement.

4.2 Measurement procedure

We described our diffractometer, the movement of its motors and a capability of various scanning modes. There are three aspects we want to explain that are connected with the successful obtaining of the diffraction curves. The first is the sample adjustment being general task. Its proper performing is crucial for the collecting of quality data with not skewed intensity. Secondly, the diffracted intensity is distributed along straight lines in the reciprocal space whereas basic scans allow to measure the distribution of intensity along the straight lines in the angular space of the motors. Since, it is essential to introduce the relations between those two spaces. From those, we are able to suggest the measurement procedure. Lastly, there is a specific obstacle complicating the measurement along Crystal Truncation Rod with our diffractometer. Although its origin is not completely understood, it seems that the reason lies in some imperfectness of the motors continuous movement when we decrease their step to the lowest limits of the machine. This can be just particular problem of our diffractometer type being observed with several similar machines.

4.2.1 Sample adjustment

When we described the sample stage and the optical elements of the diffractometer, we assumed that the central point of the sample surface is positioned exactly

in the intersection point of all rotation axes (see Figure 4.4). This is a necessary condition for the correct interpretation of the motors positions in the angular space.

Generally, the measurement usually starts with the adjustment of the diffracted beam path with the arm carrying the detectors. It is connected with the position of the x-ray tube focus, in case of our diffractometer, it can and it has to be tuned to the proper position, as well. We assume that all optical elements are adjusted by the manufacturer and there is no reason why they should be misaligned during the operation time of the diffractometer. On the other hand, the temperature change in the x-ray tube can cause the movement of the tube focus in time.

This happens mainly with the change of an operational current and voltage, i.e., when the diffractometer is awaken from the stand-by mode or non-operating state with the lower energy consumption. If the temperature in the tube is stable, which is given by the temperature and the flow of the cooling water, the x-ray tube focus should stay tuned. However, this depends on the construction of the cooling circuit and sometimes this stability is not perfect. For instance, it can be just one central cooling circuit attending several diffractometers that change their operational regime sometimes, going on, off, standby, or saving mode. One should check sometimes the intensity of the direct x-ray beam going through the optical elements and to realign the focus if necessary.

The focus can be moved by the micro-metric screw in the direction of the cylindrical tube axis that is oriented horizontally. The aim is to move the tube focus to the position of the parabolic mirror focus that the Goebel mirror works properly. As we are interested in the tuning of the incident beam path, we select the diffracted beam path with the *open detector* moved to the direct beam. It is setup with no optical elements in front of the wide window of the detector having the angular acceptance approximately 1°. The direct beam is very intense, so the attenuation foil has to be inserted to prevent the saturation of the detector. We tune the focus to obtain the highest possible intensity in the detector which means that the incident path is aligned.

Then we switch the diffraction path to the high-resolution mode which is the detector with channel-cut monochromator in front of it. The 2θ-scan across the direct beam should reveal a symmetric narrow peak (in our case with 0.0030° full width in a half of maximum (FWHM), typically). The centre of the peak corresponds to the zero 2θ, and we set the offset of the 2θ motor to satisfy this.

Now we can move the sample mounted on the sample holder approximately in the desired crystallographic orientation into the direct beam using $X-$, Y- and Z-motors. The cross-slits vertical gap and the mask are chosen to produce the beam of a vertical size being the same or rather smaller than the width of the sample, being mounted vertically. This ensures that no x-ray radiation passes around the sample sides. The horizontal gap should be tuned to a certain value, which depends on the sample length (the horizontal length). Usually, we choose the horizontal beam size to be sure that whole beam is impacting the sample during the all diffractions measurement. If this is not valid, one has to correct the measured intensity for the direct beam loss due to the passing of x-ray beam around the sample. The correction is possible, but it is not sure that the beam is homogeneous. Therefore, the intensity flux missing the sample has not to be

necessarily proportional to the corresponding area around the sample. Usually, we select the horizontal beam size $H = L \tan \alpha_i$ for the sample length L and the lowest expecting incidence angle α_i of all measurements.

When the both beam paths optics are ready, we have to move and to tilt the sample to satisfy two conditions. Firstly, the surface plane has to be perpendicular to the diffraction plane that is the horizontal plane where the detector moves. This is fulfilled if the specularly reflected beam (low $\alpha_\mathrm{i} = \frac{2\theta}{2}$) stays in the diffraction plane. We search for such a ψ-motor position where the intensity of the reflected beam by the sample is the highest. At the same time, we adjust the ω-motor to correspond the desired incident angle α_i for the fixed detector position. One has to take into account that occasionally some of the direct beam is passing around (above) the sample and the sample holder can reflect the beam, as well. Both produce some intensity increase that should not be confused with the reflected beam by the sample surface.

Secondly, the central point of the sample surface should be in the intersection point of the 2θ-axis and the primary beam axis, which coincides with the intersection point of the ω-, ψ- and ϕ- axes. This has to be reached by the alignment of the X-, Y-, Z-motors. Usually, the beam is a little bit smaller then the sample diameters, therefore X- and Y- motors can be set with rather low precision. If the first condition is fulfilled, the sample at zero incident angle should shade the half of the primary beam (if no beam is passing around the sides of the sample), therefore the optimal Z has to be carefully found.

The effect of the all three motors being aligned (ω, ψ and Z) are bound together. All of them have to be in optimal positions to satisfy both conditions introduced above. This can be achieved by their iterative adjustment consisted of Z-movement in the direct beam (α_i=0) and $\omega-$ and ψ- adjustment in the reflected beam ($2\theta \approx$ tenths of degrees, i.e., above the critical angle as far as the reflectivity is sufficient).

Finally, one has to align the azimuthally the sample (ϕ). It is found by using some asymmetric diffraction. Ideally, we switch to the open detector set to the expected 2θ value and the motor ϕ is optimized.

In practice, the measurement of each diffraction within one sample is accompanied with the fine adjustment of all motors (ω, ψ, ϕ and 2θ, as well) to reach the maximal intensity of particular diffraction. Firstly, we align the motors determining the sample orientation using the open detector. Finally, we switch to high-resolution and after 2θ optimization we realign previous motors precisely.

There are several reasons why one cannot use the very first alignment of the ψ and ϕ for any diffraction measurement. Firstly, the crystallographic planes nominally parallel to the surface are not parallel perfectly. Often, there is a small tilt called *miscut*. It can be in any direction, therefore, it can lead to misalignment of several motors. Secondly, the ϕ-rotation axis is perpendicular to the sample holder surface. This is not usually perfectly parallel to the sample surface because of the sample shape or the way of mounting on the sample holder (see Figure 4.6). Therefore, the change of the azimuth affects the real incident angle α_i. Both effects causes the need of realignment near every diffraction position, but in the vicinity of a certain position, it is possible to move just in the angular $(\omega, 2\theta)$-space (measurement).

The high-resolution works with steps 0.0001° in ω and θ and the angular res-

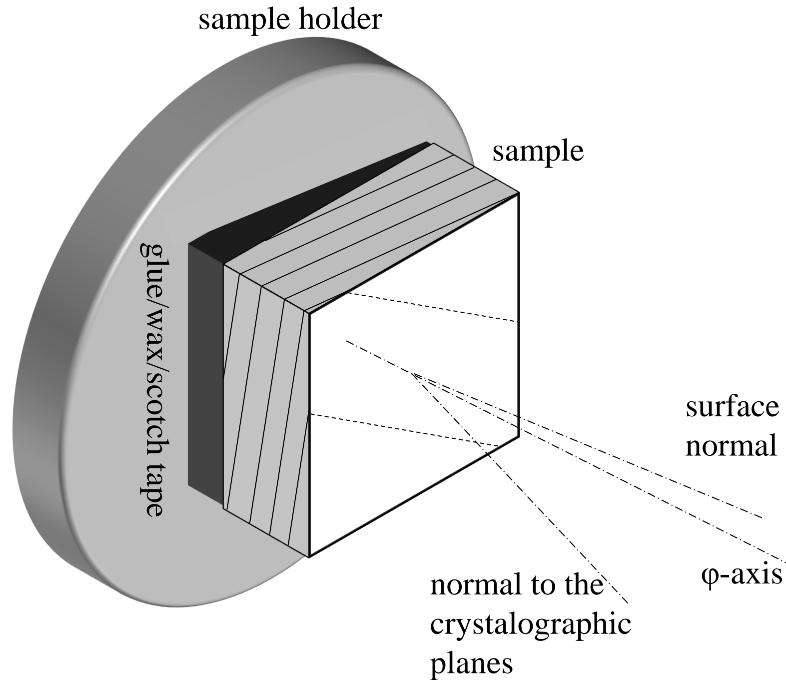

Figure 4.6: Difference of the ϕ-rotation axis and normals to the sample surface and to the crystallographic planes nominally parallel to the surface. The tilt of the crystallographic planes (miscut) is exaggerated.

olution in 2θ is definitely smaller than 0.0030° (obviously from the primary beam measurement). The intensity is distributed only along the Crystal Truncation Rods (CTRs), which are infinitesimally thin in theory. In measured data, they seem to be thicker according to the resolution of the instrument. The smallest step of the ψ and ϕ motors are 0.01°. Fortunately, the relatively high axial divergence of the primary beam and the high axial acceptance of the crystal analyser guarantee that such motors steps are sufficient for the alignment.

4.2.2 Relation between angular and reciprocal space

Let us now connect the angular space $(\alpha_\mathrm{i}(\equiv\omega), 2\theta, \phi)$ with the reciprocal space (Q_x, Q_y, Q_z) which is native for the crystallography. The length of the scattering vector $\boldsymbol{Q}$,

$$|\boldsymbol{Q}| \equiv Q = \frac{4\pi}{\lambda}\sin\theta \,, \left(\theta \equiv \frac{2\theta}{2}\right) \,, \tag{4.1}$$

is given by the diffraction angle 2θ and wavelength. It is for all our laboratory measurement the wavelength of the copper $\mathrm{K}_{\alpha1}$ radiation:

$$\lambda = 1.54056\,\text{Å} \,. \tag{4.2}$$

The coplanar diffraction makes thing much easier because the azimuth of the sample ϕ corresponds to the rotation of the reciprocal space along the axis identified with the normal to the sample surface. For the certain convenient azimuth ϕ, let us define the Q_x axis being in the direction of the incident beam and the Q_y to be perpendicular to the diffraction plane. Now, we can forget the

ϕ and the Q_y for a while, and we can introduce the bounding between spaces $(\omega, 2\theta)$ and the cut in reciprocal space (Q_x, Q_z):

$$Q_x = Q\sin(\omega-\theta) = \frac{4\pi}{\lambda}\sin(\theta)\sin(\omega-\theta)\,, \tag{4.3}$$

$$Q_z = Q\cos(\omega-\theta) = \frac{4\pi}{\lambda}\sin(\theta)\cos(\omega-\theta)\,. \tag{4.4}$$

The Jacobian of the transformation from the angular coordinates (ω, θ) to the Cartesian coordinates (Q_x, Q_z) in reciprocal space is

$$|J| = \frac{2\pi}{\lambda}\sin 2\theta\,. \tag{4.5}$$

The differentials $\mathrm{d}Q_x$ and $\mathrm{d}Q_z$ express the position change in reciprocal space caused the infinitesimally small step in the angular space:

$$\mathrm{d}Q_x = \frac{4\pi}{\lambda}\left[\sin\theta\cos(\omega-\theta)\mathrm{d}\omega + (\cos\theta\sin(\omega-\theta) - \sin\theta\cos(\omega-\theta))\,\mathrm{d}\theta\right]\,, \tag{4.6}$$

$$\mathrm{d}Q_z = \frac{4\pi}{\lambda}\left[-\sin\theta\sin(\omega-\theta)\mathrm{d}\omega + (\cos\theta\cos(\omega-\theta) + \sin\theta\sin(\omega-\theta))\,\mathrm{d}\theta\right]\,. \tag{4.7}$$

If we want to change the coordinate system due to the change of the azimuth ϕ, it would be related to this system as

$$Q'_x = Q_x\cos\phi\,, \qquad Q'_y = Q_x\sin\phi\,, \qquad Q'_z = Q_z\,. \tag{4.8}$$

The control software allows to perform the ω-, 2θ-, and $\omega/2\theta$-scans. Their paths through the reciprocal space are depicted in Figure 4.7 for several different positions, i.e., diffraction maxima of GaAs where the scans can be performed. In the same figure, we can see that not all of the (hkl) diffractions are reachable. It is obvious that some points of the reciprocal lattice are more distant from the origin than the maximal possible length of the scattering vector, e.g., GaAs(-4-46). Another limitations comes from the coplanar geometry and the fact that incident, nor the diffracted beam cannot go through the thick non-transparent sample (Brag diffraction geometry). For instance, GaAs (333) cannot be reached in coplanar geometry because the diffracted beam would be directed deep into the material. These conditions define the borders of the area achievable are in reciprocal space (see Figure 4.7).

In case of the ω-scan, we measure the intensity during the ω-motor constant movement, and all other motors are motionless. The diffraction angle is kept constant, therefore, the path of this scan through the reciprocal space is always the arc centred at the origin of the reciprocal space. In fact, we watch beams with the exit angle changing in opposite way as the incidence angel changes with ω.

Unchanged position of the 2θ-motor settle the condition $\mathrm{d}\theta = 0$ in all points of the scan, which applied to Equation 4.6 and Equation 4.7 gives the direction of the scan in a certain point in the reciprocal space. The direction is fully defined by the

$$\frac{\mathrm{d}Q_x}{\mathrm{d}Q_z} = -\tan(\omega-\theta)\,. \tag{4.9}$$

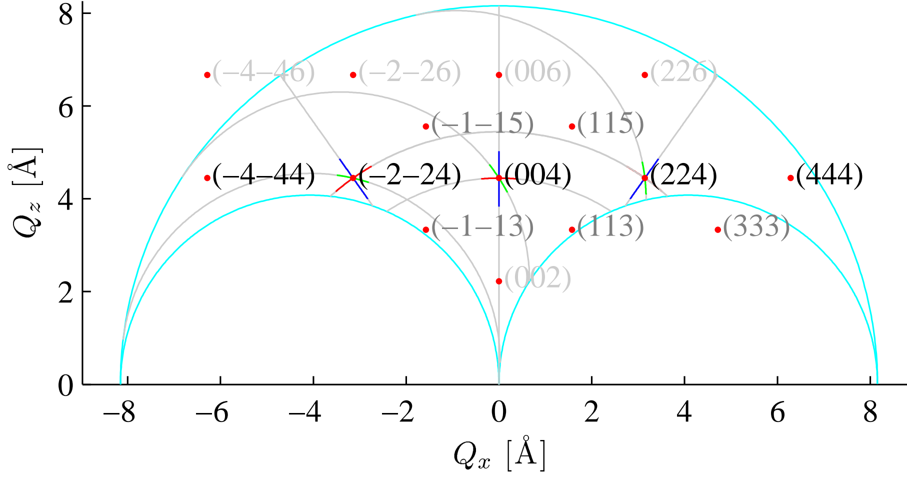

Figure 4.7: Cut through the reciprocal space. Some points from the reciprocal lattice of GaAs are plotted by the red points (orientation: $(110)||Q_x$ and $(001)||Q_z$). The labels of the lattice points are coloured with respect of diffraction type: the strong (black), the intermediate (dark grey), and the weak (light grey). The cyan arcs limits the space reachable with the diffractometer (Bragg geometry). The bigger arc is limitation due to the longest achievable scattering vector. The smaller arcs on the left and the right correspond to the lowest incidence angle and the lowest exit angle of the beam, respectively. The ω- (red), 2θ- (green) and the $\omega/2\theta$-scans (blue) with range of 10° are plotted through the diffractions (-2-24), (004) and (224). The grey elongating curves are these scans in full possible range.

The 2θ-scan keeps the constant incidence angle of the approaching x-ray beam while the arm with the detector is constantly moving (2θ-motor). From Figure 4.7, it can be viewed that the path shape of the 2θ-scan strongly depends on the ω value. From the condition $\mathrm{d}\omega = 0$, we can similarly to the previous derive the direction of a tangential vector of the path in the reciprocal space

$$\begin{aligned}
\mathrm{d}Q_x &= \frac{4\pi}{\lambda}\left(\cos\theta\sin(\omega-\theta) - \sin\theta\cos(\omega-\theta)\right)\mathrm{d}\theta \\
&= \frac{4\pi}{\lambda}\left(\cos\theta\sin(\omega-\theta) - Q_z\right)\mathrm{d}\theta\,, \qquad (4.10)
\end{aligned}$$

$$\begin{aligned}
\mathrm{d}Q_z &= \frac{4\pi}{\lambda}\left(\cos\theta\cos(\omega-\theta) + \sin\theta\sin(\omega-\theta)\right)\mathrm{d}\theta \\
&= \frac{4\pi}{\lambda}\left(\cos\theta\cos(\omega-\theta) + Q_x\right)\mathrm{d}\theta\,. \qquad (4.11)
\end{aligned}$$

Easily, we can express this tangential direction in the extremal points for the lowest exit angle of the diffracted beam (a condition $2\theta = \omega$) and for the longest

diffraction vector corresponding to the backscattering (a condition $\theta = \frac{\pi}{2}$):

$$\mathrm{d}Q_x|_{2\theta=\omega} = 0\,, \qquad \mathrm{d}Q_z|_{2\theta=\omega} = \frac{4\pi}{\lambda}\mathrm{d}\theta\,, \tag{4.12}$$

$$\left.\frac{\mathrm{d}Q_x}{\mathrm{d}Q_z}\right|_{\theta=\frac{\pi}{2}} = \tan(\omega)\,. \tag{4.13}$$

Sometimes, it is useful to imagine the tangential direction of the 2θ-scan when we plan the maps measurement in the vicinity of symmetrical diffractions as they are measured quite often (a condition $\omega = \theta$):

$$\left.\frac{\mathrm{d}Q_x}{\mathrm{d}Q_z}\right|_{\omega=\theta} = -\tan\theta \tag{4.14}$$

During the $\omega/2\theta$-scan both motors ω and 2θ are moving with a constant speed, but the second one is two times faster as the first one. The value of so called *offset* (between both motors) defined as the $\omega - \frac{2\theta}{2}$ is preserved during the motion. Both angles of the incidence and the exit are increasing with the same rate. This produces the path in the reciprocal space being the straight line which is going through the origin if it is elongated. The inclination of this straight line from the Q_z-axis is equal to the $\omega/2\theta$ offset. This follows from the condition $\mathrm{d}\omega = \mathrm{d}\theta$:

$$\frac{\mathrm{d}Q_x}{\mathrm{d}Q_z} = \tan(\omega - \theta)\,, \qquad \omega - \theta = \text{const.} \tag{4.15}$$

The special case of this scan is for the zero $\omega/2\theta$-offset which is called symmetrical $\omega/2\theta$-scan or $\theta - 2\theta$-scan. Its path is identical with the Q_z-scan going through the origin, it differs only by the non-equidistant distribution of measurement points in the reciprocal space.

From chapter 2, we know that we are interested in the intensity distribution along the CTRs, parallel to the Q_z-axis. From Figure 4.7, it is clear that except of the symmetrical diffractions (here $00l$), located on the Q_z-axis, we are not able to measure along CTRs using the previously described basic scans. For such cases, there is implemented a suitable scan in the control software. The Q-scan allows to measure intensity along straight line in the reciprocal space with equidistantly distributed measurement points. User has to move motors manually to positions corresponding to the centre of the desired line in reciprocal space. Then, the inclination with respect to Q_z-axis, the length and the step length in the reciprocal space has to be given to the control software. It calculates the sequence of the ω and 2θ positions corresponding to the measurement points and it measures along this linear path in step mode of the diffractometer. However, for the reasons explained below, we will use the different approach to measure the intensity distribution along the CTRs.

Let us say that because of some reasons discussed below, we want to measure the 2-dimensional distribution of the intensity in the reciprocal space (intensity map) instead of the Q-scan measurement that reveals the intensity only along straight line. We want to cover the area including the path of the rejected Q-scan. There are simulated paths of several two-axis measurements in Figure 4.8. For this illustrating simulation, let us assume that we have epitaxial layer on GaAs with the height of the unit cell about 1% larger. The lateral dimensions

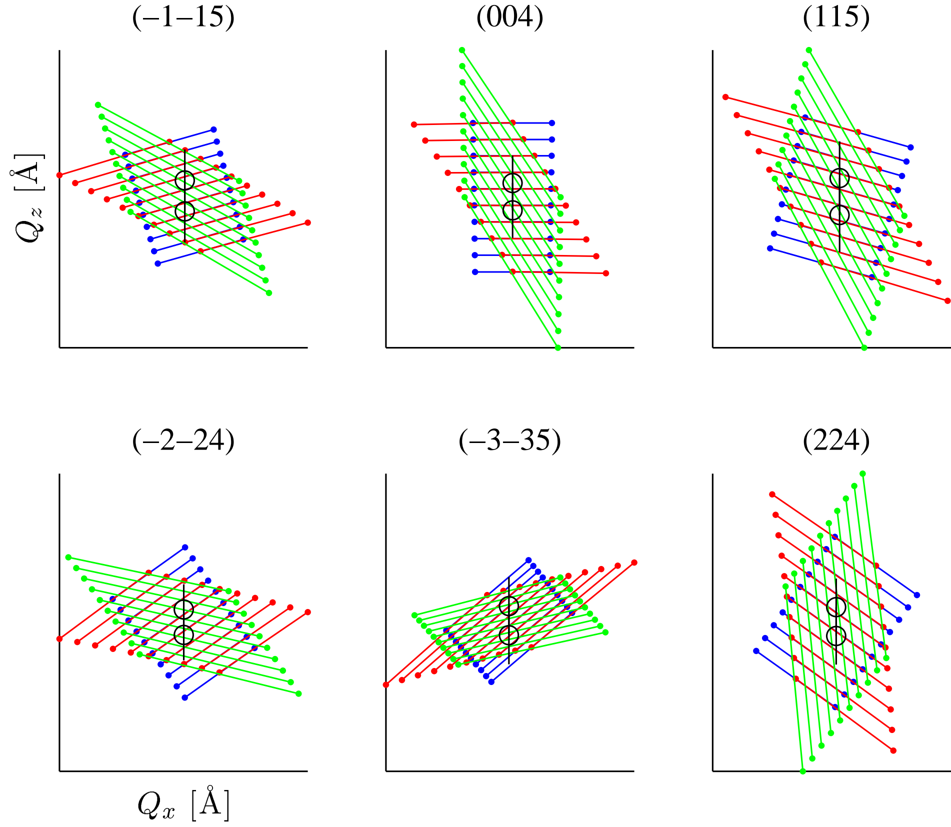

Figure 4.8: Simulated paths in the reciprocal space for a two-axis measurements in a vicinity of different diffractions. The black circles shows the substrate and the layer peak position. The black line indicates where the intensity to be collected is distributed. The coloured lines corresponds to the continuous line scans being run in the $(\omega, 2\theta/\omega)$-map (blue), $(\omega, 2\theta)$-map (red) and $(2\theta, 2\theta/\omega)$-map (green) measurement. There are no Q_x and Q_z values along, though the scaling of the axis was chosen to keep the units in both equal.

of the epilayer unit cell is identical with those of the substrate, obviously. The positions of the layer peaks are defined by $Q_z^{\text{layer}} = Q_z^{\text{GaAs(substrate)}}$ with the equal Q_x coordinates. Our task is to measure the intensity distribution along the CTR. We want the range in Q_z to be three times more than the distance of the layer/substrate peak. Usually, it is a sufficient range to see the thickness oscillations vanishing in the background.

For the simplicity, let us simulate an equally defined map measurement for several diffractions (asymmetric $(-3-35)$, $(\pm\pm 15)$ and $(\pm 2 \pm 24)$) and symmetric (004)). We have to remark that the azimuth of the sample is set with (110) direction being parallel the approaching x-ray beam with zero ω angle. Therefore, $(-|h| - |h|l)$ can be denoted as *grazing incidence* asymmetric diffractions whereas $(+|h| + h|l)$ as *grazing exit* asymmetric diffractions. This should be not confused with the expressions *grazing incidence/exit* used for very low incidence/exit angles. To show covering areas, we performed virtually

the measurement of the	$(\omega, 2\theta/\omega)$,	$(\omega, 2\theta)$,	and	$(2\theta, \omega/2\theta)$	-maps
running continuous	ω,	ω,	and	2θ	-scans with
defined ranges	$1.6°$,	$2°$,	and	$2°$,	controlled
by the 2nd axis	$2\theta/\omega$,	2θ,	and	$2\theta/\omega$	within
the range of	$4°$,	$4°$,	and	$4°$.	Results are
plotted by the	blue,	red,	and	green	colour lines

in Figure 4.8, respectively. The angular steps are not important for the illustration.

One can see that maps cover the different areas in the reciprocal space. Their shapes differ, as well, due to the different tangential direction of the scans in the positions of various diffractions as described above. It is necessary to use large ranges for both the continuous scans and the control scans to fulfil the condition of containing desired part of the CTR. Obviously, there would be mostly the background in such measured maps. Useful information would be only in very small measured points and such a measurement would be extremely time consumptive or time wasteful.

The simple solution is obvious, we can decrease the area of the map, but we can measure more of those maps in various positions to cover the demanded area in the vicinity of the CTR. Anyway, we have to choose the best combination of the continuous/control scanning axis to obtain a convenient shape of the resulted map, as closer to the ideal rectangular shape with one side parallel to the Q_z-axis as it is possible. Then, we can run several such map measurements, whose result are to be merged into one map that can be possibly trimmed to obtain a regularly shaped intensity map.

For the user's convenience, the control software allows to create so called user *batches* that is the sequence of pre-defined measurement scans and the commands for the motors movement to the desired position. This allows to pack the measurement of several maps into one job executed by the control software automatically. It also allows to run iterative loops capable to increment any of the motors positions and to repeat the measurement scan. This leads to the possibility to measure the high number of maps almost automatically if we are able to define wisely the movement of the motors in between. The extreme case but the most effective approach is to measure only line scans with certain small (unfortunately uniform) movement of the motors in the loop.

After the finished measurement scan, the control system move the motors to the positions corresponding to those just before the measurement. This defines the centre of the measured scan, as well. Let us say that we demand the small movement along the CTR. This formulates the condition $\mathrm{d}Q_x = 0$, which substituted into Equation 4.6 bounds together the movement of the main motors as

$$-\sin\theta\cos(\omega-\theta)\mathrm{d}\omega = (\cos\theta\sin(\omega-\theta) - \sin\theta\cos(\omega-\theta))\,\mathrm{d}\theta\,. \tag{4.16}$$

The length of the scattering vector Q is always incremented with the increasing Q_z along the path parallel to the CTR. We express the dependence of the step $\mathrm{d}\omega$ using the change of 2θ-motor as

$$\mathrm{d}\omega = \left(1 - \frac{\tan(\omega-\theta)}{\tan\theta}\right)\mathrm{d}\theta\,. \tag{4.17}$$

There is a practical obstacle that the ratio $d\omega/d\theta$ changes along the movement, which cannot be included in a batch loop. We have to set a certain value of this ratio to be constant for all iterations of that loop. However, if we measure very small area in the reciprocal space where the variation of the motors position is very small, the calculated ratio is nearly constant. Therefore, if we use the constant ratio calculated in the central point of the interesting area, the curvature of our path is quite small. If there is any, it can be compensated by the range of the continuous measurement scan. The range can be now definitely much smaller than for two-axis measurement. Such a loop measurement produces the intensity map covering the narrow strip around the CTR.

Similarly to the simulated paths in Figure 4.8, we simulated the path corresponding to the loop measurement described above. Again, the continuous measurement scan is the same for all diffractions, and it is ω-scan with range of $0.8°$. Inside the loop, the 2θ-motor moves within the range of $4°$ with a constant step. The step in ω direction is given by the expression in Equation 4.17 calculated in the central point of the desired map. The simulated paths are shown in Figure 4.9 together with previously two-axes measurements simulations for the comparison.

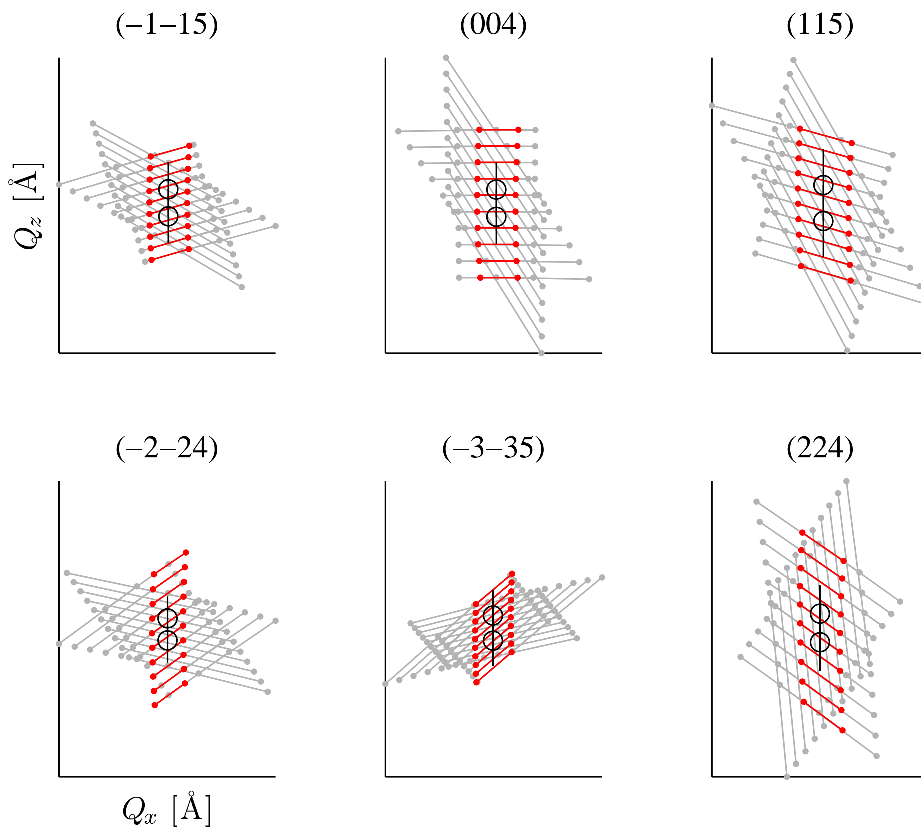

Figure 4.9: Simulated paths in the reciprocal space for the iterative batch measurement in a vicinity of different diffractions. The black features have the same meaning as in Figure 4.8. The red lines correspond to the continuous ω-scans being run in the iterative batch. The grey lines corresponds to the same two-axis measurements showed in Figure 4.8.

We can see that here we can control the shape of the measured area in contrary

to two-axis measurements. The length of the strip along the CTR is defined just by the range of the 2θ-motor. The width of the strip is tunable through the range of the continuous measurement scan. It can be decreased significantly to measure only the area where the detectable intensity is expected. The most convenient type of a continuous scan has to be selected, i.e., the scan with the local tangential direction perpendicular to the CTR as much as possible.

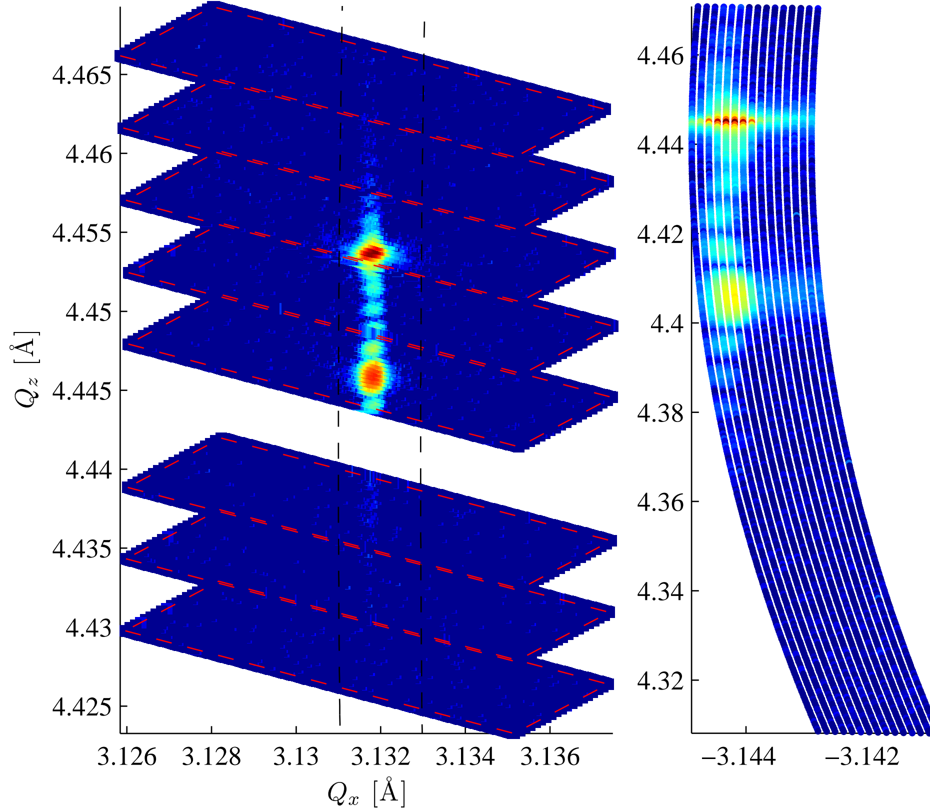

Figure 4.10: Comparison of the real experimental intensity maps for the merged multiple two-axis measurement (on the left) and for the loop batch measurement (on the right). The vicinity around Ga (224) was measured for different samples of (Ga,Mn)As on the GaAs substrate. The intensity expressed by the colour is in a logarithmic scale. The red dashed lines indicates the borders of individual maps being merged. The black dashed lines show the shape of the right map being shifted and scaled onto the left map.

Figure 4.10 compares the real experimental data obtained by two different approaches described above. First, several $(\omega, 2\theta/\omega)$-maps being measured shifted along CTR are merged to the resulted intensity map. Second, the $(\omega, Q_z^{\mathrm{pseudo}})$-map is reconstructed from plenty of ω-scans being also shifted inside the loop.

4.2.3 Snakes in reciprocal space

The theory says that in case of absence of any diffuse scattering all diffracted intensity is distributed along the infinitesimally narrow CTRs. We are interested just in the coherently scattered waves. Any diffusively scattered intensity is

assumed to be small and moreover included in the constant background. Since, it should be sufficient to measure line scans along these CTRs. Usually, this is possible if we are able to manipulate with the motors with steps at least as fine as the virtual CTRs finite width given by the resolution function. In such a case, the correct measurement along the CTRs is just a question of the proper sample adjustment and the precise direction of the line scan in the reciprocal space.

The final resolution is affected mainly by several factors. The analyser in front of the detector defines the angular acceptance of the detector in high resolution mode. It is very sensitive to the direction of the registered beam in the diffraction plane (horizontal) because it coincides with the plane where the diffraction on the analyser crystal is assumed. However, the beams being slightly deviated in the axial direction, i.e., having some wave-vector component perpendicular to the horizontal plane, still fulfil the Brag condition on the analyser crystal and they can pass through. Another broadening of the resolution function comes from the non-zero horizontal divergence and relatively high axial divergence of the primary beam.

For our diffractometer, the smallest possible steps of ω- and 2θ motors, being $0.0001°$ and $0.0002°$, respectively, are sufficient to move continuously across the CTR. And it is sufficient to see that the virtually finite width of CTR is several tens of the motors smallest steps (in FWHM). This can be observed in our measurements (see, for instance, Figure 4.10 or Figure 4.12). However, there is an apparent discrepancy between our observations and expectations arising from the theory. We measured whole intensity maps in the vicinity of several diffractions for several samples. We visualise some of those maps in Figure 4.11. No matter if they are recalculated to the reciprocal space, the intensity seems to be distributed not along straight CTRs, but the intensity maxima coming from the thickness oscillations follow some zigzag path looking like snakes laying along the CTRs.

We are not aware of any theoretical reason for such zigzag paths whereas this happens for all samples and the periodicity of these path deformation is related rather to the position in the reciprocal space, i.e., motors positions. And, it is independent on the samples, therefore, we adhere that it can be ascribed to the instrument imperfectness. For unchanged sample mounting, the deformed shape of the intensity distribution is perfectly reproducible. We presume that it is a result of going just to the limits of the motors. The quite high resolution makes the truncation rods virtually very narrow, then the motors are not able to reliably follow them. Only several smallest steps of the motors is enough to pass across the CTR.

It does not matter if the cause is in the imperfectness of the motor encoders or the non-reliability of the stepper motors themselves. We just want to eliminate its influence on the collected data. Figure 4.12 shows the typical measurement of the intensity distribution around the CTR. Although the highest intense maximum corresponding to the substrate and the second most intense maximum belonging to the epitaxial layer lay on the same straight line, the thickness oscillations are partly out from this line.

The distributed intensity is virtually shifted from the CTR in the direction perpendicular to that CTR. It is impossible to follow this zigzag path instantly during the measurement, but we can measure a whole map. As we are interested

just in the intensity distribution along the truncation rod, we can make projection of the intensity to the CTR, i.e., the integration of the registered intensity with respect to Q_x-axis. This projection corresponds to the meaningful diffraction curve.

On the other hand, if we measure just line scan intended to go along CTR, we miss several times the CTR during the zigzag movement along that. The measured map is formed by the multiple line scans relatively shifted to each other, therefore, we can extract single line scan from the map. The difference between the projection and the single scan is demonstrated in Figure 4.12. Some thickness fringes in that line scans are less intense. Sometimes, it may change the shape of the diffraction curve significantly. If we miss the layer peak during the scan, the data would not be reliable pretending the smaller intensity of the layer peak and the interpretation will give the unreal results.

It is obvious that using the single line scans for the diffraction measurement, in case of our instrument, is not reliable enough. The zigzag path of the scan

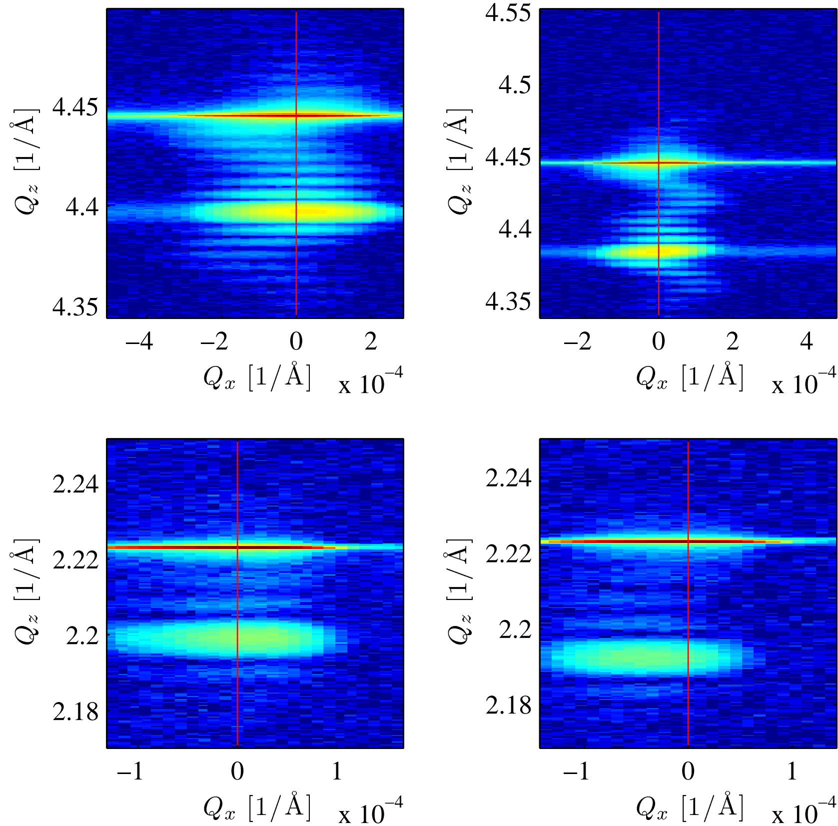

Figure 4.11: Measured intensity maps in the reciprocal space for two different samples (left and right insets) in the vicinity of the two different diffraction maxima ((002) in the bottom and (004) in the top insets). The red straight lines are guide along the path claimed by the diffractometer to be $Q_z(\equiv \theta/2\theta)$-scans. This illustrates that some intensity is missed during the line scan measurement. However, the deformation of the CTRs is only virtual. Just, the path of the line scan is deformed and it is not straight line in the reciprocal space.

in the reciprocal space is unpredictable. This is the reason why we thoroughly described the reciprocal space map measurement of atypically narrow maps in the Q_x direction covering the vicinity of the truncation rods. Projection of these maps to the Q_z-axis can be considered as the diffracted curve which can be used for the data interpretation via the fitting of the simulated diffraction experiment.

There are other two relatively easy approaches that can bring back the single line scan measurement back into the game. Both are based on the virtual broadening of the truncation rods to avoid the danger of missing it during the scanning motor movement. Firstly, we can increase the divergence of the incident beam by using different Bartels monochromator. Let us say the monochromator with asymmetrically cut crystal where the diffraction takes place on the planes not parallel to the surface, e.g., *asymmetric* Ge(220) Bartels monochromator in our diffractometer. Unfortunately, in our case this broadening showed to be not sufficient.

Secondly, we can increase the angular acceptance of the detector to cover a

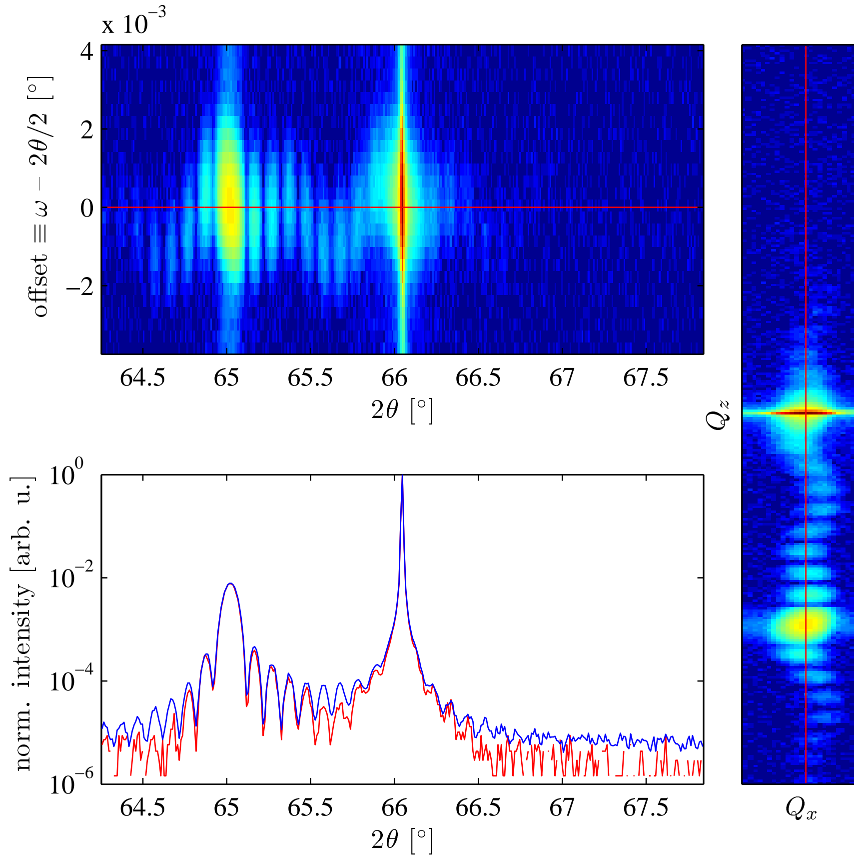

Figure 4.12: The measured intensity map in the vicinity of the symmetrical (004) diffraction in the angular space (left upper inset) and in the reciprocal space (right inset). The diffraction curve can be obtained by the projection of the measured intensity to Q_z-axis or by the extraction of the intensity along $Q_z(\equiv \theta/2\theta)$-axis denoted by the red straight line. The projection (blue curve) and the extracted Q_z-scan (red curve) both normalised are compared in the left bottom inset. The difference is apparent just from the intensity maps, the red line obviously does not follow the path with the highest intensity.

wider strip elongated along 2θ-direction in the reciprocal space. However, we would like to collect the intensity in the strip elongated along Q_x, i.e., perpendicularly to the Q_z-scan direction, but this is not possible. Then the angular acceptance has to be tuned in such a way that we still collect the intensity from the truncation rod, even we are not going perfectly along it. Concurrently, it cannot be so much wide to cover too large part of the CTR in the Q_z direction. It would lead to the broadening of all features in the diffracted curves, in other words, the instrumental function would be too large. For instance, the thickness oscillations would be smeared out from the diffraction curve then.

The technical realisation of this concept is problematic because we can hardly tune the analyser crystal to achieve the higher angular acceptance in 2θ. Then, the analyser crystal, which provides the detector with real angular resolution, can be replaced by the receiving slit with a desired window size in the horizontal plane. This size defines the angular acceptance, but another inconvenience arises. Now, the detector is not purely angular resolving. It collects the intensity of all beams that can pass through the receiving slit into the active part of the detector. The source of the diffracted radiation (the sample) is not point-like. Since, its finite dimensions affect the angular acceptance as well as the slit size.

Figure 4.13 compares the diffraction curve around (004) (Ga,Mn)As/GaAs maxima obtained by the map projection and the single scan (map extraction) with the diffraction curves measured using the open detector with receiving slits of various slit size. One can see that the single scan with the analyser crystal undervalue the intensity of the thickness fringes. We performed the Q_z-scans along the truncation rods with the open detector and the receiving slits, labelled $1°$, $1/2°$, $1/4°$, $1/8°$ and $1/32°$. These labels correspond only to the slits size with respect to the sample/detector distance. And therefore, it is only a very approximative angular acceptance. From these demonstrations, it follows that correctly selected receiving slit can lead to the equal diffraction curve as that one obtained by the map projection. On the other hand, measurement with largest slit size of the receiving slit produce the diffraction curve significantly different. In that diffraction curve, the substrate peak keeps its broadness as in other measurements, but the whole diffraction curve seems to be underlain by the very broad peak centred on the substrate peak position. It seems that all features (peaks) in the curve have changed shape with slowly decreasing tails and that one broad peak can be ascribed to those tails of the substrate peak. The convolution function which can allow to transform the reliable diffraction curve obtained by the map projection into this curve is completely unclear. Obviously, it is desirable to avoid such measurements with too large slits size. Unfortunately, there is no guide for the selection of proper slit size and it will definitely differ for the measurement in different locations of reciprocal space. All in all, such a line scan measurement has to be finally verified redundantly by the regular map measurement.

Let us see how this approach works with some asymmetrical diffraction maxima, for instance, (224) (Ga,Mn)As/GaAs. Figure 4.14 demonstrate such measurements. The upper centred inset shows the diffraction curves measured in the grazing incident/exit coplanar geometry. Both curves (red and magenta) were obtained from the reciprocal space maps projection depicted on the left and right of the inset. It is not surprising that both curves equals except for the scale and

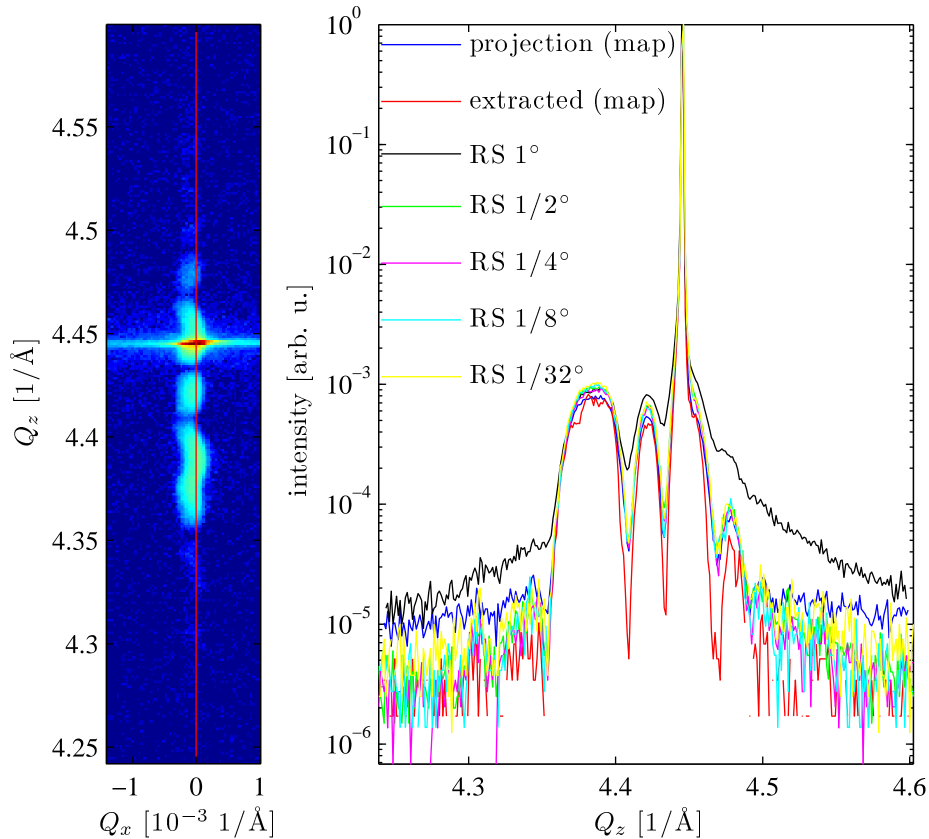

Figure 4.13: The measured intensity map of the symmetrical (004) diffraction shown in the left inset allows to synthesize the corresponding diffraction curve by its projection of intensity to Q_z-axis.Or, it is possible to extract the Q_z-scan going through the substrate maxima (red line in the map). These diffraction curves are compared with the Q-scans measured with the open detector with various receiving slits (right inset). The inserted receiving slits are labelled RS with the very roughly approximative width of the slit in the angular space.

noise obviously. To increase the statistic of the measured points we can merge both curves (blue points) and the result (blue curve) is to be compared to the line scan measurements obtained by the open detector with various receiving slits.

The line-scans measured in grazing incident coplanar geometry ($\omega < \theta$, in our notation $Q_x < 0$) exhibit similar behaviour as the diffraction curve in Figure 4.13 obtained with the largest slits size. The features in the vicinity of the substrate peaks are smeared out by the tails of the substrate peak profile for any slit size. Moreover there is some parasitic peak (streak) on the right side of the substrate maximum.

On the other hand, the diffraction curves obtained in the grazing exit coplanar geometry ($\omega > \theta$, in our notation $Q_x > 0$), are very close to the desired profile of the map projection. Here we can see the uniform broadening of all peaks and details for the measurement with the larger slit size because the narrow diffracted beam is registered by wider window in the certain 2θ range. For the smaller slit size measurement, the substrate peak is very sharp and the thickness oscillations are pronounced very well. The sharpness of the thickness fringes in case of the

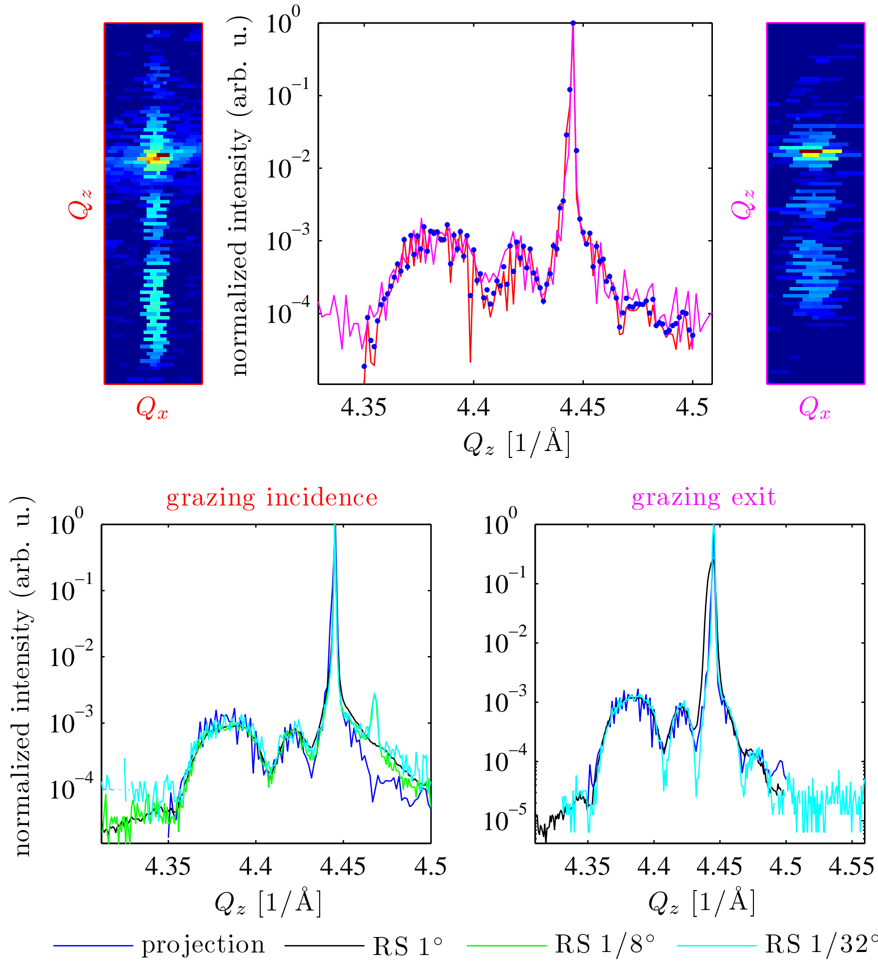

Figure 4.14: The comparison of the measurement asymmetric diffraction (224) in the grazing incidence (red) and exit (magenta) coplanar geometries. The projections of the measured maps (left and right top insets) in both geometries are compared in the central top figure, the normalized diffraction curves are corresponding as it is expected. The blue points represent the diffraction curve synthesised by merging both projection to get a better statistics. This curve is compared with the Q-scans measured with open detector with different receiving slits.

map projection is worse due to the higher step-size of the map measurement.

The grazing exit arrangement has two substantial advantages, the beam impacts the sample with the high incident angle, which allows to use the large beam size in both directions and it whole hits the sample. On the other hand, the diffracted beam leaving the sample has very small cross section in a horizontal direction, i.e., the sample appears being a point-like source from the view of the detector and the angular position of the detector better corresponds to the angular direction of the registered beam, which is more desirable for open detector arrangement.

Let us compare the measured diffraction curves with open detector for the symmetric (004) maximum and asymmetric (224) maximum in both grazing ex-

it/incidence geometries. If we recall the paths of 2θ-scans in the reciprocal space depicted in Figure 4.7, we can note that a smearing is as more manifested as the tangential direction of the 2θ path is more inclined from the CTR. The open detector integrates the intensity along the 2θ path in the approximative range controlled by the slit size. It seems to be more advantageous that tangential direction to be at most parallel to the CTR as it is possible.

Conclusion

We thoroughly described the diffractometer with its optical elements. We showed several ways how to measure the diffraction curve that is the intensity distribution along CTR. The relations between the motors positions and positions in the reciprocal space were clarified. Finally, we discussed the experimental obstacle due to the imperfectness of diffractometer motors.

However, we can say that the meaningful diffraction curve can be obtained by the map measurement with successive projection of the registered intensity to Q_z-axis. The other way how to reach the same data is the line scan measurement along CTR with the open detector. But, the appropriate slit size has to be chosen, unfortunately, its dependence on the position in the reciprocal space is rather unclear. And therefore, the results are not reliable if they are not confronted with the map measurement.

Chapter 5

Interstitial density determined by HRXD

In this chapter, we demonstrate our method of the interstitial density determination described in chapter 3. We used the etching-enhanced annealing with short annealing times to achieve inhomogeneously distributed interstitial atoms in the epitaxial layers, as well. The inhomogeneous density profile of interstitials is manifested in the x-ray diffraction data by the change of the shape of diffraction curve. Just this, we observed for one such sample.

Firstly, we describe the samples under investigation and their evolution due to the surface cleaning or the annealing. Further, we introduce the experimental data that are measured by the procedure thoroughly described in chapter 4. Using the theory from chapter 2 supplied by the structural model from chapter 3, we describe the numerical procedure for the experimental data fitting. Finally, we discuss the results of that fitting.

5.1 Samples

All samples were prepared in the Institute of Physics, ASCR, by the MBE method. The etching, annealing, and magnetometry measurements were performed there, as well. The samples stemmed from the same wafer. The (Ga,Mn)As layer with 100 nm of nominal thickness and Mn content of 14% was grown on undoped GaAs buffer with a thickness of 150 nm. The buffer was deposited on a GaAs(001) semi-insulating substrate 0.5 mm thick, the (001) planes are parallel to the surface. The deposition was performed by the MBE method. The buffer layer was grown just for the smoothing of the possibly rough substrate, and it should not differ from the material of the substrate. Therefore, it is not possible to recognize the buffer layer. We consider the samples only as epitaxial (Ga,Mn)As layers on the GaAs substrate.

After the deposition, the wafer was cleaned in Oxygen plasma and HCl acid, and it was cleaved into several parts. We had a chance to study two of those parts (denoted as A and B). The first one we labelled the *as-grown* control sample A-1 with a Curie temperature below 6 K. The second part stemmed from the same wafer was annealed in air for 24 hours at 160°C. This sample, with the Curie temperature increased to 142 K, we denoted as B-1. After the characterization by the HRXRD the results indicated, as described below, that not all

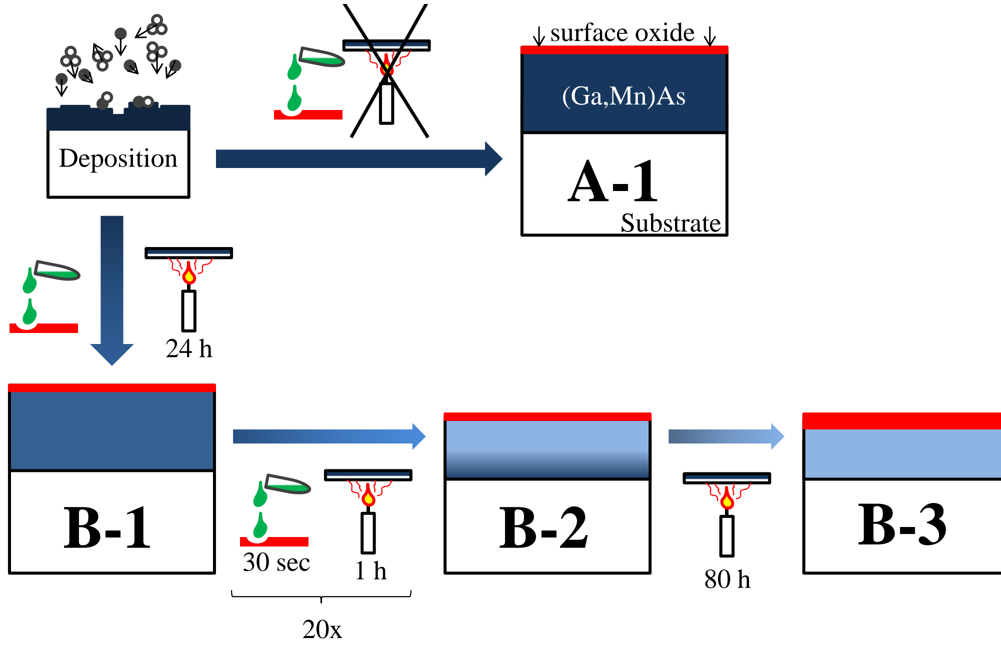

Figure 5.1: Schematic description of the samples. We assume that each etching makes the epitaxial layer thinner, and each annealing decrease the total amount of interstitials in the sample and makes thicker the surface oxide.

of the interstitial Mn atoms diffused out during the annealing. Most likely, the passivation of the surface by Mn oxide inhibited the diffusion process. To make evident that the remaining Mn interstitials in the epitaxial layer are still mobile, the sample B-1 was rinsed in HCl for 30 s to remove the surface Mn-rich layer and subsequently annealed at 160°C for one hour. This cleaning-annealing procedure was performed 20 times, and the resulted sample we label as B-2. After the HRXRD characterization, which showed the inhomogeneity of the interstitial density profile, we annealed it for 80 hours at 160°C without any preceding surface cleaning to demonstrate the homogenisation of the layer again (labelled as B-3). The evolution of the samples is schematically depicted in Figure 5.1. Table 5.1 summarizes the samples again.

5.2 Measurement

We performed HRXRD measurement on the samples A-1, B-1, B-2 and B-3 in order to determine the particular densities of the interstitials ($c_{\mathrm{int,As}}$ and $c_{\mathrm{int,Ga}}$) and possibly their depth dependence.

All measurements were performed in three steps, firstly the samples A-1 (Figure 5.2) and B-1 (Figure 5.3) were measured. The data for each sample were collected for one sample mounting in a limited time in order obey the planned x-ray machine-time schedule. The one or two days long measurement was controlled by the automatic pre-programmed batch, which ran a map measurement around several selected diffraction maxima. The batch was able to automatically align the motors to centre the map onto the substrate peak, however sometimes, the aligning scans missed it, maybe due to the thermal instability of the sample and/or x-ray equipment. Therefore, some map measurements failed completely

Sample	preceded treatment	note
A-1	deposition, surface cleaning	as-grown sample, $T_C \approx 6$ K
B-1	deposition, surface cleaning, and annealing (24 h)	annealed sample, $T_C = 142$ K
B-2	$20 \times \big($surface cleaning (rinsed in HCl for 30s) and annealing (1 h)$\big)$	inhomogenous, derived from B-1
B-3	annealing (80 h)	homogeneity restored, derived from B-2

Table 5.1: Overview of studied samples A-1, B-1, B-2, and B-3. The annealing temperature was 160°C. The surface cleaning was performed by rinsing in HCl for a short time (≈ 30 s).

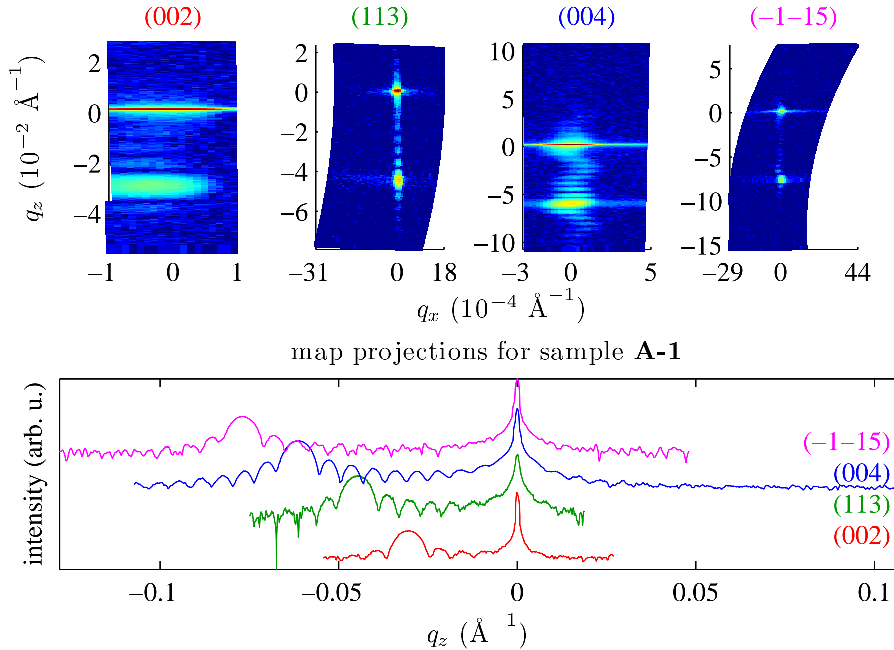

Figure 5.2: Measured data for sample A-1. Intensity maps for maxima (002), (113), (004) and (-1-15) were measured, the diffraction curves were obtained by the projection of the collected intensity to Q_z axis. The q_x and q_z coordinates are relative positions in reciprocal space relatively to the substrate peak position.

and there are no usable data from such measurements. We selected a combination of maps with unique $|h|$, $|k|$, and $|l|$. The measured maps were converted to the diffraction curves by the projection of the intensity to the Q_z-axis. We obtained four usable diffraction curves for both samples, consisting of strong (004), weak (002), and two intermediate asymmetric diffractions.

The first experiment has an aim to determine the interstitial densities testing the hypothesis that interstitial density decreases almost to zero after the annealing. The results showed that the total decrease of the interstitial concentration was rather small and the expectations of their total removal was not met.

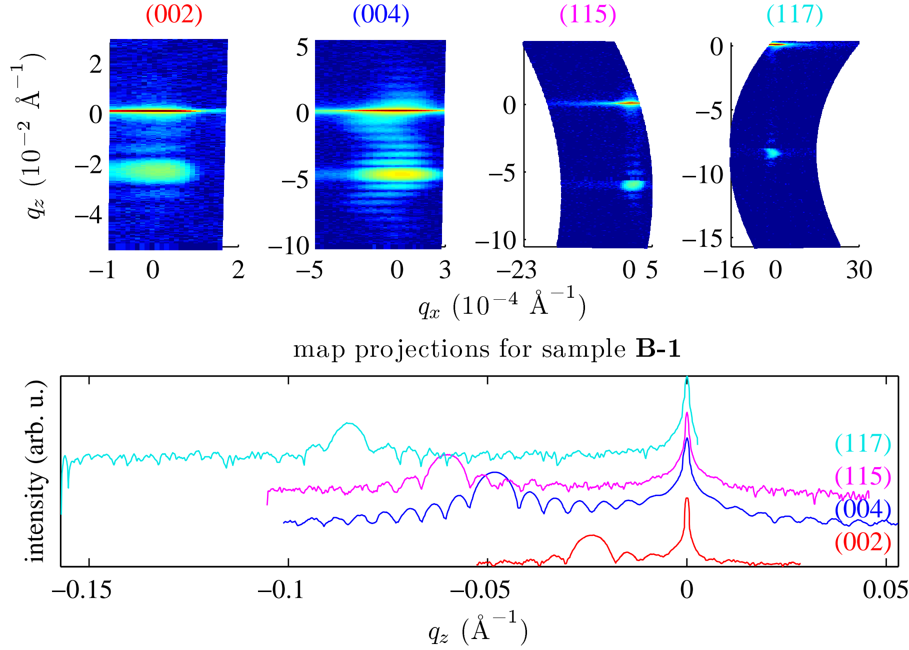

Figure 5.3: Measured data for sample B-1. Here the maps around asymmetrical diffraction (115) and (117) were successfully measured.

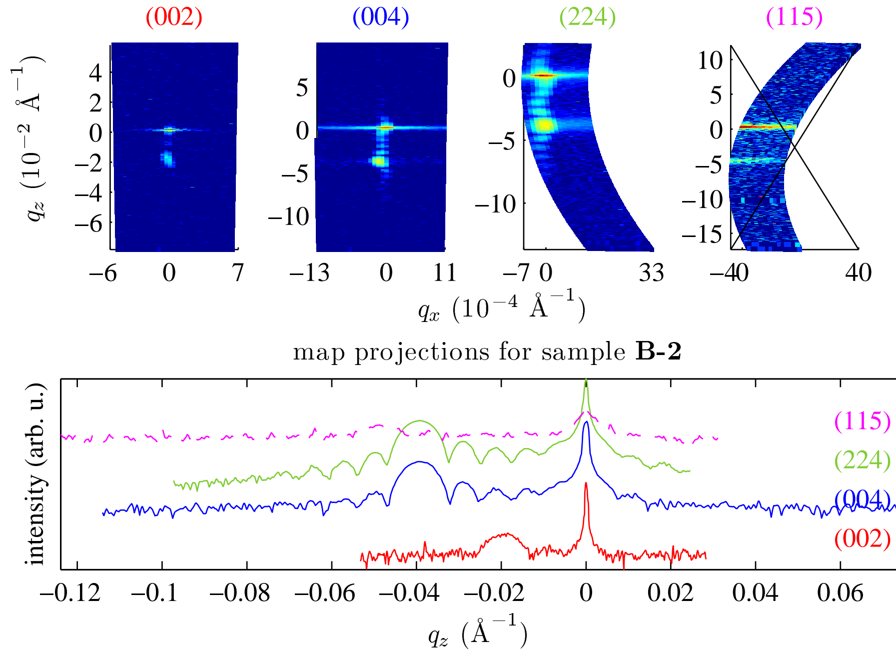

Figure 5.4: Measured data for sample B-2. Only three maps were successfully measured, the measurement around the (115) diffraction failed and its data are not usable.

Therefore, we extended our experiment for another annealing step. In order to withdraw as many interstitials from the layer as it was possible, we used the cyclical annealing combined with the etching described above. The etching ensured the decrease the influence of the surface onto an inhibition of the interstitials removal. Then, the sample B-1 underwent the cyclical etch-annealing procedure

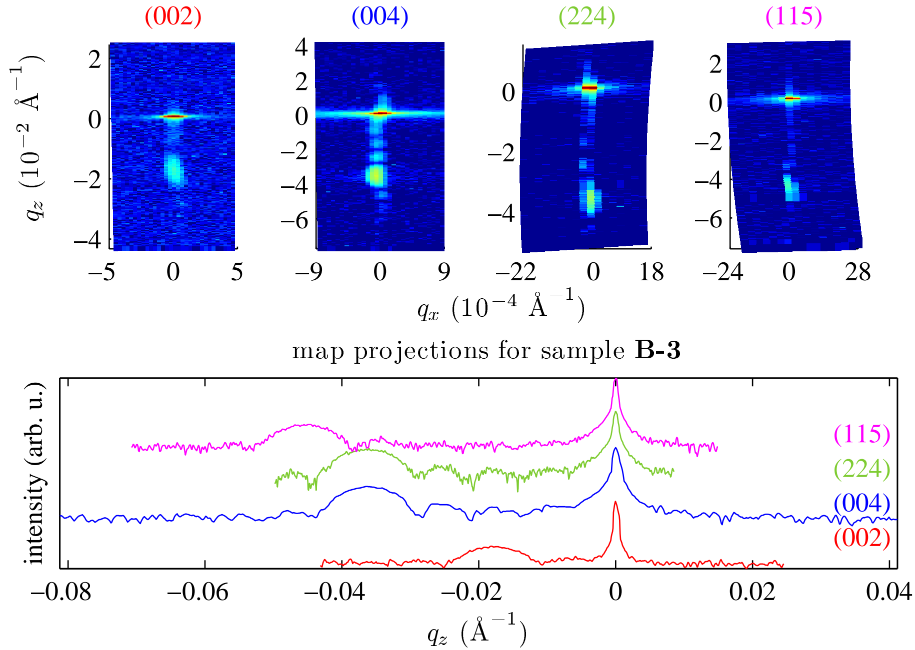

Figure 5.5: Measured data for sample B-3.

(B-1→B-2) changing to a sample B-2.

We changed a measurement strategy little bit to make the measurement faster because of limited time of x-ray machine. We kept the very important weak diffraction (002) in the measured set, but in order to measure more intense diffractions we used the symmetrical (004) and the asymmetrical (224) strong diffractions complemented by the one intermediate asymmetrical diffraction. The decision comes from the fact that the D-W factor plays important role in the right interpretation of the intensities and two strong diffractions carrying very similar information on the defect densities allows to stabilize the D-W factor optimization during the fitting procedure.

The intermediate (115) diffraction was chosen as a good compromise of three aspects. Firstly, its diffraction vector is relatively long, which is suitable for the D-W factor determination. Secondly, we expected the good intensity/noise ratio that we saw for the measurement of the first sample set. Finally, recalling the iso-intensity surfaces plot in the Figure 3.6, it carries more complementary information to the strong diffractions when comparing, for instance, with (117) diffraction.

We measured the selected intensity maps (Figure 5.4), but unfortunately, the measurement of asymmetrical (115) failed during that measurement session. We interpreted the data only from successfully measured maps bearing in mind that this could limit the ability of the defect densities estimation from the intensities. However, we were able to compensate partially this limitation by combining with the other samples measurements that we will describe later.

Several months later, the sample B-2 was annealed again without any surface treatment (B-2→B-3) and it was finally measured being labelled as a sample B-3. Four diffraction curves for (004), (224), (002) and (115) were acquired. The experimental data is plotted in Figure 5.5.

5.3 Data treatment and fitting procedure

The projection of the measured intensity map is not so straightforward as it seems. One has to realize that maps are formed by the plenty of continuous scans. And therefore, each point in the map corresponds to the intensity collected from the small area of the reciprocal space that is *not* a rectangle with the edges parallel to the $Q_{x(z)}$-axis, i.e., the points do not form the regular grid in the reciprocal space.

One has to split the q_z-axis into uniform bins which can be addressed by the coordinates of the measured point in the reciprocal space. The collected intensity in each point are summed in the appropriated bin, where the counts are normalized to the number of contributing points. Therefore, the width of the bins has to be large enough to be addressed by some points (theoretically at least one). If the width is too large, it leads to the smearing of the final curve. Anyway, the intensity points are due to the motors instability little bit shifted from their original positions (uncertain q_z) and together with the finite instrumental function it results in the broadening of the narrow features in the obtained diffraction curves. The thickness minima are slightly less shallow and narrow substrate peak is broadened, the intensity of its very top is not reliable. Therefore, we exclude the intense points of the substrate peak affected by this from the fitting, and such points are indicated in Figure 5.6.

The other artefact of the map projection is the increase of the noise. The noise is present in all measured points. If the q_x-range of the map is large, there are much more points contributing with the noise that its level can exceed the integrated signal. One has to decrease this range as much as it is possible just to eliminate the *snakes*(see in subsection 4.2.3), i.e., integrate only meaningful information.

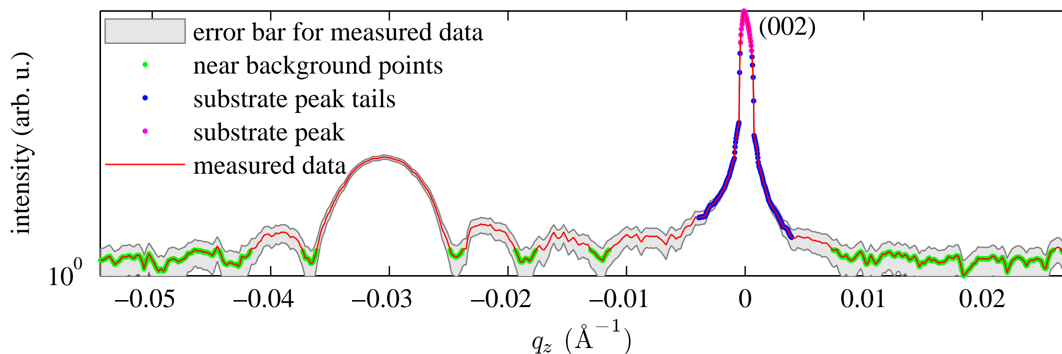

Figure 5.6: Diffraction curve with emphasised points having the different roles during the fitting procedure. Green points are close to the background signal and such data are intended for the background calculation. Magenta points correspond to the top part of the substrate peak, these points are excluded from the fit. Blue points define the substrate peak shape and they are used for the scaling factor calculation. Grey area represents the error bar of the measured data, i.e., the uncertainty of the measured intensity within the level 3σ. The whole measured diffraction curve is plotted in red colour.

The simulated diffraction curves following from the theory described in chapter 2 is normalized to the primary beam, i.e., the intensity is between 0 and 1.

For the comparison with the experimental data, one has to multiply the simulation by the proper scaling factor. The simplest choice seems to be to multiply it with the intensity of the primary beam, moreover, when the cross-section of the primary beam is small enough to hit the whole sample. Although it is not problem to measure the intensity of the primary beam, this usually does not lead to the obtaining of the reliable scaling factor. The agreement of the measured and the simulated substrate peak is only in the order of magnitude. The sample does not have to be perfectly flat, the beams with non-zero axial divergence can also participate on the registered diffracted signal and/or detected primary intensity.

The second very often used choice is to just fit the scaling factor during the fitting procedure as the free parameter or to calculate it using the least square method to get the best match of the simulated and the measured data. This approach is much more suitable as it does not rely on the experimentally measured primary intensity, which can produce some systematic error. The disadvantage is the instability of the fitting procedure, i.e., if we are not close enough to correct solution, the scaling factor can be completely wrong to satisfy the minimization of the χ^2. This can appear when the simulated layer peak has different q_z position comparing with the measured one. In such a case, the underestimated scaling factor decreases the χ^2, which complicates the move other parameters closer to optimal values.

To remove this instability, we focus on the features almost independent on the other parameters, and it is the shape of the substrate peak. From the assumption that simulated substrate peak should be identical with the measured one, we can calculate the scaling factor. This is valid if the layer peak is far enough from the substrate peak, i.e., it does not affect the substrate peak profile. If it is not true, then this approach degenerate to the scaling of the whole simulation diffraction curve onto the measured one, which is not wrong at all. In fact, the substrate peak profile is always changed by the presence of the thickness oscillations, but its variation is rather small.

In practice, we have to take into account that the very top of the measured substrate peak is not reliable due to the reasons mentioned above. On the other hand, the rest of the measured peak should match with the simulation. For the scaling factor calculation we use the region of the substrate peak with excluded point on the very top as it is depicted in Figure 5.6.

We can distinguish three different contributions to the measured signal. First one is the coherent scattering part that is just calculated in our simulations. The second one is the diffuse scattering, which is prevalent between the brag peaks. And here, in the vicinity of the Bragg peaks, it is being of unknown magnitude, but it is assumed to changing very slowly. Since, it can be included in the constant background as a constant contribution to the signal in all points of the particular diffraction curve. The third contribution can be ascribed to the noisy background radiation which is constant, as well.

We are searching for the constant representing the last two contributions to the acquired signal. Again, we have to choice to measure it or to fit/calculate it. The measurement should be far enough from the Bragg peaks not to see the coherently diffracted radiation, i.e., where the diffraction curve is constant. Usually, we do not measure as far since we are interested in the both peaks and their vicinity covering several other thickness oscillations.

The calculation of the background is analogous to the scaling factor calculation. We can use the whole range of the diffraction curve, which can bring the instability into the fitting procedure, or we can define such points where the coherently diffracted signal is low. Usually, such regions are borders of the measured q_z-range.

Following Chapter 15 in [119], we define the χ^2 function of N fitted parameters $p_1, ..., p_N$, scaling factor a and the background b as

$$\chi^2(a, b, p_1, ..., p_N) = \sum_j \frac{(af(x_j, p_1, ..., p_N) + b - y_j)^2}{\sigma_{yj}^2}\,, \tag{5.1}$$

where the parameters p (e.g., layer thickness, concentrations, D-W factors, instrumental function parameters) are used for the calculation of the simulated diffraction profile f. The measured profile is described by the pairs (x_j,y_k) which corresponds to the relative q_z position and measured intensity, respectively. The uncertainty of the intensity is expressed by the appropriate σ_{yj} values. The counting of the x-rays photons is the Poisson process that implies the σ being the square root of the measured counts (as measured, i.e., before any normalization). In order to fit the simulated curve to a measured data, we have to find optimal parameters to minimize the χ^2 value. We assume that such optimal parameters are the physical properties of the sample we want to determine.

Both discussed parameters, the scaling factor and the background, can be calculated separately after each calculation of the simulated curve in the fitting procedure. The form of the χ^2 allows to express optimal values of both parameters analytically using the least square method. For the minimal χ^2 should be its gradient equal to zero, therefore its component in a and b directions in the parametric space should be zero, as well:

$$0 = \frac{\partial \chi^2}{\partial a} = 2\sum_j \frac{af(x_j, p1, ..., p_N) + b - y)}{\sigma_{yj}} f(x_j, p1, ..., p_N) + b - y)\,, \tag{5.2}$$

$$0 = \frac{\partial \chi^2}{\partial b} = 2\sum_j \frac{af(x_j, p1, ..., p_N) + b - y_j}{\sigma_{yj}}\,. \tag{5.3}$$

This leads to the set of two linear equations, which can be solved each time the new simulated profile is calculated. Such a direct calculation of two unknown parameters effectively decrease the number of the fitted parameters and makes the fitting procedure faster.

Finally, let us remark that the sums goes every time over all relevant measured points, which generally should be *all* measured points. We mentioned above that not all of measured points are considered to be reliable (the very top of the substrate peak), such points should be excluded from the sum in Equation 5.1.

When we solve the set of equations 5.2–5.3, we can take into account that there are also some points that do not play any significant role in the first or the second equation, or eventually, we are undoubtedly convinced that they should not play any role. In other words the particular partial derivation of the sum over such points is (or should be) almost zero. Since, we can set this term to be zero from the definition doing no harm to the least square method principle. As a consequence, we can use for the sum in Equation 5.2 and Equation 5.3 just

those points that we dedicated for the calculations of the scaling factor and of the background, respectively. Such two distinct regions are depicted in Figure 5.6.

If we want to fit simultaneously M diffraction curves, we have to make clear how the appropriate χ^2 function should look like. Let us say that Equation 5.1 defines the individual functions $\chi_1^2(a_1, b_1, ...), ..., \chi_M^2(a_M, b_M, ...)$. Now we can define the merged χ^2 seemingly too generally as

$$\chi^2 = \sum_{m=1}^{M} w_m \chi_m^2, \tag{5.4}$$

where $w_1, ..., w_M$ are weights changing the importance of particular diffraction in the simultaneous fitting procedure.

There is no mathematical reason why these all weights should not be equal to one. In fact, the direct and statistically right choice is $w_1 \equiv ... \equiv w_M \equiv 1$, which changes the χ^2 to the simple sum. Then the importance of each point is given by its calculated uncertainty σ_y.

The question is what is the importance of the measured data that contain some essential information, but they are measured with a shorter counting time. This increases the relative uncertainty of all measured points. Or, if the data comes from a naturally weak intensity effect (e.g., a weak diffraction), the relative importance of such data are low comparing with the other. One can tune manually the weights to increase the importance of such data, but it is not clear how to set the weights. We suggest to set such optimal weights that the *goodness of fit* (particular χ_k^2 divided by the number of degrees of freedom) is the same for all individual fitted data (diffraction curve k). This formulates the demand that any diffraction curve are fitted as good as others. The change of the weights to fulfil this demand effectively changes the uncertainties of intensities of the particular diffraction curve. However, it is not easy and sometimes possible to implement this during-runtime changes of uncertainties into preprogrammed minimizing algorithms as in our case. Then, one has to change the weights manually again but now with the exact guide how to do it.

We formulated the recipe how to calculate the background and the scaling factor for the one particular diffraction curve fitting. This stays the same also for the simultaneous fitting of M diffraction profiles, the calculation of pairs (a_1,b_1), ..., (a_M, b_M) has to be performed separately for the appropriate diffraction curve. We can assume that the background which includes the diffuse scattering part differs for each curve. The scaling factor can differ as well due to some not properly corrected geometrical factors of the measurement and it is, in fact, the same reason why we do not use the measured primary intensity for the scaling factor. The substrate peak is a perfect reference for the scaling factor computation. Nevertheless, the different scaling factor correcting possible small misalignments of the sample/diffractometer should be random and should not show any tendency according to a diffraction vector length. If the values of the scaling factors follows the exponential decrease with a larger diffraction vector, it indicates the wrong Debye-Waller factor for the substrate and the scaling of the simulated curve brings the systematic error as a consequence.

We implemented the simulation procedures into the MATLAB software [120]. It is capable to fit several diffraction curves for several samples simultaneously. In order to achieve the maximal versatility of our program, we enabled to define

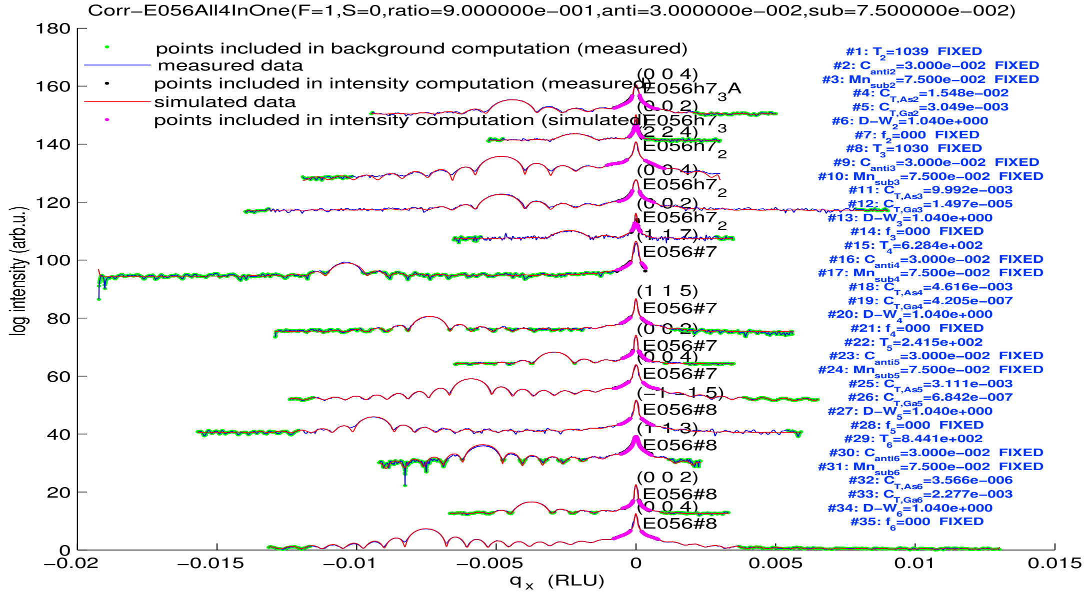

Figure 5.7: Graphical output during the fitting procedure for the demonstration. All diffraction curves for all samples are fitted simultaneously. There are 35 parameters (the blue text output on the right), some parameters of the model are shared between the samples, some parameters are just now fixed.

the sample as a stack of the arbitrary number of layers with the arbitrary number of pre-defined parameters. It allows to share some parameters (or whole model layers) between the different model samples as the simultaneous fitting has sense only if some fitting parameters are the same for the different diffraction curves and/or different samples. All properties of model samples are converted to the vector of parameters to be optimized. The output of the simulation being redirected to the minimizing procedure can be set in the form of χ^2 directly or it returns the vector of the measured and the simulated values to be evaluated by the minimizing procedure itself. We used both the MATLAB bult-in minimizing SIMPLEX algorithm [120] and the external script NLSQFIT [121] implementing the Levenberg–Marquardt method ([122]). For the demonstration, Figure 5.7 shows the output of a graphical interface reporting the best solution during the fitting procedure.

Considering the (Ga,Mn)As as the GaAs material modified by some defects, the *model layer* of GaAs is defined as a group of several parameters. Firstly by the thickness of the layer, but if the layer is the lowest one in the stack, it is considered to be a substrate, therefore its thickness assumed to be semi-infinite. Basic parameters defining the densities of the defect in the layer are c_{sub}, $c_{\mathrm{int,As}}$, $c_{\mathrm{int,Ga}}$ and c_{anti}. Besides this, our code is extended for the analogical (Al,Ga,Mn)(As,P) material modification.

Other options are related to the unit cell dimensions of the material. We can set the layer to be strictly epitaxial, when the lateral parameter is automatically taken from the layer below, or we can set and/or fit the relaxation of the unit cell. The vertical dimension of the unit cell is calculated using elastic constants for GaAs (which can be also changed/fitted for particular layer, if it is necessary). Of course we can ask the script to calculate the lattice parameter using the defect concentrations (possibly with arbitrary expansion coefficients) and the Vegard's

law for the Ga(As,P) modifications. The value of relaxed lattice parameter can be controlled directly by own parameter, which allows to separate the fitting of the position and the intensity of the layer peak.

An option is available switching on/off if the local distortion is considered in the calculation. The arbitrary repulsion factors can be given for the first and the second coordination sphere around particular defects.

The last parameter B is an exponential prefactor. The D-W prefactor for the pure GaAs strictly thermal we kept at the value $B_{\mathrm{GaAs}} = 0.595\,\text{Å}^2$ taken from Reference 123, although there is a quite large uncertainty in the range $0.5\,\text{Å}^2$—$0.8\,\text{Å}^2$ in the literature ([123–126]). We tested that this value well satisfies the exponential decrease of the substrate peak intensity with the elongating diffraction vector and therefore the scaling factor do not substitute the badly guessed D-W factor for the substrate.

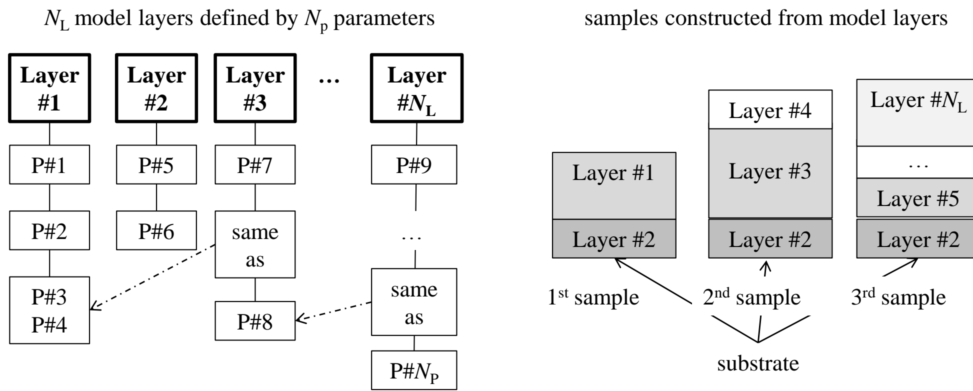

Figure 5.8: Schematic picture of a samples representation in the fitting program. The sample is stacked from the model layers, which are defined separately and independently on the sample. Samples can share some model layer (e.g., substrate) and layers can share some parameters (e.g., D-W factor). Some properties are defined by several parameters. The thickness for the lowest layer is omitted as it is assumed to be the semi-infinite substrate.

Any parameter can by connected with the other model layer, then its value is shared. Figure 5.8 schematically shows how the several model layers are predefined containing many parameters. For each diffraction curve simulation the sample is considered to be stacked from arbitrary number and order of those model layers.

To fit our experimental data we defined four samples with the same amount of the substitutional and anti-site atoms. The D-W prefactor value obviously correlates with other parameters in case of very small number of measured curves. One needs to have more measured diffractions with the significantly different diffraction vector length. Therefore we linked the D-W prefactor between all samples to be the same value, which allowed to cancel such a correlation. The higher number of the different diffraction vector lengths was available and the prefactor value had not to be arbitrary value to satisfy the fitting of just one sample. Of course this is given by the assumption that the mean squared displacement is the same in all samples, although we assume the different densities of the present defects in the same time, i.e., different disorder.

To justify our approach we have to say that firstly we fitted all data with the unique D-W prefactors for individual samples. The resulting D-W factors were very similar with larger fitting error than their differences. There were no tendencies to see the decrease of the mean squared displacements with the annealing, i.e., lower disorder with smaller amount of the defects. So the differences were interpreted as a random noise coming from the fitting. We fell that to approximate all samples with the same D-W prefactor (the same disorder) is the better solution, while there is not enough measured data to determine the unique D-W prefactors for all samples.

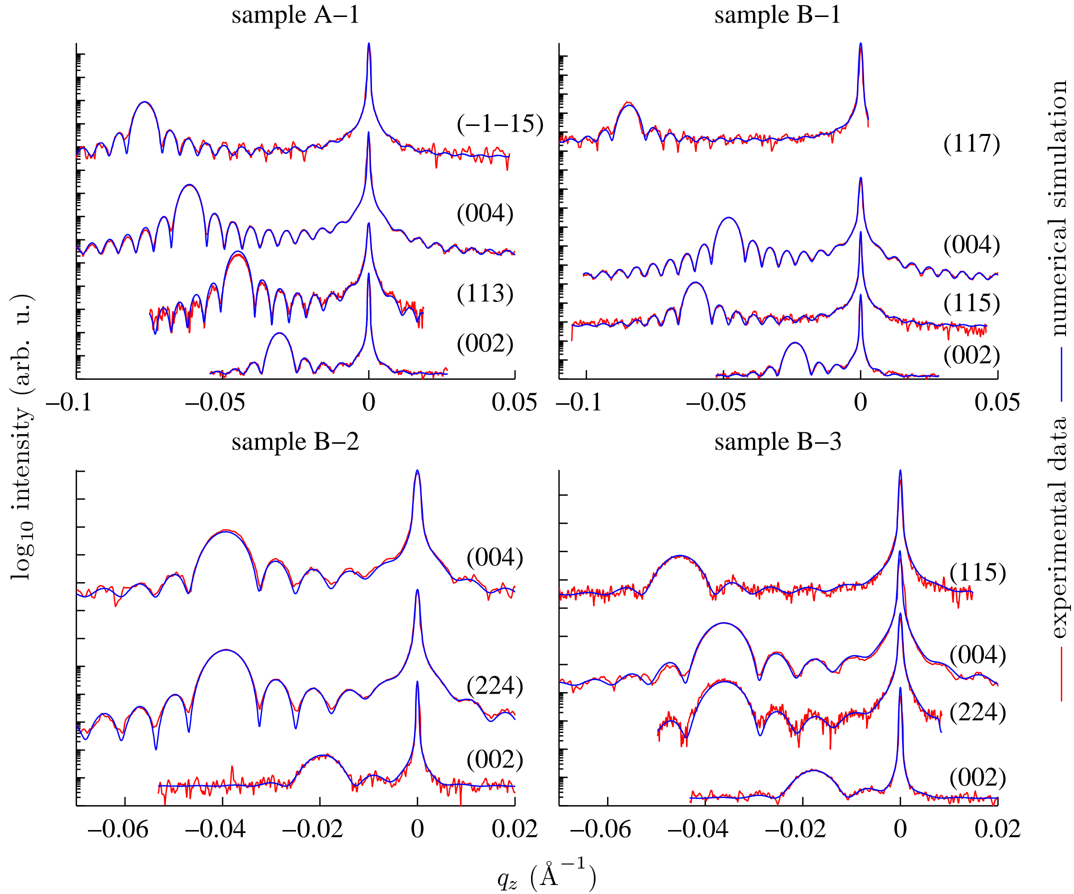

Figure 5.9: All measured diffraction curves (red) fitted with the numerical simulation (blue) for all samples. The substrate peak defines the origin of the relative position in the reciprocal space q_z. The curves are vertically shifted for the clarity.

The parameters of the layers were used for the calculation of the structure factors F_0, F_{hkl} and $F_{-(hkl)}$ as described in chapter 3. The diffraction curves are simulated according chapter 2 using the layer thickness, unit cell diameters and dielectric susceptibilities, which are related with structure factors via

$$\chi_{hkl} = -\frac{r_e \lambda^2}{\pi V_{\text{cell}}} F_{hkl} \tag{5.5}$$

where r_e is the classical electron radius and the V_{cell} is the volume of the unit cell.

5.4 Fitted experimental data

The final fitted experimental data are plotted in Figure 5.9. Firstly, we were not able to find the match of the simulated and the measured diffraction curves for sample B-2. Although the layer peak fitted quite well, the closest thickness oscillations to the layer peak had different intensities, i.e., the measured diffraction profile exhibited different asymmetry than that measured one. There was no chance how to control this asymmetry with the given parameters except considering the sample B-2 to be vertically inhomogeneous. This possibility seemed to be reasonable as the sample underwent the etch-annealing procedure, which could induce some inhomogeneity. We tried to model the (Ga,Mn)As layer with two stacked sublayers in order to decrease the number of fitting parameters. Those sublayers differed only by the interstitial density. Figure 5.10 compares the previous *single layer* solution with the model of the layers.

The other approach we tested was to model the layer by the stack of many sublayers whose densities would obey some analytic function (e.g, error function). We wanted to have the vertical profile of the densities distribution to be the smooth function not just by the step-like function represented by the two layer. Unfortunately, we failed to find the appropriate profile function with small amount of parameters, all attempts resulted in solutions which were not unambiguous. The data are not sufficiently good to allow such a profile fitting. The approximation of two homogeneous layers is the best description we can achieve from three measured diffractions.

Finally the χ^2 minimum was found for the $c_{\mathrm{anti}} = (0 \pm 1)\%$, i.e., the density of the anti-site defects is below one percent. Unfortunately, the c_{sub} correlated with other densities so strongly that we received practically the same χ^2 and identically fitted curves.

Obviously, the fitted particular interstitial densities are bounded with the c_{sub} value and we are not able to determine them all together from the fitted data. Therefore, we performed individual fits for the several fixed c_{sub} values, and just such result is plotted in the Fig. 5.11, i.e., the optimized $c_{\mathrm{int,As(Ga)}}$ values plotted with respect to arbitrary fixed c_{sub}. We observe that the fitted values are scattered along the straight lines with the dispersion corresponding to the experimental data quality. We can obtained the linear dependences by the linear interpolation of the fitted values.

Although we cannot determine the substitutional density, we can able to make qualified very rough estimation of its value. As we mention in chapter 1, it was not observed the c_{sub} density higher than 10% seeming that this is the maximal solution limit. From the Currie temperature of the sample A-1, we can deduce that the as-grown sample is almost compensated. Almost each two substitutional Mn atoms should be compensated by the one anti-site or the interstitials defect. Still, there should be some slight prevalence of the substitutional Mn atoms as there is magnetic ordering in very low temperatures. The total Mn concentration is estimated around level of 14% from the Mn flux during the deposition. This leads to a very rough estimation of the c_{sub} being somewhere between 7%—9%. This estimation was finally supported by the different experiment within the same sample (chapter 7), the concentration of the substitutional Mn was determined by anomalous x-ray diffraction method as $(8.2 \pm 1.1)\%$ [73].

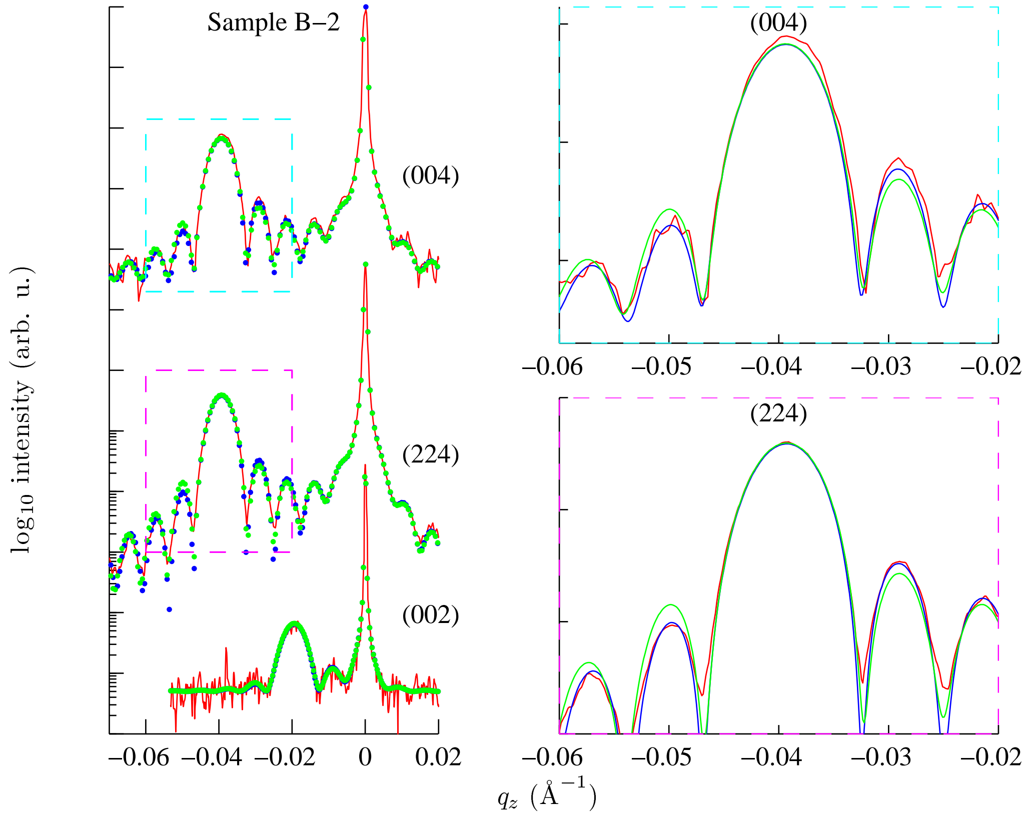

meaning of colours: experimental data simulation (1 layer model) simulation (2 layers model)

Figure 5.10: The experimental diffraction curves for sample B-2 (red colour). The numerical simulation was performed for the models with one homogeneous layer (green) and for two homogeneous sublayers (blue), as well. The curve profile around the layer maxima is asymmetric more than that corresponding to the single homogeneous layer. Model describing the epitaxial layer as two homogeneous sublayers is possible to follow such an asymmetry. The simulated diffraction curves are indicated by the points equidistantly along q_z in the left inset for the lucidity. The right insets are zoomed parts of the left inset defined by the dashed rectangles in appropriate colour. The minima of the thickness fringes are not so well pronounced as in simulations probably due to the convolution with instrumental function.

The range for the c_{sub} is quite large, even though we can estimate the other concentration with smaller uncertainty from the plotted dependence in Figure 5.11 taking into account the interval defined by the probable c_{sub} value. Within this interval of the interest we estimate the mean value of the particular interstitial densities together with the size of the corresponding uncertainty region, these quantities we define as the most probable values of $c_{\mathrm{int,As}}$ and $c_{\mathrm{int,Ga}}$ and their uncertainties, respectively.

Apparently there is a difference between the $c_{\mathrm{int,As}}$ and the $c_{\mathrm{int,Ga}}$ densities, which favours the Mn atoms sitting in the centre of the arsenic tetrahedron. Anyway, we can test the hypothesis saying that the energetic difference of both interstitial sites is too small to exhibit the prevalence of the occupancy of one particular site.

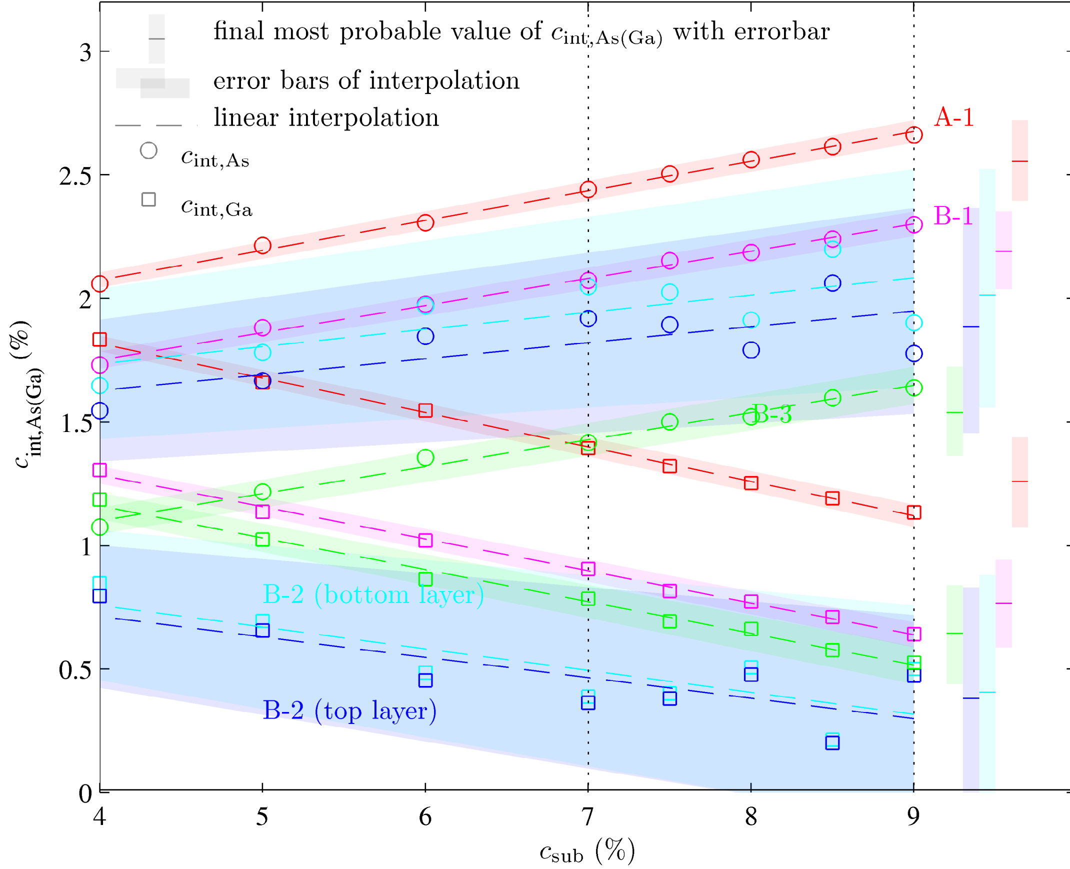

Figure 5.11: The optimized values of the interstitial densities resulted from the fit with fixed c_{sub} finished with practically the same χ^2 value. The optimized values of $c_{int,As}$ (circles) and $c_{int,Ga}$ (squares) are scattered around the straight (dashed) lines. The uncertainty of the linear interpolation is shown by the semitransparent areas with appropriate colour. The real value of the substitutional concentration should lie between 7 and 9 percent giving us the range of the interest in the plot. From this region we estimated the most probable values of the densities and their error bars that are depicted in the right part of the plot.

For now we can forget the estimation of the c_{sub} and let us optimize interstitial values for the fixed pairs of the (c_{sub}, c_{anti}). We repeated the fitting procedure for several pairs of fixed parameters forming a grid in a parametric space. Just only samples A-1, B-1 and B-3 were selected for this fitting for the better experimental data quality and the proved vertical homogeneity of the samples.

The Figure 5.12 visualises the dependences of the optimized interstitial densities on the c_{sub} for several fixed c_{anti} values. Still, the fitting favours the $c_{int,As}$ density for the higher c_{sub} concentrations. We can apply the condition that densities in both non-equivalent interstitial positions equals ($c_{int,Ga} = c_{int,As}$). This is valid for just for certain pairs (c_{sub}, c_{anti}) laying on the straight lines. This allows us to interpolate those lines obtaining the linear relation between such allowed values of c_{sub}, c_{anti}, $c_{int,Ga}(= c_{int,As})$.

We can plot the allowed triplets c_{sub}, c_{anti} and now $c_{int,Ga} + c_{int,As}$ points in a space of the fixed parameters (Figure 5.13). We know that c_{sub} and c_{anti} should

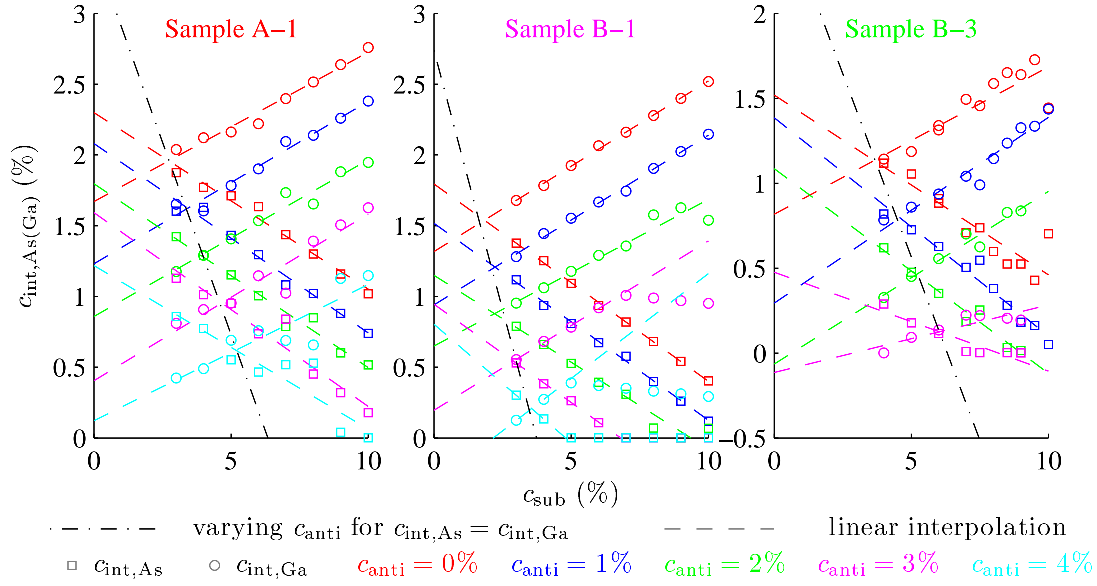

Figure 5.12: Interstitial density in both non-equivalent positions optimized for the fixed values of the substitutional Mn density and the anti-site defects density. Although the χ^2 decreases with the decreasing c_{anti}, the optimization was performed for its fixed several values. The optimal densities are linear function of the fixed c_{sub}. If the occupancies $c_{\text{int,As}}$ and $c_{\text{int,Ga}}$ were equal, the real values would lie on the dot-dashed interpolation line, in other words, the optimal densities $c_{\text{int,As}} \equiv c_{\text{int,Ga}}$ would be determined by the value of the (c_{sub},c_{anti})-pair.

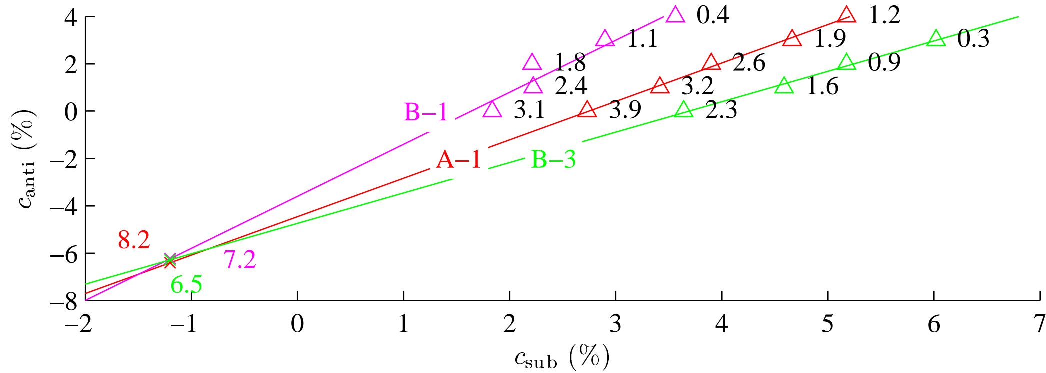

Figure 5.13: Allowed (c_{sub},c_{anti})-pairs fulfilling the condition $c_{\text{int,As}} = c_{\text{int,Ga}}$ for three samples following from the fitted simulations (triangular marks with numbers indicating the total concentration of the interstitials). If the occupancies $c_{\text{int,As}}$ and $c_{\text{int,Ga}}$ were equal, the optimal values would lie approximately on the interpolating (solid) lines. The samples should have the constant densities c_{sub} and c_{anti} because all of them stemmed from the same wafer. Then the interpolating lines should intersect in just one point (cross marks), moreover it should be in the point inside of the plot (in probable range of densities). This is not fulfilled, therefore the assumption of the equality is not valid. Coloured numbers shows the extrapolated total interstitial density for appropriate samples.

be the same in all samples as these defects are not affected by the annealing. So if the assumption $c_{\text{int,As}} = c_{\text{int,Ga}}$ was true, the interpolated (and possibly extrapolated) dependencies for all samples should intersect in just one point giving the real densities of the substitutional Mn and the anti-site defects and we would have known also the interstitial densities in all samples. Although the extrapolated dependencies more or less intersect each other in just one point, this point corresponds to the negative occupancies, which is apparently not possible.

As a conclusion we see that the interstitial site in the centre of the As tetrahedra are indeed preferred and this is valid for all measured samples.

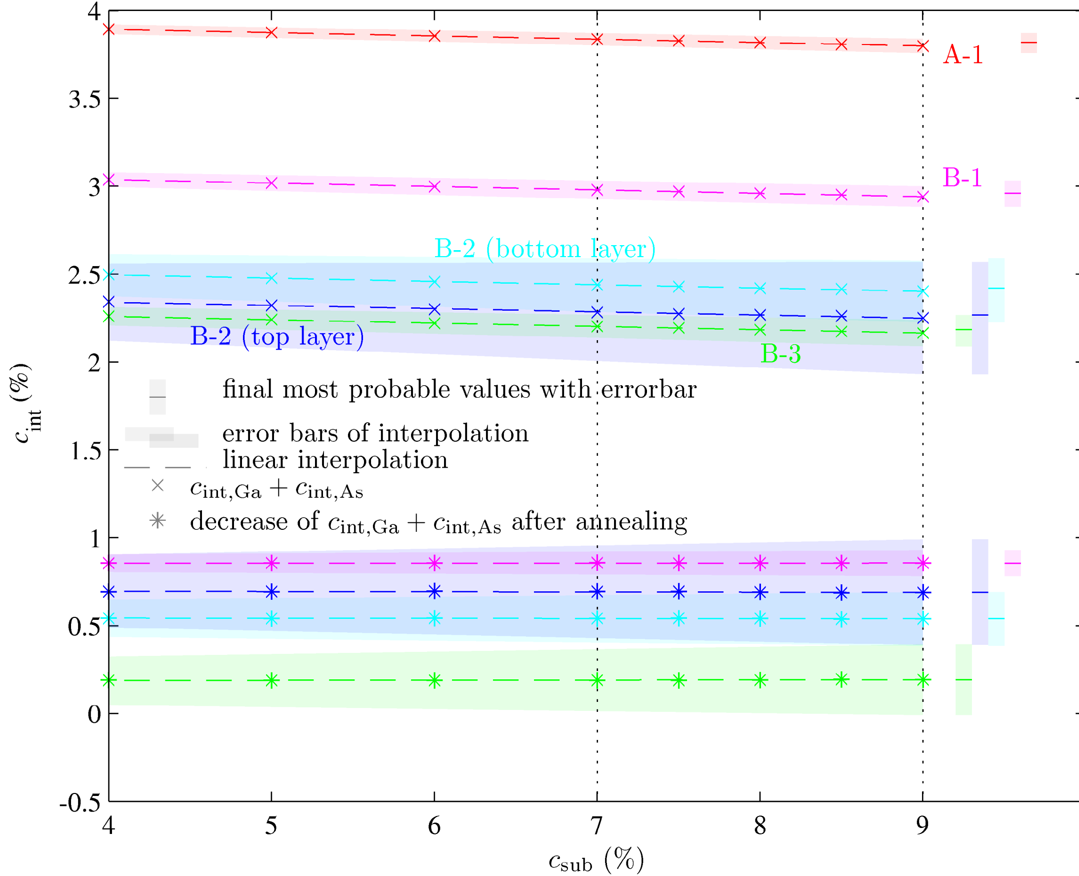

Figure 5.14: The summed interstitial densities $c_{\text{int,As}} + c_{\text{int,Ga}}$ (crosses) and their decrease (asterisks) after the annealing are displayed. The uncertainty (semitransparent areas) of the linear interpolation (dashed lines) is rather smaller due to the fact that these sums are controlled by the value of the lattice parameter due to the fitting procedure. The guessed c_{sub} between 7 and 9 percent allows to estimate the most probable values shown on the right.

Similarly to the obtaining of the particular interstitial densities, we can estimate the summed interstitial densities in all samples and their decreases after the annealing. Again, we plot the demanded quantities as a dependence on the fixed substitutional density, and from the rough guess of the c_{sub}, we can estimate the most probable values. This is done in Figure 5.15.

All previous calculations were done assuming the relation between relaxed lattice parameter of (Ga,Mn)As and the defect densities defined by Equation 3.2 derived in Reference 99. However, this is just only the theoretical prediction,

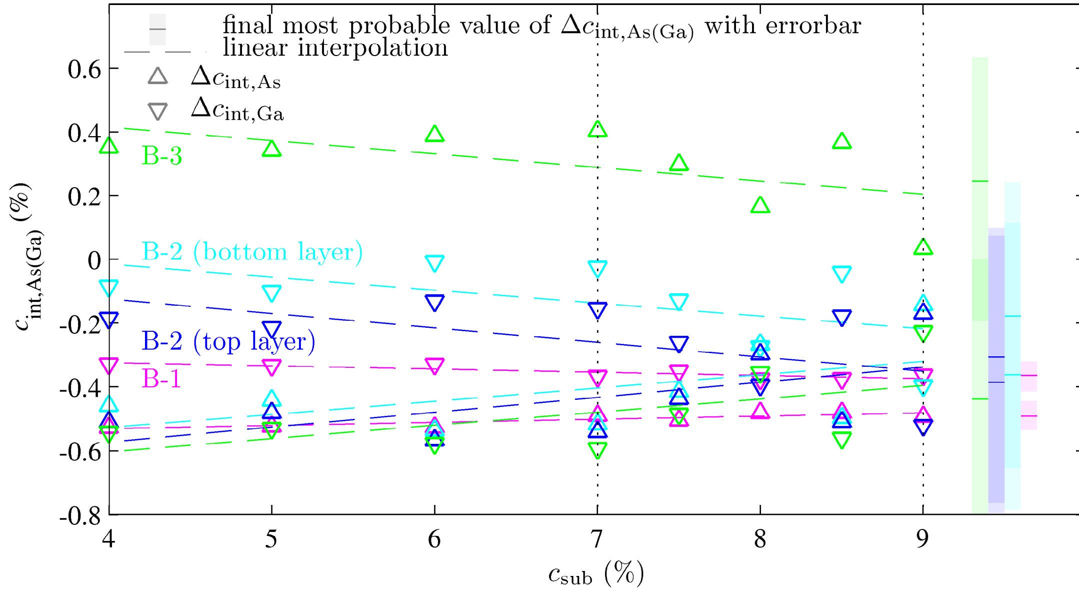

Figure 5.15: The changes in both interstitial densities ($\Delta c_{\text{int,As}}$ and $\Delta c_{\text{int,Ga}}$ plotted as triangular marks) after the annealing. The final estimated values coming from the c_{sub} guess are shown on the right. The uncertainty is small only for the A-1→B-1 annealing due to a better data quality.

which do not have to be necessarily correct. To leave this assumption we tried to separate the structure factor and the lattice parameter calculation, i.e., the layer peak intensity and the layer peak position should be no more connected. As the only one guide to calculate the lattice parameter is Equation 3.2, we have to make the lattice parameter to be the completely free and the independent fitting parameter, while everything other stays the same. As a result the lattice parameter is controlled only by the peak position and we obtain the mismatch of the relaxed lattice parameters of (Ga,Mn)As with respect to GaAs substrate.

Unfortunately, we experienced that the number of measured diffractions is too low and the data quality is not good enough to obtain reliable fit with the removal lattice parameter calculation. The parameters starts to correlate extremely with D-W factor and also the χ^2 minimum along the c_{anti} parameter is much more shallow which makes the uncertainty of the c_{anti} much bigger (up to 4%). In contrast to the previous case here the fitting procedure were able to find optimal parameters for the arbitrary values of the c_{sub} and the D-W prefactor.

We tried to repeat the fitting procedure for the several fixed values of c_{sub} and the fixed D-W prefactor optimized in previous approach. Of course, the sample B-2 was disqualified from such a final fitting procedure while the measured diffraction data (namely the number of diffraction) did not allow to find any reliable solution, in other words all parameters were correlated. We used the optimal values of the interstitial densities $c_{\text{int,As}}$ and $c_{\text{int,Ga}}$ from the previous approach as a starting point for the fitting with the free lattice parameter. Although it seems that there are several comparable local minima of χ^2 if we used the arbitrary starting points, the optimal values from these fits (denoted as $c^*_{\text{int,As}}$ and $c^*_{\text{int,Ga}}$) are very close to the previous results as it is shown in Figure 5.16. Moreover, it is sufficient to start with the comparable summed interstitial density to find the same χ^2 minima giving the same $c^*_{\text{int,As}}/c^*_{\text{int,Ga}}$ ratio.

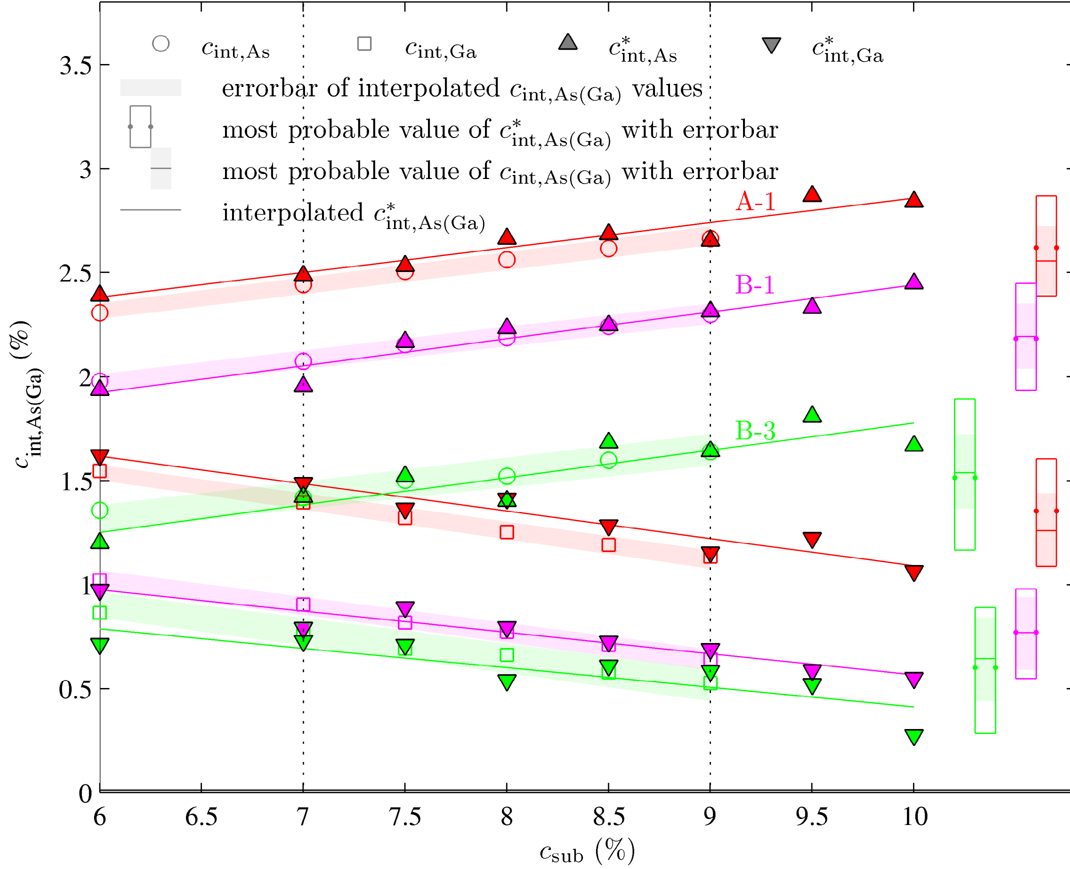

Figure 5.16: Comparison of the optimized particular interstitial densities obtained by the fitting procedure with lattice parameter calculation ($c_{\mathrm{int,As(Ga)}}$) and with the lattice parameter considered to be free and independent ($c^*_{\mathrm{int,As(Ga)}}$). Estimated final values using the c_{sub} guess are compared on the right.

Although this approach did not give us the reliable values due to the inadequate experimental data, it showed that the optimal values found with the lattice parameter condition are not in conflict with the approach neglecting the peak position. In other words, the applied condition for lattice parameter do not move forcibly the χ^2 minima systematically somewhere else.

The correlation of the interstitial densities with c_{sub} stayed similar, but there is one qualitative difference between those two approaches. Figure 5.12 indicates that the increasing fixed parameter c_{anti} drive both the particular interstitial densities to the lower values, which is obvious as the total lattice expansion has to be constant. In contrast, the optimized values $c^*_{\mathrm{int,Ga(As)}}$ tend get closer for the higher c_{anti}, if the lattice parameter constrain is removed, which is depicted in Figure 5.17. So it seems that for the higher content of the anti-site defects both approaches are not in agreement. And we assume that the more physical relevant approach is to avoid using the theoretically calculated expansion coefficients, although the lattice expansion due to the Mn presence seems to be estimated quite well. It is the expansion factor related to the anti-site defect, which forms serious doubts about its correctness. However, we have not sufficient experimental data to spare such a constraint, but at least for the low c_{anti} content expected in

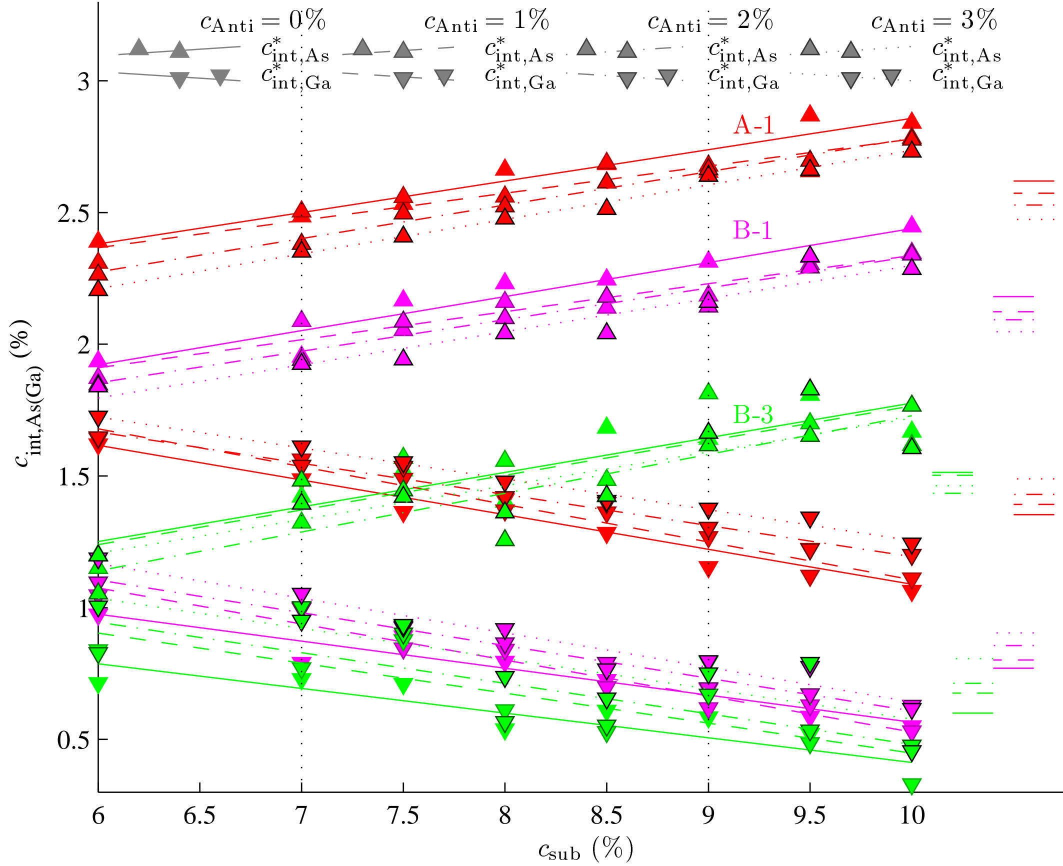

Figure 5.17: The comparison of the particular interstitial densities $c^*_{\rm int,As(Ga)}$ obtained from the fit with the fixed $c_{\rm sub}$ and several fixed $c_{\rm anti}$ parameters. The lattice parameter is free parameter not calculated from the concentrations, i.e., the layer peak position was fitted independently. The linear interpolation together with the defined range of the interest for $c_{\rm sub}$ allow to estimate the most probable values of the $c^*_{\rm int,As(Ga)}$. The results showed on the right exhibits the tendency to bring closer values of $c_{\rm int,As}$ and $c_{\rm int,Ga}$ with increasing fixed $c_{\rm anti}$ parameter.

rich Mn samples this leads to reliable values of the interstitial densities.

All obtained values are summarized in Table 5.2 for all samples. The vertical profiles of the summed densities are depicted in Figure 5.18.

The thickness parameter T results from the fit being controlled by frequency of the thickness oscillations. The decrease of the thickness for B-1→B-2 is apparently due to the etching for 20 times, the average decrease of the thickness due to the rinsing in HCl for 30 seconds was 0.8 nm. This value corresponds also to the difference between the thicknesses of the samples A-1 and B-1. Most probably, this is the thickness of a thin oxidized layer at the surface corresponding to the Mn-rich layer after annealing. On the other hand, there is another decrease of the thickness after B-2→B-3 annealing without preceding etching. Therefore, this decrease should be explained rather by the surface degradation (oxidation) during the prolonged time before the final annealing. The last decrease is smaller than expected, as well. Again this could be due to the surface change during the ageing of the sample.

Sample	A-1	B-1	B-2 top	B-2 bottom	B-3
T (nm)	103.9(2)	103.0(2)	87.0(2)		84.4(1)
			22(4)	65(4)	
$c_{\mathrm{int,As}}$ (%)	2.6(3)	2.2(3)	1.9(8)	2.0(8)	1.5(4)
$c_{\mathrm{int,Ga}}$ (%)	1.3(4)	0.8(3)	0.4(8)	0.4(9)	0.6(4)
$\Delta c_{\mathrm{int,As}}$ (%)		-0.4(1)	-0.3(7)	-0.2(8)	-0.4(7)
$\Delta c_{\mathrm{int,Ga}}$ (%)		-0.5(1)	-0.4(7)	-0.4(7)	+0.3(7)
$c_{\mathrm{int,As}} + c_{\mathrm{int,Ga}}$ (%)	3.8(2)	3.0(2)	2.3(6)	2.4(4)	2.2(2)
$\Delta(c_{\mathrm{int,As}} + c_{\mathrm{int,Ga}})$ (%)		-0.9(2)	-0.7(6)	-0.5(3)	-0.2(4)
$c^*_{\mathrm{int,As}}$ (%)	2.6(4)	2.2(5)			1.5(6)
$c^*_{\mathrm{int,Ga}}$ (%)	1.4(5)	0.8(4)			0.6(5)

Table 5.2: Determined parameters for all samples, the numbers in brackets correspond to the uncertainty of the last digit on the level of 3σ (equally to $\pm 3\sigma$). The c_{anti} concentration was estimated below 1%, the density of the substitutional Mn was guessed to be $c_{\mathrm{sub}} \approx (8 \pm 1)$%. For homogeneous samples A-1, B-1 and B-2 was successfully estimated the particular densities of interstitials with no assumption on the lattice parameter (denoted as $c^*_{\mathrm{int,As(Ga)}}$).

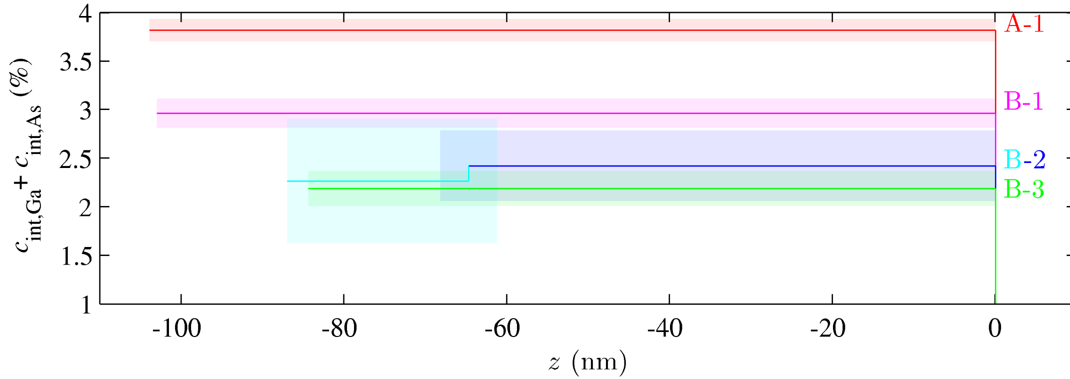

Figure 5.18: Depth profiles of the summed interstitial density determined for all samples. The uncertainty region is indicated by the coloured semitransparent areas around the most probable profile. The depth profile for the sample B-2 is estimated from the two sublayers model of the epitaxial (Ga,Mn)As layer.

Conclusion

We introduced the first set of (Ga,Mn)As sample. On them, we demonstrated the measurement and experimental data fitting. From the fitting procedure, we obtained the interstitial densities in both particular interstitial positions. We discussed the reliability of our approach and uncertainties of the estimated parameters.

In conclusion, we found that each annealing process decreased the summed interstitial density and the cyclical short annealing combined with the surface etching produced the inhomogeneous sample that was successfully modelled by the two stacked homogeneous sublayers. Unfortunately, those are the poorest experimental data for this sample with the highest number of free parameters,

which increased horribly the uncertainties of all determined parameters. Nevertheless the shape of the profiles depicted in the Figure 5.18 are given by the model being homogeneous or step-like function. Then one has to uncertainty interpret better as a vertical shift of a whole profile towards higher or lower densities.

The same is valid for the profile of the inhomogeneous B-2 sample, whose vertical profile is estimated by the step-like function. The uncertainty of the step height is much lower than it can be seemed from Table 5.2 as it was determined from the asymmetry of the thickness oscillation, i.e., just this step-like profile is the best solution with the uncertainty of the step height below 0.5%, the whole profile shift is uncertain much more. To avoid misinterpretation of the uncertainty region for the sample B-2 in Figure 5.18 one can assume the uncertainty of the shift being the larger height of both uncertainty regions.

Chapter 6

Surface Mn oxide evidenced by XAS

We decided to support our presumption that during the annealing the Mn-rich oxide layer within the surface is created, which is assumed to be responsible for a drawing of mobile interstitials from the layer. In order to show this, we measured XAS near Mn absorption edge using a grazing incidence surface-sensitive geometry.

The method is based on a measurement of the fluorescent radiation intensity when a sample is irradiated by the x-ray radiation with energy close to the absorption edge of certain element. In contrast to the fluorescence of the free atom, here the atom neighbourhood changes the shape of the absorption spectra. Moreover, if we set the incident angle of the primary x-ray beam close to the critical angle, we can tune the penetration depth and therefore we can see the depth dependence of this effect.

We introduce the second set of (Ga,Mn)As sample, for which we present experimental data obtained by XAS measurement. Having no ambition of the detailed spectroscopic study, we simulated the significant features in XAS spectra that can be ascribed to Mn oxides. We show that the annealing forms the surface oxide whereas the etching completely removes it.

6.1 Samples

Sample	preceded treatment	note
A-1	deposition, surface cleaning and natural ageing	as-grown sample, $T_C \approx 6$ K
A-2	surface cleaning, annealing (1 h)	derived from A-1
A-3	surface cleaning	derived from A-2

Table 6.1: Overview of studied samples A-1, A-2, and A-3. The annealing temperature was 160°C. The surface cleaning was performed by rinsing in HCl for a short time (≈ 30 s).

The as-grown sample was prepared by the MBE method in the Institute of

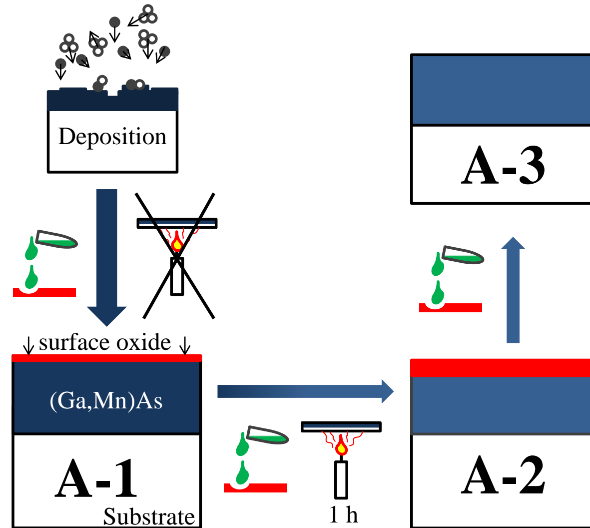

Figure 6.1: Schematic description of the samples A-1, A-2, and A-3. We assume that each etching makes the epitaxial layer thinner, each annealing makes thicker the surface oxide.

Physics, ASCR. The etching, and the magnetometry measurement of that sample were performed there, as well. We used the control as-grown sample A-1 studied in 5 to prove the presence of the surface Mn oxide layer by the XAS. During this experiment, it was etched in HCl and annealed for one hour at 160°C(labelled as A-2), and finally, the surface layer was removed by another etching (sample A-3) and immediately measured before the surface can oxidise again. This treatment is summarized in Table 6.1 and schematically depicted in Figure 6.1.

6.2 Experimental prove of Mn oxide forming

The XAS measurements have been carried out at the ANKA synchrotron source in Karlsruhe, Germany. X-Spec ionization chambers from Oxford-FMB were used for the intensity monitors and a five-element germanium detector from Canberra for the detection of the fluorescence energy. The used peaking time of the detector electronics was 500 ns. We measured the dependence of the intensity of the Mn K_α fluorescence line as a function of the energy of the primary x-ray beams for various angles α_i below and above the critical angle α_c of total external reflection, $\alpha_c \approx 0.38°$, for the used energy, around 6.5 keV (K-L_3). The surface sensitivity of the XAS measurement is achieved by the fact that by increasing α_i, the penetration depth, and consequently the depth from that the fluorescence signal is collected, increases from a few nm for $\alpha_i < \alpha_c$ to several μm.

To observe the influence of the etching and annealing on the surface, we did the XAS measurement for three modifications of sample A showed in Figure 6.2. Firstly, the original as-grown sample A-1, which was several months old and therefore some natively grown oxide on the top of the layer can be expected. Secondly, the as-grown sample A-1 was etched and annealed for one hour at 160°C to create the Mn-rich surface layer, i.e., the sample transformed to A-2. There was no additional ageing of this sample, and it was measured immediately

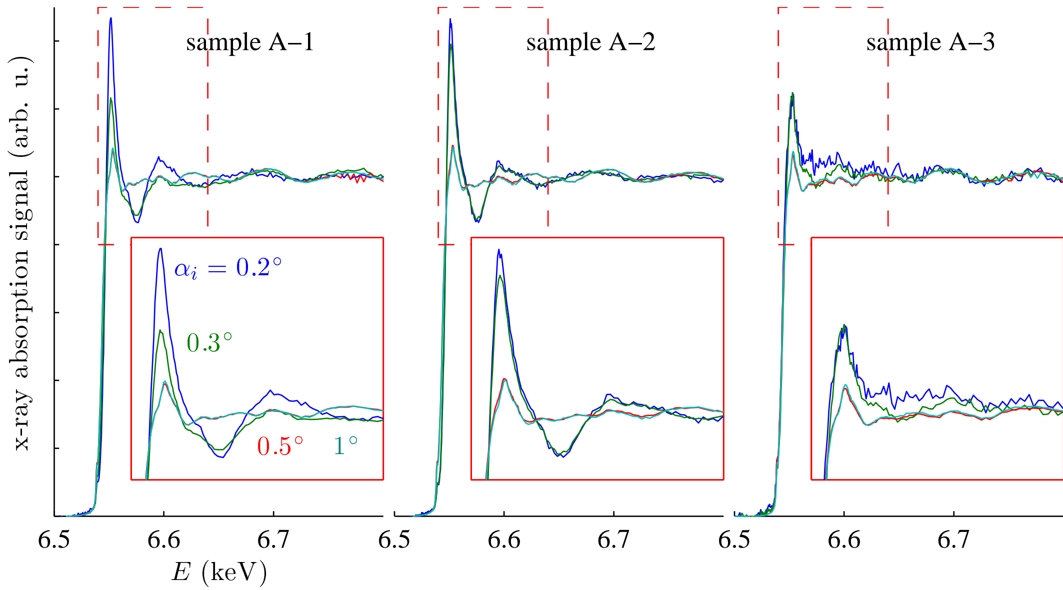

Figure 6.2: Experimental XAS spectra for the samples A-1–A-3 measured at various incidence angles α_i: 0.2° (blue), 0.3° (green), 0.5° (red), and 1° (cyan). The curves are very similar but their shapes closely above the absorption edge differ significantly. These areas bordered by the red dashed rectangle are magnified in the insets.

after annealing. Since, there should be no oxide layer due to the natural ageing of the sample. Finally, the surface layer was removed by another etching (sample A-3) to show the absence of the oxide after the etching. Again, the sample was measured immediately.

The measured spectra have the very similar shape, only the intensity of the sharp peak just above the absorption edge and the shape of the spectra approximately 100 eV far from that peak significantly differ. We want just to roughly compare the MnO amount in different samples, for which it is sufficient to quantify a signal contribution ascribable to the Mn oxide. With no ambition of a deeper analysis, in contrary to pre-edge XANES studies [127, 128], we focus only on the 100 eV wide region just above the absorption edge. There, we try to fit the measurement with the superposition of the theoretically calculated XAS spectra for all considered Mn neighbourhood arrangements. Initially, we introduce theoretical basics of anomalous diffraction approach. It extends the theory in chapter 3. However, we feel to mention it here as it is not so related with HRXRD method bundled by chapters 2–5. Finally, we interpret the experimental data and we compare the results with previous ones.

The selected parts of the XAS spectra are displayed in Figure 6.3. The measured spectra were qualitatively compared with the results of ab initio XAS simulations using the FDMNES code [129]. We calculated the XAS spectra for Mn substitutional atoms, Mn interstitial ions in two nonequivalent positions, and for two Mn-oxide phases, namely, cubic MnO (manganosite) and orthorombic MnO_2 (groutelite) (see Figure 6.3 - right inset). The measured spectra have been fitted to a weighted average of the spectra simulated for various Mn positions. From the data, it follows, indeed, that the Mn-rich layer at the surface consists of Mn oxide similarly to results found in Reference 62.

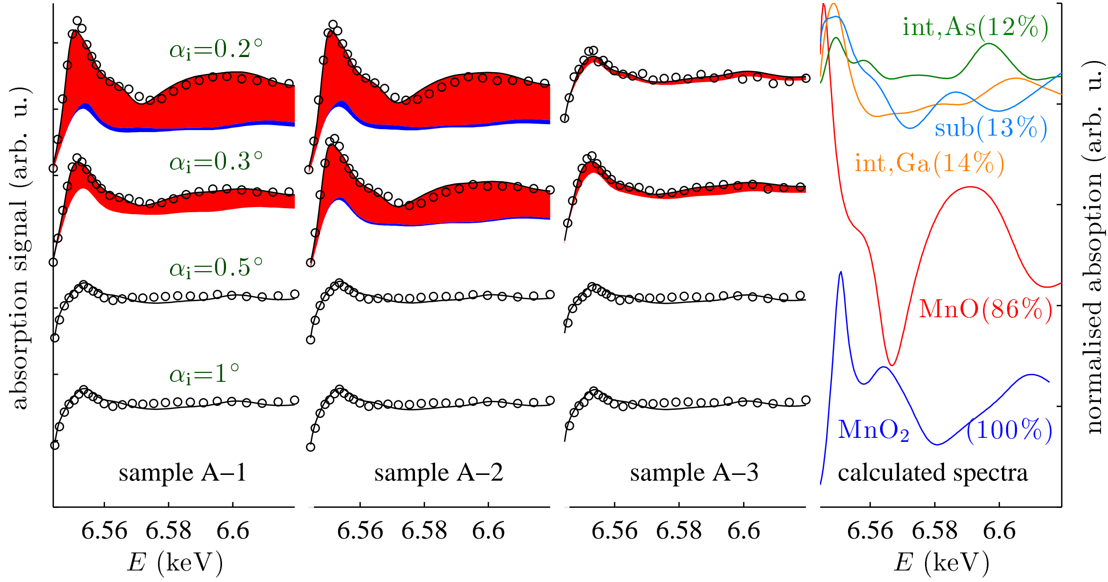

Figure 6.3: Selected parts of the measured XAS spectra closely behind the absorption edge. The experimental data (circles) measured at various incidence angles α_i (i.e., for various penetration depths of the primary beam) are shifted vertically for the clarity. The weighted sum of the calculated theoretical spectra fitting the experimental data are plotted by solid lines, while the MnO and the MnO_2 contributions of the fits are emphasized by red and blue areas, respectively. The very right inset shows the calculated spectra for both Mn oxides and Mn in various lattice positions using FDMNES code. The spectra are normalized to fit the axes, the percentages within the labels denote the ratio of their maximum and the MnO_2 maximum.

The presence of the Mn oxide can be clearly identified in the as-grown sample, this native oxide layer is very thin as the significant XAS signal from the MnO (recognizable by the sharp peak approximately at $E = 6.55$ keV) was obtained only for the smallest angle of incidence (see Figure 6.3). After the removal of the native oxide by etching and subsequent annealing, the oxide layer was thicker than in the previous case since the intensity of the signal from the MnO is present also for the larger penetration depth, i.e., for the larger angle of incidence. Finally, from the fits of the simulated spectra to experimental data, it follows that there is no Mn oxide at all after the final etching of the sample.

We fitted these XAS signals with weighted sum of all theoretical spectra shown in right inset of Figure 6.3. Although we obtained the weights of spectra representing Mn in various crystallographic positions, we do not dare to interpret them as corresponding relative occupancies. Those spectra are very similar and these individual weights have very large error bar. On the other hand, they significantly differ from the spectra of Mn oxides. And therefore, it is possible to affirm their presence quite reliably.

Conclusion

We presented an experimental XAS spectra measured on the second (Ga,Mn)As sample set. The significant features in the spectra were ascribed to the Mn oxides. We shown the evidence of the surface oxide formation during the natural ageing of the sample and during the annealing, as well.

We showed that Mn-rich oxide layer is being created during the ageing of the material at normal temperature (sample A-1) when a native oxide is formed. And obviously, the interstitials located within the surface cannot avoid of just such oxidation. Such oxide layer is very thin even after the months of ageing. The sample A-2 demonstrates that such oxide layer grows very quickly during the annealing and the Mn oxide is located in the larger depth compared with the native oxide. The etching removes all oxide from the surface (sample A-3). This all indicates that the model of the surface container in the drift-diffusion problem is can be identified with the continuously oxidizing surface layer.

Chapter 7

Mn densities determined using anomalous diffraction

Here, we present a short study of two (Ga,Mn)As layers using anomalous diffraction. The two probed samples are examined in chapter 5 (A-1 and B-2). Initially, we introduce the theoretical basics of the anomalous diffraction approach. It extends the theory described in chapter 3. However, we feel appropriate to mention it just here as it is not part of the laboratory HRXRD method thoroughly introduced by chapters 2–5. Finally, we interpret the experimental data obtained by anomalous diffraction measurement, and we compare them with those estimated in chapter 5.

We showed in chapter 3 how the structure factor of (Ga,Mn)As is affected by the presence of the different elements in the crystal lattice being different from the pure GaAs material. Simply said, the c_{sub}, $c_{\mathrm{int,As(Ga)}}$ and c_{anti} densities are estimated from the difference of the measured diffracted intensity originating from the layer and theoretical diffracted intensity expected from the layer being just GaAs, i.e., we compare the experimentally measured amplitudes of the structure factor with calculated ones. From the shape of the diffraction curve, it is not possible to say anything about nature of the defect and similarly the intensity is affected only by the product of the particular defect density and its scattering power. To remove the correlation between different defect types, i.e., to distinguish their contribution to the intensity, one has to measure several (better many) diffractions and the agreement of the measured and the calculated amplitudes of the structure factors has to be found simultaneously for all of them.

There are some severe obstacles complicating the interpretation. Firstly, some diffraction maxima types carrying the complementary information are affected rather weakly (strong and intermediate maxima) recalling the Figure 3.2. This can be in principle overcome by the very accurate measurement, but it cannot be guaranteed in practice. Secondly, there are some addition influences on the measured intensity, which change the expected intensity from the calculation for various diffraction in different way. The D-W factor can be estimated indeed, but we have to measure one or rather more additional diffraction maxima to do this.

The local distortion introduced in chapter 3, although being relatively weak effect, shows that the influence of the repulsion between the closest neighbours is comparable with the influence of the element substitution in case of intermediate diffraction maxima. Therefore, we are partially reliant on the correctness of the

estimated repulsion factors in the literature. Unfortunately, if the higher amount of anti-site defect are in the layer, the correct interpretation turns to be impossible due to the uncertainty of the appropriate repulsion factor.

Though we are able to improve the removal of the correlation by the presumed relation between the defect densities and the relaxed lattice parameter of (Ga,Mn)As (Equation 3.2, the reliability of the determined densities are given by the reliability of the estimated theoretical expansion coefficients. Evidently better, it is to measure just such amount of diffraction maxima that it is possible to avoid using of this formula, and also that it is possible to eliminate the influence of the mistaken measurements, e.g., due to some accidental misalignment.

However, there is a way how to increase the contrast of the Mn density contribution to the measured diffracted intensity. If we were able to change significantly the scattering power of the Mn atoms in the lattice, the dependence of the diffracted intensity on the Mn densities (similar to those in Figure 3.2) would also change. Then we would be able to identify the Mn contribution to the scattering from the intensity difference of the same diffraction maximum measurement for various scattering powers of Mn. Actually, we are not able to change the atomic scattering factor f of any element, but fortunately, it differs naturally for the different energy E (or wavelength λ related by a conversion formula $\lambda = E^{-1} \times 12398.54\,\text{Å}/\text{eV}$) of the x-ray radiation, of course, not exclusively.

7.1 Anomalous dispersion of atomic scattering factor

The significant change of the atomic factor is in the vicinity of the absorption edge of the certain element (*anomalous dispersion*) if we tune the energy of the probing radiation close to the energy of the intra-atomic transition energies. Then, the various scattering power of the particular element takes place in the diffraction process while the contribution of other elements stays unaffected. The influence of different energies around K_α (K-L_3) absorption edge of the Mn is showed in Figure 7.1.

The irradiated single atom elastically scatters the electromagnetic radiation in every direction and the distribution of the wave amplitudes into the directions can be described as a function of the scattering vector length ($\propto \frac{\sin(\theta)}{\lambda}$). The atomic scattering factor of a certain element is usually and sufficiently approximated by the summed series of the exponential decayed function of the scattering vector length. We use the approximation

$$f^0\left(\frac{\sin(\theta)}{\lambda}\right) = \sum_{j=1}^{5} a_j \mathrm{e}^{-b_j\left(\frac{\sin(\theta)}{\lambda}\right)^2} + c \tag{7.1}$$

with the theoretically calculated factor in Reference 102. Namely, a_j, b_j, and c values are obtained from the implementation *atominfo* [131].

Finally, the atomic scattering factor can be written as

$$f\left(\frac{\sin(\theta)}{\lambda}, \lambda\right) = f^0\left(\frac{\sin(\theta)}{\lambda}\right) + f'(\lambda) + \mathrm{i}f''(\lambda) \tag{7.2}$$

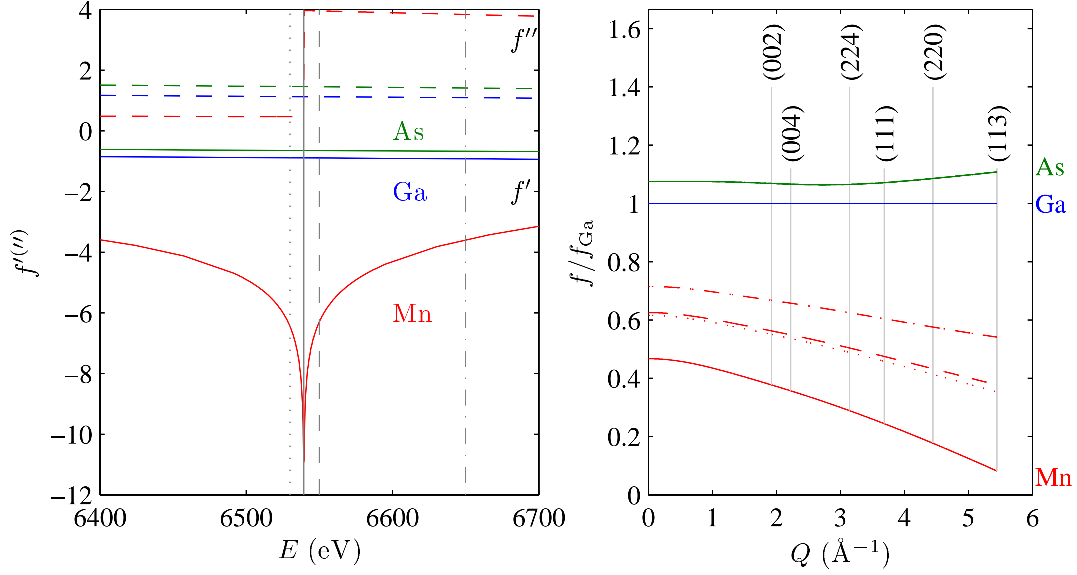

Figure 7.1: Energy correction terms f' and f'' of the scattering factors for As, Ga, and Mn elements are plotted in the left inset. There is a significant change of f_{Mn} around 6.5 eV corresponding the Mn K_α (also K-L_3 [130]) absorption edge, while atomic factors of other elements follows the normal energetic dispersion behaviour, i.e., slow continuous decay with increasing energy. The right inset shows the atomic scattering factors relatively to that of Ga. All of them are corrected for the energetic dispersion for several selected energies indicated by the differently styled black lines in the left inset.

i.e., function of a scattering vector length corrected for the energy dispersion [132]. We used the dispersion corrections extracted from the calculated values in Reference 133. Here, they are introduced as $f\,(0, \lambda) = f_1(\lambda) + \mathrm{i} f_2(\lambda)$. Since, we can obtain the correction terms as

$$f' = f_1 - \sum_{j=1}^{5} a_j - c \qquad \text{and} \qquad f'' = f_2. \tag{7.3}$$

Recalling the formula for the averaged structure factor $\langle F_{hkl}^{\mathrm{GaMnAs}} \rangle$ (Equation 3.8) and consideration that the diffuse scattering can be neglected in case of (Ga,Mn)As, we can calculate the ratios $\frac{\left|\langle F_{hkl}^{\mathrm{(Ga,Mn)As}} \rangle\right|^2}{\left|F_{hkl}^{\mathrm{GaAs}}\right|^2}$. It should correspond to the relative intensity diffracted on the (Ga,Mn)As with respect to that diffracted on the GaAs. Such calculations for individual defect densities being 1% are plotted in Figure 7.2.

As we introduced the correction of the structure factor due to the local lattice distortion around the defects, we used the resulted formula Equation 3.16 to obtain the corrected calculated curves in Figure 7.2. Evidently it plays significant role just in case of intermediate diffraction maxima, whether no role in case of strong maxima. The weak diffraction maxima are affected by this correction only for the c_{anti} density, obviously for the large (but completely uncertain) repulsion acting on anti-site neighbours.

From the calculated dependences $(\frac{F_{\mathrm{(Ga,Mn)As}}}{F_{\mathrm{GaAs}}})^2$ versus energy, it follows that

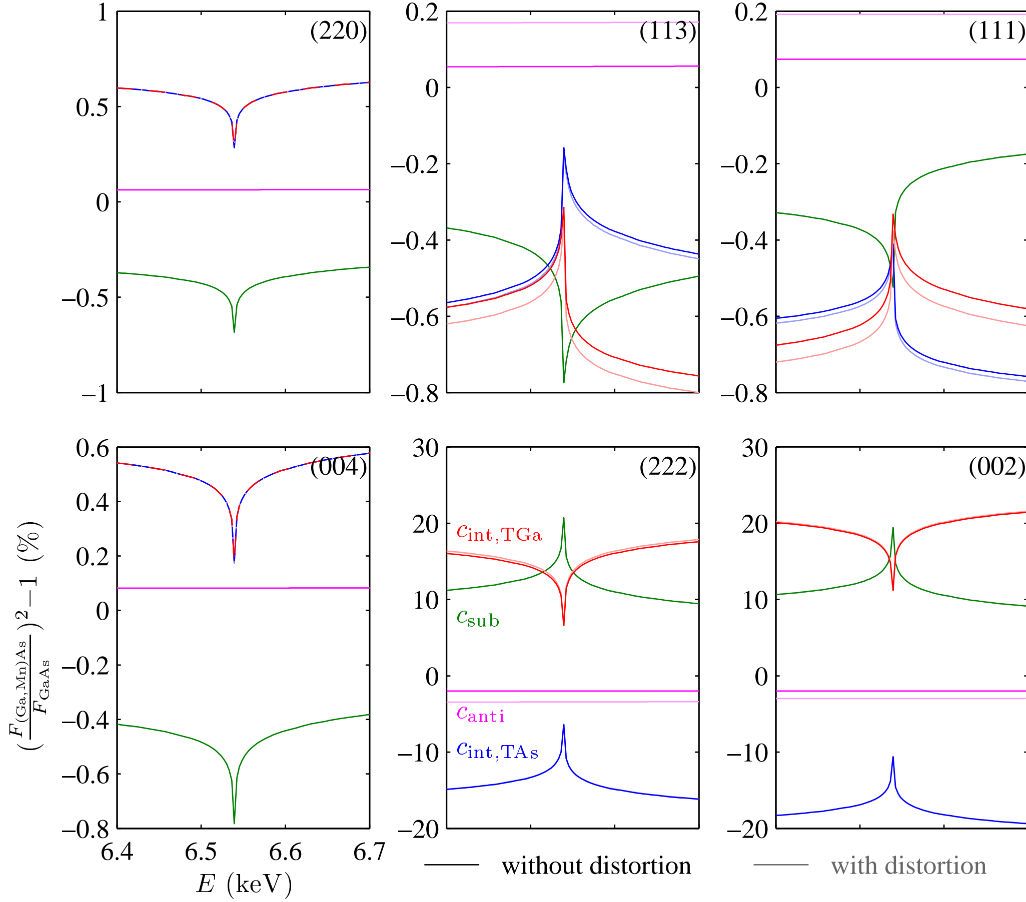

Figure 7.2: The calculated change of the intensity diffracted on (Ga,Mn)As relatively to that one corresponding to GaAs with respect to energy of the probing radiation. The calculation are shown for two of weak ((002) and (222)), intermediate ((113) and (111)) and strong ((220) and (224)) diffraction maxima. The calculations are made with the 1% defect density individually for c_{sub}, c_{anti} and $c_{\mathrm{int,As(Ga)}}$. All curves are also calculated with the consideration of the local distortion (lighter colours) to demonstrate its influence.

only the weak diffractions are sufficiently sensitive for the determination of the Mn densities in particular crystallographic positions. The intensity ratio change for the intermediate diffractions is very small (below one percent) and moreover the distortion correction cannot be neglected. Similarly, the strong diffractions are affected rather weekly and there is no chance to discriminate the contributions from the non-equivalent interstitial positions. Concluding these calculations we can concentrate experimentally on the weak diffractions neglecting the local lattice distortion correction. We can simplify the structure factor of (Ga,Mn)As to the form of

$$\begin{aligned}\langle F^{\mathrm{GaMnAs}}_{\mathrm{weak}}\rangle =&4\,[f_{\mathrm{Ga}} - f_{\mathrm{As}} + c_{\mathrm{sub}}(f_{\mathrm{Mn}} - f_{\mathrm{Ga}}) + \\ &c_{\mathrm{anti}}(f_{\mathrm{As}} - f_{\mathrm{Ga}}) + (c_{\mathrm{int,As}} - c_{\mathrm{int,Ga}})f_{\mathrm{Mn}}]\ ,\end{aligned} \tag{7.4}$$

which differs for various weak diffractions only by the different atomic scattering factor of Mn due to the different scattering vector length, i.e., there is different contribution of the Mn to the intensity. However, the main contrast is due to the significant change of atomic factor with the energy, while its decay of with

the decreasing scattering vector length is the same. Although relative values $\frac{f_{\mathrm{Mn}}}{f_{\mathrm{Ga}}}$ (see Figure 7.1) changes for different weak diffraction maxima, this difference practically only changes the scaling of the dependences in Figure 7.2 and in Figure 7.3.

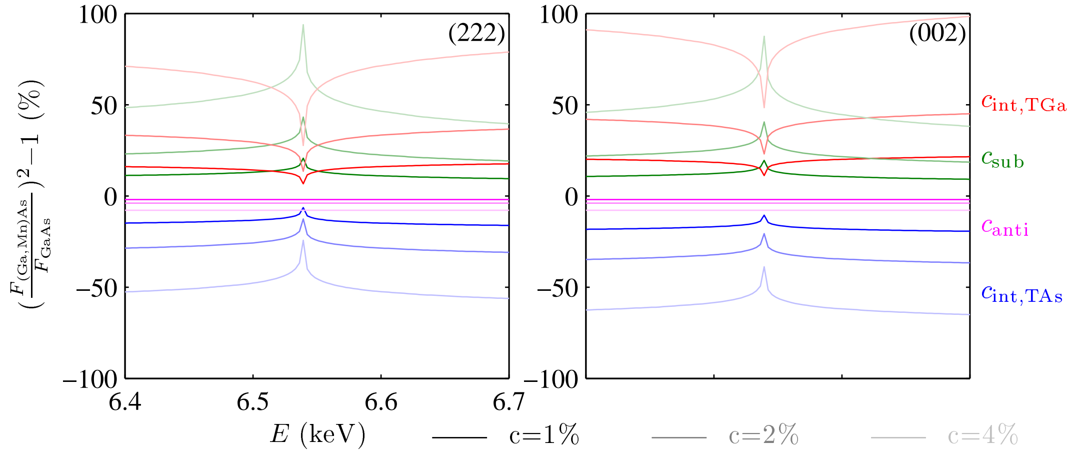

Figure 7.3: The calculated change of the relative intensity with respect to energy. The calculated curves for two of weak ((002) and (222)) are shown for the 1%, 2%, and 4% defect density (different colour saturation) individually for c_{sub}, c_{anti} and $c_{\mathrm{int,As(Ga)}}$ (distinguished by the colours).

For all calculated dependencies in Figure 7.3 we can see that the presence of the anti-site just shifts the relative intensity, while the contribution from Mn densities shifts the relative intensity but the shape of the dependence changes with the different concentration, as well. This leads to the conclusion that Mn densities can be interpreted from the experiment independently on the presence of the anti-site by the fit of the calculated dependences on the experimentally obtained data. We should be able to determine the concentration c_{sub} and the difference of the densities $c_{\mathrm{int,As}} - c_{\mathrm{int,Ga}}$, as it apparently follows from Equation 7.4.

7.2 Anomalous diffraction experiment

We measured the sample A-1 and B-2 introduced in chapter 5. The anomalous x-ray diffraction experiment was performed at the ID01 beamline at ESRF in Grenoble (France). We used the energies within the range 6.4–6.7 keV. The reciprocal (Q_x, Q_z)-space maps describing the distribution of the diffracted intensity in the vicinity of the GaAs/(Ga,Mn)As (002) diffraction maxima were measured for each energy. The linear detector positioned in the scattering plane allowed to collect data for each map during one symmetrical $\omega/2\theta$-scan.

The example of such a measured map is shown in Figure 7.4, from which it is possible to obtain the distribution of the intensity along the truncation rod by the integration of the intensity along Q_x-axis.

There is a obvious reason why we consider the relative intensity of (Ga,Mn)As maxima related to that of GaAs, although one would intuitively interpret just the dependence of the absolute intensity change corresponding to the layer with respect to energy of the probing radiation. The energy change during the experiment involving the monochromator and other optic adjustment can change

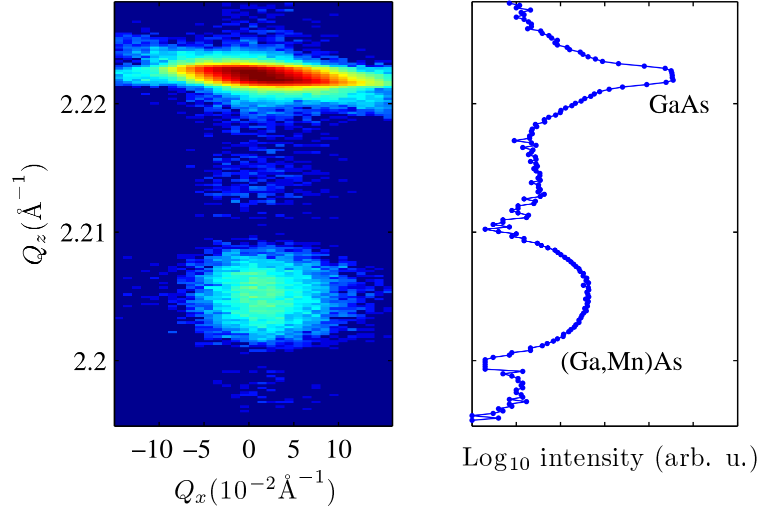

Figure 7.4: Reciprocal space map around weak (002) maxima for the sample B-2 measured at $E = 6.4$ keV (left). The maximum positioned at higher Q_z coordinates corresponds to the GaAs diffraction peak, whether the (Ga,Mn)As diffraction maximum lies below at lower Q_z. The narrow streak going through the substrate maxima is caused by the resolution of the linear detector being an experimental artefact. The integrated intensity along Q_x-axis is plotted in the right subfigure.

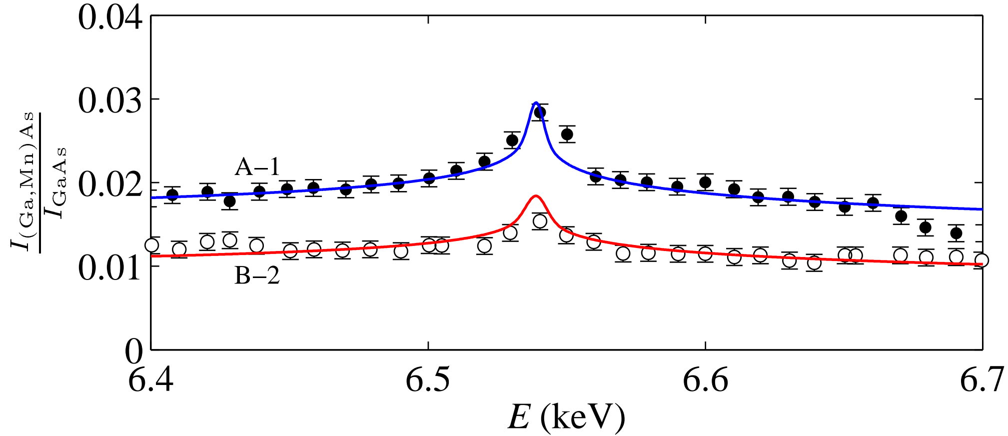

Figure 7.5: The experimental ratios of maximal intensity of the layer and the substrate peaks ($\frac{I_{(\text{Ga,Mn})\text{As}}}{I_{\text{GaAs}}}$) for the samples A-1 and B-1 with respect to the energy E of the probing radiation. Each point is represented by its most probable value (marks) and the corresponding uncertainty (error bars). Experimental data are fitted by the theoretical fits (solid coloured lines).

the experimental conditions as intensity of the primary beam or the instrumental function. The intensity of a substrate peak is a perfect natural reference for the intensities obtained from the diffraction on the layer. Both measured maxima are affected by the same experimental conditions.

The (Ga,Mn)As layer is very thin, therefore the diffraction can be treated kinematically. Then the maximum intensity of the layer peak is proportional to the layer thickness T and absolute value of the averaged structure factor squared. On the other hand, the substrate is large crystal and the intensity maximum of

its peak is generally proportional to the $|F_{\mathrm{GaAs}}|^n$, where the exponent $n \in \langle 1, 2\rangle$ ($n = 1$ for pure dynamical and $n = 2$ for kinematical diffraction). The absorption of incident and diffracted waves by the substrate passing through the very thin (Ga,Mn)As film can be neglected. The ratio of the measured maximal intensities of the layer and the substrate peak can be described by the

$$\frac{I_{\mathrm{(Ga,Mn)As}}}{I_{\mathrm{GaAs}}} = CT^2 \frac{\left|F_{\mathrm{(Ga,Mn)As}}\right|^2}{|F_{\mathrm{GaAs}}|^n}, \tag{7.5}$$

where the prefactor C is ratio of proportionality constants corresponding to $I_{\mathrm{(Ga,Mn)As}} \propto T^2 \left|F_{\mathrm{(Ga,Mn)As}}\right|^2$ and $I_{\mathrm{GaAs}} \propto |F_{\mathrm{GaAs}}|^n$. Since the prefactor contains the dependence on the Bragg angle, it changes very slowly in small energy range we performed our measurements. Being the same for both samples A-1 and B-2 we can treat it as a multiplicative constant of minor interest being an arbitrary fitting parameter.

The measured intensity ratios were fitted by the theoretical dependences based on Equation 7.4, which are plotted in Figure 7.5. The finite energy resolution of 1 eV was taken into account which smeared little bit the sharp peaks of the theoretical dependencies as they are depicted in Figure 7.2. The c_{sub} density was assumed to be the same in both samples consistently with the assumption in previous chapters. The antisite defect density is equal in both samples, as well, and being impossible to determine however just with the same multiplication effect on the dependencies, it was included in arbitrary parameter C. The fitting was performed for all values of n, fortunately, these values affects the results only very slightly and it is included in the uncertainty of the optimized parameters. From the simultaneous fitting of both measured dependencies, we obtained the optimized values of density $c_{\mathrm{sub}}^{\text{A-1}} \equiv c_{\mathrm{sub}}^{\text{B-2}} = (8.2 \pm 1.1)\%$ and differences of occupancies in non-equivalent interstitial positions for both samples $(c_{\mathrm{int,As}} - c_{\mathrm{int,Ga}})^{\text{A-1}} = (1.6 \pm 0.3)\%$ and $(c_{\mathrm{int,As}} - c_{\mathrm{int,Ga}})^{\text{B-2}} = (2.4 \pm 0.3)\%$.

The results are compared with those obtained by the HRXRD method inchapter 5 with and without constraint of theoretical expansion coefficients in Table 7.1.

	$c_{\mathrm{int,As}} - c_{\mathrm{int,Ga}}$	
	A-1	**B-2**
anomalous diffraction	1.6(3)	2.4(3)
HRXRD with exp. coeff.	1.3(6)	2(1)
HRXRD free of exp. coeff.	1.2(7)	

Table 7.1: The comparison of the difference of the occupancies in the crystallographic non-equivalent interstitial positions determined by several methods. The value in the brackets corresponds to the uncertainty in the last digit of the most probable value.

Although there is an overlap between values determined with different approaches within the ranges of the uncertainty, it is rather due to the large uncertainty regions than due to the agreement of the most probable values. Anyway, both approaches shows similarly larger difference for the annealed sample. Unfortunately, it was not possible to evaluate the B-2 data from HRXRD without considering of some expansion coefficients and the uncertainty of the difference

obtained with that consideration is extremely large. On the other hand, the c_{sub} was reliably determined and result fully justifies our rough guess in the chapter 5.

Conclusion

We introduced the theoretical basics for the anomalous diffraction technique. We showed the sensitivity of the weak diffraction to the difference of interstitial densities in non-equivalent lattice positions. In contrary to approach demonstrated in chapter 5, we were able to determine the substitutional content of Mn in the samples.

This method can be possibly improved by the fitting of the whole measured diffraction curve, when the structure factor of the (Ga,Mn)As entering into the diffraction simulation is being optimized. Similarly to approach described in chapter 5, assuming known structure factors for GaAs substrate would allow to scale the intensity using the whole substrate peak as a reference. Although this can remove the additional parameter n which bring some uncertainty , the evaluation of many diffraction curves is quite time consumptive. From the results it follows that here used much simple approach led to the reliably precious results, as well.

There are several advantages of the anomalous diffraction approach in contrast to the HRXRD measurements. Firstly, the influence of the anti-site defects is distinguishably separated from the influence of Mn content on the measured intensity. However, it is not possible to determine the anti-site density. This advantage is so important because we are not able to include lattice distortion into the calculation due to the uncertainty of the repulsion acting on anti-site neighbours. This is closely related with the second main advantage allowing to interpret data with no *a priori* assumptions arising from the unverified theoretical calculations. Besides the repulsion factor we can dispense with the relation between the relaxed lattice parameter and the defect densities.

The large number of the measured points (i.e., peak heights for many diffraction curves) eliminate also the chance to misinterpret the mistaken measurement, because all points should lie on some theoretically allowed dependence. Therefore the mistaken measurement (e.g., due to some instrumental misalignment) can be clearly identified and removed from the evaluation. The evaluation of the D-W factor is not necessary, as well, because it scales all results in the same way and it can be included in the arbitrary multiplicative constant. However, this approach demand the ability to tune the wavelength, which is not accessible in standard laboratories and the experiment has to be performed at some synchrotron facility.

Chapter 8

Diffusion of interstitials

The post-growth treatment of the deposited (Ga,Mn)As epitaxial layers is for their final magnetic properties as important as their well controlled growth itself as we showed in chapter 1. The increase of the Curie temperature of (Ga,Mn)As layers is reached after the annealing procedure. Previously, we mentioned that the annealing time can be rapidly decreased using the etching enhanced annealing [134]. It is widely accepted that the improvement of the magnetic properties is a consequence of the removal of the Mn interstitials from the as-grown (Ga,Mn)As layer [34, 39], those interstitials are passivated within the sample surface by creating Mn rich layer (oxide [34, 39] or MnAs [64, 65]) [61–63]. For the migration of the interstitials towards the surface it is necessary to increase their mobility which is achieved by higher temperature during the annealing process.

Here, we introduce a detailed numerical model of the migration of interstitials in the material. This model is described by the diffusion and the drift of interstitials [65]. We discuss the mobility parameters of the migrating interstitials and a possible concentration gradient of Mn in the (Ga,Mn)As layers. This theory will be used for the simulation of the annealing in chapter 9.

Initially, we define the drift-diffusion (D-D) equations. Further we introduce the boundary conditions for mobile particles at both air/layer and layer/substrate interfaces. On the surface, we postulate the hypothetical surface container that removes interstitials from the system. Later in the chapter, we suggest how to solve the formulated D-D equations. Finally, we briefly remark the two concurrent migration concepts for interstitials.

8.1 Drift-diffusion equations

There are two non-equivalent interstitial positions for double donor Mn (in the centres of the As or Ga tetrahedrons). The lowest energetic barrier (0.7–0.8 eV) for the jump of the Mn from the one type of interstitial position is the interstitial position of the other type [39]. Let us step out from the microscopic mechanism and let us consider the migration of these interstitial Mn ions in the (Ga,Mn)As material as a movement in the continuum. We are interested in the spatial distribution of the interstitial density $n(\boldsymbol{r})$ and in the change of this quantity in the time (in fact, $n \equiv n(\boldsymbol{r}, t)$). The charge of the migrating interstitials being the double donors is $-2|e|$. The migration is then driven by the inhomogeneity of the concentration (density) which is related to the diffusion.

Secondly, it is driven by the electrostatic force acting on charged interstitials which is related to the drift in the electrostatic potential $\phi \equiv \phi(\boldsymbol{r}, t)$. We can write D-D equations for the interstitials [65]:

$$\frac{\mathrm{d}n}{\mathrm{d}t} = \nabla \cdot (D_n \nabla n + 2\mu_n n \nabla \phi) \equiv -\nabla \cdot j_n \,, \tag{8.1}$$

where D_n is the diffusion constant of interstitials and μ_n is their mobility. According to the continuity equation we can define flux j_n of the interstitials (it is commonly denoted as the flux, although strictly speaking it is the flux of the particle density).

The electrostatic potential ϕ fulfils the Poisson equation

$$\Delta \phi = -\frac{\varrho}{\epsilon} \,, \tag{8.2}$$

where ϵ is the permittivity of the surrounding material, here assumed to be practically GaAs. The charge density ϱ is superposition of the charge densities of the interstitial Mn double-donors, homogeneously distributed substitutional Mn acceptors with the constant density c_{sub}, and finally, holes present in this p-type semiconductor:

$$\varrho(\boldsymbol{r}, t) = -e(c_{\mathrm{sub}} - 2n(\boldsymbol{r}, t) - p(\boldsymbol{r}, t)) \,. \tag{8.3}$$

If other charged defects are present in the material, e.g., As antisites, the appropriate term should be added to Equation 8.3 or the density c_{sub} can be treated as the 'effective' density including the terms coming from the other defects.

The holes described by their density $p \equiv p(\boldsymbol{r}, t)$ obey the drift-diffusion equation, as well:

$$\frac{\mathrm{d}p}{\mathrm{d}t} = \nabla \cdot (D_p \nabla p + 2\mu_p p \nabla \phi) \equiv -\nabla \cdot j_p \,. \tag{8.4}$$

The holes diffusivity D_p and their mobility μ_p is of course much higher than in case of interstitials.

The diffusivity is related to the mobility by the Einstein relation [135]

$$D_{n,p} = \frac{\mu_{n,p} k_{\mathrm{B}} T}{q_{n,p}} \,, \tag{8.5}$$

where T is the thermodynamic temperature, k_{B} the Boltzmann constant, and the q is the charge of corresponding particle ($q_n = 2|e|$ and $q_p = |e|$, recalling the charge of the electron e).

8.1.1 Laterally homogeneous (Ga,Mn)As layer

Let us restrict ourselves to the case of (Ga,Mn)As layer usually deposited on a GaAs substrate. The lateral homogeneity of the layer is assumed as it should be obviously fulfilled by the proper sample. The thickness of the deposited film, typically below 1 μm, is much smaller than diameters of the sample, usually millimetres. Therefore, we can neglect what is going on near the sample borders. We can concentrate on the majority of the material. For that, we can consider the layer being laterally infinite since the distance to the border is quite large. Due to this lateral symmetry, we can consider just one-dimensional model, where all variables change only in the direction perpendicular to the surface. It means

vertically as referenced to the sample. In this direction, we define z-axis with the origin located at the interface between the layer and the substrate. The thickness of the film is denoted as H, therefore the position of the sample surface is for $z = -H$, the situation is depicted in Figure 8.1 for the clarity.

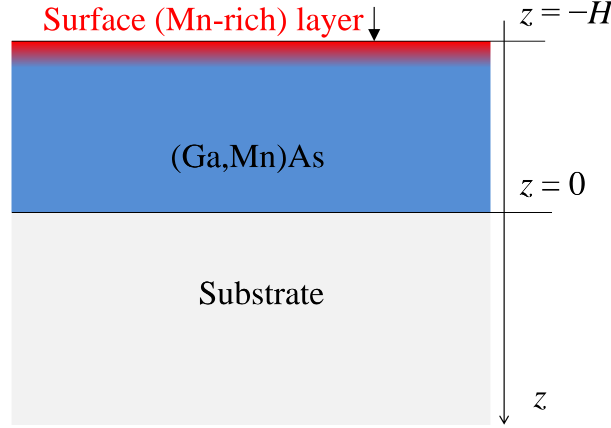

Figure 8.1: Schematic sketch of the (Ga,Mn)As single layer. Axis z is pointing toward the substrate, the origin is located at the layer/substrate interface. The thickness of the (Ga,Mn)As layer is H. The surface of the sample (the surface oxide layer) is located at coordinates $z = -H$.

The drift drift-diffusion equations 8.1 and 8.4 can be rewritten in one dimension as

$$\frac{\mathrm{d}n}{\mathrm{d}t} = \frac{\mathrm{d}}{\mathrm{d}z}\left(D_n\frac{\mathrm{d}n}{\mathrm{d}z} + \mu_n n\frac{\mathrm{d}\phi}{\mathrm{d}z}\right) \equiv \frac{\mathrm{d}}{\mathrm{d}z}(-j_n)\,, \tag{8.6}$$

$$\frac{\mathrm{d}p}{\mathrm{d}t} = \frac{\mathrm{d}}{\mathrm{d}z}\left(D_p\frac{\mathrm{d}p}{\mathrm{d}z} + \mu_p p\frac{\mathrm{d}\phi}{\mathrm{d}z}\right) \equiv \frac{\mathrm{d}}{\mathrm{d}z}(-j_p)\,, \tag{8.7}$$

and similarly, the Poisson equation changes its form to

$$\frac{\mathrm{d}^2\phi}{\mathrm{d}z^2} = (c_{\mathrm{sub}} - p - 2n)\frac{e}{\epsilon}\,. \tag{8.8}$$

We can see that all three equations (8.6, 8.7 and 8.8) are bound together via the local densities of the holes and the interstitials. One has to solve the system of three differential equations to obtain the evolution of the density profiles of interstitials in time.

8.1.2 Boundary conditions

We have to add some spatial boundary conditions to the system of the non-linear differential equations describing the drift-diffusion. Taking into account that the layer is not electrically charged, we can demand the zero electric field deep in the substrate, i.e., far below the layer/substrate interface. This results in the boundary condition for the electrostatic potential

$$\left.\frac{\mathrm{d}\phi}{\mathrm{d}z}\right|_{z\to\infty} \equiv 0\,. \tag{8.9}$$

The GaAs substrate is not charged, the holes and the interstitials both being positively charged can migrate to the substrate due to the diffusion, but obviously they cannot migrate very far from the interface as there is no external electric field. Each positively charged particle going into the substrate will produce the lack of the positive charge in the layer, causing the electric field pulling these particles back to the layer. The equilibrium between the diffusion into the substrate and the drift force keeping the charged particles in the layer will produce the gradient of their concentration within the layer/substrate interface partly smearing this interface. This means, if there is no electric current going through the sample, then there is no fluxes of the charged particles deep in the substrate. We will obtain the boundary conditions for $j_{n(p)}$:

$$j_n|_{z\to\infty} \equiv 0\,, \qquad\qquad j_p|_{z\to\infty} \equiv 0\,. \tag{8.10}$$

8.1.3 Surface container

On the other side of the layer, near the surface, the situation is more complicated. We know that interstitial Mn near the surface are passivated by the oxygen. The interstitials do not diffuse just to the very surface to be in a contact with the surrounding air, they are oxidized close to the surface by the oxygen diffusing in the opposite direction, i.e., into the layer [25]. The formation speed of the Mn-rich oxide layer depends on the local concentration of the interstitials and also on the amount of the oxygen ready to react with them. The oxygen has to go through the native oxide at the very surface and it has to go through more and more growing oxide layer. It would be very complicated to model this process and we do not know the diffusivity of the oxygen. Moreover, it can be presumed that this value is strongly dependant on the local density of the previously oxidized atoms. The rate of the reaction is unclear, as well.

To avoid this complications, we will consider the vicinity of the surface being the infinitesimally thin layer with the limited ability to trap the interstitials located there. Let us call it the surface container. It means that our model material consists of this container bordering on side the area, where the drift-diffusion equations introduced above are valid. This area is the main (Ga,Mn)As layer together with the substrate thick enough to consider it as semi-infinite.

The interstitial, being positively charged with charge $2|e|$, is passivated by the oxygen which results in a creation of two holes in order to maintain the charge conservation. Therefore, the general property of the container is removing the 'free' interstitial ion from the system at the expense of the releasing two holes back to the system. This property formulate the equality

$$2j_n|_{z=-H} \equiv -j_p|_{z=-H} \tag{8.11}$$

at the border of the area ($z = -H$) bounding together the fluxes of holes and interstitials flowing into/out of there.

A specific property of the container given by the chosen phenomenological model formulates just the flux $j_{n(p)}$ at the border $z = -H$. We emphasize the word *phenomenological* as the parameters used in any model can be hardly compared to theoretical microscopic/macroscopic quantities, though they can be intuitively associated to them.

We will formulate the several conditions which should be fulfilled by the model of the container. The exact mathematical prescription of the container has to based on them. The first requirement is the limited capacity of the container, it can absorb only certain amount of the interstitials. Let us label this capacity as $N_{\mathrm{S,max}}$. The capacity corresponds to the possible maximum number of the trapped Mn ions per unit area. When the container is completely filled up, no other particles can be drawn from the system, then the (density of) flux of the particles is zero.

Secondly, as the number of trapped ions in unit area is denoted as N_{S}, its increment in time has to be defined $\frac{\mathrm{d}N_{\mathrm{S}}}{\mathrm{d}t}$. The interstitials removed from the migration area are stored in this container. The transfer from the migration area to the container is represented by flux $j_n|_{z=-H}$, i.e., the number of particles going through unit area per unit time inside the container. No other migration of particles through the interface of the container is allowed. The drift and diffusion are not valid here, the interface act as a sink for interstitials and source for holes. The spatial continuity of the fluxes is then requested. Apparently, the flux $j_n|_{z=-H} \equiv j_{n\mathrm{S}}$ is equal to the increment of the trapped ions per infinitesimal time:

$$j_{n\mathrm{S}} = \frac{\mathrm{d}N_{\mathrm{S}}}{\mathrm{d}t} \qquad \Longrightarrow \qquad N_{\mathrm{S,max}} = \int_{-\infty}^{\infty} j_{n\mathrm{S}}(t)\,\mathrm{d}t\,. \tag{8.12}$$

Thirdly, we request the inhibition of the trapping with the growing amount of the trapped interstitials. This corresponds to more difficult diffusion of the oxygen and the interstitials into already oxidized layer. The number of trapped particles per time has to be decreasing function with respect to filling of the container for any constant arrangement of other parameters discussed further:

$$\forall\, N_{\mathrm{S}}, N'_{\mathrm{S}} :\ N_{\mathrm{S,max}} > N_{\mathrm{S}} > N'_{\mathrm{S}} > 0 \Rightarrow\ j_{n\mathrm{S}}(N_{\mathrm{S}}) < j_{n\mathrm{S}}(N'_{\mathrm{S}})\,, \tag{8.13}$$

$$j_{n\mathrm{S}}(N_{\mathrm{S,max}}) = 0\,. \tag{8.14}$$

The fourth and the last demand grows from the consideration that the number of reacting interstitials should be proportional to the number of the interstitials located in the vicinity of the container, i.e., on the border of the migration area. There for the container should fulfil the condition

$$j_{n\mathrm{S}}(t) \propto n|_{z=-H}(t)\,. \tag{8.15}$$

There is no serious reason which mathematical formulation fulfilling conditions Equations 8.12–8.15 of the model container to choose. We will adopt the prescription suggested in Reference 25. The number of trapped particles per second, i.e., flux into the container, is linearly proportional to three quantities: the density of the interstitials in the vicinity of the container, the free space in the container and the scaling constant:

$$j_{n\mathrm{S}}(t) = S_0 \left(\frac{N_{\mathrm{S,max}} - N_{\mathrm{S}}(t)}{N_{\mathrm{S,max}}} \right) n|_{z=-H}(t)\,. \tag{8.16}$$

The scaling constant S_0 is the *trapping rate* of the empty container in units of $[\mathrm{m}\cdot\mathrm{s}^{-1}]$. It can be unclearly associated with the rate of the oxidization reaction

and the diffusivity of the oxygen into the sample. Therefore, we can assume that it should be roughly the same for any sample although it is not clear, if it is somehow dependant on the composition of the (Ga,Mn)As, the roughness of the surface and other possible parameters. As it is not possible to estimate this phenomenological parameter theoretically, it has to be adjusted from the comparison of the numerical simulations of the diffusion with the experimentally determined density profiles of the interstitials after annealing (diffusion).

The capacity of the container $N_{\mathrm{S,max}}$ can be estimated at least from other experimental results, such ones are published in Reference [62]. There, the thin (Ga,Mn)As layers were studied using XRSW. In this work, the (Ga,Mn)As layers were being annealed at 200 °C for 4 hours to reach the fully annealed state. The authors determine the total Mn density in the 3-nm-thick surface layer, from which we calculated the areal density of the Mn considering the 3-nm-thick layer as our infinitesimally thin (in fact, 2-dimensional) model container. This result ($N_{\mathrm{S}}^{[62]} \approx 4 \times 10^{19}$ particles/m^2) can be used for the estimation of $N_{\mathrm{S,max}}$.

8.2 Numerical computation of D-D equations

Apparently, it is not possible to solve the D-D equations (Equations 8.6–8.7) bounded view Poisson equation 8.8 analytically, we have to solve this system of non-linear differential equations numerically.

Let us say that our system is heated to 160 °C, for that such temperature the diffusivity of the holes is $D_p \sim 10^{-3}$ m^2/s [136]. The estimation of the diffusivity of interstitial Mn in (Ga,Mn)As is published uniquely, we found just study of the diffusivity, which was performed by the resistivity measurements during the annealing [39]. From the temperature dependence of the interstitial diffusivity described in that work we extracted the diffusivity $D_n^{[39]} \approx 1.4 \times 10^{-21}$ m^2/s.

8.2.1 Bounded D-D equations

Usually, it is not problem to implement these D-D equations using built-in solvers for non-linear differential equations with boundary conditions, e.g., MATLAB or COMSOL multiphyscs. Let us outline the implementation in Matlab, where the solver for initial-boundary value problems for parabolic-elliptic PDEs in 1-D is available (function `pdepe`). It uses the spatial discretization of parabolic equation in one space variable (algorithm can be found in Reference 137). The similar solver should be available in other computing languages and tools.

The general form solved by `pdepe` is the system on N equations indexed by k

$$c_k\left(x, t, u_1, ..., u_N, \frac{\partial u_1}{\partial x}, ..., \frac{\partial u_n}{\partial x}\right)\frac{\partial u_k}{\partial t} = s_k\left(x, t, u_1, ...u_n, \frac{\partial u_1}{\partial x}, ..., \frac{\partial u_N}{\partial x}\right) + x^{-m}\frac{\partial}{\partial x}\left(x^m f_k\left(x, t, u_1, ..., u_N, \frac{\partial u_1}{\partial, ..., \frac{\partial u_N}{\partial x} x}\right)\right), \quad (8.17)$$

where x is the spatial coordinate, t is the time and exponent m is defined by the symmetry of the problem ($m = 0$ in our case, which corresponds to the slab symmetry). Functions c_k, s_k and f_k operating with the N variables $u_{1,...,N}(x, t)$

are defined by the user. The D-D equations rewritten in form of user defined functions are:

$$c_1 \equiv 1, \qquad s_1 \equiv 0, \qquad f_1 = D_n \frac{\partial u_1}{\partial x} + \mu_n u_1 \frac{\partial u_3}{\partial x}, \tag{8.18}$$

$$c_2 \equiv 1, \qquad s_2 \equiv 0, \qquad f_2 = D_p \frac{\partial u_2}{\partial x} + \mu_p u_2 \frac{\partial u_3}{\partial x}, \tag{8.19}$$

$$c_3 \equiv 0, \qquad s_3 = (c_{\text{sub}} - u_2 - 2u_1)\frac{e}{\epsilon}, \qquad f_3 = -\frac{\partial u_3}{\partial x}. \tag{8.20}$$

The first line corresponds to Equation 8.6 and u_1 is associated with the n. The second line similarly corresponds to Equation 8.7 with the varible $u_2 \equiv p$. Finally, the third line represents the Poisson equation (Equation 8.8) and u_3 is the electrostatic potential ϕ.

The boundary conditions are by the solve required in the form

$$P\left(x,t,u_1,...,u_N\right) + \\ + Q\left(x,t,u_1,...,u_N,\right) f\left(x,t,u_1,...,u_N,\frac{\partial u_1}{\partial x},...,\frac{\partial u_n}{\partial x}\right) = 0 \tag{8.21}$$

with user-defined function P and Q defined on the borders, i.e., for points $x_{\text{min}} \equiv -H$ and $x_{\text{max}} \to \infty$. Our boundary conditions are then straightforwardly rewritten as

$$P_1|_{x=-H} = j_{n\text{S}}(t), \qquad Q_1|_{x=-H} = +1, \tag{8.22}$$

$$P_1|_{x\to\infty} = 0, \qquad Q_1|_{x\to\infty} = +1, \tag{8.23}$$

$$P_2|_{x=-H} = j_{p\text{S}}(t) \equiv -2j_{n\text{S}}(t), \qquad Q_2|_{x=-H} = +1, \tag{8.24}$$

$$P_2|_{x\to\infty} = 0, \qquad Q_2|_{x\to\infty} = +1. \tag{8.25}$$

The boundary conditions for the Poison equation demand the zero electric intensity deep in the substrate ($-\frac{\mathrm{d}\phi}{\mathrm{d}z}$). The electrostatic potential is not unambiguous as any constant can be added without consequences. We use the boundary condition at $x = -H$ for the calibration of if the electrostatic potential setting its value as arbitrary value $\phi|_{x=-H}$ there. These conditions we rewrite as

$$P_3|_{x=-H} = u_3 - \phi|_{x=-H}, \qquad Q_3|_{x=-H} = 0, \tag{8.26}$$

$$P_3|_{x\to\infty} = 0, \qquad Q_3|_{x\to\infty} = +1. \tag{8.27}$$

One has to assume the starting density profile $p_0(z)$ for the interstitials. The starting local density of the holes can be estimated by the relation

$$p_0(z) = c_{\text{sub}} - 2n_0(z)\,, \tag{8.28}$$

which fulfils the charge conservation and condition that sample is no charged. However, this density profile obviously does not support the thermodynamic equilibrium state, in which we would expect the holes at the very beginning of the simulation. This does not matter very much as the very mobile holes start to distribute to the state of the thermodynamic equilibrium very soon in the numerical simulation, therefore this estimation is sufficient.

8.2.2 Solving D-D equations for particles with incomparable diffusivities

Unfortunately, the large difference in the diffusivities of the holes and the interstitials (about 19 orders of magnitude) makes the solving of the D-D equations finally tricky. Taking into account that annealing process takes several hours and the largest time step in numerical calculation has to be very small due to the high diffusivity of the holes, one would have to do large number of calculations. In fact, to make all calculation in a reasonable time exceeds the capability of nowadays computers and the computation time is much higher than the annealing time. To evade these long time calculations we suggest following procedure.

We are interested in the migration of the interstitials, therefore we have to solve the Equation 8.6. As we mentioned above, the movement of the holes is incomparable faster than that of the interstitials. Holes move as fast as they are able to spread themselves in the sample with the spatial distribution corresponding to the thermodynamic equilibrium before the interstitials move significantly. From the point of view of the slow Mn interstitials the holes are each time in the thermodynamic equilibrium. In other words, we do not need to simulate the evolution of the hole density in time, it is enough to calculate the thermodynamically equilibrated density profile of holes in the time scale relevant for the interstitial movement.

The simultaneous solving of two D-D equations can be replaced by the two 'independent' D-D equations being solved independently. We can solve just the D-D problem for the interstitials while the thermodynamic equilibrium solution is used for the holes density used in Equation 8.6 and Poisson equation condition. Not being interested in hole movement in time, we will transform the D-D Equation 8.7 for the holes to the form reached in the thermodynamic equilibrium, i.e., the state where is no change of the local density. This is substantiated by the fact that all other parameters in the system change so slowly that there is enough time to reach this state, in fact, we will obtain the solution for $p(t) : t \to \infty \,, n(t) = \text{const.}$. The stable hole density is expressed by $\frac{\mathrm{d}p}{\mathrm{d}t} = 0$:

$$0 = \frac{\mathrm{d}}{\mathrm{d}z}\left(D_p \frac{\mathrm{d}p}{\mathrm{d}z} + \mu_p p \frac{\mathrm{d}\phi}{\mathrm{d}z}\right) \equiv \frac{\mathrm{d}}{\mathrm{d}z}(-j_p)\,, \tag{8.29}$$

This condition means that the flux of the holes are constant everywhere in the space. It is either a stationary case of an electric current flow for non-zero flux, or a static case for zero flux. There is no electric current in our sample, the boundary condition for the holes deep in the substrate stays the same (zero flux). As we are in the different time scale where no interstitials are being trapped and no additional holes are created. We have to replace the boundary condition for the holes in the vicinity of the surface by the zero flux, as well. Let us say that this replacement is just formal because we have the zero flux everywhere not needing any such boundary conditions.

We can write

$$j_p \equiv 0 \implies D_p \frac{\mathrm{d}p}{\mathrm{d}z} + \mu_p p \frac{\mathrm{d}\phi}{\mathrm{d}z} = 0\,, \tag{8.30}$$

which describes an expected state from many semiconductor-textbook examples. The diffusion, aiming to uniformly spread particles in the space, is are in equi-

librium with the drift, trying to distribute those charged particles to screen the spatially stable electric charge.

Now the time dependence disappeared from the equations and we have the system of two differential equations Equation 8.30 and Equation 8.8 (Poisson) for the spatial variables p and ϕ.

To find the unique solution we have to add a condition on the total charge in the sample which is zero. For the time dependent D-D equations it is silently hidden in the starting values of both holes and interstitials densities. Here we have to formulate it as

$$\int_{-H}^{\infty} p(z)\,\mathrm{d}z = c_{\mathrm{sub}}H - \int_{-H}^{\infty} n(z)\,\mathrm{d}z \equiv N_{\mathrm{p}}\,. \tag{8.31}$$

The problem formulated above is identical to the charge density computation of p-n junction without external electric field which can be found in plenty of textbooks. The general case of steady state calculations in one-dimension can be solved, for instance, by Gummel's method [138]. The solution of such a problem is much less demanding on computing power than the solving of two bounded D-D equations.

8.2.3 Final remarks on calculation method

If we summarize above described calculation methods. We have two choices. We can simply solve the two bounded D-D equations simultaneously, which is easy to implement. However, usual solvers are not able to tune the computation time step in that such wise way to increase the calculation speed reasonably.

The second approach concentrates on the D-D equation for interstitials evaluating their density profile in time, while the density of the holes are calculated separately for each change of the interstitial density profile. This can be achieved by the static state calculation of the holes distribution. It needs obviously more complicated implementation.

We can modify the second approach realizing that the spatial distribution of the holes is not very far from the thermodynamic equilibrium. For some iterative methods can be advantageous to set the starting density profile of the holes for such a separate calculation equal to the last known density profile. This decrease the number of iterations which enhance the speed of the calculation.

It is possible to evade the implementation of the static state density calculation, as well, although we can preserve the separation of the D-D equations solution. Then it is necessary to evolve the density of the holes solving separated D-D Equation 8.7 until the holes stop migrating, and this has to be done for all points in time when solving the D-D Equation 8.6 for the interstitials. In fact, this is what we would wish from the built-in solver to change wisely the time step. By the word *wise* we mean the possibility of fast rescaling from the time steps relevant for the holes to the time steps relevant for the interstitials. Usually, the built-in solvers have already the possibility to automatically rescale its time steps relatively to amplitudes of the change in a system, the Matlab solver `pdepe` is capable to do this, as well. Unfortunately, the incomparable difference between time step in our case is not convenient for such solvers. By the separated solving of D-D equations. with different time scales, we are able to partially substitute

this missing property of the solver. However, we have to realize that, inside of the run of the solver computing the interstitials migration, we have to execute another solver repeatedly. We have to conclude that each initialization of the relatively advanced solver takes so many times that the resulting calculation time is not comparable with the approach calculating the static state density.

However, it is possible to use a *dirty* trick to keep the implementation simple and to reach the best calculation time. We operate with the certain value of diffusivity of the holes. Recalling the Einstein relation between a diffusivity and a mobility of a particle, it is evident from the static state Equation 8.30 that the final distribution of the particles is not dependent on the diffusivity value itself. It does not matter if the diffusivity of the holes is higher or lower. Its value does not affect the result of the interstitials migration. This is true if the holes are fast enough to reach the thermodynamic equilibrium in time, i.e., in the smaller time than the time step relevant for the computation of the interstitials migration.

For the purpose of the computation, we can decrease the value of diffusivity for holes to such a minimal value when preceding condition is still fulfilled. It brings nearer the time scales of both D-D equations. Therefore, a numerical solving of both bounded D-D equations can be performed with the time step convenient for the holes, which are now unnaturally slower. As we previously said, the result is not changed but the calculation time is significantly decreased. It is necessary to adjust the optimal value of the hole diffusivity individually because it depends on the properties of the particular solver. We recommend to verify the consistency of such obtained results with the results coming from the *clean* method or with results obtained for higher diffusivity coefficients of the holes.

8.3 Diffusion only

Here, we make only a small remark on the drift included in our model. Usually it is spoken only about the *diffusion* of the interstitials in the (Ga,Mn)As when one is searching in the literature. If we want to omit the drift of the interstitials just for the comparison of the obtained results of the simulation with the solution of the full D-D equations, we have to modify our model as follows.

Our model should be restricted only to the interstitials, drift current will be removed and the continuity equation

$$\frac{\mathrm{d}n}{\mathrm{d}t} = \frac{\mathrm{d}}{\mathrm{d}z}\left(D_n \frac{\mathrm{d}n}{\mathrm{d}z}\right) \equiv \frac{\mathrm{d}}{\mathrm{d}z}(-j_n)\,, \tag{8.32}$$

has to be solved.

We are not interested in the electrostatic potential although it plays its role for the diffusion of the interstitials to the substrate. Actually, this process is well described just by the D-D equations, which results in a limited penetrated depth of those interstitials. This can be hardly explained just by the diffusion.

First possible argument, defending simple diffusion process, can claim that the diffusivity can be connected with other point defects in the material, i.e., it can be increased due to the presence of some defects, such as vacancies. And therefore, the interstitials are not as mobile in the low-defect GaAs as in (Ga,Mn)As. Although the diffusivity can be different, the low penetration depth is also observed

for the sample with low-temperature GaAs buffer layer between the (Ga,Mn)As film and the substrate. There we can expect the same amount of the defects.Since, We can assume that the diffusivity is similar in the LT-GaAs as in the (Ga,Mn)As. This argument fails.

Second possible argument claiming that diffusivity can be so low that the interstitials have not enough time to penetrate deeper into the substrate is not valid. If the diffusivity is so small, interstitials would not have enough time to migrate towards the surface. Moreover, the inhomogeneity of the (Ga,Mn)As would be regularly observed which does not happen.

So, it is quite certain that both the diffusion and drift forces are present. Therefore, the migration of the interstitials into the substrate has to be denied intentionally in simple diffusion model. It formulates the boundary conditions setting the zero flux of the interstitials through the film/substrate interface ($j_p|_{z=0} = 0$). We can restrict ourselves spatially only to the layer ($z \in \langle -H, 0\rangle$). The model for our container defining the second boundary condition stays the same.

Summary

We introduced the drift-diffusion model for the interstitials that consists of D-D equations with boundary conditions at both borders of the layer, i.e., surface and layer/substrate interface. The model presumes the behaviour of the interstitials near the surface that can be modelled by the hypothetical surface container.

As the solving of the D-D equations turned out to be little bit tricky, we suggest the implementation of this task for a particular solver. Finally, we made remark on the different concept of the interstitial migration, a simple diffusion. However, both approaches have to be tested by the comparison with experimental data (chapter 9).

Chapter 9

Simulation of annealing procedure

In this chapter, we use the theory from chapter 8 for the simulation of the annealing. The simulated density profiles of interstitials are compared to the interstitial density determined in chapter 5. We simulate both the long-term annealing and consecutive etching-enhanced long-term annealing of sample B-1. From chapter 5 we know that sample B-2 has some gradient in the depth profile of interstitial density. We search for the parameters of the drift-diffusion model to match the profiles resulted from the x-ray diffraction and drift-diffusion calculation, i.e., annealing simulation.

We start by the initial guess of the diffusion-model parameters. They are guessed from previously reported experiments or taken from the literature. Finally, we show the optimized values of those parameters. They were tuned to the qualitatively and also as much as possible quantitatively replicate the experimentally obtained profiles.

9.1 Initial guess at D-D model parameters

The motivation for the (drift-)diffusion simulations arose from the unambiguous experience with the vertical inhomogeneity of the sample B-2 that was found to be homogeneous before the cyclical etch-annealing treatment. Actually, the annealing combined with the etching of the oxidised surface were primarily performed to achieve the fully annealed sample possibly free of any interstitials. As we saw, the decrease of the interstitials was not dramatic as we expected, moreover the distribution of the interstitials became inhomogeneous in such a way that there were lower interstitial density near the surface. Now we assume that the annealing times were coincidentally so short together with the frequent surface cleaning that such a density profile can be achieved. As the inhomogeneous distribution reminded a concentration gradient due to some flow of the interstitials through the surface interface, it was good opportunity to study the annealing process.

Later, we were interested if the inhomogeneity is not a result of some degradation of the sample, e.g., the formation of some stable interstitial complexes deep in the layer or the formation of some new defect which is not further affected by the annealing. As we saw in the previous section, the final long annealing makes the layer vertically homogeneous again and the interstitial density decreased again,

thus the larger decrease was expected.

We used the theory described in chapter 8 for the simulation of the annealing in order to obtain the qualitatively same interstitial profiles as we determined by the HRXRD in the previous section. The D-D model contains three unknown parameters ($N_{\mathrm{S,max}}$, S_0 and D_n) which had to be estimated to get match simulated and determined profiles.

Firstly, let us guess the capacity of the model container $N_{\mathrm{S,max}}$ from the decrease of the summed interstitial density during A-1→B-1 (denoted as $\Delta c_{\mathrm{int}}^{\text{A-1}\to\text{B-1}}$). The resulted sample was determined to be homogeneous, therefore, we assume that the surface container was at least severally saturated; the flow into that was low. And the mobile interstitials just redistributed themselves to reach thermodynamic equilibrium, i.e., homogeneous distribution. The decrease of the interstitial density can be expressed in units of particles per volume as

$$\Delta c_{\mathrm{int}}^{\text{A-1}\to\text{B-1}} = (-0.9 \pm 0.2)\% = (2.0 \pm 0.4) \cdot 10^{20}\,\mathrm{cm}^{-3}\,, \tag{9.1}$$

which multiplied by the layer volume give the amount of interstitials removed during the annealing from the layer. The D-D solving of the laterally homogeneous layer is one-dimensional problem, therefore we are interested in the number of removed interstitials per unite area of the surface:

$$N_{\mathrm{S}}^{\text{A-1}\to\text{B-1}} = \Delta c_{\mathrm{int}}^{\text{A-1}\to\text{B-1}} T^{\text{B-1}} = (2.1 \pm 0.5) \cdot 10^{15}\,\mathrm{cm}^{-2}\,. \tag{9.2}$$

The value of $N_{\mathrm{S}}^{\text{A-1}\to\text{B-1}}$ corresponds to the container filling after the A-1→B-1 annealing and it can be good estimation of the container capacity at least in order of magnitude. This quantity is comparable with the suggested value for the container capacity $N_{\mathrm{S}}^{[62]} \approx 4 \times 10^{15}$ particles/cm^2 in chapter 8 , whose estimation is based on the experimental results in Reference 62.

Our simulation consisted from three steps. Firstly, the determined density profile of the sample A-1 was taken as a starting point and the drift-diffusion during the A-1→B-1 annealing was simulated. Then the density profile obtained from that simulation was taken as the starting point for the simulation of the etch-annealing procedure. Each time the surface container was emptied and the thickness of the model layer was decreased for 0.8 nm, then the one hour annealing was simulated and its result was used for the next iteration. Such a computation ran 20 times to obtain the simulated density profile for the sample B-2. Finally, the 80 hours long annealing was simulated with the partially filled container remained from the B-1→B-2 process.

The question arose how to qualify the match of the resulted profiles with those obtained from the diffraction method. It is hard to define suitable criteria to evaluate just such match, e.g., χ^2 function. In principle, it should be possible to optimize numerically to fit the experimental diffraction data, which means to solve the D-D problem for all samples with certain diffusion parameters and to use an obtained solution for the diffraction curves simulation.

Unfortunately, this approach is extremely slow due to the time consuming calculations of D-D solution, and moreover, the sensitivity of the diffraction profiles to the diffusion parameters is very problematic. The average interstitial density in the sample is crucible for the match of the diffraction data, on the other hand the layer inhomogeneity changing the intensity of the thickness oscillations

affects the χ^2 rather weakly. Therefore, any local optimization method tends to fit firstly the layer peak and this can drive the solution towards nearly arbitrary inhomogeneous density profiles. Such solutions are close to local minima of χ^2 function and the match cannot be further meaningfully improved. We assume that such a fitting can be successful only for the good guess of the starting parameters being close the global optimum. The other option could be to use some of enhanced global fitting methods (e.g., genetic algorithm), which are usually much more demanding on the number of function evaluations. However, here just one evaluation is so time consumptive that this task can be hardly performed with available calculation capacity.

We would be satisfied with just a qualitative agreement, which means that homogeneous profile for samples B-1 and B-3 are more acceptable though possibly shifted than the inhomogeneous profile going closer to the determined level of the interstitial density. Therefore we performed D-D simulations A-1→B-1→B-2→B-3 for many sets of the diffusion parameters D_n, $N_{\mathrm{S,max}}$ and S_0, covering all possible combinations of values on the discrete grid within the limit of several orders of magnitude around the expected values. Then we manually evaluated the results as more or less satisfying in order to get closer to the most probable values of the diffusion parameters.

The lowest limit for the container capacity we set to $N_{\mathrm{S}}^{\text{A-1}\rightarrow\text{B-1}}$, obviously the container has to be able to store at least such an amount of the interstitials. Hereafter, we searched for the diffusivity value around 10^{-21} m^2/s being inspired by the $D_n^{[39]}$ found in Reference 39. The phenomenological S_0 is hard to guess and evidently the wider range of the orders of magnitude has to be checked. Though we can speculate little bit considering that too low value would lead to the removal of the insufficient number of interstitials, for each considered (D_n, $N_{\mathrm{S,max}}$) we can find very quickly the lowest S_0, which allows at least any change within the scale of annealing times.

On the other hand, S_0 increased above certain value causes the complete depletion of the interstitials at the boundary of the region where the D-D is considered. This corresponds to the situation that all interstitials are passivated instantly as they come closer to the surface. Actually, this can be viewed as unconstrained continuous flow of the interstitials from the system, and we experienced the numerical problems when we tried to solve the D-D equations with S_0 above such a high limit. Anyway, the high S_0 values leads to extremely inhomogeneous density profiles below the surface, if the total decrease of the interstitials should more or less correspond to the densities determined by the HRXRD.

We can guess very roughly the time scale of the fastest interstitial removal from the system, which can be similar to the time scale of the free flow of the interstitials through the layer and out of the layer. Let say the order of magnitude of such S_0 can be roughly compared with an averaged speed of the interstitial ion on the journey through our whole 100 nm thick sample that would last whole annealing (24 hours). The removal rate S_0 should be approximately $\frac{10^{-7}\,\mathrm{m}}{24\times 3600\,\mathrm{s}} \approx 10^{-12}$ m/s to absorb such a flux.

9.2 Guess at D-D model parameters from D-D simulation

From the manual evaluation of the obtained simulation we selected those bringing the best agreement of the simulated profiles and the depth profiles determined by HRXRD. And similarly to the previous step we repeated the simulations on the finer grids around all triads of diffusion parameters being good candidates in the mean of previous evaluation. This highly time consumptive searching allowed us to find a satisfactory solution of the D-D equations qualitatively corresponding to the determined interstitial densities. Using this procedure, we found the following values: $\mu_n \sim 2 \times 10^{-18}$ $\mathrm{m^2 \cdot V^{-1} \cdot s^{-1}}$, $D_n \sim 4 \times 10^{-20}\,\mathrm{m^2 \cdot s^{-1}}$, and $S_0 \sim 3 \times 10^{-13}\,\mathrm{m \cdot s^{-1}}$. The diffusion coefficient estimated from our simulations is approximately 30 times larger than $D_n^{[39]}$.

If we used the published value of the diffusion coefficient in our model, we would not be able to explain more or less simultaneously both the observed inhomogeneity and the decrease of the total amount of the interstitials. Unfortunately, there is a lack of published values of the interstitial diffusivity in (Ga,Mn)As for a detailed comparison, anyway, there is a large discrepancy between them. For instance, in Reference 64, the value $D_n^{[64]} \approx 2.1 \times 10^{-23}\,\mathrm{m^2 \cdot s^{-1}}$ is smaller by several orders of magnitude than the values extrapolated from the results in Reference 39 for the same annealing temperature as in Reference 64(210°C). Our diffusivity is much higher although out annealing temperature is lower (160°C).

The comparison of the simulated concentration profiles and the profiles determined from the HRXRD measurements are shown in Figure 9.1. The uncertainty of the HRXRD results that evidently affects also the initial values for the simulation, allows us to estimate the diffusivity only very roughly. For the demonstration of the sensitivity of the profile on the diffusivity value, we included also the simulation results for 10 times larger and 10 times smaller diffusivities in Figure 9.1, the latter value being close to that in Reference 39.A higher diffusivity leads to a more homogeneous concentration profile, whereas a smaller diffusivity yields a highly inhomogeneous profile.

The optimized value of the maximum container capacity following from the numerical simulation of the diffusion is $N_{\mathrm{S,max}} \sim 3 \times 10^{19}\,\mathrm{particles/m^2}$.

Finally, from the diffraction data of sample B-3 it follows that the layer was homogenized again during the final 80-hour annealing (B-2→B-3); the thickness of the crystalline layer is smaller even without the etching procedure, most probably, due to the strong oxidization of the surface during the long time delay before the final annealing. Therefore most probably, we were not able to estimate the state of the surface container before the final annealing and this we consider to be a reason why the simulated and the measured profile of the interstitial concentration in the sample B-3 could not be compared. The HRXRD measurement of the sample B-3 indicates that the inhomogeneity in the previous sample state (B-2) was not caused by the formation of any immobile defects during the annealing, because the inhomogeneity disappeared after the annealing.

Concluding our observations from the numerical simulations, we formulate the interpretation of the annealing process in (Ga,Mn)As layers, very often identified with out-diffusion of the interstitials. The highly mobile holes reach very quickly an equilibrium state in which their diffusion flux is compensated by the drift flux.

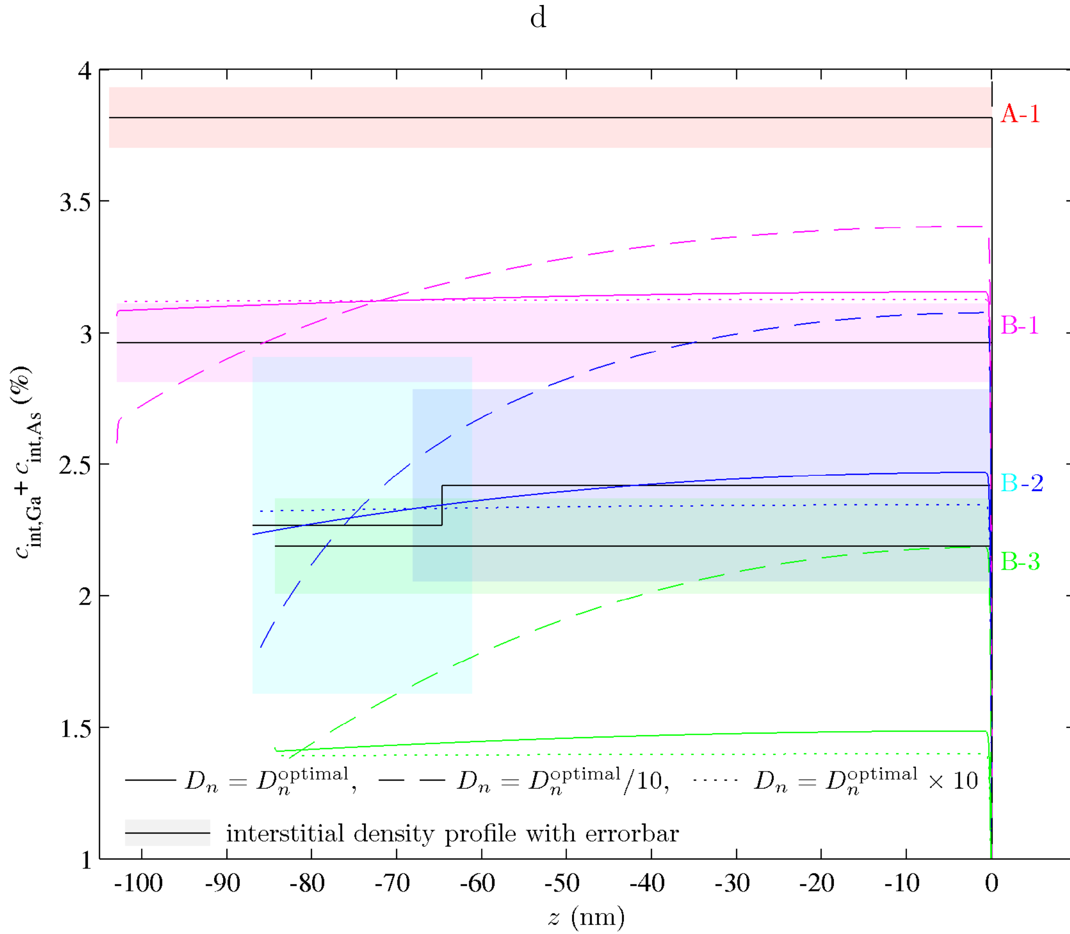

Figure 9.1: Depth profiles of the interstitial concentration in sample A, B-1, B-2 and B-3. The concentration profiles determined by HRXRD are represented by the black solid curves with coloured semitransparent areas indicating the uncertainty of the profiles. The profiles obtained from the diffusion simulations for the interstitial diffusion constant $D_n^{\text{optimal}} = 4 \times 10^{-20}\,\text{m}^2/\text{s}$ are plotted by solid coloured lines; the concentration profiles simulated for 10 times smaller and 10 times larger values of the Mn diffusion constant are plotted by dashed and dotted and dashed lines, respectively. The initial concentration profile for the A-1→B-1 simulation is given by the concentration of Mn interstitials in sample A-1. The starting density profile for the simulation of every following annealing comes out from the result of the preceding one.

This stable state is the result of two driving forces: the compensation of the local charge unbalance and the uniform distribution of the particles driven by the diffusion. If the diffusion of the holes was neglected, it would be equivalent to the situation when the holes would perfectly screen the charge of the substitutional Mn ions. In this case, of a perfect screening, the Mn interstitials would not feel the electric field and their migration would be driven only by the diffusion.

The calculated profiles of the interstitial densities including and neglecting the diffusion process of the holes are compared in Figure 9.2. The excess holes near the surface, caused by the passivation of the interstitials, diffuse deeper into the layer leaving the space below the surface negatively charged. On the other hand, the bottom part of the layer starts charging positively as more holes

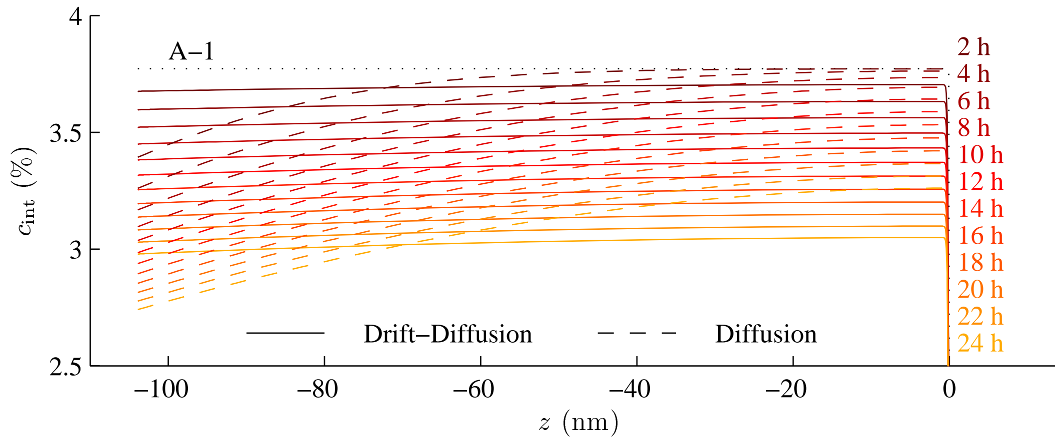

Figure 9.2: Depth profiles of the Mn interstitial concentration following from the numerical simulations for a post-growth annealing of sample A-1 (the A-1→B-1 process). The solution of the drift-diffusion equations (solid lines) is compared to the solution neglecting the drift and including only diffusion (dashed lines). The time evolution of the depth profile is represented with the time step of 2 hours by the different colours. The dotted line shows the initial concentration profile of uniformly distributed interstitials.

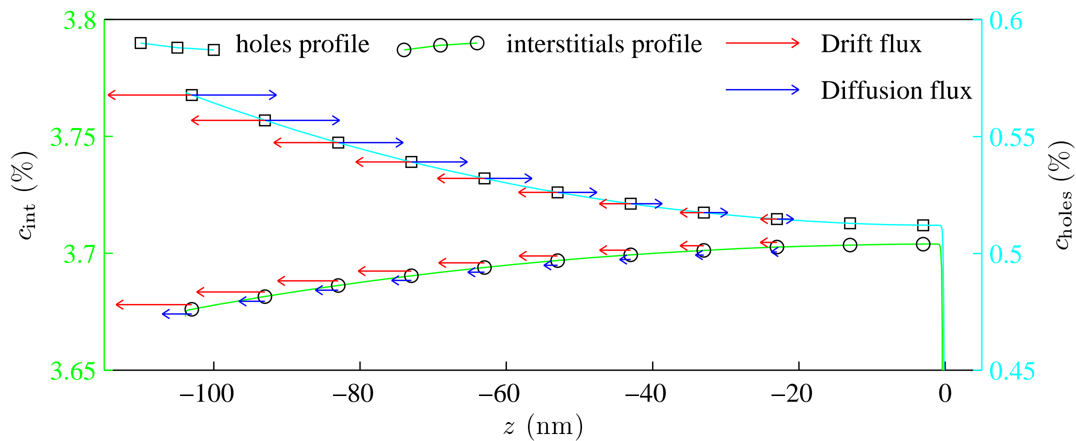

Figure 9.3: The simulated depth profile of interstitial concentration (circles) and the holes (squares) after 2 hours of the post-growth annealing A-1→B-1. The calculated fluxes caused by the diffusion (blue) and the drift (red) are illustrated by the arrows indicating the direction and the magnitude of the local flux. The arrows have different scales for the holes and for the interstitials. For the interstitials, the arrows for the diffusion flux are 10 times magnified with respect to the arrows representing drift flux for clarity.

arrive here by the diffusion. This charge unbalance produces an electric field acting on the interstitials. The resulting electrostatic force acts on the interstitials in the same direction as on the holes since both particle types are positively charged. However, in contrast to the holes, the surface layer acts as a sink for the interstitials and consequently the interstitials diffuse to the surface. The effects of drift and diffusion are superimposed creating the resulting density profiles of the holes and interstitials shown in Figure 9.3.

Conclusion

We guessed the initial values for diffusion-model parameters from the experimental results in chapter 5 and chapter 7. Some parameters were taken from the literature. The D-D equations were solved with varying diffusion-model parameters. And, we optimized these parameters to reach the correspondence of solved and experimentally determined depth profiles of interstitials.

In conclusion, from our simulations, it follows that the drift flux of the interstitials is larger than the diffusive flux. As Figure 9.2 demonstrates, the diffusion of the interstitials itself produce an inhomogeneous layer with a large concentration gradient. Such a large inhomogeneity was not observed by HRXRD; the (Ga,Mn)As layers are usually homogeneous even for the samples in which the annealing was stopped before reaching the best possible improvement of their magnetic properties. On the other hand, the model including both migration processes of the interstitials and the holes produces a small gradient of the interstitial concentration and the number of the interstitials in the layer after the annealing is smaller than in case of the diffusion alone. Therefore, we consider that the main process responsible for the interstitial migration is the drift driven by the rapid diffusion of the holes.

Chapter 10

(Ga,Mn)As/AlGaAs multilayers studied by x-ray reflectivity

Here, we present briefly one of our minor x-ray experiments, which is related to the (Ga,Mn)As topic. Though it does not overcome an extent of usual characterization methods, we feel appropriate to mention these experimental results although their deeper physical interpretation would need other complementary experiments/information on the samples.

Originally, it was performed as a characterization measurement in order to support other experimental work [139]. The aim was to determine (or to verify) the amount of Al content in the multilayers. However, it turned out that the accuracy of the results was not very high. On the other hand, we got very precisely the relation between electron density variation in the periodic part of the samples. Here, we focus on the interpretation of this result.

Firstly, we describe the x-Ray Reflectivity (XRR) experiment. Then, we propose the interpretation of resulted parameters. Finally, we see that it allows to estimate roughly the ratio of substitutional and interstitial Mn in the (Ga,Mn)As sublayers.

There is a several interest on super-lattices (denoted also multi-layers), which consist of alternating magnetic and non-magnetic both semiconducting layers. It was theoretically shown that such a semiconductor magneto-resistance system could by used for making of spin-filters, spin-valves and magnetic tunnel junction [140]. Moreover, according to prediction in Reference 141, if the holes were confined in the magnetic quantum-wells, it would lead to the significant increase of the Curie temperature. Just such increase was indeed observed in (Ga,Mn)As/GaAs super-lattices, when the thickness of the paramagnetic GaAs spacer was below 10 monolayers [142].

10.1 Experiment

We examined the series of four (Ga,Mn)As/AlGaAs super-lattices samples fabricated at the Nottingham University in UK by the MBE growth ([139], where they are denoted as Mn340–Mn343). The intentional doping level was 2.25% of Mn in magnetic layers. Just such level was chosen in order to decrease the number of interstitial defects, i.e., to incorporate the Mn atoms mainly into the Ga substitutional lattice positions as it is expected for such a low doping [34, 37]. As

well, this low doping level allowed the higher growth temperature, which should significantly reduce the anti-site defect formation.

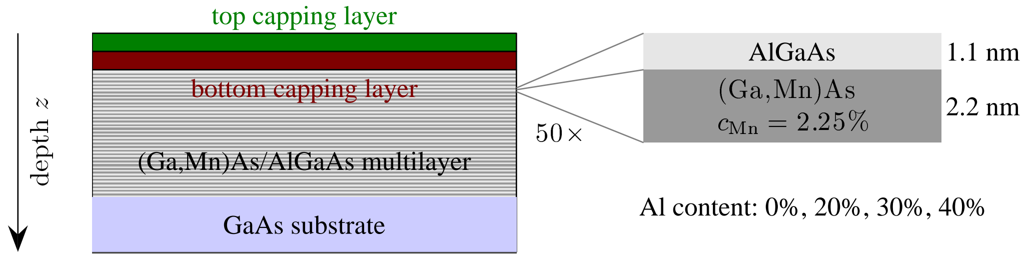

Figure 10.1: Schematic picture of the samples. Finally, we have to assume two distinctive capping layers to obtain the reliable fit.

The super-lattice consists of 50 magnetic/paramagnetic bilayers grown on GaAs substrate. Each bilayer was formed by 8 monolayers of magnetic (Ga,Mn)As (2.2 nm) and 4 non-magnetic $\mathrm{Al}_x\mathrm{Ga}_{1-x}\mathrm{As}$ monolayers (1.1 nm) with Al content $x = 0\%$, 20%, 30% and 40%. Here we denote the samples as AlX, where X is a nominal percentage concentration of aluminium. The whole super-lattice is covered by a non-magnetic low-temperature capping layer(s) to protect the super-lattice from the oxidation. The sample description is summarized in Figure 10.1.

We performed the XRR measurement in order to obtain the depth profile of the electron density in the sample. The measurement was carried on the laboratory diffractometer Panalytical X'Pert MRD. We used the x-ray parabolic mirror behind the x-ray tube to produce the parallel beam. The divergence in the plane of reflection (equatorial) was limited by the divergence slit (labelled as 1/4°) reducing the effective area of the mirror. The axial divergence was controlled by the 0.04 rad short Soller slits, and beam-size in the plane of reflection was defined by the 2mm-mask.

The proportional detector was mounted behind the graphite monochromator. The axial acceptance was given by the short 0.02 rad Soller slits. The equatorial acceptance in the plane of reflection was limited by the 0.27° parallel plate collimator and just only its one central pass was selected by the reflectivity slit.

We measured the intensity of the specular reflectivity $R(\alpha_{\mathrm{i}} = \alpha_{\mathrm{f}})$ up to 5.5°, measured reflectivity curves are plotted in Figure 10.2. Here, the total reflection plateau is not flat, which results from the geometry of the experiment. For the samples with aluminium, there are super-lattice maxima with the frequency corresponding to the bilayer thickness. In case of no aluminium, these super-lattice maxima changes into the weak modulation, as the contrast is given by the mean-electron density difference between the bilayer constituents. Actually, this difference is quite small between the GaAs and (Ga,Mn)As.

A slow modulation of the whole reflectivity curve comes from the capping layer thickness. Apparently, the high-frequency thickness oscillations corresponding to the thickness of the whole periodic part is not observable in the measured data, the angular step is too big to pronounce them.

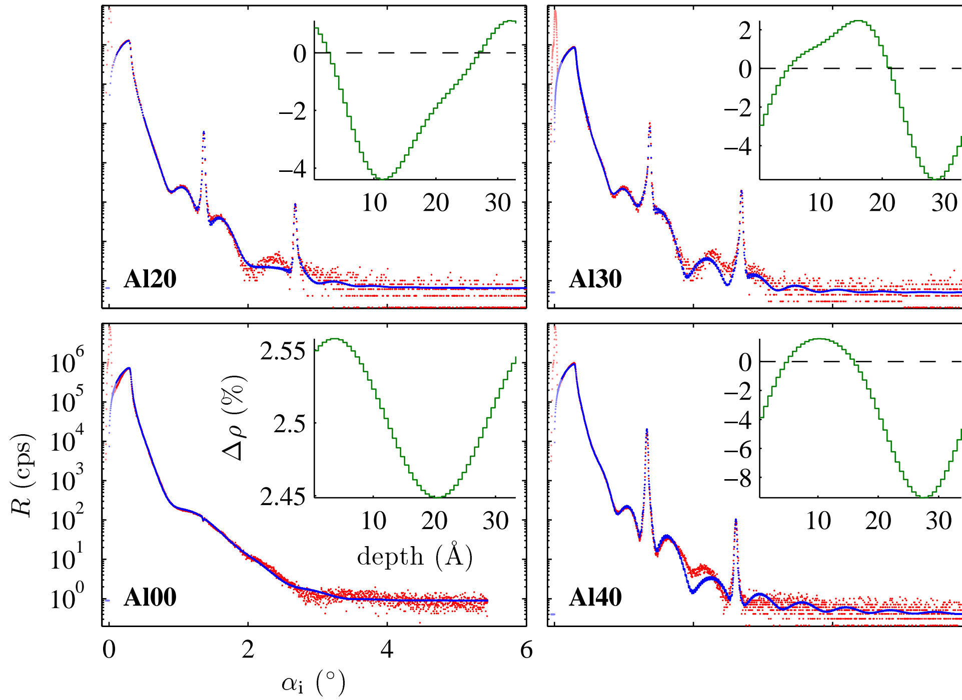

Figure 10.2: Experimental reflectivity curves (red dots) fitted with the numerical simulations (blue curves) for all samples. There is the region $\alpha_\mathrm{i} \to 0$ with the experimental artefact (primary beam) which is not relevant for the fitting procedure (lighter colours). The sharp peaks corresponds to the superstructure periodicity. The resulted modulation of the electron density within one bilayer is plotted in the insets, the step-like shapes of curves depict the discrete homogeneous thin layers entering into the numerical calculation.

Assuming the following model, we fit the experimental reflectivity curves by the numerical simulations based on the dynamical scattering theory. In this case, only refracted and reflected waves are propagating in a material [91].

Let us remind the definition of refractive index $n \equiv 1 - \delta + i\beta$, which can be written in alternative form [133]:

$$n \equiv 1 - \frac{r_0}{2\pi}\lambda^2 \sum_q \rho_q f_q(0)\,. \tag{10.1}$$

Here, r_0 is the classical electron radius and λ the wavelength of the radiation. The summation goes over all atom types in the material. Present atoms of the element q with a density ρ_q have a forward-scattering factor $f_q(0) = f_q^0(0) + f_q' + \mathrm{i}f_q''$. The term $f_q^0(\boldsymbol{Q})$ is a Fourier transformation of the electron density of the isolated single atom q, the latter two terms correspond to dispersion corrections [92]. The forward-scattering factors of the majority of elements for energy range 50–30 000 eV are tabulated in Reference 133.

As found in the literature, the XSTM technique, performed on the various (Ga,Mn)As/GaAs super-lattices, shows the diffusion of the Mn atoms into the adjacent GaAs spacer layers [83]. Therefore, one can expect the smoothed electron density profiles. Obviously, it is not advantageous to describe the (Ga,Mn)As/AlGaAs bilayer as two homogeneous layers with well-defined interfaces. Here, the as-

sumption of some interface roughness is not well relevant because we expect the interfaces rather perfectly smoothed than just rough. The model of a continuous electronic density in the whole bilayer seems to be the most physically relevant assumption. Let us the bilayer thickness denote as L. We define the refractive index $n(z)$ as a function of depth z in the whole periodic region within the range of $50L$ described generally by the Fourier series

$$n(z) = 1 - (\delta - \mathrm{i}\beta)_{\mathrm{GaAs}} \left(\delta_0 + \sum_{j=1}^{\infty} \delta_j \cos\left(\frac{2\pi j}{L} z + \phi_j\right)\right) . \qquad (10.2)$$

The refractive index of GaAs, or better its difference from unity ($(\delta - \mathrm{i}\beta)_{\mathrm{GaAs}}$) corresponding to the electron density of GaAs is used as a reference. In fact, β introduces the absorption into the refractive index via f'', and generally, it should be written as another Fourier series separately. However, the absorption of studied compounds derived from GaAs should not differ significantly. We are completely insensitive to the modulation of absorption in the multilayer. Therefore, we keep the β for GaAs in the definition, but further we talk just about depth profile of δ quantity in the sample. Then, the δ_0 is related to the relative average electron-density in the bilayer, ρ_j and ϕ_j are amplitudes and phases of the Fourier coefficients, respectively.

The numerical realization of the simulation consists in the assumption of the large number of thin flat homogeneous layers with the electron density according to the formula 10.2 inside the periodic region. The rest of the sample (a substrate and capping layers) is described by the stack of thick homogeneous layers. The roughness is considered for the interfaces above, between, and below the capping layers.

The experimental reflectivity curves together with their theoretical fits are plotted in Figure 10.2. The optimized parameters for all samples are summarized in Table 10.1. We have to assume two capping layer to find reasonably good match with the experimental data. Since we see only two intensity satellites corresponding to the super-lattice periodicity, just the first two Fourier components are sufficient to describe the electron density in the periodic region.

Exception was the sample Al00, for which the density modulation was described by only one Fourier term to obtain the unique solution. However, the relative density varies very slightly in this super-lattice, so the contrast is very weak.

The density profiles for all samples are visualised in Figure 10.3. Our model contains several layers, in which the parameters are determined. The thickness and the density of the capping layers have quite large uncertainty complicating the compare the depth profiles of the different samples, because these uncertainties accumulate. However, we can interpret the bilayers parameters, which are quite reliable.

The pairs of capping layers are probably not very important and unfortunately we have no details on the growth finalization. Let us overlook the tendency of increasing mean density in the top capping layer with the higher Al content and let us overlook that there is no similar tendency for the bottom capping layer at all. Probably, we are trying to describe a single vertically inhomogeneous capping layer by many parameters. This produce cumulated uncertainty affecting also

sample	Al00	Al20	Al30	Al40
nominal c_{Al} (%)	0	20	30	40
top capping layer				
rms roughness (nm)	0.4(2)	0.8(2)	0.8(3)	0.8(2)
thickness (nm)	2.6(3)	3.2(2)	3.2(3)	2.8(2)
δ_0 (%)	73(9)	76 (5)	80(1)	84(5)
bottom capping layer				
rms roughness (nm)	0.8(6)	0.3(1)	0.2(1)	0.7(1)
thickness (nm)	2.6(7)	8.1(7)	7.1(8)	6.9(2)
δ_0 (%)	105(6)	99(3)	103(5)	102(4)
multilayer				
rms roughness* (nm)	0.5(2)	0.3(2)	0.4(1)	0.2(1)
period L (nm)	3.36(1)	3.32(1)	3.30(1)	3.41(1)
δ_0 (%)	103(2)	98(5)	99(4)	97(4)
δ_1 (%)	0.05(9)	2.5(3)	3.8(4)	5.5(4)
δ_2 (%)	—	0.6(3)	0.7(5)	0.7(4)
ϕ_1 (rad)	5.66(1)	0.70(1)	0.73(1)	4.41(1)
ϕ_2 (rad)	—	1.50(1)	5.97(1)	2.47(1)

Table 10.1: Optimized parameters of the stacked samples resulted from the fitting of the reflectivity curves. The root mean squared (rms) roughness for the multilayer (denoted by the * is the roughness of the interface between the multilayer and its closest capping layer.

the determined mean density of the multilayer. Therefore, we will focus on the optimized parameters for the periodic area.

10.2 Interpretation of relative electron densities

The unit cell of GaAs contains $4\times(31+33)$ electrons belonging to Ga (with atomic number $N = 31$) and As ($N = 33$) atoms. The number of electrons in unit cell decreases by 18 for each Ga atom substituted by the Al ($N = 13$). Similarly Mn atom ($N = 25$) decrease this number by 6 while each As anti-site defect adds two electrons. Each interstitial defect fully contributes to the number of electrons. The real part of the forward-scattering atomic factor f_1 is approximately equal to N. However, for our interpretation, it is necessary to include the dispersion correction, which is about 2%–4% of N value. We use f_1^{element} values tabulated in Reference 133.

From the fitting, we obtained the relative value of the δ with respect to that of a GaAs. For $\mathrm{Al}_x\mathrm{Ga}_{1-x}\mathrm{As}$, we can write this ratio as

$$\frac{\delta_{\mathrm{AlGaAs}}}{\delta_{\mathrm{GaAs}}} = \frac{V^{\mathrm{ucell}}_{\mathrm{GaAs}}}{V^{\mathrm{ucell}}_{\mathrm{AlGaAs}}} \frac{4(1-x)f_1^{\mathrm{Ga}} + 4f_1^{\mathrm{As}} + 4xf_1^{\mathrm{Al}}}{4f_1^{\mathrm{Ga}} + 4f_1^{\mathrm{As}}}\,, \tag{10.3}$$

where x is an Al occupancy of Ga lattice sites, and $V^{\mathrm{ucell}}_{\dots}$ is the volume of a unit cell of a particular material.

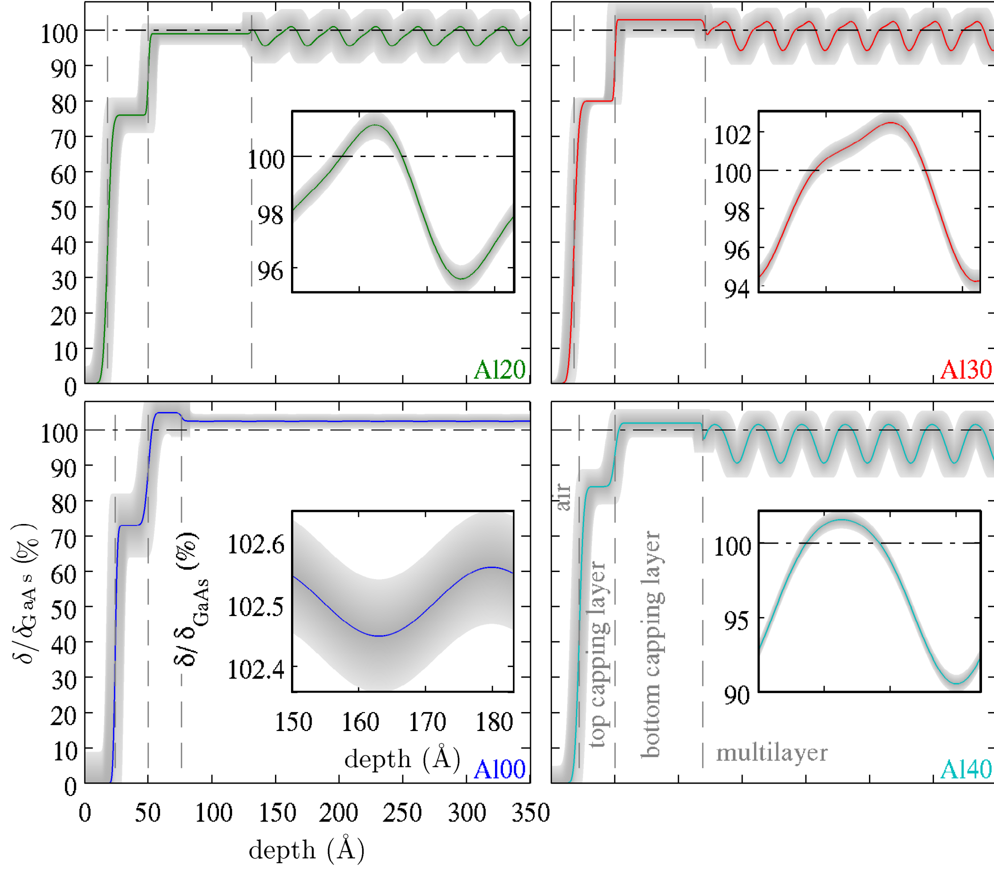

Figure 10.3: Depth profiles of the relative δ are plotted for all samples. Here, this change can be approximatively viewed as a relative electron density with respect to a pure GaAs. The top part of the samples is depicted showing the both capping layers and several periods of the super-lattice. The resulted values for the interface roughness are used to smear the step-like profiles of homogeneous layers. We assumed the density to have the shape of the error function near the interface. The smeared grey areas indicate the uncertainty of the determined most probable profiles. The relative-density profile of the one bilayer is plotted in the insets. Here the uncertainty region is smaller as individual parameters describing the bilayer are more accurate.

Similarly, we can express the relative δ for (Ga,Mn)As

$$\frac{\delta_{\text{(Ga,Mn)As}}}{\delta_{\text{GaAs}}} = \frac{V^{\text{ucell}}_{\text{GaAs}}}{V^{\text{ucell}}_{\text{(Ga,Mn)As}}} \frac{4(1-c_{\text{sub}})f_1^{\text{Ga}} + 4f_1^{\text{As}} + 4(c_{\text{sub}}+c_{\text{int}})f_1^{\text{Mn}}}{4f_1^{\text{Ga}} + 4f_1^{\text{As}}} \tag{10.4}$$

The δ_{GaAs} is modified by the presence of substitutional and interstitial Mn atoms. Here, we should remind that $c_{\text{int}} \equiv c_{\text{int,As}} + c_{\text{int,Ga}}$, therefore, a double multiplicity of the interstitial lattice sites are hidden in this definition and not present in the prefactor in Equation 10.4.

Taking into account that all layers are epitaxially strained on the substrate, the relative volume of unit cells is exactly the ratio of the vertical lattice parameters of the layer ($a_\perp$) and the substrate (a_{GaAs}). The relation between $a_\perp$ and the relaxed lattice parameter a of the layer follows from the elasticity theory. Denoting $\mathfrak{f}$ the lattice mismatch between the layer and the substrate relaxed lattice

parameters ($a = (1+\mathfrak{f})a_{\text{GaAs}}$), we can write

$$a_\perp = a - 2\frac{c_{12}}{c_{11}}(a_{\text{GaAs}} - a) = \left(1 + \frac{2c_{12} + c_{11}}{c_{11}}\mathfrak{f}\right) a_{\text{GaAs}} \equiv (1 + C\mathfrak{f})a_{\text{GaAs}}\,, \quad (10.5)$$

where c_{11} and c_{12} are elastic constants of the cubic materials, finally summarized in the material constant C for the simplicity.

Generally both quantities $\mathfrak{f}$ and C varies with the concentration of the aluminium and the manganese. Those are

$$a_{\text{GaAs}}\mathfrak{f}_{\text{AlGaAs}} = x \times 0.0078\,\text{Å}\,, \qquad C = \frac{22.64 + 0.76x}{11.88 + 0.14x} \quad (10.6)$$

for the $\text{Al}_x\text{Ga}_{1-x}\text{As}$ [143]. However, the $C(x)$ dependence is not very important. We processed all numerical calculations with $C(x)$ being replaced by the $C(0)$, as well; the numerical difference was few orders of magnitude smaller than uncertainties of the final values. Therefore, all further calculations can be treated with the approximation of the elastic properties identical to whose of the GaAs, although there is no principal need of this approximation.

On the other hand, the elastic constants for (Ga,Mn)As are not known, but it is assumed that their difference from those of GaAs is negligible taking into account the very low Mn concentration. The exact relation of the $a_{\text{(Ga,Mn)As}}$ and the Mn content is much more important but much more problematic, as well. Here, we keep the unknown function $\mathfrak{f}_{\text{(Ga,Mn)As}} \equiv \mathfrak{f}_{\text{(Ga,Mn)As}}(c_{\text{sub}}, c_{\text{int}})$

Anywhere in the periodic area, the relative electron density as well as relative δ can be expressed as a weighted sum of two different contributions: pure (Ga,Mn)As and pure AlGaAs. The weights are given by the level of (Ga,As)Mn/AlGaAs intermixing. Including the possible presence of anti-site defects, we can write general expressions for the relative δ of the pure (Ga,Mn)As

$$\frac{\delta_{\text{(Ga,Mn)As}}}{\delta_{\text{GaAs}}} = \frac{1 + \frac{f_1^{\text{Mn}} - f_1^{\text{Ga}}}{f_1^{\text{Ga}} + f_1^{\text{As}}} c_{\text{sub}} + \frac{f_1^{\text{Mn}}}{f_1^{\text{Ga}} + f_1^{\text{As}}} c_{\text{int}} + \frac{f_1^{\text{As}} - f_1^{\text{Ga}}}{f_1^{\text{Ga}} + f_1^{\text{As}}} c_{\text{anti}}}{1 + C(\mathfrak{f}_{\text{(Ga,Mn)As}} + \mathfrak{f}_{\text{LT}})} \quad (10.7)$$

and of the pure AlGaAs

$$\frac{\delta_{\text{AlGaAs}}}{\delta_{\text{GaAs}}} = \frac{1 + \frac{f_1^{\text{Al}} - f_1^{\text{Ga}}}{f_1^{\text{Ga}} + f_1^{\text{As}}} x + \frac{f_1^{\text{As}} - f_1^{\text{Ga}}}{f_1^{\text{Ga}} + f_1^{\text{As}}} c_{\text{anti}}}{1 + C(\mathfrak{f}_{\text{LT}} + x \times 0.0078\,\text{Å})}\,. \quad (10.8)$$

The growth low-temperature conditions are the same for both materials in the bilayer. Therefore, both the concentration (c_{anti}) of the anti-site defect and corresponding expansion ($\mathfrak{f}_{\text{LT}}$) should be identical in both materials. However, in our case, the anti-site concentration is reduced due to the higher growth temperature, therefore the anti-site terms can be omitted.

10.3 Estimation of substitutional-interstitial ratio

From the determined density profiles of the bilayers in Figure 10.3, we can see that amplitude of the density modulation increases with the higher Al content.

Obviously, the number of electrons in the unit cell decreases while the unit cell diameters tend to increase. Realizing this, we can assume that maximum of the density profile (and δ) corresponds to the pure (Ga,Mn)As material and the minimum to the pure AlGaAs. Therefore, the difference of those extremes can be expressed as

$$\Delta \equiv \frac{\delta_{(\mathrm{Ga,Mn})\mathrm{As}}}{\delta_{\mathrm{GaAs}}} - \frac{\delta_{\mathrm{AlGaAs}}}{\delta_{\mathrm{GaAs}}} = \frac{1 + \frac{f_1^{\mathrm{Mn}} - f_1^{\mathrm{Ga}}}{f_1^{\mathrm{Ga}} + f_1^{\mathrm{As}}} c_{\mathrm{sub}} + \frac{f_1^{\mathrm{Mn}}}{f_1^{\mathrm{Ga}} + f_1^{\mathrm{As}}} c_{\mathrm{int}}}{1 + C\mathfrak{f}_{(\mathrm{Ga,Mn})\mathrm{As}}} - \frac{1 - \frac{f_1^{\mathrm{Al}} - f_1^{\mathrm{Ga}}}{f_1^{\mathrm{Ga}} + f_1^{\mathrm{As}}} x}{1 + Cx \times 0.0078\,\text{Å}}, \tag{10.9}$$

Determined differences Δ obey this formula for all samples except Al00. Apparently, we are not able to simply decide if the maximum of the relative density in the bilayer corresponds to the GaAs or the (Ga,Mn)As because there is no significant decrease usually provided by the presence of an aluminium. The (Ga,Mn)As has definitely a larger volume than GaAs, but the decrease of the density caused by the expansion can be compensated by the presence of a larger amount of the interstitials, which can possibly lead to the increase of the density.

All multilayers were grown within the same conditions, therefore, we can assume that pure parts of the bilayers should be almost identical. Since, we can search for identical parameters c_{sub}, c_{int}, and $\mathfrak{f}_{(\mathrm{Ga,Mn})\mathrm{As}}$ that suit for all samples simultaneously at the most.

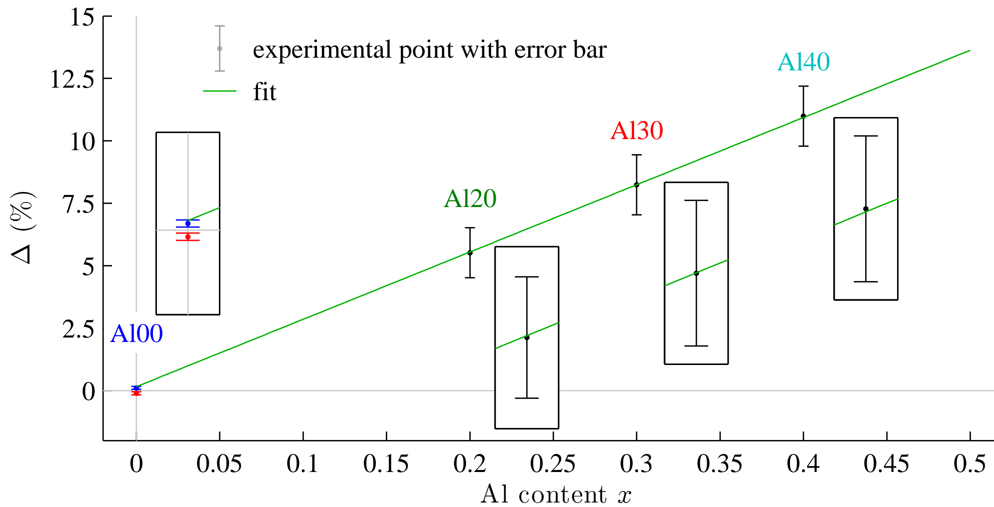

Figure 10.4: Experimental Δ for samples Al(20,30 and 40). The concentrations c_{sub}, c_{int} are optimized to fit the experimental data (black points with errorbars). Both positive (blue) and negative (red) values of Δ for sample Al00 are plotted. The green curve corresponds to our model with fitted parameters. The vicinity of the experimental points are plotted in the insets showing the difference in detail. It is evident that the model curve approaches the positive Δ value for sample Al00.

Unfortunately, all these parameters are completely correlated, and we are not able to determine them. Since, we are only able to determine allowed pairs

(c_{sub},c_{int}) while some expansion of the lattice is assumed. We assumed the expansion between zero and the estimated lattice parameter from Equation 3.2. From the fitting of the to differences (Δ) of the extremes in the experimentally determined bilayer depth profiles (Figure 10.4), we obtained such allowed pairs of (c_{sub},c_{int}).

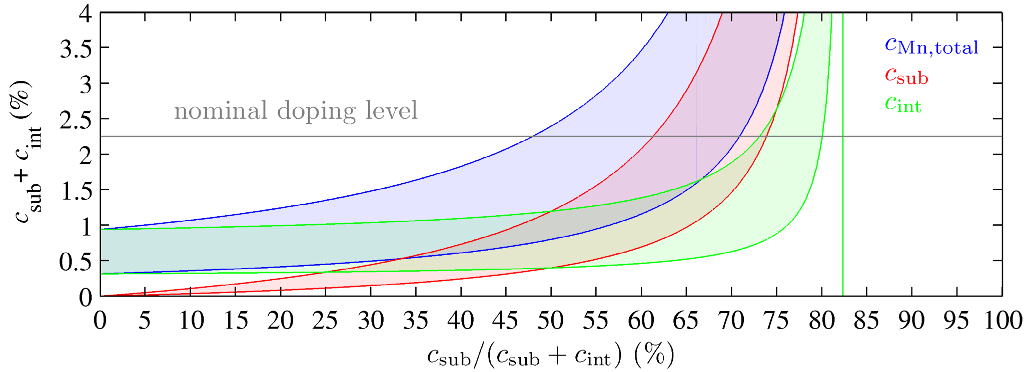

Figure 10.5: Calculated Mn concentrations (c_{sub}, c_{int}, and $c_{\text{sub}}+c_{\text{int}}$) for all possible values of relative Mn substitutional content. All points are numerically allowed in the transparent areas. Probably the most relevant solutions are given by the intersection of the uncertainty area and the horizontal line corresponding to the intended doping level.

The numerically allowed (but not necessarily possible) concentrations are a hyperbolic function of the ratio $\frac{c_{\text{sub}}}{c_{\text{sub}}+c_{\text{int}}} \in \langle 0, 1\rangle$ (i.e, the share of substitutional Mn on the total Mn content). We plot the numerically allowed concentrations with respect to an arbitrary share of the substitutional Mn on the total content (Figure 10.5). The uncertainty region of this dependence is formed by all possible hyperbolas calculated for various expansion of the lattice.

The additional information on the total Mn content in the sample, for instance, from the SIMS, allows to determine from Figure 10.5 the Mn fraction incorporated in the substitutional positions. Here, we can estimate the total content by the intended doping level of the growth (2.25%). It allows to very roughly estimate that there are 48%–70% of the Mn atoms in the substitutional lattice positions.

Let us go back to sample Al00, for which the extremes of the relative density profiles are not yet identified with the GaAs or (Ga,Mn)As part of the bilayer. From the Figure 10.4, we can see, that the case of positive Δ more suits to our model. Therefore, we can conclude that the relative density (or δ) is higher than that of GaAs. In other words, the minimum of the relative density profile corresponds to the (Ga,Mn)As part of the bilayer.

Concurrently, there are HRXRD measurements of these samples published in Reference 139, where the experimental diffraction curves are fitted with the bilayer model of non-defected AlGaAs (i.e., obeying the Vegard's law for pure GaAs/AlAs) and GaMnAs. From this work, the mismatch between the (Ga,Mn)As in the bilayer and the substrate follows as $\mathfrak{f}_{(\text{Ga,Mn})\text{As}} \approx 1.13\%$. Considering the Mn content on the intended doping level, it corresponds to the 74% of Mn atoms being substitutional when calculated using Equation 3.2. Here, the theoretical formula predicts the substitutional share from the lattice expansion due to the

presence of the Mn atoms in the GaAs lattice and guessed total Mn content. It corresponds to our estimated upper limit on the substitutional share. Nevertheless, the theoretical lattice-expansion formula is rather predictive than a general rule. Therefore, the qualitative agreement that a majority of Mn atoms are in the substitutional positions is quite satisfying.

The author in Reference 139 measure the diffraction on the same samples, here Al(00,20,30,40), using HRXRD. There, the experimental intensity distributed along CTR in the vicinity of GaAs(004) maxima is fitted. Shortly said, the fitted lattice mismatch is converted to the Mn concentration using Vegard's law and the model of a hypothetical cubic MnAs [144]. Unfortunately, this approach is not consistent with the theoretically prediction on lattice parameter as a function of particular Mn concentrations. However, using the empirical approach [144], author estimates the Mn content as 2.7%–3.0% regarding the particular sample, being aware that it can be slightly overestimated. On the other hand, author determined the effective Mn concentration, i.e., $c_{\mathrm{sub}} - 2c_{\mathrm{int}}$, from the magnetometry measurement as 1.9% for the sample Al00. This number corresponds to 87%–95% of Mn in substitutional positions assuming the total concentration between the overestimated value and the intended doping level. These numbers are slightly higher than our estimated interval, even if we consider a higher total Mn content inspired by the Reference 139.

Conclusion

We presented the XRR measurement of (Ga,Mn)As/AlGaAs multilayers. From the experimental data, we obtained relatively uncertain electron-density profiles in the sample. However, the density variation in periodic part is determined quite accurately and reliably.

Concluding our experiment, we were able from the reflectivity measurement estimate, however only very roughly, the share of the substitutional Mn on the total content. The resulted numbers are physically relevant, i.e., numerical allowed solutions contains those with the total Mn content matching the expected doping level. Moreover, the agreement of our model with the positive value of Δ_{Al00} indicated the lower electron density of the Mn richer part of that super-structure bilayer.

The estimations showed the prevalence of the substitutional Mn at the expense of those in interstitial positions. Taking into account that each interstitial Mn atom compensate two substitutional atoms, we find the bottom limit at $\frac{c_{\mathrm{sub}}}{c_{\mathrm{sub}}+c_{\mathrm{int}}} > \frac{2}{3} \approx 67\%$ for the (Ga,Mn)As to be magnetic. However, this value is close to the border of our estimated interval. But the samples are magnetic, indeed [139]. Since, it seems that our values for substitutional share are still underestimated.

However, the agreement with the different experiment was just qualitative, showing the minority presence of the interstitials. Actually, there are some expectations which do not need to be satisfied. We really do not know, how the inter-mixing affects the central part of original sublayers in the bilayer. Probably, the composition there does not correspond to the nominal values due to the inter-diffusion. This experiment could by definitely improved, if the bilayer are thicker, and the volume with the gradient of the properties are negligible.

Moreover, we do not really know, if there are any other defects present in the AlGaAs. We do not know if the consideration of the same defect level in whole bilayer is correct. Unfortunately, we have just three points in our statistic, i.e., Al20, Al30, and Al40. Figure 10.4 shows the experimental points in the detail. From such low points we cannot decide if there is any tendency, i.e., if the tangent of the dependence differs from that given by our model. Also, we are not completely sure that all original (Ga,Mn)As layers are identical.

Particularly for the (Ga,Mn)As study, we dispensed with the expansion formula Equation 3.2. We used just AlGaAs as a reference, since we used the well known properties of the AlGaAs alloy.

These experiment can be considered as a demonstration of the x-ray reflectivity capability, being complementary technique for other methods. There are only few assumptions necessary for the interpretation. Finally, we do not need any theoretical predictive formulas on the lattice parameter, we just need to measure the vertical mismatch between the layers and the substrate. These values can be obtained experimentally, e.g., from the x-ray diffraction. It is very helpful to know the relative amount of constituting elements from the SIMS, for instance, or the estimation from the growth conditions.

The main advantage is a relatively straightforward interpretation allowed by the additive contribution of the elements to the local number of the electrons. Not sensitive to the microscopic geometry of the material, but the method is sensitive to mainly to the vacancies, interstitials, and substitutions of the elements with quite different atomic number.

Unfortunately, it is demanding on the sample construction and quality. For the simple interpretation, it is convenient to stack the layers from the known reference material and the studied one. The stacking of layers, the electron density contrast and the very low roughness is crucial for such a reflectivity measurement.

Chapter 11

(Ga,Mn)As microbars

Here we present an experiment whose aim was to verify calculations of a strain distribution in (Ga,Mn)As micro-bars, which were lithographically fabricated on the GaAs substrate. Our x-ray experimental work supported the study of the magnetic anisotropy controlled by the strain published in Reference 145.

Firstly, we introduce the two sample sets of microfabricated arrays of (Ga,Mn)As micro-bars. Further, we describe the calculation of the strain distribution in these micro-bars. As the investigation method is x-Ray Diffraction (XRD), we describe the theoretical basics necessary for the simulation of diffraction measurements of micro-bar periodic arrays. Finally, we present both the strain calculations and experimental diffraction data, compared to each other.

11.1 Samples

Two sets of patterned (Ga,Mn)As epilayers grown on GaAs substrate were studied, no sample was annealed before patterning and neither later. The samples were grown at the Institute of Physics ASCR, the microfabrication was performed by the Microelectronics group at Cavendish Laboratory (Cambridge). The first set of samples denoted as F077 with the nominal Mn concentration of 2% and the layer thickness of 500 nm were patterned into 25 mm^2 arrays of stripes intended to be oriented in two different crystallographic directions: along the [1-10] (F077#10 and F077#11) and along [100] direction (F077#12).

The Atomic Force Microscope (AFM) measurement revealed the stripes to be 1 μm wide, 100 μm long, and separated by 1 μm gaps. Thus, the lateral periodicity $L = 2$ μm. In the direction along the micro-bars, we approximatively consider the sample being uniform neglecting the gaps (relatively small in contrast to long micro-bars). The fabrication was done by electron beam lithography and wet chemical etching using a solution of phosphoric acid and hydrogen peroxide. Etch depth determined by the Atomic Force Microscopy (AFM) is summarized in Table 11.1.

The samples in the second set denoted as F127 with the nominal doping level of 7% Mn were the epitaxial layers 200 nm thick. The samples were patterned into arrays of 1 μm wide stripes separated by the 1 μm wide gaps, as well. The samples F127#10 and F127#11 have micro-bars oriented along the [1-10] crystallographic direction. The demonstrative micrograph of the last of this set labelled as C127#12 as obtained by the Scanning Electron Microscopy (SEM),

sample	layer thickness* (nm)	Mn content* (%)	etching depth (nm)	micro-bars direction
C077#10	500	2	1250–1300	[1-10]
C077#11	500	2	620–650	[1-10]
C077#12	500	2	600	[100]
C127#10	200	7	180	[1-10]
C127#11	200	7	600–750	[1-10]
C127#12	200	7	700–1100	[100]

Table 11.1: The summary for the both sample sets with the etching depths determined by the AFM. The possible ranges of the etching depths corresponds to the lateral non-uniformity of the sample. The parameters denoted by the asterisk are estimated from the growth of the layers based on the long-term calibration.

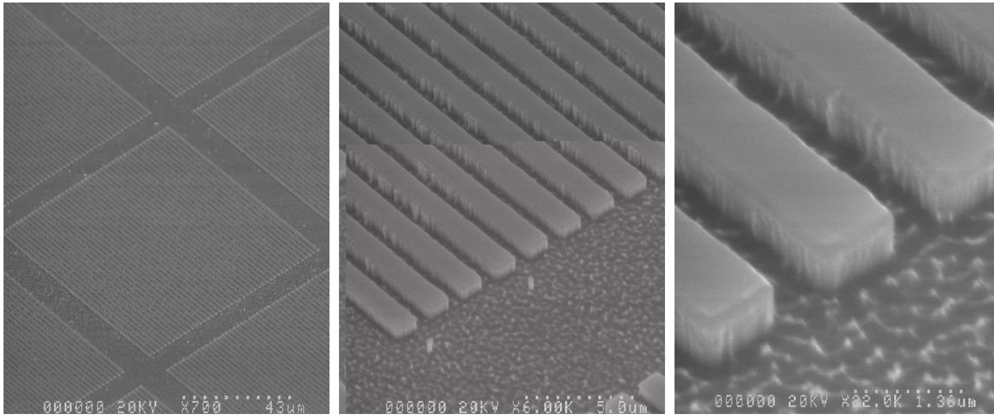

Figure 11.1: Micrograph for the sample C127#12 obtained by the SEM. The same place observed with different magnification is shown.

its micro-bars are parallel to the [010] direction. The fabrication was done by electron beam lithography and dry chemical etching, as well, the final etching depth estimations by AFM are summarized in Table 11.1.

11.2 Strain field computations

The relaxed lattice parameter of (Ga,Mn)As material differs from that of GaAs. This difference can be described by the *mismatch*

$$f = \frac{a^{\text{relaxed}}_{\text{(Ga,Mn)As}} - a_{\text{GaAs}}}{a_{\text{GaAs}}} \tag{11.1}$$

which is connected somehow with the defect densities in the (Ga,Mn)As. Usually, the mismatch is quite small and the thickness of the layers epitaxially grown on the GaAs substrates are small, as well, therefore the strain induced by the substrate on the film can absorbed elastically and no misfit dislocations are necessary to be formed; the layer is *pseudomorphic*.

The lattice of a homogeneous epitaxial layer has no chance to relax laterally as it is 'glued' to the substrate, only the unimportant volume near the edges of the

sample can partially relax in the lateral direction. Therefore, the lateral atomic periodicity follows that of the substrate. This compress strain results in the increase of atom distances in the vertical directions, i.e., lattice spacing. However, if we similarly to the sample edges create such free 'edges' in non-negligible amount, it would affects the large volume allowing to relax the (Ga,Mn)As laterally, as well. The patterned micro-bars are just such system following this idea.

Assuming just the *linear* elastic deformation in the (Ga,Mn)As and partially in the top part of the substrate due to the third Newton's law of motion, it should be possible to use the classical theory of the elasticity to find the equilibrium distribution of the strain in the micro-bar. We treat the both materials as an anisotropic continuum with the certain elastic stiffness tensor $\mathbf{C}$, which is for a cubic symmetry fully defined by c_{11}, c_{12} and c_{44} independent components. Those are well known being

$$c_{11} = 11.90 \cdot 10^{11}\,\mathrm{dyn/cm}^2\,, \qquad (11.2)$$

$$c_{12} = 5.34 \cdot 10^{11}\,\mathrm{dyn/cm}^2\,, \qquad (11.3)$$

$$c_{44} = 5.96 \cdot 10^{11}\,\mathrm{dyn/cm}^2 \qquad (11.4)$$

for the GaAs [98].

We do not have the exact values for the (Ga,Mn)As and moreover they would be dependant on the defect densities in the material, however we can assume that they do not differ very much from those for GaAs, whose values can be taken as a sufficient approximation.

The equilibrium condition is defined by the

$$-\nabla \cdot \boldsymbol{\sigma} = \mathbf{F}\,, \qquad (11.5)$$

where $\mathbf{F}$ denotes volume forces and σ is a stress tensor (through $\boldsymbol{\sigma} = \mathbf{C} \cdot \boldsymbol{\epsilon}$ related to a strain $\boldsymbol{\epsilon}$). The details can be found in Reference 146. For the solving of the partial differential equations defined by Equation 11.5 we use a solver based on finite-element method (FEM) implemented in COMSOL Multiphysics software (Structural Mechanics Module) [146].

There are three last points concerning to the strain calculation. Firstly, the continuum media is assumed to be GaAs. The part corresponding to (Ga,Mn)As differs from the rest by the *a priori* pre-set initial strain, which should be equivalent to the mismatch of the (Ga,Mn)As with respect to the GaAs substrate. However, we do not need to use this certain and possibly not yet known value, while we can use the arbitrary number. Considering linear elasticity the finally calculated results scales linearly with this number, as well. Therefore, we can use, for instance, mismatch of 1% and the scaling can be performed later according to the match with the diffraction data.

Secondly, obviously there are some boundary conditions. We do not calculate numerically the strain field in whole sample but apparently only in the periodic part, i.e in one micro-bar and the half of the gap around it in both directions. Therefore some constraints has to be added to express the periodicity on the vertical borders of our area. No lateral deformation of the substrate on the borders can be a sufficient condition, which respects the symmetry of the problem. Moreover, the micro-bars are long enough (100 μm) not allowing any relaxation in the direction parallel to them, therefore we can fix the deformations in that

direction and only the two-dimensional problem concerning the strain field in the micro-bar cross-section has to be treated. Laterally we are now focused only on the direction perpendicular to the micro-bars, vertically we can restrict ourselves just into the certain depth of the substrate, where the strain field induced from the micro-bar is negligible. We experienced that for such a depth suits the one as ten times larger as the height of the micro-bar. No deformation in such a depth will be the boundary condition there.

Lastly, considering the sample to be a continuous medium, the relation to the crystallographic orientation was seemingly lost. However, the model assumes the anisotropy of such medium, but apparently the most suitable coordinate system does not need to coincide with the crystallographic orientation. Not necessarily but probably, one denotes the lateral direction perpendicular to the micro-bars to be x-axis and intuitively vertical direction as z-axis. Then the y-axis will be parallel with the micro-bar and perpendicular to its cross-section. For samples #10 and #11 we can use the elastic stiffness matrix as defined since $x \parallel [100]$, $y \parallel [010]$, $z \parallel [001]$, but for the samples #12 the crystallographic directions [100] and [010] are rotated in the plane (001) for 45°. For these particular case we have to transform the stiffness matrix to reflect the anisotropy of the material in our (x, y, z)-coordinates.

For the case of $x \parallel [-1-10]$, $y \parallel [1-10]$, $x \parallel [001]$, we use the stiffness matrix

$$\mathbf{C} = \begin{pmatrix} \frac{c_{11}+c_{12}}{2} + c_{44} & \frac{c_{11}+c_{12}}{2} - c_{44} & c_{12} & 0 & 0 & 0 \\ \frac{c_{11}+c_{12}}{2} - c_{44} & \frac{c_{11}+c_{12}}{2} + c_{44} & c_{12} & 0 & 0 & 0 \\ c_{12} & c_{12} & c_{11} & 0 & 0 & 0 \\ 0 & 0 & 0 & c_{44} & 0 & 0 \\ 0 & 0 & 0 & 0 & c_{44} & 0 \\ 0 & 0 & 0 & 0 & 0 & \frac{c_{11}-c_{12}}{2} \end{pmatrix} \tag{11.6}$$

for the elastic continuum.

The software from the proposed shape of the micro-bar calculates the equilibrium distribution of the strain. Actually, we are interested in the local deformation $\mathbf{u} = (\mathbf{u_x}, \mathbf{u_y} \equiv \mathbf{0}, \mathbf{u_z})$ being related to the strain via $\boldsymbol{\epsilon} = (\nabla \mathbf{u}; \nabla \cdot \mathbf{u})$, which is also outputted. The distribution of the displacements u_x and u_z will take place later in the simulation of the diffraction experiment.

11.3 Simulation of x-ray diffraction experiment on micro-bars

The micro-bars dimensions are very small and the absorption and the secondary extinction can be neglected in such small objects. Therefore, we can treat the diffraction kinematically. We can assume that the coherence of a probing synchrotron radiation is large enough to let the waves, which diffracted on the individual perfectly distributed spatially periodic objects, interfere together. If the assumption of the *perfectness* is correct, which should be fulfilled by the microfabricated patterned layers. This interference manifests by the concentrating the diffracted intensity only along the side crystal truncation rods (*satellites*), in other words the constructive interference takes place periodically in the reciprocal space in the direction perpendicular to the periodicity in the real space.

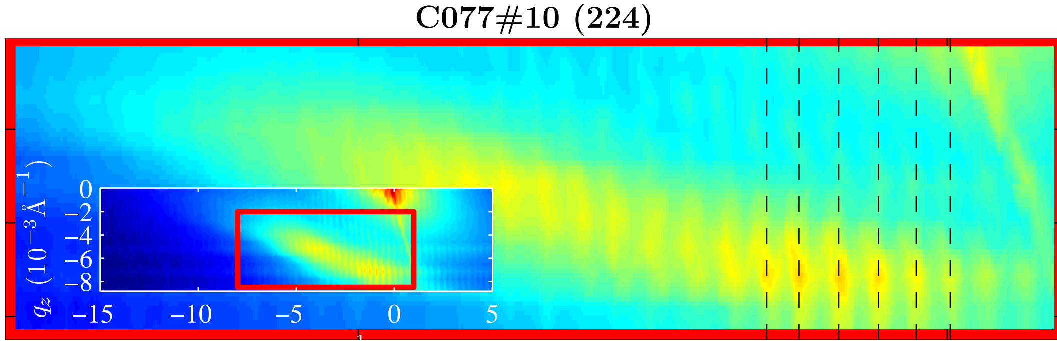

Figure 11.2: Selected part of the measured distribution in the reciprocal space around the (224) for the sample C077#10. The whole intensity map showed in the inset with the indication of the magnified window by the red rectangle. The satellites can be distinguished even in small map, however in the selected view they are clearly visible. From the separations of the dashed guiding lines following some satellites we verified the spatial periodicity being $L = 2\ \mu$m.

From the experimental data, which are in detail shown in Figure 11.2 we can conclude that the periodicity in the reciprocal space is observable. The intensity distribution between the satellites is due to the smearing from the convolution with the instrumental function. Partially, there can be possibly the contribution to an inter-satellite intensity due to some aperiodicity, as well. However, we are satisfied just with the obtaining of the envelope curve of the intensity concentrated in the satellites. The shape of this envelope curve approximates the distribution of the satellites intensities quite well.

If the coherence of the probing radiation was worse, such an interference would not be observed and we would see the diffraction on the individual object spreading intensity continuously along the reciprocal space. The signal would be strengthen by the superposition of intensities from all irradiated objects. Interpretation of the diffracted data would be equivalent. For the calculation of the diffracted intensity we follow the theory described in Reference 91.

From the later numerical evaluations of the strain field it follows that the strain is much less than unity. Therefore, the Takagi approximation assuming the spatially constant structure factor, i.e., neglecting its variance in whole sample [91]. We know from chapter 3 that strong diffraction maxima are affected very weekly by the defect densities. Some phase change inside of the structure factor due to the unit cell distortion is not probable. It could be induced by the strain, which is however small. Then the dielectric susceptibility $\chi_{\mathbf{h}}(\mathbf{r}) \equiv \chi_{\mathbf{h}}$ for the appropriate reciprocal GaAs lattice vector $\mathbf{h}$.

The diffracted intensity $I_{\mathbf{h}}$ should follow the following proportionality

$$I_{\mathbf{h}}(\mathbf{q}) \propto \sum_{\mathbf{H}} \delta^{(2)}\left(\mathbf{q}_{\parallel} - \mathbf{H}_{\parallel}\right) \left| \int \mathrm{d}\mathbf{r}^3 \Omega(\mathbf{r}) \chi_{\mathbf{h}}(\mathbf{r}) \mathrm{e}^{\mathrm{i}\mathbf{h}\cdot\mathbf{u}(\mathbf{r})} \mathrm{e}^{-\mathrm{i}\mathbf{q}\cdot\mathbf{r}} \right|^2 , \tag{11.7}$$

where the integration goes over the periodic volume. The relative position $\mathbf{q} = \mathbf{Q} - \mathbf{h}$ in the reciprocal space from the substrate peak position. The summation over the discrete satellites relative positions $\mathbf{H}_m = \left(\frac{2\pi}{L} m, 0, 0\right)$ together with the delta function arrange the non-zero intensity only to the satellites.

The shape function of the crystal $\Omega(\mathbf{r})$ is unity in the material and zero everywhere else. The pre-calculated deformation within the elasticity theory corresponds in our assumptions to the displacement $\mathbf{u}(\mathbf{r})$ of a whole unit cell from its reference position, i.e., where it would be located if all material was just the unstrained pure GaAs.

In a case of the coplanar diffraction the diffraction plane (q_x, q_z) is perpendicular to the micro-bars to observe the satellite maxima. In our coordinate system concluding the previous considerations we can write

$$I_{\mathbf{h}}(\mathbf{q}) \propto \sum_m \delta\left(q_x - \frac{2\pi}{L}m\right) |\chi_{\mathbf{h}}|^2 \left|\left(\Omega(\mathbf{r})\mathrm{e}^{\mathrm{i}\mathbf{h}\cdot\mathbf{u}(\mathbf{r})}\right)^{\mathrm{FT}}\right|^2 , \tag{11.8}$$

which concludes that the shape of the envelope function continually interpolating the discretely distributed intensity is given by the expression $\left|\left(\Omega(\mathbf{r})\mathrm{e}^{\mathrm{i}\mathbf{h}\cdot\mathbf{u}(\mathbf{r})}\right)^{\mathrm{FT}}\right|^2$, i.e., the function following the diffracted intensity distribution of just one standalone virtual micro-bar.

We can speculate how the intensity distribution would evolve if the number of the micro-bars increased from the aperiodic limit case of one standalone micro-bar to the infinite number of them. The envelope function would be constant, but it would be gradually modulated due to the interference. Finally the intensity would be concentrated just into the satellites. Of course, the intensity will proportionally grow with the squared number of the micro-bars. The sense of this speculation reveals in the interpretation of the influence of the probing radiation coherence. The number of the coherently irradiated micro-bars is analogical to the overall number of micro-rods in our speculation. The diffracted intensity of micro-bars more distant than the coherent length will be summed together as there is no interference. Concluding, if all micro-bars are identical and perfectly periodically spaced, there is not qualitative difference for arbitrary coherence length.

The substrate, being a large crystal, does not diffract kinematically and it is not included in the proportionality in Equation 11.8. There is a contribution of only small part of substrate, feeling the strain field induce by the micro-bar, close to the surface. Actually, increasing the volume (i.e., considered depth) of the unstrained substrate embedded in the model increase the intensity of the substrate peak, treated in the kinematical approximation. However, we are not interested in the substrate peak intensity at all, therefore we do not have to derive any correction. In the simulated intensity map we just replace the substrate peak intensity with the arbitrary value to match the experiment.

If the elastic properties of the (Ga,Mn)As are considered to be identical with those of GaAs, what are the quantities we want to determine from the comparison with the experiment? Firstly, there are uninteresting parameters just to be determined in order to get the match with the experimental data and they can be determined very easily. Those are the instrumental function smearing the intensity in the map being determined from the substrate peak shape and the mismatch of the layer, which scales linearly the displacements and consequently resizes the whole simulated map. Tough the latter parameter is physically relevant, it can be obtained much easier just from the XRD measurements before the patterning. Here we have to scale the simulated map to fit the experimental one, while this scaling factor is the ratio between the real mismatch and that one used in the displacements calculations.

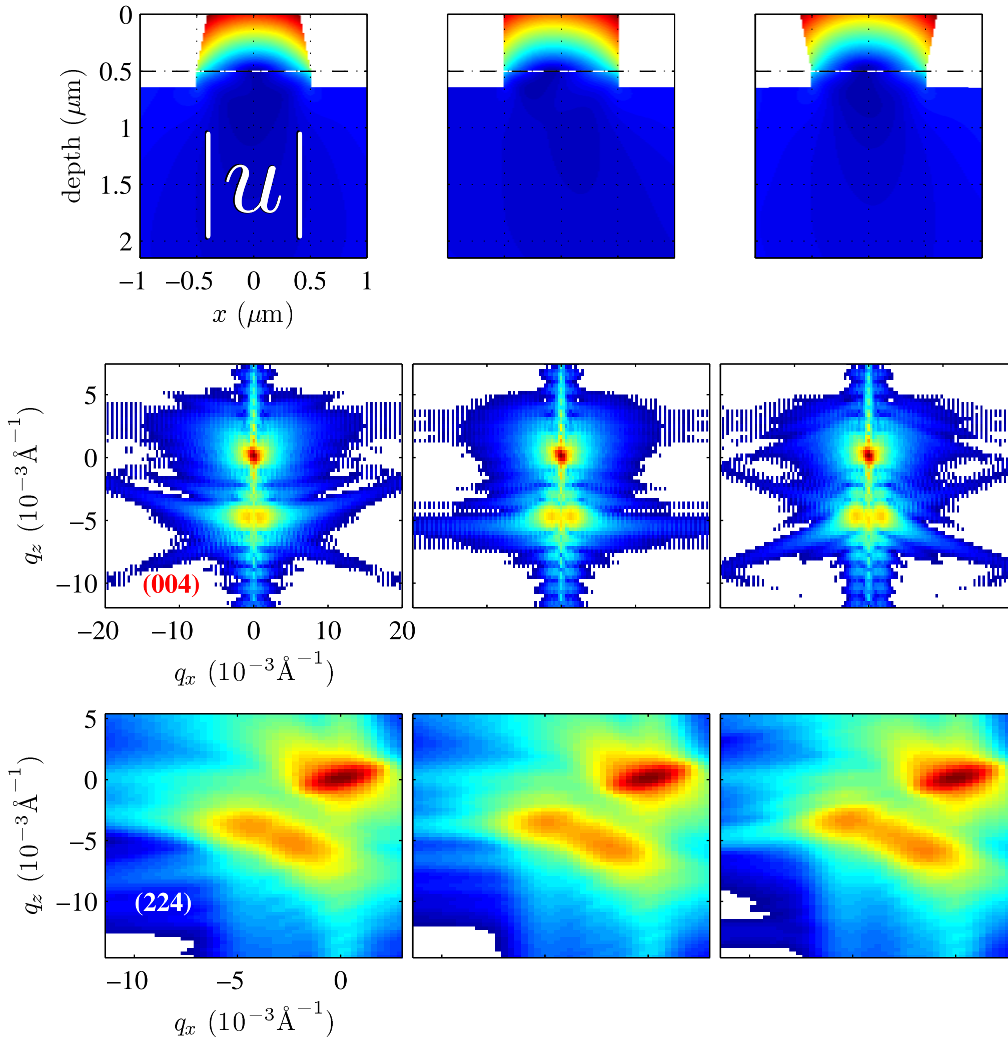

Figure 11.3: The demonstration of the shape function influence in the simulated diffraction maps. Three demonstration calculations for the different simple shapes of the micro-bar similar to those in sample C077#11 (different columns). The first row shows the calculated distribution of the total displacement for particular shape. The second and the third rows shows the simulated intensity maps for (004) and (224) diffractions, respectively. The most intensive point corresponds to the substrate peak, simulated map was convoluted with instrumental function arisen from the real measurement.

However, the valuable information which can be obtained from such an experiment is the shape of the micro-bars. The shape represented by the shape function $\Omega(\mathbf{r})$ appears not only directly in the expression for the intensity calculation, but indirectly, as well. Apparently, it plays non-negligible role in the calculation of the strain field distribution in the micro-rod. For the illustration, we performed some strain field calculation for the three distinctive and simple shapes of the micro-wires for the virtual nominally identical sample to C077#11. The Fig. 11.3 shows the differences in shapes, calculated displacements and simulated diffraction maps for micro-bars being ideally etched, under-cut and over-cut.

If the GaMnAs was completely relaxed, i.e., no strain (which is *not* zero or constant displacements field), we would see only the Fourier transformation of

the shape function giving all maps the same appearance. The very weak straight streaks visible for all demonstrative micro-bar shapes in (004) maps (Fig. 11.3 corresponds to the facets, being perpendicular to them.

To ease the implementation and to make simulation of the diffraction map faster, we can use the commonly implemented discrete two dimensional Fast Fourier Transformation (FFT). Anyway, we have the displacement u_x and u_z calculated discretely, therefore if we transform them into equidistant discrete grid (x_i, z_j) with the lateral spacing Δx and Δz, we can obtain

$$I_{\mathrm{envelope}}(q_{xi}, q_{zj}) \propto \left| \mathrm{FFT}\left(\Omega(x_i, z_j) \mathrm{e}^{\mathrm{i}(h_x u_x(x_i,z_j)+h_z u_z(x_i,z_j))} \right) \right|^2 \tag{11.9}$$

on the equidistant grid (q_{xi}, q_{zj}) in the reciprocal space.

The spacing in the reciprocal space is given by the steps $\Delta q_x = \frac{2\pi}{L}$ (i.e., prescribed) and $\Delta q_z = \frac{2\pi}{D_{\mathrm{etched}}+D_{\mathrm{sub}}}$. The etching depth D_{etched} corresponds actually to the micro-bar height and it is also prescribed by the sample, whereas the depth D_{sub} from which the substrate is included into the calculation is an arbitrary parameter to set minimally to the depth, where the strain field is negligible. The spatial grid has to be oversampled in the vertical direction to omit the FFT artefacts arising from the fact, that there is no vertical periodicity ($\Delta z \gg 2\pi/(\text{desired range in } q_z)$).

11.4 Experiment

Both sample sets were measured using coplanar high-resolution x-ray diffraction in at the synchrotron facility ESRF in Grenoble (beamline ID10B). The photon energy of a probing radiation was 7.95 keV.

From Equation 11.8, it follows that the measurement of the diffraction maxima $(00l)$ will be sensitive only to the shape function and the vertical component of the deformation, while the measured intensity distribution around any asymmetrical diffraction maxima will be affected also by the deformation in lateral direction. Apparently, the measurement of both a symmetrical and an asymmetrical diffraction it allows to filter out the u_x and also to obtain the complete information. Therefore, we measured an intensity map around (004) diffraction for all samples being azimuthally oriented to have the micro-bars perpendicular to the diffraction plane. The asymmetrical maps for the samples #10 and #11 were measured at the (224) diffraction, whereas the (044)-maps were measured for the samples #12 to keep the micro-bars perpendicular to the diffraction plane.

The evaluation of the measured maps were as follows. We started with the model of a rectangular cross-section of the micro-bar for all samples. The lateral periodicity L and etching depths D_{etched} are taken from the reliable AFM measurements. Although the layer thickness determination is quite easy with x-ray diffraction/reflectivity, we did not have a chance to measure samples before the microfabrication. Therefore, we relied on the estimation from the calibrated MBE growth, which is quite reliable considering from our long-term experience (compare the nominal thickness with that determined by XRD in chapter 5).

From this model we calculated the strain field distribution in the micro-bar, which were then used for the diffraction simulations. The calculated intensity maps were convoluted with the two dimensional instrumental function, whose

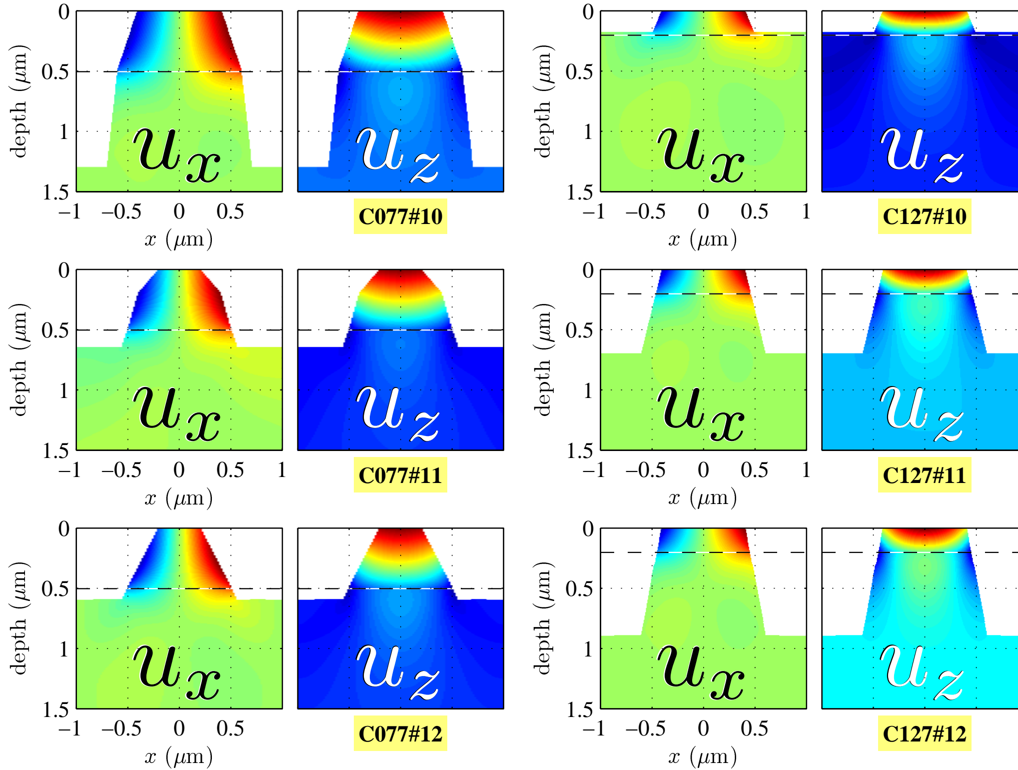

Figure 11.4: The visualisation of the calculated strain field distribution in all samples. The dashed line denotes the interface between (Ga,Mn)As and GaAs.

shape was optimized to obtain the substrate peak spot matching with that in experimental data being elliptical. Simultaneously the mismatch f (i.e., magnify ratio of the calculated map) was optimized to achieve the best match with the measured intensity map. Actually, it was sufficient to set just such value to move the most intensive spot of the layer peak area to the identical position with the experiment.

Such finalized simulated maps were compared with the experimentally obtained intensity maps for both diffractions, for instance, in Figure 11.5 and in Figure 11.6. The qualitative evaluation of the match was done by eye, all features should be in agreement with those in the experiment: the intensive spots shapes and positions, the directions and curvatures of streaks, frequency of the thickness oscillations. For the quantitative comparison, the projection of experimental and simulated maps were made to both q_x and q_z axis. However, this comparison is only informative. It overemphasized the most intensive features, whereas we were interested in the overall visual match. The shape of the micro-bar in the model was manually updated on the basis of such a comparison.

The strain field was recalculated for the updated micro-bar shape and the diffraction experiment simulation and its evaluation was iteratively repeated until the satisfactory agreement was achieved. It showed that the instrumental function and the mismatch as needed no update after the first estimation. There is just one guide how to change the micro-bar shape for the further iteration and it is the direction of the streaks being perpendicular to the facets of the micro-bar. The diverging streak indicates the curvature of the facet. Nevertheless, the finding of

	#10	#11	#12
C077	$(9.6 \pm 0.2) \cdot 10^{-4}$	$(8.0 \pm 0.2) \cdot 10^{-4}$	$(9.7 \pm 0.2) \cdot 10^{-4}$
C127	$(3.7 \pm 0.1) \cdot 10^{-3}$	$(3.9 \pm 0.1) \cdot 10^{-3}$	$(3.8 \pm 0.1) \cdot 10^{-3}$

Table 11.2: The mismatch f of the (Ga,Mn)As layer for all particular samples (columns) of both sample sets (rows). The higher mismatch of the samples C127 corresponds to the fact that the Mn content is nominally higher (7%) than in samples C077 (2%).

the final satisfactory shape is a question of trial and error.

The final cross-sections of micro-bars for all samples resulted from this optimizing procedure are depicted in Figure 11.4 together with the calculated displacements u_x, u_z. The determined mismatch parameters are summarized inTable 11.2. The simulated diffraction maps together with those experimentally obtained are shown for all samples in Figures 11.5, 11.6 (C077#10), 11.7 (C077#11), 11.8 (C077#12), 11.10 (C127#10), 11.11 (C127#12), 11.11 (C127#12), all attached at the end of chapter.

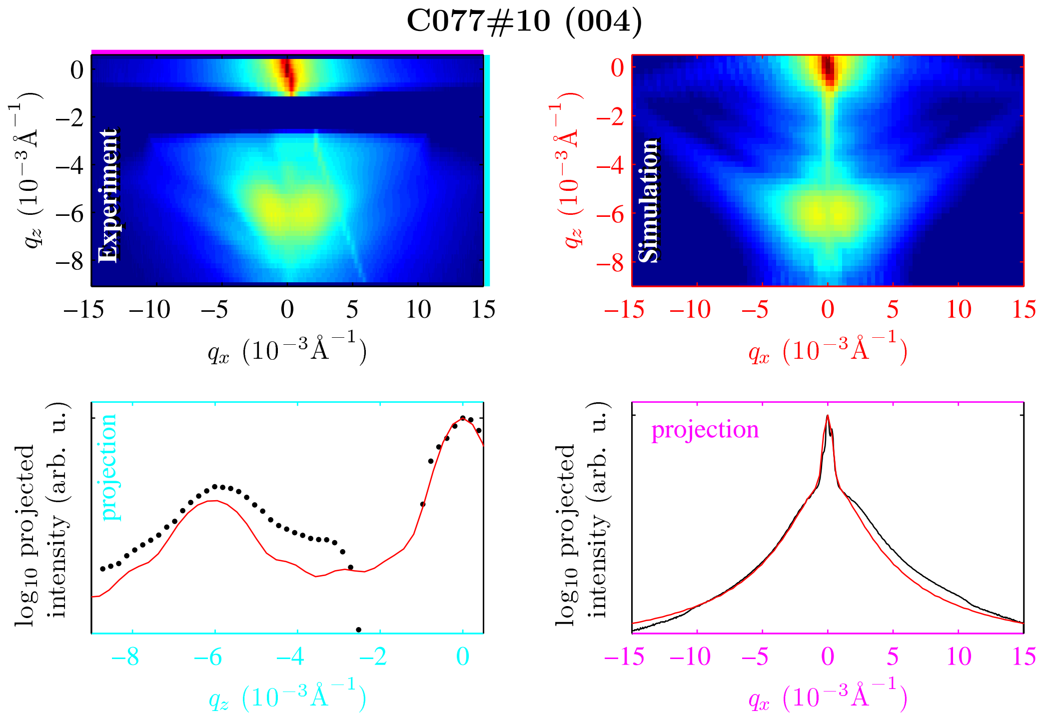

Figure 11.5: Comparison of the measured (upper left) and the simulated (upper right) intensity (004)-maps. There are two maxima corresponding to the reciprocal lattice points of the GaAs substrate ($q_z = 0$, $q_x = 0$) and the (Ga,Mn)As layer (negative q_z, $q_x = 0$). The left bottom and the right bottom subfigures shows the intensity projection to the q_z and the q_x axis, respectively, for both simulation (red) and the experimen (black).

The remarkable agreement of the measured and the simulated diffraction maps shows that the model of the lattice deformation as elastic continuum, which can be treated by the mean of linear elasticity theory, is quantitatively relevant in determining the strain field distribution, i.e., the local relaxation of the lattice. The micro-bars have usually a trapezoidal cross-section seeming to be over-cut

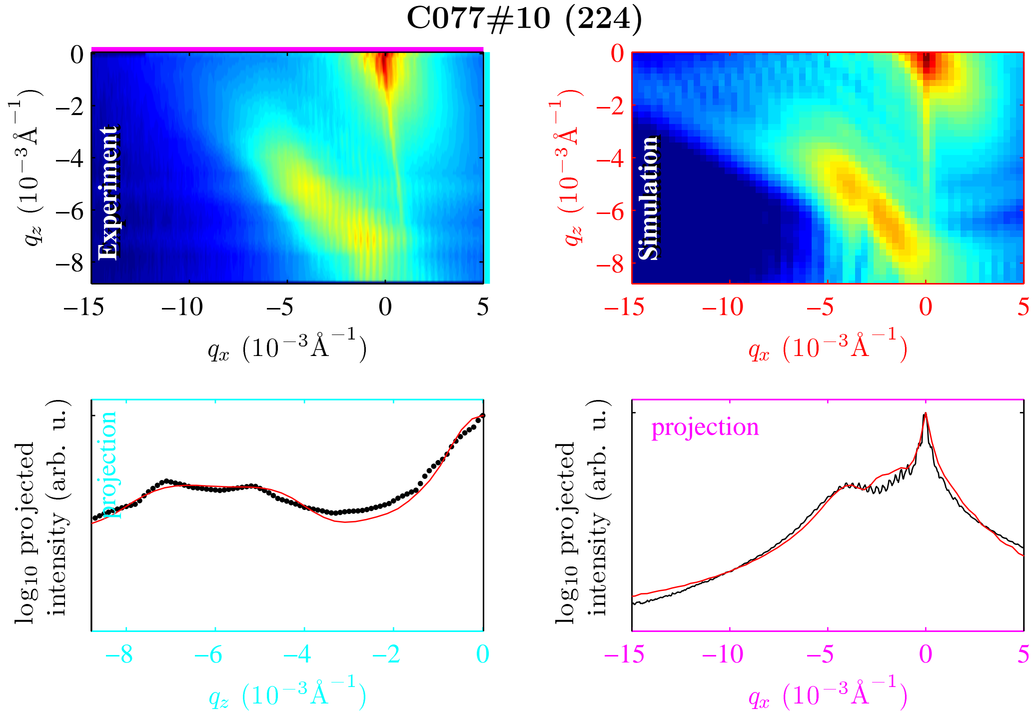

Figure 11.6: Measured intensity map (upper left) for the asymmetrical (224) diffraction compared to the simulation (upper right). Similarly to the Fig.11.5 the bottom left and the bottom right subfigures compares the intensity projection of the maps to the q_z and the q_x axis, respectively.

probably by the wet etching. The slopes of the facets are for few degrees larger then it is typical for the patterning process.

However, the SEM did not observe such a significant shape determining it being rather rectangular. Nevertheless, the streak directions originated in the direct influence of the shape on the diffraction indicates such a shape clearly. We explain this discrepancy by the different sensitivity of both methods. If we accept that the SEM determines the shape of the micro-bar surface, whereas the diffraction technique is sensitive to the crystalline core of the micro-bar, we explain it by some degradation of the rectangle upper corners. So the over-cut can be explained better by the degradation during the etching, which can leave a non-uniform amorphous coating on the micro-bars.

The interpretation of the experimental data are complicated by the qualitative evaluation and the manual trial and error like updating of the model. In principle, it is possible to define some quantitative criteria evaluating the match of measured and simulated data giving some goodness-of-fit value, which can be used for automatic update of the model. However, such criteria have to reflect the importance of the weak but significant features. Moreover, the automatic update would need more extensive implementation, which is behind our intentions, here we manually changed the model in the graphical front-end.

We have to admit, that in contrast to our technique which *a priori* assumes that linear elasticity is valid here, moreover that elastic constants are available, it is possible to determine the strain field just from the diffraction data by the mean of the well sophisticated *phase retrieval* method. Simply said, it is based on the complicated searching for diffraction waves phases, whereas their amplitudes

we measured. The consecutive transformation of the found solution between the spatial and the reciprocal space back and forth allows to apply some specific constrains on the solution in both spaces, which should lead to the optimal solution. Just such work performed on the same samples was published in Reference 147. The authors successfully found the unknown phases, i.e., just the strain field in the micro-bar. If we compare the results, we can see that their micro-bar shape stayed the rectangular in contrast to our finding. Here arises a question if the discrepancy comes from some imperfectness of our model (e.g., different elastic constants, inhomogeneous mismatch) or it is due to the some limitation of the phase retrieval used there (e.g., allowed degrees of freedom for the *support*, which corresponds to our cross-section), which is hard to resolve.

Conclusion

We described the calculation procedure allowing to obtain the strain distribution in the relaxed micro-bar. The theoretical basics for the interpretation of XRD data, we described, as well. It was used for the comparison of the calculated strain distributions and XRD measurements. It turned out that this comparison allows to determine the cross-section of crystalline core of the micro-bar.

The determination of the micro-bar cross-section was demonstrated on several samples with different etching depth, different crystallographic orientation of the spatially periodic micro-bars, and different mismatch of (Ga,Mn)As. The agreement of the experimental data and those being calculated from the resulted micro-bar cross-section is quite well, definitely better than for the initial rectangular cross-section.

The facet directions are supported by the weak streaks in the diffraction maps originated directly in the cross-section shape. Therefore, we dare say that the discrepancy with the literature is given by the certain ambiguity of the phase retrieval solution.

Accompaniments

the attached large figures follow on next pages

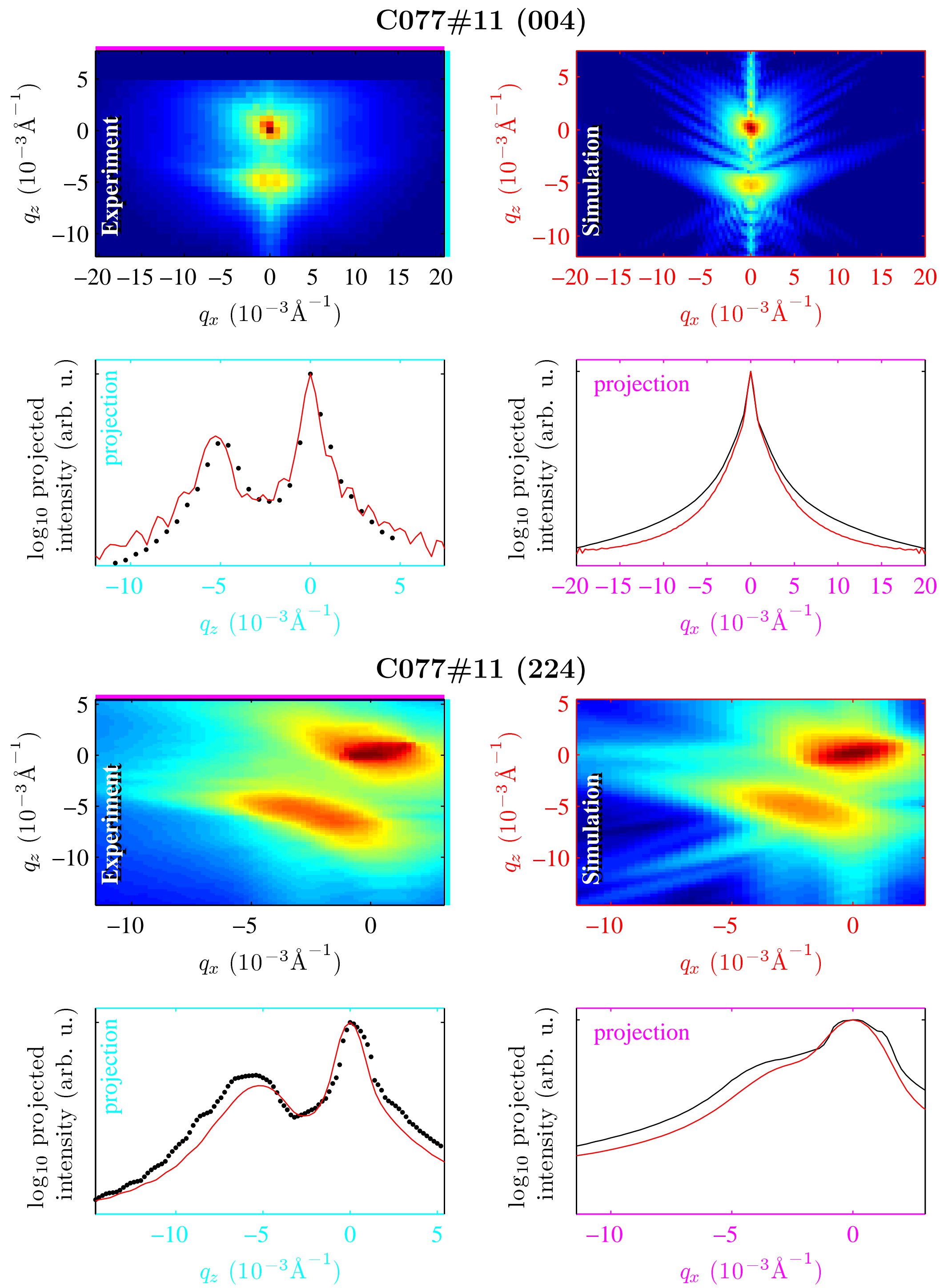

Figure 11.7: Experimental data compared to the simulation for C077#11.

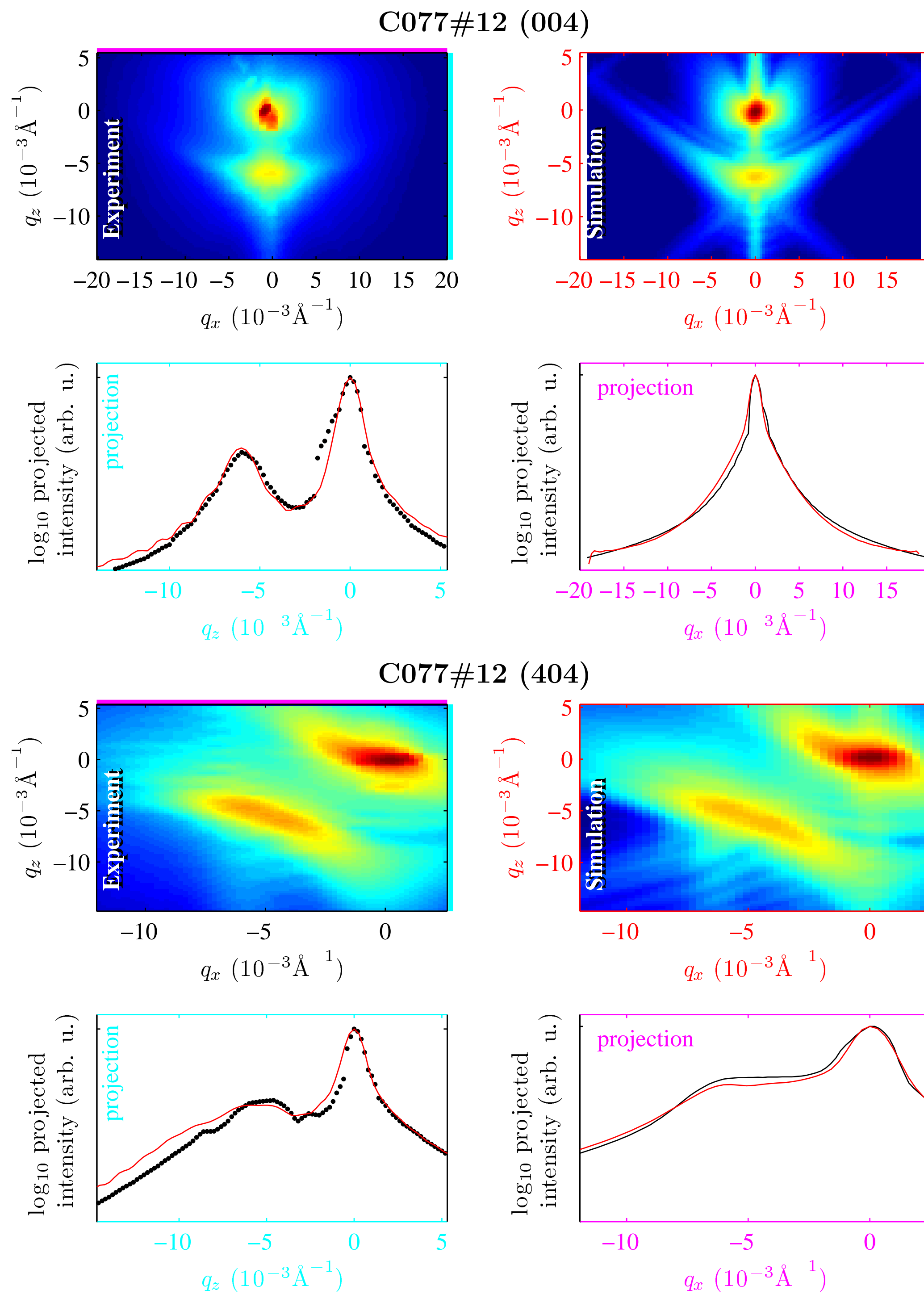

Figure 11.8: Experimental data compared to the simulation for C077#12.

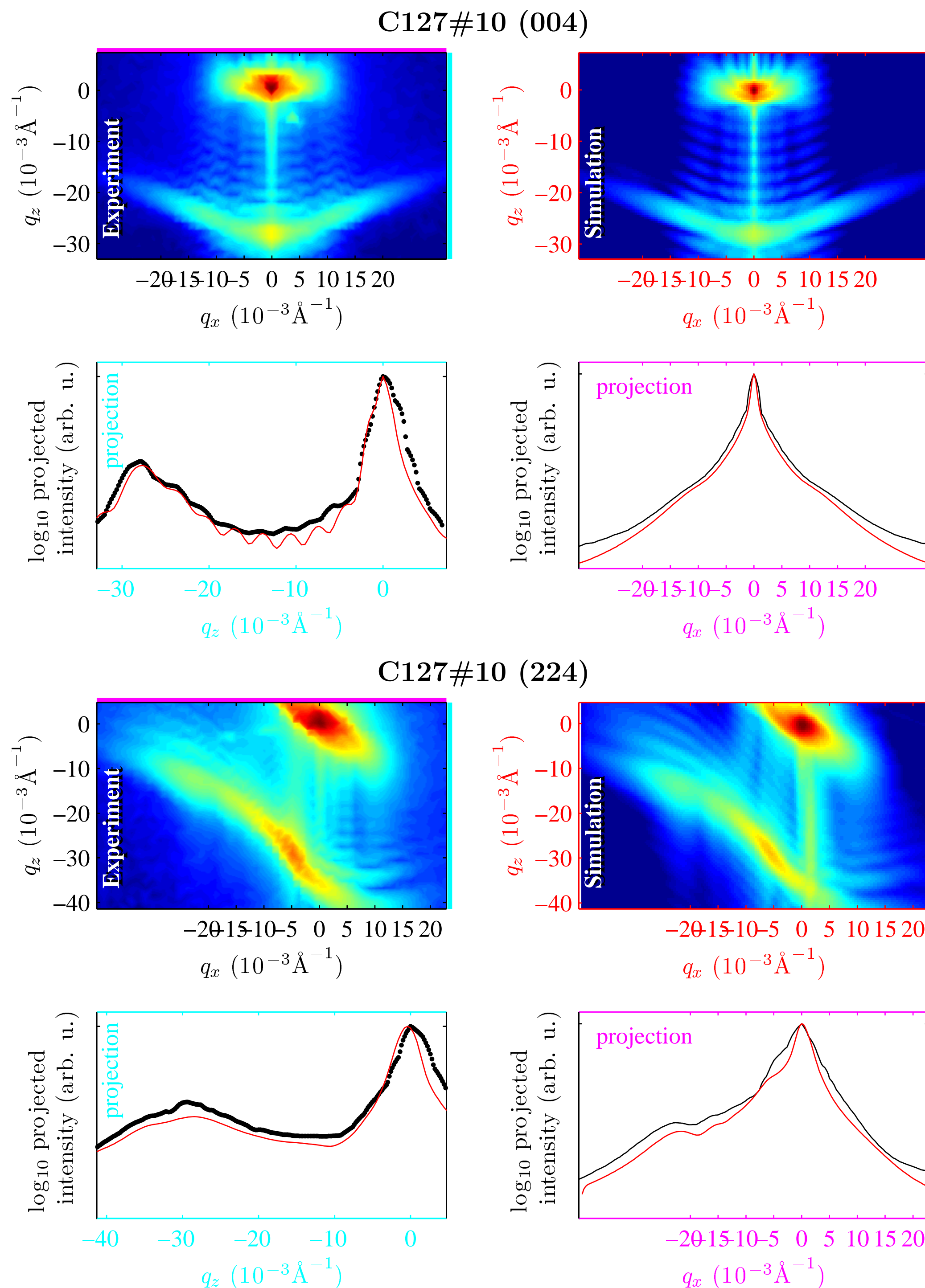

Figure 11.9: Experimental data compared to the simulation for C127#10.

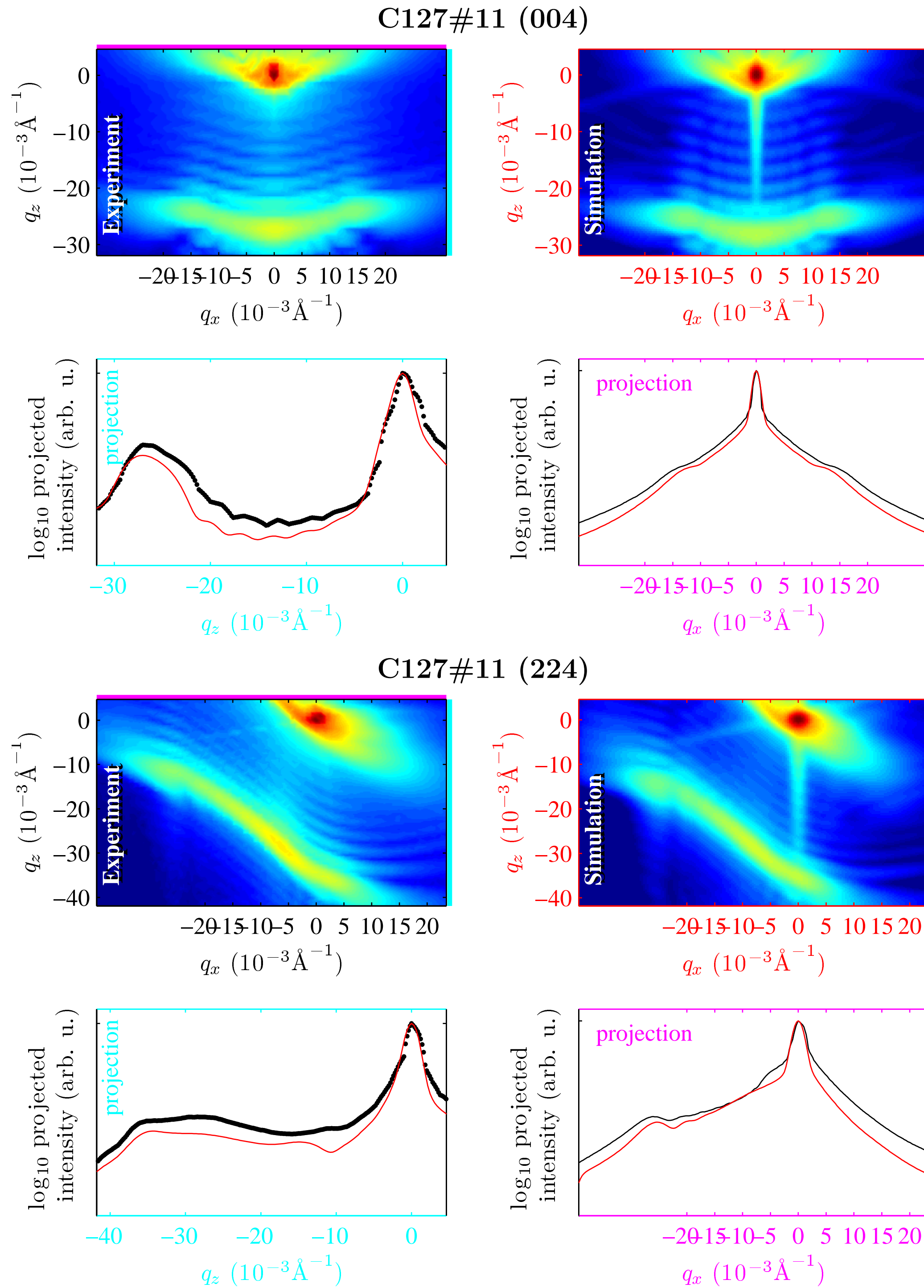

Figure 11.10: Experimental data compared to the simulation for C127#11.

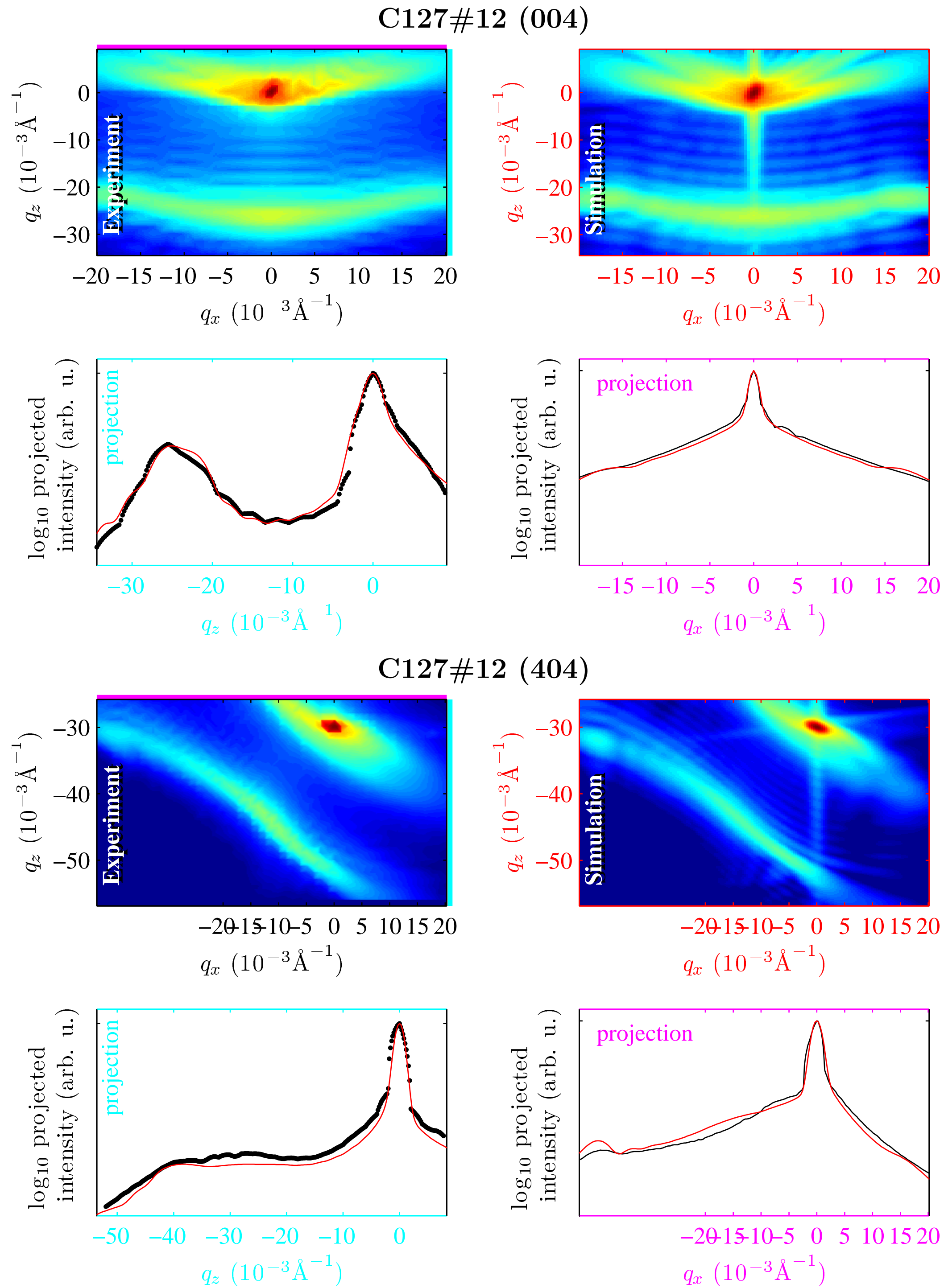

Figure 11.11: Experimental data compared to the simulation for C127#12.

Summary

As we introduced in the preface of this thesis, there are two main objectives of our work, methodological and principal.

Regarding to the first objective, we suggested a routine characterization method of epitaxially deposited (Ga,Mn)As layers on a GaAs substrate. Its capability is to determine the defect density in crystallographically non-equivalent positions. We discussed the sensitivity of the method to different defect types. Unfortunately, the diffraction contrast between Ga atom and its substitutive, Mn, is too weak to determine the Mn substitutional concentration reliably. On the other hand, its correlation with other densities is rather small in the mean of contribution to the diffracted intensity. Therefore, a quite large uncertainty of the probable substitutional density does not affect very much the most probable values of other defect densities together with their uncertainties. However, the substitutional content cannot be estimated with this method and the information on that has to be supplied by some other complementary method.

The experimental procedure consists of the diffracted-intensity distribution measurement in the vicinity of the several diffraction maxima. From these intensity maps, the diffraction curves, i.e., intensity along the so called crystal truncation rods, are extracted. In case of some specific samples, we showed that for a reliable fit a minimum of four diffraction maxima has to be measured. From the calculations of structure factors and the discussion on the concentration sensitivity, it follows that all three diffraction maxima types (*weak*, *strong*, and *intermediate*) have to be included in the measurements. Of course, the higher number of measured maxima decrease the uncertainties of final determined densities. Also, one has to keep in mind that the Debye-Waller factor affects the measured intensity. Therefore its desirable to choose the diffraction maxima of the same type with large difference of the scattering vector length in order to identify and remove the Debye-Waller contribution.

Generally, the weak maxima, where the waves diffracted on the Ga and As lattice site are in antiphase, emphasizes the difference between both non-equivalent interstitial lattice sites. Also, there is a strongest contribution of substitutional Mn. On the other hand, the strong diffraction maxima corresponds to the constructive interference of the waves diffracted by all atoms, i.e., all atoms contributes fully with their scattering power to the final detected intensity. Similarly, the intermediate diffractions resulted from the interference of the waves diffracting on Ga and As lattice sites having a phase difference $\pm\frac{\pi}{2}$. Since the density of all defects is rather small and the relative change of the intensity occurring through their presence is roughly proportional to their density, the intensity is affected quite weakly. Nevertheless, the intensity is measurable with the smaller uncertainty than the expected effect.

The evaluation of the experiment is performed by the fitting of the theoretical simulation to the measured diffraction curve simultaneously for all measured maxima. Be the means of the dynamical theory, it is possible to calculate the theoretical diffraction curves. The sample is modelled by a homogeneous layer or a stack of such layers with optimizing parameters corresponding to four densities: Mn in substitutional and two non-equivalent interstitial positions and As anti-site substituting Ga atom.

However, there are several uncertainties and maybe daring assumptions. Firstly, the theoretical relation between the relaxed lattice parameter of the (Ga,Mn)As and the concentrations of particular defects has to be assumed. To omit this relation, it would be necessary to measure many more diffraction maxima, which is not a principal obstacle. Then, the lattice parameter can be an arbitrary parameter meeting the experimental position of the layer peak.

Secondly, there is an assumption of attractively or repulsively influenced neighbourhood around the defect. For the low defect concentration, it is possible introduce the simple correction of the undisturbed structure factor. Here, the repulsion of the closest atoms around the Mn in all crystallographic positions are known from some published experiments. Unfortunately, there is no agreement on the certain value representing the repulsion of As atoms around the As anti-site defect. Moreover, theoretical works predict the stronger repulsion than around other defects. From our simulation, it seems that this correction plays some role also for anti-site defects but we are not able to apply it. If the layer contains some anti-site defects, its more safe to go through the fitting procedure for both limits of suggested repulsion factors, and to increase the uncertainty of the fitted parameters with respect to the solution shift due to the different considered repulsion.

Here we are turning our focus to the second objective of the thesis. We used the approach summarized above for the characterization of the as-grown and the annealed (Ga,Mn)As thin layer. Except of the annealing, both samples were identical, therefore only the interstitial densities were assumed to be different. From the fitting procedure, it followed that the overall interstitial density decreased after the annealing treatment, indeed. Both samples exhibited the prevalence of the interstitials located in the centre of the tetrahedra formed by the As atoms; their occupancy was $(2.6 \pm 0.3)\%$ for the as-grown and $(2.2 \pm 0.3)\%$ for the annealed sample. Nevertheless, the other interstitial sites were occupied, as well ((1.3 ± 0.4) – as grown, (0.8 ± 0.3) – annealed).

To our surprise, the annealed sample contained relatively a lot of interstitial defect still. Only 23% of interstitial atoms were removed from the (Ga,Mn)As system. Therefore we extended our experiment for another annealing treatment, but this time we used the sequential etch-annealing procedure. The later characterization revealed the further decrease of the interstitials by another 13%–18% of the original amount. For this sample, the resulted interstitial densities were $(1.9\text{–}2.0 \pm 0.8)\%$ and $(0.4 \pm 0.9)\%$ inside of As and Ga tetrahedra, respectively.

On these two samples, i.e., the as-grown and the etch-annealed, we perform the anomalous diffraction experiment. From the measured diffraction maxima for many energies of the x-ray primary beam, we were able to quantify the substitutional content represented with the occupancy $(8.2 \pm 1.1)\%$. This method allowed to determine the difference of both interstitial occupancies in As and Ga tetrahe-

drons; $(1.6 \pm 3)\%$ for that as-grown and $(2.4 \pm 0.3)\%$ for that etch-annealed. The obtained values are comparable with those determined from the high resolution diffraction in range of the error. In contrast, the anomalous diffraction allowed to estimate these numbers without any *apriori* assumed relation between the lattice parameter and the particular densities.

Finally, the etch-annealed sample was treated by the long-term annealing without any preceding etching, and the same characterization procedure reveal the further decrease of the overall interstitial density. This time, only the 5% of the very original interstitial content was removed from the system.

We re-evaluate all the data for all samples with no lattice-parameter constrain, i.e., with arbitrary lattice parameters. Unfortunately, the data for the etch-annealed sample were not good enough to obtain a reliable fit. Nevertheless, with the justified assumption that the presence of anti-site defect is suppressed, we were able to estimate the interstitial occupancy inside of the arsenic and gallium tetrahedra for the as-grown, the annealed, and the long-term annealed sample. The resulted values did not differ from those previously determined.

Going back to the etch-annealed sample, the unintended consequence of the etching-enhanced annealing was the vertical inhomogeneity of the layer. This was manifested by the changed shape of the diffraction curve, namely, the asymmetry of the side maxima around the layer peak. This shape was successfully fitted using a model of two homogeneous layers. The results indicated the lower interstitial concentration close to the surface. On the other hand, this sample after the long-term annealing was, evidently, homogeneous again.

In order to understand the annealing process more clearly, we introduced the model describing the migration of the interstitials. Commonly the migration process is considered to be diffusion of the particles in fact. It is known that annealing causes the increase of the Mn content close to the sample surface. The reason why the interstitial atom is capable to travel through the whole (Ga,Mn)As layer towards the surface, but the diffusion into the substrate is limited, is its charge. Inspired by this, we considered the migration of the charged interstitials together with the migration of the free charge carriers, holes.

The known fact that annealing changes the sample only in ambient air or with the arsenic capping layer was earlier explained by the formation of the Mn oxide or MnAs within the surface, i.e., the charged particle is neutralised. With the charged state, the electrostatic force repulsing other interstitials disappears, as well. The surface processes are relatively complicated and can be hardly quantified with our knowledge of this material. Therefore we assumed some hypothetical surface container accepting the flux of the charged interstitials, trapping them, and releasing the holes for each trapped particle. As a result, the migration was described by the *drift*-diffusion, rather than just only diffusion.

Firstly, we wanted to verify the assumption that Mn oxide is formed within the surface during the annealing, and the assumption that etching clearly removes all of the oxide. From the x-ray absorption spectroscopy around the Mn absorption edge, we deduced following. A virgin sample with some thin native Mn oxide on the surface was etched and annealed. After that, the presence of the rich Mn oxide being also slightly deeper was revealed. On the other hand, the etching successfully removed the whole oxide layer from the surface.

From the x-ray diffraction, the depth profiles of the interstitial density in all

samples were available. Actually, all samples except that etch-annealed were homogeneous. The depth profile of the inhomogeneous etch-annealed sample was approximated by the step-like function, which followed from the model of two stacked homogeneous layers. We performed many simulations of the annealing treatment, i.e., solving the drift-diffusion equations for both the interstitials and the holes. The homogeneous depth profile corresponding to the as grown sample was considered as a starting density for the simulation. The sequential etch-annealing was treated by the periodical removal of the surface area with emptying of the surface container. All simulations were compared with the previously determined depth-profiles of the interstitial density. We emphasized the qualitative match of the profiles, i.e., we applied a criteria of homogeneity and inhomogeneity of appropriate depth profiles. From the qualitatively sufficient solutions, we chose the quantitatively best one.

The unknown parameters, which we wanted to guess by the comparisons, were the capacity and the trapping rate of the surface container. Though, the capacity can be roughly estimated since it corresponds to the maximal possible decrease of the overall interstitial density, i.e., decrease in the sample where further annealing does not improve the magnetic or transport properties. The trapping rate, we defined as purely phenomenological quantity, and its value can be hardly interpreted. Nevertheless, we tuned these parameters together with the unknown but essential interstitial diffusivity, or mobility, parameter. Finally, the optimal container capacity corresponded to the expected value, indeed, at least in order of magnitude. The optimal diffusion coefficient we estimate approximatively to $4 \times 10^{-20}\,\mathrm{m}^2 \cdot \mathrm{s}^{-1}$. If we compare this value with the published value obtained from the transport measurements, our diffusivity is about 30 times larger. Unfortunately, there is a lack of diffusivity values in the literature. However, the other diffusivity did not lead to the qualitative match neither for any arbitrary values of the other parameters.

The annealing process taken place in (Ga,Mn)As is often considered to be just simple diffusion. We showed the internal electric field is important, as well. In our picture the holes, being very fast, redistribute themselves neither uniformly, nor perfectly screening the interstitial charge, but into the state corresponding to the thermodynamic equilibrium because their time scale is incomparably different. Thus, there is a competition between the tendency of charge screening and the tendency of uniform distributing. However, the interstitials are slow, they feel both their concentration gradient and the electrostatic force. While for holes both forces are in equilibrium, the interstitials are driven by both forces towards the surface. There, they are trapped, i.e., their density locally decreases at the expense of the holes creation.

In this thesis, we presented two other experiments. First one was the x-ray reflectivity measurement of the (Ga,Mn)As/AlGaAs multilayer. From the specular reflectivity, we were able to determine the depth profile of the electron density. Although the whole profile is quite uncertain, i.e., possible shifted to the higher or lower densities, the depth profile in the repeating bilayer consisted of (Ga,Mn)As and AlGaAs layers is determined reliable because of the high density contrast and the periodicity itself. Therefore, we used the AlGaAs constituent as a reference, and from the density difference between both constituents, we estimated the number of electrons in the (Ga,Mn)As unit cell. Finally, this

number formulate the ratio between the substitutional and the interstitial Mn atoms in the unit cell. Our result of the substitutional Mn prevalence was in qualitative agreement with an expectation.

The last presented experiment is the high-resolution diffraction on the patterned (Ga,Mn)As micro-bars. Here the epitaxial fully strained (Ga,Mn)As layer deposited on the GaAs substrate was lithographically micro-fabricated to the periodic long stripes. It allows the (Ga,Mn)As to relax partially into the formed gap between the micro-bars. The inhomogeneous strain field together with the cross-section shape of the micro-bar determinate the distribution of the diffracted intensity in the reciprocal space. We measured the intensity map in the vicinity of two diffraction maxima, symmetrical and asymmetrical. The experimental data, we compared with the experiment simulation. For this purpose, we calculated the strain distribution in the micro-rods by the mean of finite element method. We assumed the validity of the linear elasticity. We determined the mismatch of relaxed (Ga,Mn)As lattice parameter related to the substrate lattice parameter. We were able to sufficiently fit the experimental intensity maps with those simulated. The cross-section shape giving the best agreement, we considered to be the real shape of the crystalline core of the micro-bar. This proved that linear elasticity is valid in the (Ga,Mn)As, and therefore, it together with a finite element method can be used for the strain field computation.

All demonstrated methods can be applied for other material in the future, as well. The laboratory x-ray method for the interstitial density determination is possible to extent to other similar materials, for instance, (Ga,Mn)(As,P). However, every additional impurity increases the number of parameters we want to determine. Therefore, the adaptation of method should be mainly in the higher number of measured diffraction maxima. However, the described theory stays the same. The structure factor has to be constructed in a similar way as here.

In this thesis we studied the (Ga,Mn)As with the x-ray high resolution diffractometry, the x-ray absorption spectroscopy, the anomalous diffraction, and the x-ray specular reflectivity. From these experiments, it was possible in several ways to determine the occupancy of the Mn in substitutional positions and both crystallography non-equivalent interstitial positions. We showed that there is prevalence of the interstitials in the tetrahedrons formed by the As atoms. And finally, we formulated the migration picture of the interstitials during the annealing treatment.

Bibliography

[1] S. A. Wolf, D. D. Awschalom, R. A. Buhrman, J. M. Daughton, S. von Molnár, M. L. Roukes, A. Y. Chtchelkanova, and D. M. Treger, "Spintronics: a spin-based electronics vision for the future." Science **294**, 1488–95 (2001).

[2] I. Stolichnov, S. W. E. Riester, H. J. Trodahl, N. Setter, A. W. Rushforth, K. W. Edmonds, R. P. Campion, C. T. Foxon, B. L. Gallagher, and T. Jungwirth, "Non-volatile ferroelectric control of ferromagnetism in (Ga,Mn)As," Nat Mater **7**, 464–467 (2008).

[3] J. a. Haigh, M. Wang, a. W. Rushforth, E. Ahmad, K. W. Edmonds, R. P. Campion, C. T. Foxon, and B. L. Gallagher, "Manipulation of the magnetic configuration of (Ga,Mn)As nanostructures," Appl. Phys. Lett. **95**, 062502 (2009).

[4] T. Wosinski, T. Andrearczyk, T. Figielski, J. Wrobel, and J. Sadowski, "Domain-wall controlled (Ga,Mn)As nanostructures for spintronic applications," Phys. E Low-dimensional Syst. Nanostructures **51**, 128–134 (2013).

[5] S. W. E. Riester, I. Stolichnov, H. J. Trodahl, N. Setter, a. W. Rushforth, K. W. Edmonds, R. P. Campion, C. T. Foxon, B. L. Gallagher, and T. Jungwirth, "Toward a low-voltage multiferroic transistor: Magnetic (Ga,Mn)As under ferroelectric control," Appl. Phys. Lett. **94**, 063504 (2009).

[6] E. Mikheev, S. W. E. Riester, I. Stolichnov, and N. Setter, "Polarization Screening in Multiferroic (Ga,Mn)As/P(VDF-TrFE) Transistors," Ferroelectrics **421**, 98–102 (2011).

[7] G. E. Moore, "Cramming more components onto integrated circuits," Electronics **38** (1965).

[8] M. N. Baibich, J. M. Broto, A. Fert, F. N. Van Dau, and F. Petroff, "Giant Magnetoresistance of (001)Fe/(001)Cr Magnetic Superlattices," Phys. Rev. Lett. **61**, 2472–2475 (1988).

[9] G. Binasch, P. Grünberg, F. Saurenbach, and W. Zinn, "Enhanced magnetoresistance in layered magnetic structures with antiferromagnetic interlayer exchange," Phys. Rev. B **39**, 4828–4830 (1989).

[10] G. A. Prinz, "Magnetoelectronics," Science (80-.). **282**, 1660–1663 (1998).

[11] T. Fukumura, H. Toyosaki, and Y. Yamada, “Magnetic oxide semiconductors,” Semicond. Sci. Technol. **20**, S103–S111 (2005).

[12] S. Chambers, T. Droubay, C. Wang, K. Rosso, S. Heald, D. Schwartz, K. Kittilstved, and D. Gamelin, “Ferromagnetism in oxide semiconductors,” Mater. Today **9**, 28–35 (2006).

[13] J. K. Furdyna, “Diluted magnetic semiconductors,” J. Appl. Phys. **64**, R29 (1988).

[14] J. K. Furdyna and J. Kossut, “DMSs Semiconductor and Semimetals, vol. 25,” (1988).

[15] T. Story, R. Galazka, R. Frankel, and P. Wolff, “Carrier-concentration-induced ferromagnetism in PbSnMnTe.” Phys. Rev. Lett. **56**, 777–779 (1986).

[16] Y. Ohno, D. K. Young, B. Beschoten, F. Matsukura, and H. Ohno, “Electrical spin injection in a ferromagnetic semiconductor heterostructure,” **402**, 1–3 (1999).

[17] H. Ohno, “Making Nonmagnetic Semiconductors Ferromagnetic,” Science (80-.). **281**, 951–956 (1998).

[18] H. Ohno, D. Chiba, F. Matsukura, T. Omiya, E. Abe, T. Dietl, Y. Ohno, and K. Ohtani, “Electric-field control of ferromagnetism.” Nature **408**, 944–6 (2000).

[19] J. Yang, H. Yasuda, S. Wang, F. Matsukura, Y. Ohno, and H. Ohno, “Surface morphologies of III-V based magnetic semiconductor (Ga,Mn)As grown by molecular beam epitaxy,” Appl. Surf. Sci. **166**, 242–246 (2000).

[20] K. Olejník, V. Novák, and M. Cukr, “MnAs Clustering on Epitaxial GaMnAs Surface,” in *WDS’06 Proc. Contrib. Pap.* (MATFYZPRESS, Prague, 2006) pp. 54–57.

[21] H. Munekata, H. Ohno, S. von Molnár, A. Segmüller, L. L. Chang, and L. Esaki, “Diluted magnetic III-V semiconductors,” Phys. Rev. Lett. **63**, 1849–1852 (1989).

[22] H. Ohno, H. Munekata, S. von Molnár, and L. L. Chang, “New III-V diluted magnetic semiconductors (invited),” J. Appl. Phys. **69**, 6103 (1991).

[23] H. Ohno, H. Munekata, T. Penney, S. von Molnár, and L. L. Chang, “Magnetotransport properties of p-type (In,Mn)As diluted magnetic III-V semiconductors,” Phys. Rev. Lett. **68**, 2664–2667 (1992).

[24] H. Ohno, A. Shen, F. Matsukura, A. Oiwa, A. Endo, S. Katsumoto, and Y. Iye, “(Ga,Mn)As: A new diluted magnetic semiconductor based on GaAs,” Appl. Phys. Lett. **69**, 363 (1996).

[25] K. Olejník, M. Owen, V. Novák, J. Mašek, A. C. Irvine, J. Wunderlich, and T. Jungwirth, "Enhanced annealing, high Curie temperature, and low-voltage gating in (Ga,Mn)As: A surface oxide control study," Phys. Rev. B **78**, 054403 (2008).

[26] R. Chapman and W. Hutchinson, "Photoexcitation and Photoionization of Neutral Manganese Acceptors in Gallium Arsenide," Phys. Rev. Lett. **18**, 443–445 (1967).

[27] M. Linnarsson, E. Janzén, B. Monemar, M. Kleverman, and A. Thilderkvist, "Electronic structure of the GaAs:MnGascenter," Phys. Rev. B **55**, 6938–6944 (1997).

[28] W. Schairer and M. Schmidt, "Strongly quenched deformation potentials of the Mn acceptor in GaAs," Phys. Rev. B **10**, 2501–2506 (1974).

[29] T. Lee and W. Anderson, "Edge emission involving manganese impurities in GaAs at 4.2 °K," Solid State Commun. **2**, 265–268 (1964).

[30] T. Jungwirth, J. Mašek, J. Kučera, and a. H. MacDonald, "Theory of ferromagnetic (III,Mn)V semiconductors," Rev. Mod. Phys. **78**, 809–864 (2006), arXiv:0603380 [cond-mat] .

[31] D. E. Bliss, W. Walukiewicz, J. W. Ager, E. E. Haller, K. T. Chan, and S. Tanigawa, "Annealing studies of low-temperature-grown GaAs:Be," J. Appl. Phys. **71**, 1699 (1992).

[32] J. De Boeck, R. Oesterholt, a. Van Esch, H. Bender, C. Bruynseraede, C. Van Hoof, and G. Borghs, "Nanometer-scale magnetic MnAs particles in GaAs grown by molecular beam epitaxy," Appl. Phys. Lett. **68**, 2744 (1996).

[33] R. Campion, K. W. Edmonds, L. X. Zhao, K. Y. Wang, C. Foxon, B. Gallagher, and C. Staddon, "High-quality GaMnAs films grown with arsenic dimers," J. Cryst. Growth **247**, 42–48 (2003).

[34] K. Yu, W. Walukiewicz, T. Wojtowicz, I. Kuryliszyn, X. Liu, Y. Sasaki, and J. K. Furdyna, "Effect of the location of Mn sites in ferromagnetic Ga1-xMnxAs on its Curie temperature," Phys. Rev. B **65**, 201303 (2002).

[35] F. Máca and J. Mašek, "Electronic states in Ga1-xMnxAs: Substitutional versus interstitial position of Mn," Phys. Rev. B **65**, 235209 (2002).

[36] P. Korzhavyi, I. Abrikosov, E. Smirnova, L. Bergqvist, P. Mohn, R. Mathieu, P. Svedlindh, J. Sadowski, E. Isaev, Y. Vekilov, and O. Eriksson, "Defect-Induced Magnetic Structure in (Ga1-xMnx)As," Phys. Rev. Lett. **88**, 187202 (2002).

[37] K. Y. Wang, "Influence of the Mn interstitial on the magnetic and transport properties of (Ga,Mn)As," J. Appl. Phys. **95**, 6512 (2004).

[38] K. W. Edmonds, K. Y. Wang, R. P. Campion, a. C. Neumann, N. R. S. Farley, B. L. Gallagher, and C. T. Foxon, “High-Curie-temperature Ga[sub 1 - x]Mn[sub x]As obtained by resistance-monitored annealing,” Appl. Phys. Lett. **81**, 4991 (2002).

[39] K. W. Edmonds, P. Bogusławski, K. Wang, R. P. Campion, S. V. Novikov, N. R. S. Farley, B. L. Gallagher, C. T. Foxon, M. Sawicki, T. Dietl, M. Buongiorno Nardelli, and J. Bernholc, “Mn Interstitial Diffusion in (Ga,Mn)As,” Phys. Rev. Lett. **92**, 037201 (2004).

[40] B. Rache Salles, J. C. Girard, C. David, F. Offi, F. Borgatti, M. Eddrief, V. H. Etgens, L. Simonelli, M. Marangolo, and G. Panaccione, “Electronic properties of embedded MnAs nano-clusters in a GaAs matrix and (Ga,Mn)As films: Evidence of distinct metallic character,” Appl. Phys. Lett. **100**, 203121 (2012).

[41] K. Lawniczak-Jablonska, J. Libera, a. Wolska, M. T. Klepka, P. Dluzewski, J. Bak-Misiuk, E. Dynowska, P. Romanowski, J. Z. Domagala, J. Sadowski, a. Barcz, D. Wasik, a. Twardowski, and a. Kwiatkowski, “Structural and magnetic properties of GaAs:(Mn,Ga)As granular layers,” Phys. Status Solidi **248**, 1609–1614 (2011).

[42] M. Moreno, B. Jenichen, V. M. Kaganer, W. Braun, A. Trampert, L. Däweritz, and K. Ploog, “MnAs nanoclusters embedded in GaAs studied by x-ray diffuse and coherent scattering,” Phys. Rev. B **67**, 235206 (2003).

[43] P. J. Wellmann, J. M. Garcia, J.-L. Feng, and P. M. Petroff, “Formation of nanoscale ferromagnetic MnAs crystallites in low-temperature grown GaAs,” Appl. Phys. Lett. **71**, 2532 (1997).

[44] J. Shi, J. M. Kikkawa, D. D. Awschalom, G. Medeiros-Ribeiro, P. M. Petroff, and K. Babcock, “Magnetic properties and imaging of Mn-implanted GaAs semiconductors,” J. Appl. Phys. **79**, 5296 (1996).

[45] S. S. A. Seo, “Nondestructive spectroscopic method to detect MnAs metallic nanocrystals in annealed GaAs:Mn,” J. Appl. Phys. **95**, 8172 (2004).

[46] A. Kovács, T. Kasama, J. Sadowski, T. Dietl, and R. E. Dunin-Borkowski, “Aberration-corrected electron microscopy of MnAs and As nanocrystals and voids in annealed (Ga,Mn)As,” J. Phys. Conf. Ser. **326**, 012018 (2011).

[47] I. N. Demchenko, K. Lawniczak-Jablonska, T. Story, V. Osinniy, R. Jakiela, J. Z. Domagala, J. Sadowski, M. Klepka, a. Wolska, and M. Chernyshova, “Modification of the local atomic structure around Mn atoms in (Ga, Mn)As layers by high temperature annealing,” J. Phys. Condens. Matter **19**, 496205 (2007).

[48] M. Moreno, A. Trampert, B. Jenichen, L. Däweritz, and K. H. Ploog, “Correlation of structure and magnetism in GaAs with embedded Mn(Ga)As magnetic nanoclusters,” J. Appl. Phys. **92**, 4672 (2002).

[49] M. Yokoyama, H. Yamaguchi, T. Ogawa, and M. Tanaka, "Zinc-blende-type MnAs nanoclusters embedded in GaAs," J. Appl. Phys. **97**, 10D317 (2005).

[50] M. Moreno, a. Trampert, L. Däweritz, and K. Ploog, "MnAs nanoclusters embedded in GaAs: synthesis and properties," Appl. Surf. Sci. **234**, 16–21 (2004).

[51] M. Moreno, V. Kaganer, B. Jenichen, A. Trampert, L. Däweritz, and K. Ploog, "Micromechanics of MnAs nanocrystals embedded in GaAs," Phys. Rev. B **72**, 115206 (2005).

[52] D. W. Rench, P. Schiffer, and N. Samarth, "Structural and magnetic characteristics of MnAs nanoclusters embedded in Be-doped GaAs," Phys. Rev. B **84**, 094434 (2011), arXiv:arXiv:1105.4669v1 .

[53] C. Zener, "Interaction between the d-Shells in the Transition Metals. III. Calculation of the Weiss Factors in Fe, Co, and Ni," Phys. Rev. **83**, 299–301 (1951).

[54] C. Zener, "Interaction Between the d Shells in the Transition Metals," Phys. Rev. **81**, 440–444 (1951).

[55] T. Dietl, "Zener Model Description of Ferromagnetism in Zinc-Blende Magnetic Semiconductors," Science (80-.). **287**, 1019–1022 (2000).

[56] T. Dietl, "Hole-mediated ferromagnetism in tetrahedrally coordinated semiconductors," Phys. Rev. B **63**, 195205 (2001).

[57] T. Dietl, "Ferromagnetic semiconductors," Semicond. Sci. Technol. **17**, 377–392 (2002).

[58] T. Jungwirth, K. Y. Wang, J. Mašek, K. W. Edmonds, J. König, J. Sinova, M. Polini, N. Goncharuk, A. MacDonald, M. Sawicki, A. Rushforth, R. P. Campion, L. X. Zhao, C. T. Foxon, and B. L. Gallagher, "Prospects for high temperature ferromagnetism in (Ga,Mn)As semiconductors," Phys. Rev. B **72**, 165204 (2005).

[59] F. Matsukura, H. Ohno, and T. Dietl, "III-V Ferromagnetic Semiconductors," in *Handb. Magn. Mater.*, Vol. 14, edited by K. H. J. Buschow (Elsevier, Amsterdam, 2002) pp. 1–87.

[60] V. Novák, K. Olejník, M. Cukr, L. Smrčka, Z. Remeš, and J. Oswald, "Substrate temperature changes during molecular beam epitaxy growth of GaMnAs," J. Appl. Phys. **102**, 083536 (2007).

[61] K. W. Edmonds, N. R. S. Farley, R. P. Campion, C. T. Foxon, B. L. Gallagher, T. K. Johal, G. van der Laan, M. MacKenzie, J. N. Chapman, and E. Arenholz, "Surface effects in Mn L[sub 3,2] x-ray absorption spectra from (Ga,Mn)As," Appl. Phys. Lett. **84**, 4065 (2004).

[62] V. Holý, Z. Matěj, O. Pacherová, V. Novák, M. Cukr, K. Olejník, and T. Jungwirth, "Mn incorporation in as-grown and annealed (Ga,Mn)As layers studied by x-ray diffraction and standing-wave fluorescence," Phys. Rev. B **74**, 245205 (2006).

[63] L. Horák, J. Matějová, X. Martí, V. Holý, V. Novák, Z. Šobáň, S. Mangold, and F. Jiménez-Villacorta, "Diffusion of Mn interstitials in (Ga,Mn)As epitaxial layers," Phys. Rev. B **83**, 245209 (2011).

[64] J. Adell, I. Ulfat, L. Ilver, J. Sadowski, K. Karlsson, and J. Kanski, "Thermal diffusion of Mn through GaAs overlayers on (Ga, Mn)As." J. Phys. Condens. Matter **23**, 085003 (2011).

[65] K. Olejník, V. Novák, M. Cukr, O. Pacherová, Z. Matěj, V. Holý, and M. Maryško, "GaMnAs annealing under various conditions: air vs. As cap," in *AIP Conf. Proc.*, Vol. 893 (AIP, 2007) pp. 1219–1220.

[66] D. A. Allwood, R. T. Carline, N. J. Mason, C. Pickering, B. K. Tanner, and P. J. Walker, "Characterization of oxide layers on GaAs substrates," Thin Solid Films **364**, 33–39 (2000).

[67] B. Schmid, *Surface preparation and Mn states of (Ga,Mn)As investigated by means of soft- and hard x-ray photoemission spectroscopy*, Ph.D. thesis, Universität Würzburg, Am Hubland, 97074 Würzburg (2010).

[68] L. X. Zhao, R. P. Campion, P. F. Fewster, R. W. Martin, B. Y. Ber, A. P. Kovarsky, C. R. Staddon, K. Y. Wang, K. W. Edmonds, C. T. Foxon, and B. L. Gallagher, "Determination of the Mn concentration in GaMnAs," Semicond. Sci. Technol. **20**, 369–373 (2005).

[69] R. Bacewicz, A. Twaróg, A. Malinowska, T. Wojtowicz, X. Liu, and J. K. Furdyna, "Local structure of Mn in (Ga,Mn)As probed by X-ray absorption spectroscopy," J. Phys. Chem. Solids **66**, 2004–2007 (2005).

[70] F. Glas, G. Patriarche, L. Largeau, and A. Lemaître, "Determination of the Local Concentrations of Mn Interstitials and Antisite Defects in GaMnAs," Phys. Rev. Lett. **93**, 086107 (2004).

[71] I. Frymark and G. Kowalski, "Mn impurity lattice location in the ferromagnetic zincblende gallium manganese arsenide layer structure," J. Phys. D. Appl. Phys. **38**, A160–A163 (2005).

[72] J. Mašek and F. Máca, "Interstitial Mn in (Ga,Mn)As: Binding energy and exchange coupling," Phys. Rev. B **69**, 165212 (2004).

[73] V. Holý, X. Martí, L. Horák, O. Caha, V. Novák, M. Cukr, and T. U. Schülli, "Density of Mn interstitials in (Ga,Mn)As epitaxial layers determined by anomalous x-ray diffraction," Appl. Phys. Lett. **97**, 181913 (2010).

[74] T.-L. Lee, C. Bihler, W. Schoch, W. Limmer, J. Daeubler, S. Thieß, M. S. Brandt, and J. Zegenhagen, "Fourier transform imaging of impurities in the unit cells of crystals: Mn in GaAs," Phys. Rev. B **81**, 235207 (2010).

[75] A. Mikkelsen, J. Gustafson, J. Sadowski, J. Andersen, J. Kanski, and E. Lundgren, "A study of the surface structure and composition of annealed $Ga_{0.96}Mn_{0.04}As(1\ 0\ 0)$," Appl. Surf. Sci. **222**, 23–32 (2004).

[76] T. Tsuruoka, R. Tanimoto, N. Tachikawa, S. Ushioda, F. Matsukura, and H. Ohno, "Microscopic identification of dopant atoms in Mn-doped GaAs layers," Solid State Commun. **121**, 79–82 (2002).

[77] A. M. Yakunin, A. Y. Silov, P. Koenraad, W. Van Roy, J. De Boeck, and J. Wolter, "Charge manipulation and imaging of the Mn acceptor state in GaAs by cross-sectional scanning tunneling microscopy," Superlattices Microstruct. **34**, 539–545 (2003).

[78] A. M. Yakunin, A. Silov, P. Koenraad, J. Wolter, W. Van Roy, J. De Boeck, J.-M. Tang, and M. Flatté, "Spatial Structure of an Individual Mn Acceptor in GaAs," Phys. Rev. Lett. **92**, 216806 (2004).

[79] A. Yakunin, A. Silov, P. Koenraad, J.-M. Tang, M. Flatté, W. Roy, J. Boeck, and J. Wolter, "Spatial Structure of Mn-Mn Acceptor Pairs in GaAs," Phys. Rev. Lett. **95**, 256402 (2005).

[80] S. J. C. Mauger, M. Bozkurt, P. Koenraad, A. D. Giddings, R. P. Campion, and B. L. Gallagher, "Short-period (Ga,Mn)As/(Al,Ga)As multilayer structures studied by cross-sectional scanning tunneling microscopy," Phys. Rev. B **84**, 104432 (2011).

[81] B. Grandidier, J. P. Nys, C. Delerue, D. Stiévenard, Y. Higo, and M. Tanaka, "Atomic-scale study of GaMnAs/GaAs layers," Appl. Phys. Lett. **77**, 4001 (2000).

[82] A. Mikkelsen, B. Sanyal, J. Sadowski, L. Ouattara, J. Kanski, S. Mirbt, O. Eriksson, and E. Lundgren, "Defect structure of $Ga_{1-x}Mn_xAs$: A cross-sectional scanning tunneling microscopy study," Phys. Rev. B **70**, 085411 (2004).

[83] A. Mikkelsen, L. Ouattara, H. Davidsson, E. Lundgren, J. Sadowski, and O. Pacherova, "Mn diffusion in $Ga_{1-x}Mn_xAs$/GaAs superlattices," Appl. Phys. Lett. **85**, 4660 (2004).

[84] J. Garleff, C. Çelebi, W. Van Roy, J.-M. Tang, M. Flatté, and P. Koenraad, "Atomically precise impurity identification and modification on the manganese doped GaAs(110) surface with scanning tunneling microscopy," Phys. Rev. B **78**, 075313 (2008).

[85] J. N. Gleason, M. E. Hjelmstad, V. D. Dasika, R. S. Goldman, S. Fathpour, S. Charkrabarti, and P. K. Bhattacharya, "Nanometer-scale studies of point defect distributions in GaMnAs alloys," Appl. Phys. Lett. **86**, 011911 (2005).

[86] G. Mahieu, P. Condette, B. Grandidier, J. P. Nys, G. Allan, D. Stiévenard, P. Ebert, H. Shimizu, and M. Tanaka, "Compensation mechanisms in low-temperature-grown $Ga_{1-x}Mn_xAs$ investigated by scanning tunneling spectroscopy," Appl. Phys. Lett. **82**, 712 (2003).

[87] A. Stroppa, X. Duan, M. Peressi, D. Furlanetto, and S. Modesti, "Computational and experimental imaging of Mn defects on GaAs (110) cross-sectional surfaces," Phys. Rev. B **75**, 195335 (2007).

[88] J. M. Sullivan, G. I. Boishin, L. J. Whitman, a. T. Hanbicki, B. T. Jonker, and S. C. Erwin, "Cross-sectional scanning tunneling microscopy of Mn-doped GaAs: Theory and experiment," Phys. Rev. B **68**, 235324 (2003).

[89] A. Oiwa, S. Katsumoto, A. Endo, M. Hirasawa, Y. Iye, H. Ohno, F. Matsukura, A. Shen, and Y. Sugawara, "Nonmetal-metal-nonmetal transition and large negative magnetoresistance in (Ga, Mn)As/GaAs," Solid State Commun. **103**, 209–213 (1997).

[90] K. W. Edmonds, N. Farley, T. Johal, G. van der Laan, R. P. Campion, B. Gallagher, and C. Foxon, "Ferromagnetic moment and antiferromagnetic coupling in (Ga,Mn)As thin films," Phys. Rev. B **71**, 064418 (2005).

[91] U. Pietsch, V. Holý, and T. Baumbach, *High-resolution X-ray Scattering from Thin Films to Lateral Nanostructures*, 2nd ed. (Springer, New York, 2004).

[92] J. Als-Nielsen and D. McMorrow, *Elements of Modern X-Ray Physics* (Wiley, New York, 2001).

[93] M. Abramowitz and I. A. Stegun, *Hanbook of Mathematical Functions* (National Bureau of Standards - U.S. Government Printing Office, 1972).

[94] L. Horák, Z. Šobáň, V. Holý, and K. Petr, "Study of Mn interstitials in (Ga, Mn)As using high-resolution x-ray diffraction." J. Phys. Condens. Matter **22**, 296009 (2010).

[95] K. M. Yu, M. Kaminska, and Z. Liliental-Weber, "Characterization of GaAs layers grown by low temperature molecular beam epitaxy using ion beam techniques," J. Appl. Phys. **72**, 2850 (1992).

[96] R. Feenstra, J. Woodall, and G. Pettit, "Observation of bulk defects by scanning tunneling microscopy and spectroscopy: Arsenic antisite defects in GaAs," Phys. Rev. Lett. **71**, 1176–1179 (1993).

[97] X. Liu, A. Prasad, J. Nishio, E. R. Weber, Z. Liliental-Weber, and W. Walukiewicz, "Native point defects in low-temperature-grown GaAs," Appl. Phys. Lett. **67**, 279 (1995).

[98] M. Levinshtein and M. Shur, *Handbook series on semiconductor parameters* (World Scientific Publishing Co. Pte. Ltd., 1995).

[99] J. Mašek, J. Kudrnovský, and F. Máca, "Lattice constant in diluted magnetic semiconductors (Ga,Mn)As," Phys. Rev. B **67**, 153203 (2003), arXiv:0302150 [cond-mat] .

[100] A. Shen, H. Ohno, F. Matsukura, Y. Sugawara, N. Akiba, T. Kuroiwa, A. Oiwa, A. Endo, S. Katsumoto, and Y. Iye, "Epitaxy of (Ga, Mn)As, a new diluted magnetic semiconductor based on GaAs," J. Cryst. Growth **175-176**, 1069–1074 (1997).

[101] A. Guinier, *X-Ray Diffraction: In Crystals, Imperfect Crystals, and Amorphous Bodies*, Dover Books on Physics (Dover Publications, 2013).

[102] D. Waasmaier and A. Kirfel, "New analytical scattering-factor functions for free atoms and ions," Acta Crystallogr. Sect. A Found. Crystallogr. **51**, 416–431 (1995).

[103] F. Glas, "The effect of the static atomic displacements on the structure factors of weak reflections in cubic semiconductor alloys," Philos. Mag. **84**, 2055–2074 (2004).

[104] A. Rosenauer, M. Schowalter, F. Glas, and D. Lamoen, "First-principles calculations of 002 structure factors for electron scattering in strained $In_xGa_{1-x}As$," Phys. Rev. B **72**, 085326 (2005).

[105] T. R. Welberry, *Diffuse X-Ray Scattering and Models of Disorder*, International Union of Crystallography Monographs on Crystallography (OUP Oxford, 2010).

[106] M. Krivoglaz, *Diffuse Scattering of X-Rays and Neutrons by Fluctuations* (Springer-Verlag, 1996).

[107] P. Wochner, M. Castro-Colin, S. N. Bogle, and V. N. Bugaev, "Of fluctuations and cross-correlations: finding order in disorder," Int. J. Mater. Res. (formerly Zeitschrift fuer Met. **102**, 874–888 (2011).

[108] F. D'Acapito, G. Smolentsev, F. Boscherini, M. Piccin, G. Bais, S. Rubini, F. Martelli, and A. Franciosi, "Site of Mn in Mn δ-doped GaAs: X-ray absorption spectroscopy," Phys. Rev. B **73**, 035314 (2006).

[109] S. Mirbt, B. Sanyal, and P. Mohn, "Magnetic properties of 3d impurities substituted in GaAs," J. Phys. Condens. Matter **14**, 3295–3302 (2002).

[110] R. Shioda, K. Ando, T. Hayashi, and M. Tanaka, "Local structures of III-V diluted magnetic semiconductors Ga1-xMnxAs studied using extended x-ray-absorption fine structure," Phys. Rev. B **58**, 1100–1102 (1998).

[111] F. D'Acapito, "Advanced methods for the analysis of x-ray absorption spectroscopy data applied to semiconductors," Semicond. Sci. Technol. **26**, 064004 (2011).

[112] J. Dabrowski and M. Scheffler, "Isolated arsenic-antisite defect in GaAs and the properties of EL2," Phys. Rev. B **40**, 10391–10401 (1989).

[113] D. J. Chadi and K. J. Chang, "Metastability of the Isolated Arsenic-Antisite Defect in GaAs," Phys. Rev. Lett. **60**, 2187–2190 (1988).

[114] J. I. Landman, C. G. Morgan, J. T. Schick, P. Papoulias, and A. Kumar, "Arsenic interstitials and interstitial complexes in low-temperature grown GaAs," Phys. Rev. B **55**, 15581–15586 (1997).

[115] T. Staab, R. Nieminen, J. Gebauer, R. Krause-Rehberg, M. Luysberg, M. Haugk, and T. Frauenheim, "Do Arsenic Interstitials Really Exist in As-Rich GaAs?" Phys. Rev. Lett. **87**, 045504 (2001).

[116] F. Tuomisto, K. Pennanen, K. Saarinen, and J. Sadowski, “Ga Sublattice Defects in (Ga,Mn)As: Thermodynamical and Kinetic Trends,” Phys. Rev. Lett. **93**, 055505 (2004).

[117] J. Sadowski and J. Z. Domagała, “Influence of defects on the lattice constant of GaMnAs,” Phys. Rev. B **69**, 075206 (2004).

[118] T. Dietl and H. Ohno, “Engineering magnetism in semiconductors,” Mater. Today **9**, 18–26 (2006).

[119] W. T. Vetterling, *Numerical Recipes Example Book (C++)*, Numerical recipes series (Cambridge University Press, 2002).

[120] “MATLAB,” (2006).

[121] Z. Matěj, “NLSQFIT,” .

[122] D. W. Marquardt, “An Algorithm for Least-Squares Estimation of Nonlinear Parameters,” J. Soc. Ind. Appl. Math. **11**, 431–441 (1963).

[123] T. Matsushita and J. Hayashi, “X-ray structure factors and the debye-waller factor of gallium arsenide crystals determined from full widths at half maximum of bragg case diffraction curves,” Phys. status solidi **139**, 139–145 (1977).

[124] N. Van Hung, C. S. Thang, N. C. Toan, and H. K. Hieu, “Temperature dependence of Debye-Waller factors of semiconductors,” Vacuum **101**, 63–66 (2014).

[125] A. W. Stevenson, “Thermal vibrations and bonding in GaAs: an extended-face crystal study,” Acta Crystallogr. Sect. A Found. Crystallogr. **50**, 621–632 (1994).

[126] R. Saravanan, S. K. Mohanlal, and K. S. Chandrasekaran, “Anharmonic temperature factors, anomalous-dispersion effects and bonding charges in gallium arsenide,” Acta Crystallogr. Sect. A Found. Crystallogr. **48**, 4–9 (1992).

[127] A. Titov, E. Kulatov, Y. A. Uspenskii, X. Biquard, D. Halley, S. Kuroda, E. Bellet-Amalric, H. Mariette, and J. Cibert, “Pre-edge features in X-ray absorption structure of Mn in GaMnN, GaMnAs and GeMn,” J. Magn. Magn. Mater. **300**, 144–147 (2006).

[128] N. A. Goncharuk, J. K. U. v. Era, and L. S. M. R. v. Ka, “Pre-edge XANES structure of Mn in (Ga,Mn) As from first principles,” **2**, 34–38 (2009).

[129] Y. Joly, “X-ray absorption near-edge structure calculations beyond the muffin-tin approximation,” Phys. Rev. B **63**, 125120 (2001).

[130] R. Jenkins, R. Manne, R. Robin, and C. Senemaud, “IUPAC—nomenclature system for x-ray spectroscopy,” X-Ray Spectrom. **20**, 149–155 (1991).

[131] R. W. Grosse-Kunstleve, "AtomInfo - Scattering factors etc. for ANSI C," (1996).

[132] K. Lonsdale, C. H. Macgillavry, and G. D. Rieck, eds., *International Tables for X-ray Crystallography Vol. III: Physical and chemical tables*, International Tables for X-ray Crystallography No. sv. 3 (Kynock Press, Birmingham, 1968).

[133] B. Henke, E. Gullikson, and J. Davis, "X-Ray Interactions: Photoabsorption, Scattering, Transmission, and Reflection at E = 50-30,000 eV, Z = 1-92," At. Data Nucl. Data Tables **54**, 181–342 (1993).

[134] K. Olejník, V. Novák, M. Cukr, J. Mašek, and T. Jungwirth, "Etching enhanced annealing of GaMnAs layers," J. Cryst. Growth **311**, 2151–2154 (2009).

[135] N. W. Ashcroft and N. D. Mermin, *Solid state physics* (Brooks Cole, 1976).

[136] S. M. Sze and K. K. Ng, *Physics of Semiconductor Devices* (John Wiley & Sons, New Jersey, 2007).

[137] R. D. Skeel and M. Berzins, "A Method for the Spatial Discretization of Parabolic Equations in One Space Variable," SIAM J. Sci. Stat. Comput. **11**, 1–32 (1990).

[138] H. Gummel, "A self-consistent iterative scheme for one-dimensional steady state transistor calculations," IEEE Trans. Electron Devices **11**, 455–465 (1964).

[139] A. Giddings, *Dilute magnetic semiconductor nanostructures*, Ph.D. thesis, University of Nottingham (2008).

[140] T. Jungwirth, W. Atkinson, B. Lee, and A. MacDonald, "Interlayer coupling in ferromagnetic semiconductor superlattices," Phys. Rev. B **59**, 9818–9821 (1999).

[141] I. Vurgaftman and J. Meyer, "Curie-temperature enhancement in ferromagnetic semiconductor superlattices," Phys. Rev. B **64**, 245207 (2001).

[142] J. Sadowski, R. Mathieu, and P. Svedlindh, "Ferromagnetic GaMnAs/GaAs superlattices—MBE growth and magnetic properties," Thin Solid Films (2002).

[143] S. Adachi, "GaAs, AlAs, and AlxGa1-xAs Material parameters for use in research and device applications," J. Appl. Phys. **58**, R1 (1985).

[144] I. Kuryliszyn-Kudelska, J. Z. Domagała, T. Wojtowicz, X. Liu, E. Lusakowska, W. Dobrowolski, and J. K. Furdyna, "The Effect of Mn Interstitials on the Lattice Parameter of Ga(1-x)Mn(x)As," J. Appl. Phys. **95**, 26 (2004).

[145] C. S. King, J. Zemen, K. Olejník, L. Horák, J. A. Haigh, V. Novák, A. C. Irvine, J. Kučera, V. Holý, R. P. Campion, B. L. Gallagher, and T. Jungwirth, "Strain control of magnetic anisotropy in (Ga,Mn)As microbars," Phys. Rev. B **83**, 115312 (2011), arXiv:arXiv:1007.2766v1 .

[146] "Multiphysics COMSOL MODELING GUIDE," (2005).

[147] A. A. Minkevich, E. Fohtung, T. Slobodskyy, M. Riotte, D. Grigoriev, T. Metzger, A. C. Irvine, V. Novák, V. Holý, and T. Baumbach, "Strain field in (Ga,Mn)As/GaAs periodic wires revealed by coherent X-ray diffraction," EPL (Europhysics Lett. **94**, 66001 (2011).

List of tables

5.1 Overview of studied samples A-1, B-1, B-2, and B-3 69
5.2 Determined parameters for A-1, B-1, B-2, and B-3 samples by HRXD 87

6.1 Overview of studied samples A-1, A-2, and A-3 89

7.1 Comparison of $c_{\mathrm{int,As}} - c_{\mathrm{int,Ga}}$ determined by several methods . . . 100

10.1 Parameters of multilayers resulted from fitting of reflectivity curves 124

11.1 Overview of sample sets C077 and C127 132
11.2 The determined mismatch of the (Ga,Mn)As layer for samples sets C077 and C127 140

List of figures

1.1 Photo of MBE device 11
1.2 Phasediagram of (Ga,Mn)As growth 12

2.1 Coordinate system $q_1 q_2$ in reciprocal space 19
2.2 Boundary conditions for Electromagnetic-intensities vectors in S- and P-polarization case 21
2.3 Schematic sketch of layered sample 22

3.1 Sketch of (Ga,Mn)As unit cell 26
3.2 Dependence of diffracted intensity on various-defect concentration 30
3.3 Atomic factors of Ga, As and Mn for different scattering vector length 32
3.4 Distortion correction with respect to individual defect concentrations 36
3.5 Distortion correction for anti-site defects 37
3.6 Calculated iso-intensity surfaces in parametric space 38

4.1 Sketch of HRXD setup 42
4.2 Optical elements in incident beam path of diffractometer 44
4.3 Photo of real experimental HRXRD machine 46
4.4 Sketch of rotation axes of diffractometer 47
4.5 Comparison of the two basic measurement modes 48
4.6 Tilt of diffractometer axis with respect to sample surface and crystallographic planes 52
4.7 Cut through reciprocal space showing diffraction maxima positions 54
4.8 Simulated paths in reciprocal space for two-axis measurement . . 56
4.9 Simulated paths in reciprocal space for iterative batch measurement 58
4.10 Comparison of merged two-axis measurement and loop-batch measurement 59
4.11 Measured intensity distribution along zigzag path for various samples 61
4.12 Extracted intensity compared with projected intensity map . . . 62
4.13 Comparison of high-resolution and open-detector measurements . 64
4.14 Comparison of measurements in grazing incidence and grazing exit coplanar geometries 65

5.1 Schematic description of the samples A-1, B-1–B-3 68
5.2 Measured data for sample A-1 69
5.3 Measured data for sample B-1 70

5.4 Measured data for sample B-2 70
5.5 Measured data for sample B-3 71
5.6 Emphasis of importance of different features in diffraction curve for fitting procedure 72
5.7 Demonstrative screenshot of fitting-program output 76
5.8 Schematic picture of samples representation in fitting program . 77
5.9 All measured diffraction curves fitted by numerical simulation . . 78
5.10 Experimental diffraction curves for sample B-2 80
5.11 Optimized values of interstitial densities resulted from numerical fit with fixed c_{sub} 81
5.12 Interstitial density in both non-equivalent positions optimized for the fixed values of c_{sub} and c_{anti} 82
5.13 Allowed (c_{sub},c_{anti})-pairs fulfilling the condition $c_{\mathrm{int,As}} = c_{\mathrm{int,Ga}}$ . . 82
5.14 Summed interstitial densities $c_{\mathrm{int,As}} + c_{\mathrm{int,Ga}}$ and their decrease after annealing 83
5.15 The changes in both interstitial densities after annealing 84
5.16 Comparison of $c_{\mathrm{int,As(Ga)}}$ for lattice parameter being calculated and being free fitting parameter 85
5.17 Comparison of $c^*_{\mathrm{int,As(Ga)}}$ obtained from fit with fixed c_{sub} and various fixed c_{anti} 86
5.18 Depth profiles of summed interstitial density determined for all samples 87

6.1 Schematic description of samples A-1, A-2, and A-3 90
6.2 Experimental XAS spectra for samples A-1–A-3 91
6.3 Selected parts of measured XAS spectra closely behind absorption edge 92

7.1 Energy corrections for scattering factors of As, Ga, and Mn . . . 96
7.2 Calculated change of diffracted intensity with respect to energy of radiation for various diffraction maxima 97
7.3 Calculated change of relative intensity with respect to energy for various defect density 98
7.4 Reciprocal space map around weak (002) maxima for sample B-2 99
7.5 Measured and fitted ratios of maximal intensity of the layer and the substrate peaks for samples A-1 and B-1 with respect to E . 99

8.1 Schematic sketch of the (Ga,Mn)As single layer 104

9.1 Depth profiles of the interstitial concentration in sample A, B-1, B-2 and B-3 followed from annealing simulation 117
9.2 Comparison of Drift-Diffusion and Diffusion simulations 118
9.3 Simulated depth profiles particle densities after 2 hours of post-growth annealing 118

10.1 Schematic picture of multilayer samples 121
10.2 Experimental reflectivity curves fitted with numerical simulations 122
10.3 Depth profiles of relative electron density plotted for multilayers 125
10.4 Experimental Δ for samples Al(20,30 and 40) 127

10.5 Calculated Mn concentrations (c_{sub}, c_{int}, and $c_{\mathrm{sub}} + c_{\mathrm{int}}$) for all possible values of relative Mn substitutional content 128

11.1 Micrograph for the sample C127#12 132
11.2 Selected part of reciprocal space map (224) for sample C077#10 135
11.3 Demonstration of shape-function influence in simulated diffraction maps. 137
11.4 Visualisation of calculated strain field distribution in all samples 139
11.5 Comparison of measured and simulated intensity maps (004) . . 140
11.6 Comparison of measured and simulated intensity maps (224) . . 141
11.7 Experimental data compared to simulation for C077#11 143
11.8 Experimental data compared to simulation for C077#12 144
11.9 Experimental data compared to simulation for C127#10 145
11.10 Experimental data compared to simulation for C127#11 146
11.11 Experimental data compared to simulation for C127#12 147

List of Abbreviations

AFM .... Atomic Force Microscopy
CTR .... Crystal Truncation Rod
D-D .... Drift-diffusion
DMS .... Diluted Magnetic Semiconductor
D-W .... Debye-Waller
EDX .... Energy Dispersive x-Ray
EPMA .... Electron Probe Microanalysis
EXAFS .... Extended x-Ray Absorption Fine Structure
FWHM .... Full width in a half of maximum
(Ga,Mn)As .... Gallium Manganese Arsenide
HRXRD .... High-Resolution x-Ray Diffraction
LT-GaAs .... Low-temperature GaAs
LT-MBE .... Low-Temperature Molecular Beam Epitaxial
MBE .... Molecular Beam Epitaxy
SEM .... Scanning Electron Microscopy
SIMS .... Secondary Ion Mass Spectrometry
STM .... Scanning Tunneling Microscopy
T_C .... Curie temperature
TEM .... Transmission Electron Microscopy
XANES .... X-Ray Near-Edge Structure
XAS .... X-Ray Absorption Spectroscopy
XMCD .... X-Ray Magnetic Circular Dichroism
XRD .... X-Ray Diffraction
XRF .... X-Ray Fluorescence
XRR .... X-Ray Reflectivity
XRSW .... X-Ray Standing-Wave
XSTM .... Cross-Sectional Scanning Tunneling Microscopy

List of Publications

1. L. Horák, V. Holý, C. R. Staddon, N. R. S. Farley, S. V. Novikov, R. P. Campion, and C. T. Foxon, "X-ray in-plane scattering investigation of GaN nanorods," J. Appl. Phys. **104**, 103504 (2008)

2. J. Krčmář, V. Holý, L. Horák, T. H. Metzger, and J. Sobota, "Standing-wave effects in grazing-incidence x-ray diffraction from polycrystalline multilayers," J. Appl. Phys. **103**, 033504 (2008)

3. V. Holý, R. Lechner, S. Ahlers, L. Horák, T. Metzger, A. Navarro-Quezada, A. Trampert, D. Bougeard, and G. Bauer, "Diffuse x-ray scattering from inclusions in ferromagnetic $Ge_{1-x}Mn_x$ layers," Phys. Rev. B **78**, 144401 (2008)

4. L. Horák, Z. Šobáň, V. Holý, and K. Petr, "Study of Mn interstitials in (Ga, Mn)As using high-resolution x-ray diffraction." J. Phys. Condens. Matter **22**, 296009 (2010)

5. X. Marti, T. Cechal, L. Horák, and V. Novak, "Structural and magnetic evidence of confined strain fields in GaMnAs grown on ordered arrays of zero-dimensional nanostructures," ArXiv e-prints (2010)

6. V. Holý, X. Martí, L. Horák, O. Caha, V. Novák, M. Cukr, and T. U. Schülli, "Density of Mn interstitials in (Ga,Mn)As epitaxial layers determined by anomalous x-ray diffraction," Appl. Phys. Lett. **97**, 181913 (2010)

7. L. Horák, J. Matějová, X. Martí, V. Holý, V. Novák, Z. Šobáň, S. Mangold, and F. Jiménez-Villacorta, "Diffusion of Mn interstitials in (Ga,Mn)As epitaxial layers," Phys. Rev. B **83**, 245209 (2011)

8. L. Horák, J. Matějová, X. Martí, V. Holý, V. Novák, Z. Šobáň, S. Mangold, and F. Jiménez-Villacorta, "STUDY OF Mn INTERSTITIALS IN (Ga, Mn) As USING HRXRD," Mater. Struct. **18**, 194–198 (2011)

9. C. S. King, J. Zemen, K. Olejník, L. Horák, J. A. Haigh, V. Novák, A. C. Irvine, J. Kučera, V. Holý, R. P. Campion, B. L. Gallagher, and T. Jungwirth, "Strain control of magnetic anisotropy in (Ga,Mn)As microbars," Phys. Rev. B **83**, 115312 (2011), arXiv:arXiv:1007.2766v1

10. M. Buljan, O. Roshchupkina, A. Šantić, V. Holý, C. Baehtz, A. Mücklich, L. Horák, V. Valeš, N. Radić, S. Bernstorff, and J. Grenzer, "Growth of a three-dimensional anisotropic lattice of Ge quantum dots in an amorphous alumina matrix," J. Appl. Crystallogr. **46**, 709–715 (2013)

11. J. Liu, J. H. Chu, C. R. Serrao, D. Yi, J. Koralek, C. Nelson, C. Frontera, D. Kriegner, L. Horak, E. Arenholz, J. Orenstein, A. Vishwanath, X. Marti, and R. Ramesh, "Tuning the electronic properties of $J_{\text{eff}} = 1/2$ correlated semimetal in epitaxial perovskite SrIrO3," ArXiv e-prints (2013), arXiv:1305.1732

List of Conference contributions

2007 **Struktura 2007** (Dvůr Králové, Czech Republic)
Annual Conference of Czech and Slovak Crystallographic Association
'Study of the Structure of GaMnAs thin layers' (oral presentation - student section)

2008 **X-TOP 2008** (Linz, Austria)
9th Biennial Conference on High Resolution X-Ray Diffraction and Imaging
'X-Ray Laboratory Investigation of GaN Nano-Rods' (poster presentation)

2009 **Struktura 2009** (Hluboká n. V., Czech Republic)
Annual Conference of Czech and Slovak Crystallographic Association
'Determination of Mn and P concentration in $Ga_{1-x}Mn_xAs_{1-y}P_y$*'* (oral presentation - student section)

2010 **X-TOP 2010** (Warwick, UK)
10th Biennial Conference on High Resolution X-Ray Diffraction and Imaging
'Study of Mn Interstitials in (Ga,Mn)As Using High-Resolution X-Ray Diffraction' (oral presentation)

2011 **Struktura 2011** (Turnov, Czech Republic)
Annual Conference of Czech and Slovak Crystallographic Association
'Study of Mn Interstitials in (Ga,Mn)As using HRXRD' (oral presentation - student section)

2011 **E-MRS 2011 Fall Meeting** (Warsaw, Poland)
European Materials Research Society conference
'Diffusivity of Mn Interstitials in Thin (Ga,Mn)As Layers Studied by High-Resolution X-Ray Diffraction' (oral presentation)

2012 **Struktura 2012** (Klatovy, Czech Republic)
Annual Conference of Czech and Slovak Crystallographic Association
'Simulation of Reciprocal Space Maps from Elastic Strain Field in Periodical Nanostructures' (oral presentation)

2012 **MRS Spring Meeting** (San Francisco, USA)
Conference of Materials Research Society
'Diffusivity of Mn Interstitials in Thin (Ga,Mn)As Layers Studied by High-Resolution X-Ray Diffraction (oral presentation)